Suborbital Soft X-Ray Spectroscopy with Gaseous Electron Multipliers

by

Thomas D. Rogers

B.A. Physics, University of Colorado, 2009

B.A., Astronomy, University of Colorado, 2009

M.S., Astrophysics, University of Colorado, 2011

A thesis submitted to the

Faculty of the Graduate School of the

University of Colorado in partial fulfillment

of the requirements for the degree of

Doctor of Philosophy

Department of Astrophysical and Planetary Sciences

2016

This thesis entitled:
Suborbital Soft X-Ray Spectroscopy with Gaseous Electron Multipliers
written by Thomas D. Rogers
has been approved for the Department of Astrophysical and Planetary Sciences

Prof. Webster Cash

Prof. Kevin France

Prof. James Green

Prof. Robert Marshall

Prof. Randall McEntaffer

Date

The final copy of this thesis has been examined by the signatories, and we find that both the content and the form meet acceptable presentation standards of scholarly work in the above mentioned discipline.

Rogers, Thomas D. (Ph.D., Astrophysics)

Suborbital Soft X-Ray Spectroscopy with Gaseous Electron Multipliers

Thesis directed by Prof. Webster Cash

This thesis consists of the design, fabrication, and launch of a sounding rocket payload to observe the spectrum of the soft X-ray emission (0.1-1 keV) from the Cygnus Loop supernova remnant. This instrument, designated the Off-plane Grating Rocket for Extended Source Spectroscopy (OGRESS), was launched from White Sands Missile Range on May 2nd, 2015. The X-ray spectrograph incorporated a wire-grid focuser feeding an array of gratings in the extreme off-plane mount which dispersed the spectrum onto Gaseous Electron Multiplier (GEM) detectors. The gain characteristics of OGRESS's GEM detectors were fully characterized with respect to applied voltage and internal gas pressure, allowing operational settings to be optimized. The GEMs were optimized to operate below laboratory atmospheric pressure, allowing lower applied voltages, thus reducing the risk of both electrical arcing and tearing of the thin detector windows. The instrument recorded 388 seconds of data and found highly uniform count distributions over both detector faces, in sharp contrast to the expected thermal line spectrum. This signal is attributed to X-ray fluorescence lines generated inside the spectrograph. The radiation is produced when thermal ionospheric particles are accelerated into the interior walls of the spectrograph by the high voltages of the detector windows. A fluorescence model was found to fit the flight data better than modeled supernova spectra. Post-flight testing and analysis revealed that electrons produce distinct signal on the detectors which can also be successfully modeled as fluorescence emission.

Dedication

To Stephanie, my wife, who waited for me.

Acknowledgements

There are many people who helped make this project happen, either as direct team members or greatly needed moral support. I will first thank my team at the University of Iowa. The community you made me a part of is something I don't expect to find again: Randy, who gave me this opportunity and exposed me to my first sounding rocket; Ted and Kristi, who made me truly feel part of their family; Drew and Jake for all the hard work and for being awesome travel partners (OG3 for life!); Casey, James, Hannah, and Tom, for both help in the lab and sanity outside it.

Thanks go to my advisor, Web, for giving me so many opportunities, starting in high school and culminating in a PhD.

Thanks must be given to the personell at Wallops Flight Facility and White Sands Missile Range for their hospitality and concerted efforts to make this rocket fly.

To the folks at CASA, whether you've moved on or are still there, you've been my community from my earliest days of rocketry. Thanks to Randy (again), Phil, and Ben, for laying the groundwork for this project; Eric and Brennan, for providing more inspiration for rocketry; Bobby, Nico, and Sarah, for being great friends and coworkers. A special thanks goes to Mikey, who taught me everything I know about working in a lab. An extra special thanks goes to Eric; it's not every day you meet someone who'll let you work on a rocket *and* marry their sister.

To my parents, who made me the person I am and believed in me every step of the way.

Finally, thank you to my wife, Stephanie, who now has more experience with sounding rockets than most rocket PhDs do.

Contents

Chapter

Tables

Table

Figures

Figure

Chapter 1

Introduction

Supernova explosions are some of the most common and energetic events in the universe. They occur in two main types. In Core-collapse supernovae, a massive star has exhausted its nuclear fuel, collapses in upon itself and then rebounds in a massive explosion. In thermonuclear supernovae a white dwarf accretes enough mass to pass the Chandrasekhar limit. When this occurs, the white dwarf explodes at the sudden onset of nuclear fusion. In both cases, the explosion leaves behind a supernova remnant (SNR), which consists of an expanding cloud of debris, or ejecta, from the explosion, as well as surrounding material that gets swept up along the way. SNRs contain a wealth of information about their progenitor object, as well as the explosion process itself. SNRs also profoundly influence their surrounding environment (and vice versa). Each supernova releases $\sim 10^{51}$ ergs of kinetic energy. The ejecta expand and sweep up material from the surrounding interstellar medium (ISM). This process mixes the metal-enriched material from the SNR into the ISM, and helps seed the next generation of stars. Indeed, SNRs are a major contributor to matter redistribution within the galaxy and the universe. Ejected material can expand outside the disk of the galaxy where it can either escape into the intergalactic medium (IGM) or rain back down in a galactic fountain. SNRs are directly or indirectly connected to the lives and deaths of massive stars (or white dwarfs), the dynamics and kinematics of the ISM, the metal-enrichment of the universe, and the initiation of new star formation.

1.1 Supernova Remnant Evolution

SNRs evolve over time as they expand and sweep up more material from their surrounding environments in a massive shock wave. SNRs follow four general stages of evolution, assuming the ejecta expand into a homogeneous environment. In the first phase, the mass of the ejecta greatly exceeds that of any swept-up material, and the remnant expands relatively unimpeded. In the second stage, the mass of the swept-up material exceeds that of the ejecta, and the expansion begins to slow down. In this phase, the expansion is still rapid, and the ejecta have little time to cool, resulting in adiabatic expansion. In the third phase, energy losses from radiation have become important. This occurs because the remnant has had substantial time to cool. Additionally, cooling processes become more efficient at lower temperatures, providing positive feedback. In this stage, the shock can be thought of as isothermal. The fourth and final phase (sometimes referred to as the Confusion phase) occurs when the pressure within the remnant equals that of the surrounding ISM, at which point the SNR will merge with, and become indistinguishable from, its surrounding environment.

1.1.1 Phase I: Free Expansion

The earliest stage is known as the Free-Expansion stage. In this stage, the mass of the ejecta expands unimpeded with energy of $\sim 10^{51}$ ergs and an initial blast velocity of $\sim 10^4$ km/s (Chevalier [1977]). The surrounding ISM material moves at only ~ 10 km/s and is swept-up during this process, becoming shocked. The stage ends when the mass of the swept-up ISM equals that of the ejecta. This occurs when

$$M_{ISM} = \frac{4}{3}\pi R^3 n_0 \mu m_H = M_{ejecta} \tag{1.1}$$

where R is the radius of the remnant, n_0 is the number density of the surrounding ISM (assuming a homogeneous surrounding), μ is the mean molecular weight (assumed to be 1 for simplicity), and m_H is the mass of hydrogen. This gives a radius of

$$R_{SNR}(phase\ I) = \left(\frac{3M_{ejecta}}{4\pi n_0 m_H}\right)^{1/3}. \tag{1.2}$$

For typical conditions, this corresponds to

$$R_{SNR}(phase\ I) = 2.0\left(\frac{n_0}{1\ \mathrm{cm}^{-3}}\right)^{-1/3}\frac{M_{ejecta}}{1M_\odot}^{1/3}\ \mathrm{pc} \tag{1.3}$$

where $M_\odot$ is the solar mass. In the Free-Expansion phase, the velocity of the expansion is considered to be constant and, for typical conditions takes the value

$$v_0(phase\ I) = 10,000\left(\frac{E_{SNR}}{10^{51}\mathrm{erg}}\right)\left(\frac{1M_\odot}{M}\right)^{1/2}\mathrm{km/s}. \tag{1.4}$$

The amount of time it take to reach $R_{SNR}(phase\ I)$ can be simply estimated as

$$t \sim \frac{R_{SNR}(phase\ I)}{v_0} \sim 202\left(\frac{n_0}{1\ \mathrm{cm}^{-3}}\right)^{-1/3}\left(\frac{M_{ejecta}}{1M_\odot}\right)^{1/3}\left(\frac{v_0}{10,000\mathrm{km/s}}\right)^{-1}\mathrm{yr} \tag{1.5}$$

$$= 202\left(\frac{n_0}{1\ \mathrm{cm}^{-3}}\right)^{-1/3}\left(\frac{M_{ejecta}}{1M_\odot}\right)^{1/3}\left(\frac{E_{SNR}}{10^{51}\mathrm{ergs}}\right)^{-1/2}\mathrm{yr}. \tag{1.6}$$

Thus, the Free-Expansion phase lasts 200 years in which time the SNR expands to several parsecs in diameter. Toward the end of this phase, the outer ejecta begin to decelerate. Assuming that energy is conserved in this phase, the outer ejecta will end with a velocity of $v = v_0/\sqrt{2} \sim 7,000$ km/s. As the more interior ejecta catch up with the outer ejecta, a reverse-shock is formed that reheats the interior of the SNR. This reverse-shock actually travels outwards (at least at first), but more slowly than the ejecta or forward-shock.

1.1.2 Phase II: Adiabatic Expansion

When the mass of the swept-up material exceeds that of the ejecta, the SNR enters the Adiabatic, or Sedov-Taylor phase. During this phase, the SNR continues to expand due to its high pressure, but steadily slows down as more mass is swept up. As long as the shock velocity remains above 250 km/s (corresponding to $\sim 10^6$ K), gas cooling is inefficient due to the low density, and

because nearly all atoms are fully ionized. Thus, energy is still conserved, and we can consider this conservation of energy when discussing the dynamics of this phase of expansion. To begin, we will consider the kinetic energy of the swept-up material

$$E_k = \frac{1}{2}\int_0^{R_{SNR}} 4\pi R^2 \rho v^2 \mathrm{d}R = \frac{2\pi}{3} R_{SNR}^3 \rho_0 v_s^2 \phi_k, \tag{1.7}$$

where ϕ_k is defined as the average kinetic energy in units of Mv_s^2,

$$\phi_k = \frac{1}{Mv_s^2}\int_0^{R_{SNR}} 4\pi R^2 \rho v^2 \mathrm{d}R, \tag{1.8}$$

with M and v_s being the mass of the SNR and the shock velocity. We have also ignored the mass of the ejecta relative to that of the swept-up material. The internal energy of the swept up gas is

$$E_i = \int_0^{R_{SNR}} 4\pi R^2 \frac{P}{\gamma - 1}\mathrm{d}R = \frac{4\pi}{3} R_{SNR}^3 \rho_0 v_s^2 \frac{2}{\gamma^2 - 1}\phi_i, \tag{1.9}$$

where P is the pressure, γ is the ratio of specific heats, and ϕ_i is the average pressure of the gas in the hot bubble in units of the post-shock pressure, P_1,

$$\phi_i = \frac{3}{4\pi R_{SNR}^3 P_1}\int_0^{R_{SNR}} 4\pi R^2 P \mathrm{d}R, \tag{1.10}$$

and we have used $P_1 = 2\rho_0 v_s^2/(\gamma + 1)$. The ratio of the kinetic to the internal energy of the blast wave is then

$$\frac{E_k}{E_i} = \frac{(\gamma^2 - 1)\phi_k}{4\phi_i}. \tag{1.11}$$

Both the kinetic and the internal energy of the hot gas in the bubble have now been expressed in terms of the kinetic energy of a mass $M = 4\pi R_{SNR}^3 \rho_0/3$, of hot gas expanding at the shock velocity, v_s. From energy conservation, ($E_{SNR} = E_k + E_i$), we find that

$$R_{SNR}^3 v_s^2 = \left(\frac{2}{5}\right)^2 \xi_0 \frac{E_{SNR}}{\rho_0}, \tag{1.12}$$

where ξ_0 is

$$\xi_0 = \frac{75}{8\pi}(\phi_k + \frac{4}{(\gamma^2-1)}\phi_i)^{-1}. \tag{1.13}$$

Assuming that ϕ_k and ϕ_i are constants during this phase, v_s will scale with $R_{SNR}^{-3/2}$. Because $v_s = \mathrm{d}R_{SNR}/\mathrm{d}t$, this equation can be integrated to give

$$R_{SNR}(t)(phase\ II) = \left(\frac{\xi_0 E_{SNR}}{\rho_0}\right)^{1/5} t^{2/5}, \tag{1.14}$$

and the shock velocity,

$$v_s(t)(phase\ II) = \frac{2}{5}\left(\frac{\xi_0 E_{SNR}}{\rho_0}\right)^{1/5} t^{-3/5}. \tag{1.15}$$

The temperature corresponding to the average pressure of the hot bubble is then

$$T_1 = \left(\frac{\phi_i}{+1}\right)\frac{8}{25k}\left(\frac{\xi_0 E_{SNR}}{\rho_0}\right)^{2/5} t^{-6/5}. \tag{1.16}$$

Thus, the expansion of the SNR is determined by the total energy of the explosion, the density of the ambient medium, and by the constants ϕ_k and ϕ_i or, equivalently, the mean pressure and mean kinetic energy of the gas in the hot bubble. For a blast wave expanding in a homogeneous medium with a constant ratio of specific heats of $\gamma = 5/3$ (adiabatic conditions), $\phi_k = 0.417$ and $\phi_i = 0.470$ (Tielens [2005]). With these values, $\xi_0 = 2.026$, and $E_k/E_i = 0.394$. We can now write the size, shock velocity, and post-shock temperature of the SNR in terms of typical conditions:

$$R_{SNR}(t)(phase\ II) \simeq 12.6\left(\frac{E_{SNR}}{10^{51}\mathrm{erg}}\right)^{1/5}\left(\frac{n_0}{1\ \mathrm{cm}^{-3}}\right)^{-1/5}\left(\frac{t}{10^4\mathrm{years}}\right)^{2/5}\mathrm{pc}, \tag{1.17}$$

$$v_s(t)(phaseII) \simeq 496\left(\frac{E_{SNR}}{10^{51}erg}\right)^{1/5}\left(\frac{n_0}{1\ \mathrm{cm}^{-3}}\right)^{-1/5}\left(\frac{t}{10^4\mathrm{years}}\right)^{-3/5}\mathrm{km/s}, \tag{1.18}$$

$$T_1 \simeq 6\times10^6\left(\frac{E_{SNR}}{10^{51}\mathrm{erg}}\right)^{2/5}\left(\frac{n_0}{1\ \mathrm{cm}^{-3}}\right)^{-2/5}\left(\frac{t}{10^4\mathrm{years}}\right)^{-6/5}\mathrm{K}. \tag{1.19}$$

This phase is generally considered to last until the shock velocity drops to 250 km/s ($T \simeq 10^6$ K) where radiative cooling becomes effective. This occurs at $t \simeq 3.9\times10^4$ years when the remnant

is $\sim$ 25 pc in size. The total swept-up mass is roughly 2200 $M_\odot$ at an ambient density of 1 cm^{-3}. Note that, in practice, these values can vary greatly from remnant to remnant depending on ambient conditions. In particular, a SNR evolving in a non-homogeneous medium may evolve quite differently in different areas, and can even be in different evolutionary phases in different areas.

1.1.3 Phase III: Radiative Expansion

The third phase of SNR evolution is known as the Radiative phase. At this point, the gas has cooled to $\sim 10^6$ K, and atoms can now efficiently recombine and produce radiative cooling. The shock wave can now be considered as isothermal. The remnant continues to expand due to a high internal pressure relative to the surrounding medium, but energy is no longer conserved, as the remnant loses significant energy to radiative cooling. When the post-shock temperature approaches the temperature of the pre-shock medium, the density contrast across the shock can become very large (>100). The recently shocked material is almost stationary in the frame of the shock, and a thin, dense shell of shocked gas will develop. If we assume that all the mass in the SNR is located in this dense shell at R_{SNR}, moving into the ISM at a velocity v_s, the dynamics of the SNR during this phase is governed by the momentum equation,

$$\frac{d(Mv_s)}{dR_{SNR}} = \frac{4\pi R_{SNR}^2}{v_s}(\bar{P} - P_0), \tag{1.20}$$

with $\bar{P}$ being the mean pressure of the hot gas and P_0 being the external pressure. We make the additional assumptions that the hot gas interior to the dense shell has no radiative energy losses and that the external pressure can be ignored. This allows us to consider the expansion as self-similar. For the pressure of the hot gas, $\bar{P} \sim V^{-\gamma}$, with V being the volume of the remnant and γ being the ratio of the specific heats. For a monatomic gas, $\gamma = 5/3$, and $P \sim R^{-5}$. The mass of swept-up gas is $4\pi R_{SNR}^3 \rho_0/3$. Under the assumption of self-similarity, $R = R_0 t^\eta$ and $v_s = \eta R_0 t^{\eta-1}$ results in $\eta = 2/7$ and $\bar{P} = \rho_0 v_s^2/6$. We will normalize these results to the mass, M_0, and the velocity v_0, at the end of phase II. We will use $v_0 = 250$ km/s, as discussed in the previous section. This results in a mass of

$$M_0 = 1400\left(\frac{E_{SNR}}{10^{51}\mathrm{erg}}\right)^{11/45}\left(\frac{n_0}{1\ \mathrm{cm}^{-3}}\right)^{4/15} M_\odot, \tag{1.21}$$

at the end of phase II and the beginning of phase III. The evolution of the SNR during phase III can now be given with the following equations:

$$R_{SNR}(t)(phase\ III) = 21.6\left(\frac{E_{SNR}}{10^{51}\mathrm{erg}}\right)^{11/45}\left(\frac{n_0}{1\ \mathrm{cm}^{-3}}\right)^{-11/45}\left(\frac{t}{t_0}\right)^{2/7} \mathrm{pc}, \tag{1.22}$$

$$M(t)(phase\ III) = M_0\left(\frac{t}{t_0}\right)^{6/7} M_\odot, \tag{1.23}$$

$$v_s(t)(phase\ III) = 250\left(\frac{t}{t_0}\right)^{-5/7} \mathrm{km/s}, \tag{1.24}$$

where the normalization time, t_0, is given by

$$t_0(phase\ III) = 2.4\times10^4\left(\frac{E_{SNR}}{10^{51}\mathrm{erg}}\right)^{11/45}\left(\frac{n_0}{1\ \mathrm{cm}^{-3}}\right)^{-11/45} \mathrm{years}. \tag{1.25}$$

This stage lasts until the shock velocity has fallen to approximately the ISM speed of sound ($\sim$12 km/s). This corresponds to a time,

$$\tau = 1.7\times10^6\left(\frac{E_{SNR}}{10^{51}\mathrm{erg}}\right)^{11/45}\left(\frac{n_0}{1\ \mathrm{cm}^{-3}}\right)^{-11/45} \mathrm{years} \tag{1.26}$$

corresponding to a final size of $\sim$ 74 pc. At this point, the remnant becomes indistinguishable from the ISM and disappears. It is likely that much of the diffuse X-ray emission within the galaxy is associated with SNRs which have merged with the ISM.

1.1.4 Expansion into a Decreasing Density Gradient

The discussion in the previous sections has addressed the case of a SNR expanding into a homogeneous medium, which is rarely the case in true astrophysical environments. Due to its relevance to the Cygnus Loop, the science target of this investigation, we will now consider the case of a phase II SNR evolution expanding into a medium with a decreasing density gradient, as would be generated by winds from a precursor star. In this case, the density of the ambient medium is not

constant but follows a R^{-2} dependence. Following the derivation of Ostriker and McKee [1988], the evolution of a SNR expanding into a precursor wind can be described with the following equations:

$$R_{SNR}(t) = 41.7\left(\frac{E_{SNR}}{10^{51}\text{erg}}\right)^{1/3}\left(\frac{n_0 R_{phaseI}}{1\ \text{cm}^{-3}}\right)^{-1/3}\left(\frac{t}{10^4\text{years}}\right)^{2/3}\text{pc} \tag{1.27}$$

$$v_s(t) = 2725\left(\frac{E_{SNR}}{10^{51}\text{erg}}\right)^{1/3}\left(\frac{n_0 R_{PhaseI}}{1\ \text{cm}^{-3}}\right)^{-1/3}\left(\frac{t}{10^4 years}\right)^{1/3}\text{km/s}. \tag{1.28}$$

To slow to $v_s \simeq 250$ km/s now takes $\sim 1.3\times10^7$ years. This never occurs in practice, however, as the SNR will encounter inhomogeneities long before it reaches the ~ 5000 pc scale associated with this time. Even if this were not the case, the span of the R^{-2} density gradient is limited to a much smaller size by the lifetime of the progenitor star. Regardless, (1.27) and (1.28) demonstrate that a SNR expanding into a pre-made stellar wind cavity will not enter phase III until it has encountered the cavity walls or some other inhomogeneity within the ISM.

1.2 X-Ray Emission from Supernova Remnants

Due to the high energies involved, SNRs are generally best observed in X-rays. SNRs produce vast quantities of thermal X-ray emission due to the high temperature of the ejecta and the subsequent shock-heating of the swept-up material. An in-going shock wave is also generated which reheats the interior of the remnant. A substantial amount of nonthermal X-ray emission is also produced due to the acceleration of energetic particles, leading to synchrotron radiation. Unfortunately, X-rays are easily absorbed by interstellar gas, making it difficult to observe most SNRs at these energies. This is particularly true at the softest energies (<1 keV) associated with many of the most abundant elements, such as carbon and oxygen. For this reason, soft X-ray observations of SNRs are limited to objects which are relatively close (within several kpc), such that the interstellar absorption is low.

1.2.1 Bremsstrahlung

Bremsstrahlung, or free-free emission, occurs when charged particles collide (and accelerate each other) in a plasma. Due to the mass difference, ions are accelerated far less than electrons, and their emission is generally considered to be negligible. To understand the emission process of bremsstrahlung, we will consider the case of a single electron or equivalently, an electron population with a single uniform speed. We will consider an electron (charge e) moving past an ion of charge Ze with an impact parameter of b, (see Figure 1.1). The dipole moment is $\mathbf{d}(t) = -e\mathbf{R}$, and its second derivative is

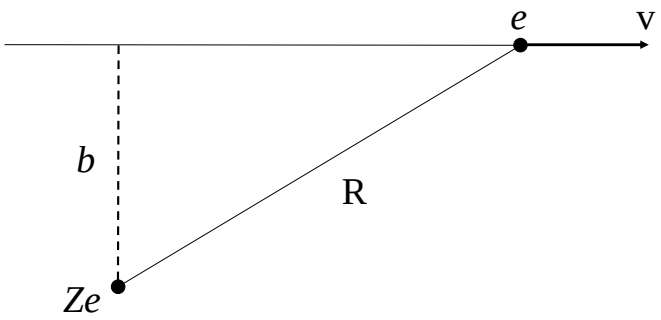

Figure 1.1: An electron of charge e moving past an ion of charge Ze will be accelerated and emit bremsstrahlung radiation.

$$\ddot{\mathbf{d}}(t) = -e\dot{\mathbf{v}}, \tag{1.29}$$

where $\mathbf{v}$ is the velocity of the electron. The Fourier transform of $\mathbf{d}$ can be defined as

$$\mathbf{d}(t) = \int_{-\infty}^{\infty} e^{-i\omega t}\hat{\mathbf{d}}(\omega)d\omega \tag{1.30}$$

so that

$$\ddot{\mathbf{d}}(t) = -\int_{-\infty}^{\infty} \omega^2 \hat{\mathbf{d}}(\omega) e^{-i\omega t} d\omega. \tag{1.31}$$

The Fourier transform of $\ddot{\mathbf{d}}$ is then

$$\hat{\ddot{\mathbf{d}}} = -\omega^2 \hat{\mathbf{d}}(\omega) = \frac{e}{2\pi} \int_{-\infty}^{\infty} \dot{\mathbf{v}} e^{i\omega t} dt. \tag{1.32}$$

We now define the collision time, representing the interval over which the electron has close interaction with the ion,

$$\tau = b/v, \tag{1.33}$$

and use it to derive expressions for $\hat{\mathbf{d}}(\omega)$ in the asymptotic limits of large and small frequencies, leading to

$$\hat{\mathbf{d}}(\omega) \sim \begin{cases} \dfrac{e}{2\pi\omega^2} \Delta\mathbf{v}, & \omega\tau \ll 1 \\ \\ 0, & \omega\tau \gg 1, \end{cases} \tag{1.34}$$

where $\Delta\mathbf{v}$ is the change in velocity during the collision. We now combine this result with the general equation for energy per frequency range (assuming the dipole approximation), given by Rybicki and Lightman [1979] as

$$\frac{dW}{d\omega} = \frac{8\pi\omega^4}{3c^3} |\hat{d}(\omega)|^2 \tag{1.35}$$

to obtain

$$\frac{dW}{d\omega} = \begin{cases} \dfrac{2e^2}{3\pi c^3} |\Delta\mathbf{v}|^2, & \omega\tau \ll 1 \\ \\ 0, & \omega\tau \gg 1. \end{cases} \tag{1.36}$$

We now wish to estimate $\Delta\mathbf{v}$, as this will ultimately determine the emission of the electron. We have assumed in this derivation that the path is nearly linear, so $\Delta\mathbf{v}$ will be approximately normal to the path of travel. Thus, $\Delta\mathbf{v}$ can be calculated as

$$\Delta \mathbf{v} = \frac{Ze^2}{m} \int_{-\infty}^{\infty} \frac{b\, dt}{(b^2 + v^2 t^2)^{3/2}} = \frac{2Ze^2}{mbv}, \tag{1.37}$$

so the emission from a single collision can now be written as

$$\frac{dW(b)}{d\omega} = \begin{cases} \dfrac{8Z^2 e^6}{3\pi c^3 m^2 v^2 b^2}, & b \ll \frac{v}{\omega} \\ \\ 0, & b \gg \frac{v}{\omega}. \end{cases} \tag{1.38}$$

The emission per time per volume per frequency is then

$$\frac{dW}{d\omega dV dt} = 2\pi n_i n_e v \int_{b_{min}}^{b_{max}} \frac{dW(b)}{d\omega} b\, db, \tag{1.39}$$

where n_i and n_e are the ion and electron densities, v is the electron speed. The flux of electrons onto a single ion will be $n_e v$, and the element of area about an ion is $2\pi b db$. b_{min} and b_{max} represent the range of impact parameters which lead to emission. Substituting Equation (1.38) into (1.39), we now find

$$\frac{dW}{d\omega dV dt} = \frac{16e^6}{3c^3 m^2 v} n_e n_e Z^2 \int_{b_{min}}^{b_{max}} \frac{db}{b} = \frac{16e^6}{3c^3 m^2 v} n_e n_i Z^2 \ln\left(\frac{b_{max}}{b_{min}}\right), \tag{1.40}$$

or

$$\frac{dW}{d\omega dV dt} = \frac{16e^6}{3\sqrt{3} c^3 m^2 v} n_e n_i Z^2 g_{ff}(v, \omega) \tag{1.41}$$

where

$$g_{ff}(v, \omega) = \frac{\sqrt{3}}{\pi} \ln\left(\frac{b_{max}}{b_{min}}\right) \tag{1.42}$$

is known as the *Gaunt factor*. $g_{ff}(v, \omega)$ is determined by b_{min} and b_{max}, which in turn depend on the energy of the electron and the frequency of the emission.

We can now extend these results to determine the spectrum of a population of electrons with a range of velocities. This discussion will focus on electrons following a thermal distribution of

velocities, as this ultimately results in the emission of thermal bremsstrahlung from SNRs. We will begin by considering the probability dP that a particle has velocity in the range $d^3\mathbf{v}$. For a thermal population, this probability will follow a maxwellian distribution resulting in

$$dP \propto e^{\frac{-E}{kT}} d^3\mathbf{v} = \exp\bigg(- \frac{mv^2}{2kT}\bigg) d^3\mathbf{v} \propto v^2 \exp\bigg(- \frac{mv^2}{2kT}\bigg) dv, \tag{1.43}$$

where the final step above results from the fact that the velocity distribution is isotropic. To find the emitted spectrum, we now must integrate Equation (1.41) over this function. The lower limit of integration is taken to be $v_{min} \equiv (2h\nu/m)^{1/2}$, as an electron must have a minimum velocity to create a photon such that

$$h\nu \leq \frac{1}{2} m v^2. \tag{1.44}$$

Thus, the integral will be

$$\frac{dW(T,\omega)}{dV\, dt\, d\omega} = \frac{\int_{v_{min}}^{\infty} \frac{dW(v,\omega)}{d\omega\, dV dt} v^2 \exp(-mv^2/2kT) dv}{\int_0^{\infty} v^2 \exp(-mv^2/2kT) dv}. \tag{1.45}$$

Now by inserting v_{min} and using $d\omega = 2\pi d\nu$, we obtain

$$\frac{dW}{dV dt\, d\nu} = \frac{2^5 \pi e^6}{3mc^3} \bigg(\frac{2\pi}{3km} \bigg)^{1/2} T^{-1/2} Z^2 n_e n_i e^{-h\nu/kT} \bar{g}_{ff} \tag{1.46}$$

where $\bar{g}_{ff}$ is the velocity-averaged Gaunt factor. In cgs units, we can now find the spectrum due to thermal bremsstrahlung to be

$$\varepsilon_\nu^{ff} \equiv \frac{dW}{dV dt\, d\nu} = 6.8 \times 10^{-38} Z^2 n_e n_i T^{-1/2} e^{-h\nu/kT} \bar{g}_{ff} \quad \text{erg/s/cm}^3\text{/Hz}, \tag{1.47}$$

or, when considering multiple ion species,

$$\varepsilon_\nu^{ff} \equiv \frac{dW}{dV dt\, d\nu} = 6.8 \times 10^{-38} T^{-1/2} e^{-h\nu/kT} \bar{g}_{ff} n_e \sum_i n_i Z_i^2 \quad \text{erg/s/cm}^3\text{/Hz}. \tag{1.48}$$

The spectral shape of thermal bremsstrahlung emission is shown in Figure 1.2. Note that the shape depends on the velocity distribution of the electrons and will be different for a nonthermal population.

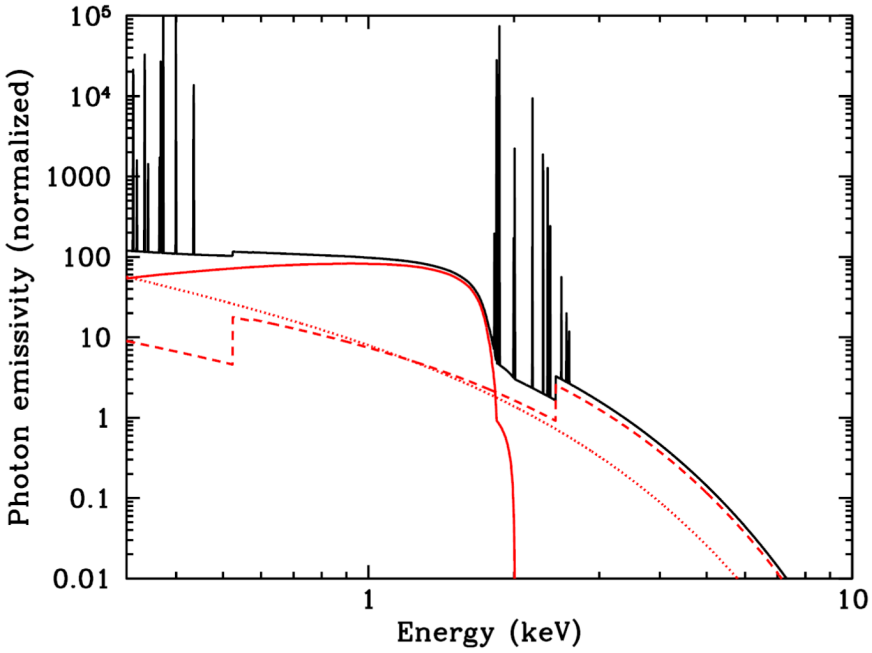

Figure 1.2: Various X-ray emission processes are displayed including two-photon emission (solid red line), free-bound emission (dashed red line), and bremsstrahlung (dotted red line). Line emission is also prominent. Each emission process adds a distinct shape to the overall spectrum. The image is taken from Vink [2012] (using code from Kaastra et al. [2003]) and represents a purely Silicon plasma out of ionization equilibrium ($kT_e = 1$ keV, $n_e t = 5 \times 10^{10}$ cm^{-3}s).

1.2.2 Free-Bound Emission

Free-bound emission occurs when electrons and ions recombine. Continuum emission is produced in this process with each photon having an energy $h\nu_n = E_e + \chi_n$, where E_e is the kinetic energy of the free electron and χ_n is the energy required to ionize the atom from the recombined energy state (n corresponding to the principle quantum number). Although free-bound emission produces a continuum, there are periodic breaks in the spectrum corresponding to bound energy states of the atoms in the plasma (see Fig. 1.2).

The number of recombinations per unit time per unit volume in the speed range dv will be

$$n_{i+1} n_e \sigma_{fb}(v) f(v) v \, dv, \tag{1.49}$$

where n_e and n_{i+1} are the electron and ion (at a certain ionization level) densities, $\sigma_{fb}(v)$ is the recombination cross section for electrons with velocity v, and $f(v)$ is the velocity distribution which we will take to be Maxwellian. In thermal equilibrium, the number of recombinations per unit time must equal the number of photonionizations. Assuming a blackbody radiation field, the photoionization rate per time per volume is

$$\frac{4\pi}{h\nu} n_i \sigma_{bf} (1 - e^{-h\nu/kT}) B_\nu \, d\nu, \tag{1.50}$$

where n_i denotes that the photoionizations occur from some initial ionization state (which may be neutral). The factor $(1 - e^{-h\nu/kT})$ removes the effect of stimulated recombinations and leads to the true photoionization rate. Equating Equations (1.49) and (1.50), substituting in the Planck function, and realizing that $h \, d\nu = (p/m_e) dp = m_e v \, dv$, we find

$$\frac{\sigma_{fb}}{\sigma_{bf}} = \frac{n_i}{n_{i+1} n_e} e^{-h\nu/kT} \frac{8\pi m_e \nu^2}{f(v) h c^2}. \tag{1.51}$$

We can now substitute the equation for a Maxwellian velocity distribution,

$$f(v) = 4\pi \left(\frac{m_e}{2\pi kT} \right)^{3/2} v^2 e^{-m_e v^2/2kT}, \tag{1.52}$$

and the Saha equation,

$$\frac{n_{i+1} n_e}{n_i} = \left(\frac{2\pi m_e kT}{h^2} \right)^{3/2} \frac{g_e g_{i+1}}{g_i} e^{\chi/kT} \tag{1.53}$$

into Equation (1.51). The final step is to recall that $h\nu = \frac{1}{2} m_e v^2 + \chi$ to obtain

$$\frac{\sigma_{fb}}{\sigma_{bf}} = \frac{2 g_i}{g_e g_{i+1}} \left(\frac{m_e c v}{h\nu} \right)^2, \tag{1.54}$$

where g_e, g_i, and g_{e+1} are the statistical weights of the free electron and the atom before and after recombination. Equation (1.54) is known as the Milne relation, and it represents an example of *detailed balancing*. This means that Equation (1.54) is a relationship between atomic properties and is therefore independent of whether the plasma is in thermal equilibrium. σ_{bf} (the photoionization cross section) is

$$\sigma_{bf} = \left(\frac{64\pi ng}{3\sqrt{3}Z^2}\right)\alpha a_0^2\left(\frac{\chi_n}{h\nu}\right)^3. \tag{1.55}$$

Using the Milne relation, we can now integrate Equation (1.49) over a range of velocities to acquire the total recombinations per unit time per unit volume $n_{i+1}n_eR_n$, where R_n is known as the recombination coefficient. This integral is nontrivial, even assuming a Maxwellian velocity distribution, but ends with the result

$$n_{i+1}n_eR_n = n_{i+1}n_e\int vf(v)\sigma_{fb}dv = 3.262\times10^{-6}\frac{e^{\chi_n/kT}}{n^3T^{3/2}}E_1\left(\frac{\chi_n}{kT}\right), \tag{1.56}$$

where we have used $g_e = 2$, $g_{i+1} = 1$, and $g_i = 2n^2$ for the statistical weights, and

$$E_1(x) \equiv \int_x^\infty \frac{e^{-t}}{t}dt \tag{1.57}$$

which can be evaluated numerically (see Cillié [1932] for a full derivation). The full spectrum due to free-bound emission will, of course, depend directly on the velocity distribution of the electrons as well as on the recombination rate (which also depends on the velocity distribution). Finding the equation for emissivity (erg $\mathrm{s}^{-1}\mathrm{cm}^{-3}\mathrm{Hz}^{-1}$) requires performing another integral over the velocity distribution, in similar fashion to the steps followed for bremsstrahlung radiation. The process is can be carried out numerically and is provided by Vink [2012] as

$$\varepsilon_{fb} = \left(\frac{2}{\pi}\right)^{1/2}n_en_{i+1}\frac{g_i}{g_{i+1}}\left(\frac{ch\nu}{\chi_n}\right)\left(\frac{\chi_n^2}{m_ec^2kT}\right)^{3/2}\sigma_{bf}(h\nu)\exp\left(-\frac{(h\nu-\chi_n)}{kT}\right). \tag{1.58}$$

Notice that this equation applies to a single atomic species at a specific ionization state which recombines with an electron into a specific excited state. Finding the full spectrum requires summing

over all atomic species, ionization states, and excited bound states found in the plasma. As shown in Figure 1.2, the spectrum of free-bound emission qualitatively resembles that of bremsstrahlung, but with breaks corresponding to ionization energies and the energy levels bound states.

1.2.3 Line Emission

Following free-free and free-bound, we come to bound-bound emission which occurs when bound electrons transition to a lower energy state. The plasma in SNRs is optically thin, so this emission will manifest as line emission corresponding to the various ionized elements which are present (see Fig. 1.2). Due to the high ionization states associated with SNRs, this emission will correspond to X-ray energies. Excited states are produced primarily through collisional excitation (mostly electron-ion collisions), but can also occur by photon absorption, recombination, and inner shell ionization. In thermal equilibrium, the density of atoms in an excited state follows the Boltzmann law,

$$n_j = \frac{n}{U} g_j e^{E_j/kT} \text{ cm}^{-3}, \tag{1.59}$$

where n_j is the number density of atoms in state j, n is the total number density of the atom, g_j is the degeneracy of state j, E_j is the energy of state j (above the ground level). U is known as the partition function, and takes the form

$$U = \sum g_j e^{-E_j/kT}, \tag{1.60}$$

which ensures that $n = \sum n_j$. In principle, the sum in Equation (1.60) goes to infinity, but in practical situations is taken over all bound states until perturbations from neighboring atoms can cause ionization. In the simplest case, the density n_j can be used to find the line power P_{kj} (photons per unit time per unit volume) for emission occuring when an electron relaxes from state j to state k,

$$P_{kj} = A_{kj} n_j, \tag{1.61}$$

where A_{kj} is the Einstein coefficient for spontaneous emission between j and k. In reality, of course, there will be many complications. For instance, the excited state may have access to other de-excited states, and emission will be distributed among them based on the Einstein coefficiencts for each. Of course, the total line emission will correspond to a summation over all atomic species (including their ionization states) and all possible state transitions.

A complicating factor for SNRs is that the plasma will typically be in Non-Equilibrium Ionization (NEI), rather than Collisional Ionization Equilibrium (CIE). This occurs because SNR plasma is young and has low density, meaning there has simply not been enough time for ionization levels to reach the equilibrium level associated with the plasma's high temperature. As a result, SNRs will be underionized compared to the expectation based on their temperature alone, and the Saha equation (1.53) does not adequately describe the plasma. For NEI, the ionization state of each atomic species becomes a function of $n_e t$, often referred to as the *ionization age* of the plasma. Thus, accurate estimates of $n_e t$ are important to determine the ionization state of the plasma. Figure 1.3 demonstrates the ionization process that a young plasma will go through. As $n_e t$ increases, atoms will become more ionized until CIE conditions are reached.

1.2.4 Synchrotron Emission

Each emission mechanism described so far is typically considered when occuring in local thermodynamic equilibrium (LTE), although each mechanism can be created by any distribution of electron velocity. Synchrotron emission, in contrast, is only created by a population of distinctly nonthermal electrons. Synchrotron emission occurs when electrons (and other charged particles) are accelerated around magnetic field lines to relativistic energies. Magnetic fields can be quite high in SNRs. There is residual magnetic field from the precursor star, and the expanding blast wave tends to compress and amplify existing magnetic field lines in the ISM. Synchrotron emission manifests as continuum that spans a very wide range of energy, from X-rays down to radio wavelengths. We

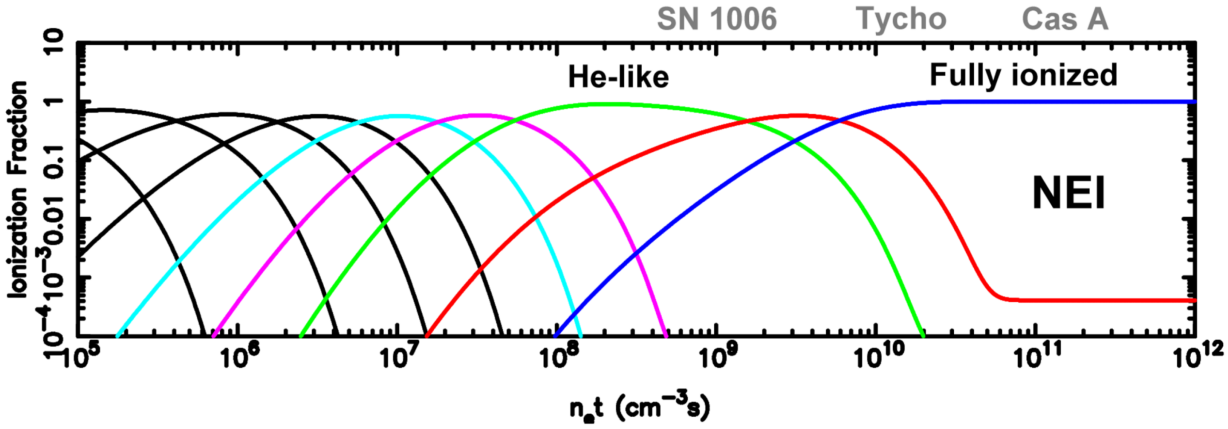

Figure 1.3: The effects of non-equilibrium ionization (NEI) for oxygen. Assuming a constant temperature, oxygen becomes more highly ionized as $n_e t$ increases until full ionization is reached. The different curves represent the populations of various ionization states of oxygen (the red curve represents H-like O; the neon green curve represents He-like O, for example). The figure assumes a temperature of $kT = 1.5$ keV. Approximate values of $n_e t$ are displayed for SN 1006, Tycho's SNR, and Cas A. Image taken from Vink [2006]

will not carry out a full derivation of the expected spectrum from synchrotron radiation here, as it is quite involved, but we will derive the total emitted power and discuss the spectral characteristics.

The motion of a relativistic charged particle in a magnetic field is governed by the following equations:

$$\frac{d}{dt}(\gamma m \mathbf{v}) = \frac{q}{c}\mathbf{v} \times \mathbf{B}, \tag{1.62}$$

$$\frac{d}{dt}(\gamma m c^2) = q\mathbf{v} \cdot \mathbf{E} = 0, \tag{1.63}$$

where m and q are the mass and charge of the particle, and $\gamma \equiv (1 - v^2/c^2)^{-1/2}$. The second equation implies that γ (and therefore $|\mathbf{v}|$) is constant. Therefore, Equation (1.62) can be rewritten as

$$m\gamma \frac{d\mathbf{v}}{dt} = \frac{q}{c}\mathbf{v} \times \mathbf{B}. \tag{1.64}$$

Splitting Equation (1.64) into the velocity components parallel ($\mathbf{v}_{||}$) and perpendicular ($\mathbf{v}_{\perp}$) to the field lines yields

$$\frac{d\mathbf{v}_{||}}{dt} = 0, \qquad \frac{d\mathbf{v}_{\perp}}{dt} = \frac{q}{\gamma mc}\mathbf{v}_{\perp}\times\mathbf{B}. \tag{1.65}$$

Because $|\mathbf{v}|$ and $\mathbf{v}_{||}$ are constant, $|\mathbf{v}_{\perp}|$ must also be constant, leading to circular motion in the plane perpendicular to the field lines. The orbital frequency of the particles around the field lines will be

$$\omega_B = \frac{qB}{\gamma mc}. \tag{1.66}$$

The acceleration of the particle will be perpendicular to velocity, with a magnitude

$$a_{\perp} = \omega_B v_{\perp}. \tag{1.67}$$

For a nonrelativistic particle, the emitted power is given by the *Larmor formula*,

$$P = \frac{2q^2a^2}{3c^3}. \tag{1.68}$$

In relativistic scenarios, this equation becomes

$$P = \frac{2q^2}{3c^3}\gamma^4(a_{\perp}^2 + \gamma^2 a_{||}^2). \tag{1.69}$$

Thus, for synchrotron radiation,

$$P = \frac{2q^2}{3c^3}\gamma^4\frac{q^2B^2}{\gamma^2m^2c^2}v_{\perp}^2 = \frac{2r_0^2\gamma^2B^2}{3c}v_{\perp}^2 \tag{1.70}$$

where $r_0 \equiv q^2/mc^2$ is the *classical electron radius*.

For an isotropic distribution of velocities, Equation (1.70) must be averaged over all angles for a given speed. If the angle between the field lines and the velocity is θ, the average velocity over all angles is

$$\langle v_{\perp}^2\rangle = \frac{v_{\perp}^2}{4\pi}\int \sin^2\theta\, d\Omega = \frac{2v^2}{3}. \tag{1.71}$$

Thus, the power emitted by an isotropic distribution of electrons moving with a speed $|\mathbf{v}|$ perpendicular to the magnetic field is

$$P = \left(\frac{2}{3}\right)^2 r_0^2 \gamma^2 B^2 \frac{v^2}{c} = \frac{4}{3}\sigma_T c \beta^2 \gamma^2 U_B, \tag{1.72}$$

where $\sigma_T = 8\pi r_0^2/3$ is the Thomson cross section, $U_B = B^2/8\pi$ is the magnetic energy density (or magnetic pressure), and $\beta = v/c$. Equation (1.72) illustrates that the strength of synchrotron emission depends directly on the strength of the magnetic field present in the plasma, as well as the speed of the electrons (through β and γ).

It has already been mentioned that synchrotron radiation has an extremely broad spectrum. This basic feature arises due the *beaming effect* associated with relativistic particles. A nonrelativistic particle will emit radiation in all directions (of differing strength) when accelerated. A relativistic particle, in contrast, will emit radiation in a cone which points in the direction of travel. As a result, each electron (or other charged particle) will appear to emit very short pulses of radiation when viewed from a single direction. The length of each pulse is ultimately determined by the speed of the particle (or equivalently by how relativistic the particle is) which factors into the gyration frequency (ω_B) around the field lines and the half angle of the radiation cone ($\theta_{cone} = 1/\gamma$). When radiation is emitted over a discrete time interval, the spectrum of that radiation has a width of $\Delta\omega > 1/\Delta t$. Thus, for synchrotron emission, the narrowest spectrum we might consider observing would be of order $\Delta\omega_B = 1/\Delta t_{orbit}$. In reality, the width will be greater than this by a factor of $\sim \gamma^3$ due to a combination of the beaming effect and Doppler shift. This ultimately leads to a spectrum broad enough to span the range from radio waves to X-rays.

A full analytic derivation of a synchrotron spectrum is beyond the scope of this explanatory section. The full solution can be found in Rybicki and Lightman [1979] and is given as

$$P_{tot}(\omega) = \frac{\sqrt{3}\, q^3 \mathrm{C} B \sin\theta}{2\pi m c^2 (p+1)} \Gamma\left(\frac{p}{4} + \frac{19}{12}\right) \Gamma\left(\frac{p}{4} - \frac{1}{12}\right) \left(\frac{mc\omega}{3qB\sin\alpha}\right)^{-(p-1)/2}, \tag{1.73}$$

where θ is once again the angle between particle velocity and the magnetic field. This formula

assumes that the electrons follow a *power-law distribution* of the form

$$N(E)dE = \mathrm{C}E^{-p}dE \qquad \text{or} \qquad N(\gamma)d\gamma = \mathrm{C}\gamma^{-p}d\gamma, \tag{1.74}$$

where C is a quantity that varies with pitch angle (θ), and p is known as the particle distribution index. The result is a spectrum that also follows a power-law, but with a *spectral index* s where

$$s = \frac{p-1}{2}. \tag{1.75}$$

The assumption that the electrons follow a power-law distribution is generally valid when synchrotron emission is substantial. Strong magnetic fields can easily accelerate electrons to a power-law distribution when the particle density is low (and collisions are rare).

1.2.5 Other Emission Processes

There are additional emission processes at work in SNRs. These processes are generally less prominent than the types described above, but this varies based on specific circumstances.

Two-photon emission occurs when a bound electron is in a metastable state and decays via a "forbidden" transition by emitting 2 photons. The $2s$ state of hydrogen-like atoms is a good example of this, as decay to the ground state involves a dipole-forbidden transition ($\Delta s = 0$). A transition of this type results in continuum emission, where the total energy of the emitted photons equals the energy of the electron's transition. This type of emission can be important in metal-rich young SNRs.

Another type of emission associated with metal-rich young SNRs is line emission associated with radioactivity. Radioactive elements are produced during the initial SN explosion which can emit substantial amounts of radiation. Immediately following the SN, the most important element is ^{56}Ni, which decays first into ^{56}Co (with a 8.8 day half-life) and then into ^{56}Fe. This radiation forms the bulk of a SN's initial light curve, but is basically irrelevant within a single year. ^{44}Ti lasts significantly longer than ^{56}Ni, with a half-life of 85 years. Thus, this radiation continues

to be important in young SNRs beyond the initial explosion, and can still be seen prominently in SN1987a (CITE SOMEONE). This radiation becomes negligible beyond the first phase of SN expansion.

1.2.6 Spectral Parameters

We will now briefly discuss certain physical parameters which have a significant effect on a SNR's observed spectrum. These are the parameters that the spectrum ultimately probes.

1.2.6.1 Temperature

Obviously, temperature has a large effect on all thermal emission, including bremsstrahlung, free-bound, bound-bound line, and two-photon emission. Temperature is a primary factor in the Maxwell-Boltzmann distribution affecting how fast the particles move. This determines the dipole interaction for bremsstrahlung and the interaction cross-sections for free-bound emission. Temperature determines the population of excited states, the ionization level, and thus the number densities of electrons and ions.

1.2.6.2 Elemental Abundances

Along with temperature, elemental abundances (or metallicity) are probably the most important parameter for SNR spectra. Due to the large signal in narrow frequency bands, line emission is almost always easily distinguished from continuum emission and prominently displays the elements' spectral signatures. Metallicity (along with temperature) directly determines the ion and electron number densities. The spectral breaks in free-bound emission are determined by the energy states available to recombining electrons, which is determined by the elements present.

1.2.6.3 Ionization State

As mentioned above, ionization state can be a tricky parameter in SNRs, as the plasma typically has not had time to come to CIE. Thus, the ionization state is impacted by the metallicity,

temperature, age, and density of the plasma. In turn, the ionization state directly affects electron and ion number densities, free-bound spectral breaks, and the signature of line emission.

1.2.6.4 Magnetic Field Strength

The strength of the magnetic field contained in a SNR plasma most markedly affects synchrotron radiation. The magnetic field determines the energy distribution (and distribution index p) of the nonthermal electron population. This, in turn, determines the spectral index and overall strength of the synchrotron emission.

1.3 The Cygnus Loop Supernova Remnant

The Cygnus Loop SNR presents a rare opportunity to view a SNR from relatively nearby and to see the soft X-ray emission without much concern for interstellar absorption. At only 540 pc (Blair et al. [2005]), Cygnus has a relatively low absorption. The foreground neutral hydrogen column density is estimated to be $\sim 4 \times 10^{20}$ cm^{-2} (Inoue et al. [1980]; Kahn et al. [1980]). Its close distance and low absorbing column result in Cygnus being one of the brightest extended objects in the soft X-ray sky. Cygnus is estimated to be a middle-aged SNR (∼10,000 years) in the adiabatic phase (Leahy and Hassan [2013b]). Cygnus appears as one of the largest objects in the X-ray sky, with an angular size of $\sim 3^\circ \times \sim 3^\circ$ (Leahy et al. [1997]; Levenson et al. [1997]; Aschenbach and Leahy [1999]). Due to the realities of the chaotic ISM, Cygnus does not appear to be a simple example of a point explosion in a homogeneous medium. Rather, the surrounding environment appears to have significant structural variations which have influenced the evolution of the remnant. It appears that a cavity was formed by strong winds from the precursor star, and that the explosion occurred in a rarefied environment (McCray and Snow [1979]). Relatively recently, the ejecta have reached the edges of the pre-formed cavity and have encountered denser material, resulting in bright emission from the shock-heated gas. The walls of the cavity appear to be inhomogeneous and show large variations in density. As a result, the X-ray intensity varies substantially along the borders of the SNR, with brightness indicating regions where higher density

gas has been encountered. In this section, we will review the previous observations of Cygnus (focusing mostly on X-ray observations) in roughly chronological order.

Due to its proximity, Cygnus is one of the most studied SNRs. The quest to understand Cygnus has been long and arduous. Oort [1946] suggested that the Cygnus Loop "nebula" was probably a supernova remnant which glowed as a result of the expanding ejecta shock-heating the surrounding ISM. Minkowski [1958] studied the radial velocities of the remnant (in the optical) and found typical velocities of ∼100 km/s. When combined with a proper motion of ∼0.03"/year, the distance to Cygnus was calculated as 770 pc, and an upper limit to its age was set at 150,000 years. Cygnus was mapped at radio frequencies by Moffat [1971] (at 1420 MHz) and Kundu and Becker [1972] (at 6 cm, see Fig. 1.4) who both found that the radio emission traces the optical emission. They also found that the southern portion of the remnant was partially polarized, implying a magnetic field aligned parallel to the shell structure.

The 1970s could be described as the heyday of X-ray rocketry, as suborbital rockets were the primary vehicle for observations of celestial X-rays. Soft X-rays were first detected in Cygnus by Grader et al. [1970]. Gorenstein et al. [1971] used a sounding rocket to scan the Cygnus Loop in soft X-rays (0.2 – 1 keV). They found that the X-ray emission was roughly contained within the region of optical emission and that the spectrum was consistent with a thermal plasma at 4×10^6 K and inconsistent with sychrotron emission. Borken et al. [1972] performed a similar experiment and resolved Cygnus into two distinct regions associated with several major optical filaments. The first map of Cygnus' X-ray structure was created based on further sounding rocket measurements by Rappaport et al. [1973] and Rappaport et al. [1974] (see Fig. 1.5). These results were improved upon by Rappaport et al. [1979]. Woodgate et al. [1974] detected optical emission from coronal lines of [Fe XIV] at 5303 Å associated with strong X-ray-emitting regions in Cygnus. They find the emission to be consistent with thermal emission at $(2.8 \pm 0.3) \times 10^6$ K. Kirshner and Taylor [1976] measured low surface brightness Hα filaments and found radial velocities of +200 to -300 km/s, values high enough to account for the $2 - 3 \times 10^6$ K temperatures, and bringing into question the velocities measured by Minkowski [1958] and the age of $\sim 18,000$ years calculated by Rappaport

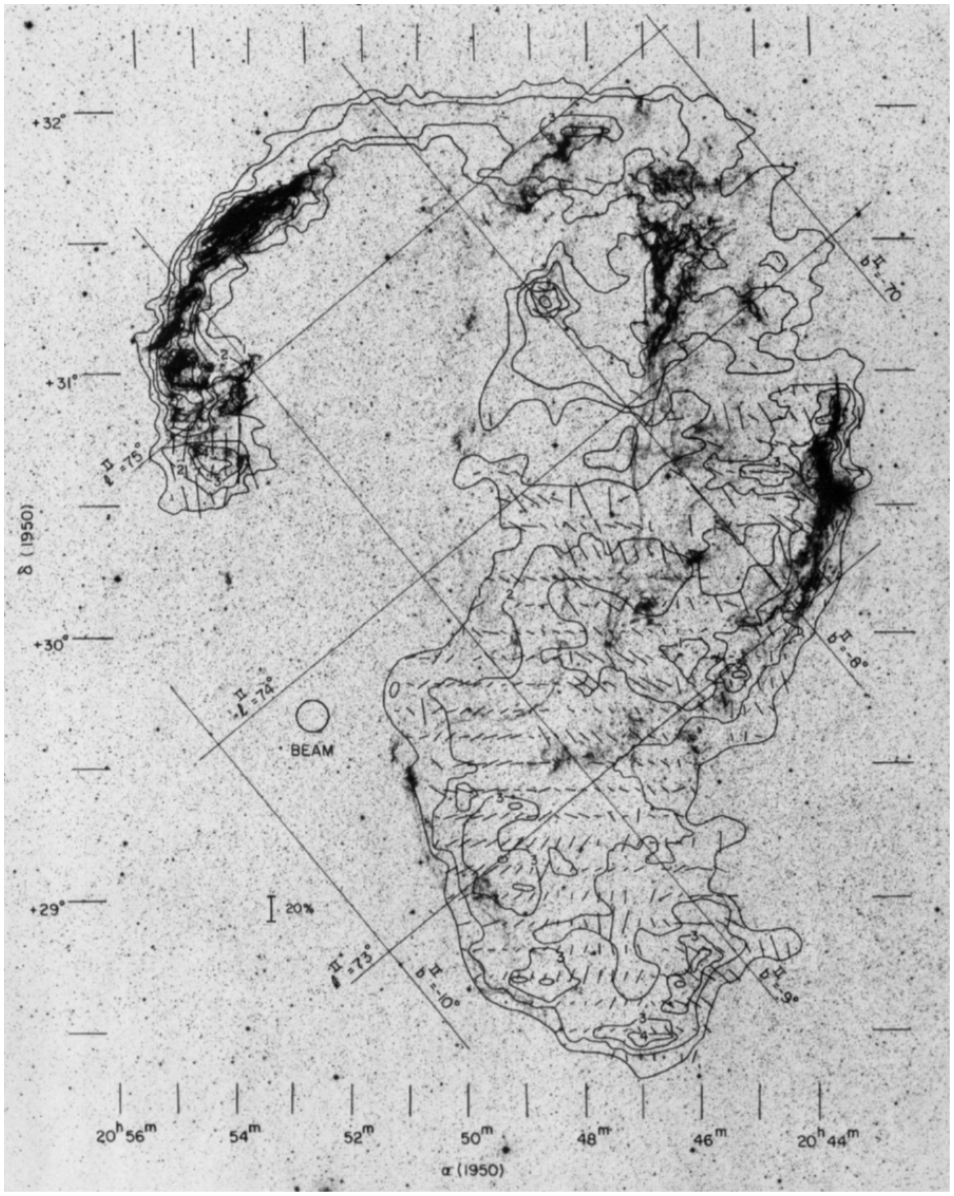

Figure 1.4: 6 cm radio contours overlaid on an optical photograph of Cygnus. The radio emission traces the optical emission. Image taken from Kundu and Becker [1972].

et al. [1974]. McCray and Snow [1979] carried out a thorough review of theory and observations of the interstellar medium, with the general conclusion that the interstellar medium is usually out of equilibrium and is turbulent. Supernova explosions were suggested as the primary source of energy for the ISM, with stellar winds being another significant contribution. The authors noted that for the Cygnus Loop the velocity of the blast wave inferred from the temperature of the

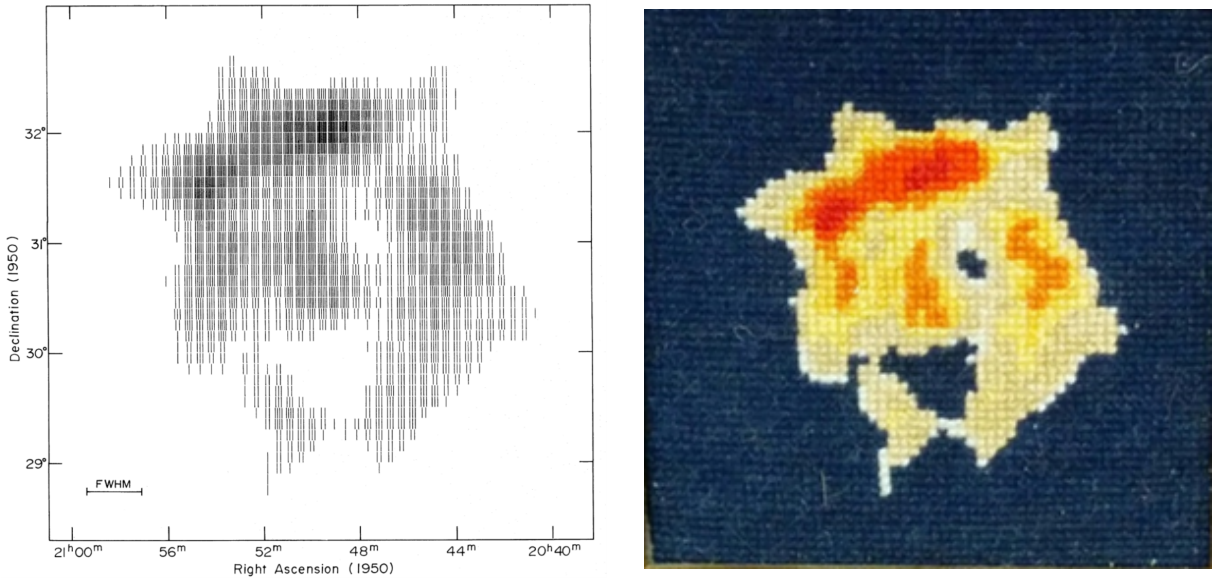

Figure 1.5: *Left*: The first map of Cygnus' X-ray surface brightness (0.15—0.85 keV), taken by Rappaport et al. [1974]. *Right*: The same image as a cross-stitch, fabricated by Cash [1974].

observed soft X-rays exceeds the velocities of the optical filaments by roughly a factor of 3. As an explanation for this discrepancy, they suggest that the Cygnus Loop Supernova occured in a preexisting cavity which was carved out by strong winds from the progenitor star, and that the ejecta are now encountering the boundary of this cavity.

In the 1980s, sounding rocket observations began to be replaced by those of orbiting satellites. The first far ultraviolet spectrum of Cygnus was obtained with the *International Ultraviolet Explorer* (*IUE*) by Benvenuti et al. [1980]. The spectrum is interpreted as a radiative shock wave from a Phase III SNR with depleted elemental abundances and a range of shock velocities ($\sim 80 - 130$ km/s). Contini and Shaviv [1982] confirmed the depleted abundances, but added that fast shocks ($v \geq 240$ km/s) are also present in areas of lower density and lower surface brightness. Gronenschild [1980] mapped the X-ray brightness of Cygnus with the ANS satellite in three soft X-ray bands (0.16 – 0.284 kev, 0.32 – 0.46 keV, and 1 – 2.5 keV). They find that the overall behavior of the remnant is best described by: temperature $T = (2.26 \pm 0.10) \times 10^6$ K; explosion energy $E_0 = (1.1 \pm 0.3) \times 10^{50}$ erg; mean ambient interstellar density $n_0 = (0.15 \pm 0.03)$ cm^{-3}; and age $t = (21,000 \pm 4,000)$ years. They found, however, that there was considerable spatial variation in each of these parameters.

Kahn et al. [1980] observed the Cygnus Loop using the *HEAO 1* satellite between 0.1−2.0 keV. Their observations conclusively demonstrated the presence of oxygen- and iron-line emission between 0.6 and 0.9 keV. They found a best-fit X-ray temperature of $T = 3.2 \times 10^6$ K and an interstellar column density of a few times 10^{20} cm^{-2}. Further optical characterization was carried out by Fesen et al. [1982] who observed 17 gas filaments in the Cygnus Loop. These observations confirmed the variable nature of the remnant, displaying a range of shock velocities ($200 - 400$ km/s).

Braun and Strom [1986] used the *Infrared Astronomical Satellite* (*IRAS*) to map Cygnus in the infrared (12, 25, 60, and 100 μm) by observing shock-heated dust (see Fig. 1.6). They arrive at a revised distance estimate of 460 ± 160 pc. Hester and Cox [1986] carried out a detailed comparison of the X-ray and optical emission for a portion of Cygnus along its southeast edge using the High-Resolution Imager (HRI) instrument aboard the *Einstein Observatory*. They find the close spatial relationship to be consistent with a thin ($\leq$ 0.2 pc) zone of enhanced X-ray emission lying immediately behind the much thinner sheet of optical emission. The data suggest that the ISM around Cygnus consists of large ($\geq$ 1 pc) clouds, rather than many tiny ($\leq$ 0.01 pc) cloudlets. Straka et al. [1986] made a comparison of radio (18 cm) and optical (Hα, [O III], [S II], [O I]) data for the northeast portion of Cygnus. The radio filaments match the optical filaments very well, particularly those which are bright in Hα. However, a few bright radio features have no optical counterparts. The radio and optical structure can be explained by a model in which shocked interstellar clouds form filaments due to unstable cooling and compression.

Vedder et al. [1986] acquired the first (and only) high-resolution X-ray spectrum of Cygnus using the Focal Plane Crystal Spectrometer (FPCS) on the *Einstein Observatory* (see Figs. 1.7 and 1.8). This observation targeted a northern portion of the Cygnus Loop and scanned several narrow bandpasses around emission from O VII, O VIII, and Ne IX. They found that the lack of forbidden lines in the trio of O VII lines indicates that the emitting plasma in Cygnus is not yet in CIE. This is a notable result, as low-resolution observations up to this point had been consistent with ionization equilibrium. This is an excellent example of the benefits of increased spectral resolution. They constrained the electron temperature to $T_e \geq 3 \times 10^6$ K and found the ionization age (see

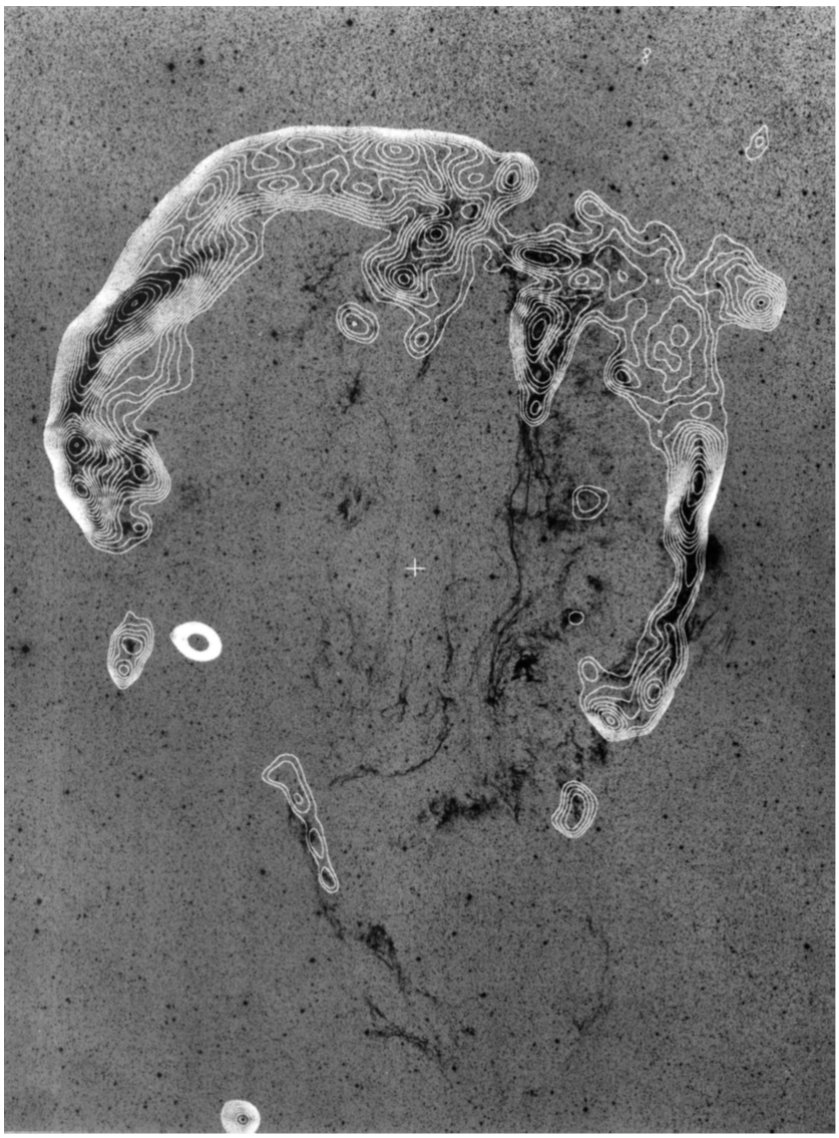

Figure 1.6: Contours of 60 μm emission overlaid on an optical photograph of Cygnus. The IR and optical emission match each other in certain areas, but not others. Image taken from Braun and Strom [1986].

section 1.2.3) to be $n_e t = 10^{10} - 3 \times 10^{11}$ cm^{-3} s.

Graham et al. [1991a] and Graham et al. [1991b] obtained infrared Fabry-Perot spectra of Cygnus' northeastern ridge. Their results indicate that the shocks propagating into the ISM are preceded by a magnetic precursor of charged particles which stream in front of the shock and preheat the unshocked medium. This result lends weight to the theory of particle acceleration

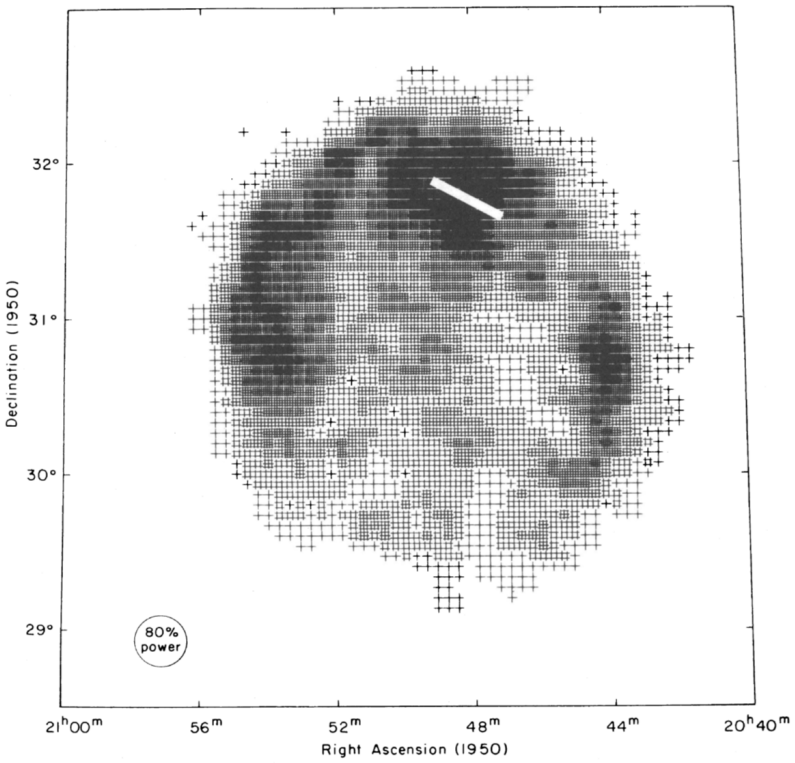

Figure 1.7: The region of Cygnus observed by Vedder et al. [1986] is represented by the white rectangle. The background image of Cygnus is taken from Rappaport et al. [1979].

in compressed magnetic fields associated with fast shocks. Blair et al. [1991] observed the far ultraviolet spectrum of Cygnus using the Hopkins Ultraviolet Telescope (HUT) and acquired the first data to resolve the sub-Lyman-α emission of an interstellar shock wave. They observed strong emission of C III 977 Å, N III 991 Å, and O VI 1032 & 1038 Å. They find this shock to have a measured velocity of $\sim$ 170 km/s. Shull and Hippelein [1991] report radial velocities and proper motion at 39 locations within Cygnus and find velocities ranging from $150 - 380$ km/s. Based on these results, they concluded that Cygnus is roughly 600 pc distant. Sauvageot and Decourchelle [1995] observed coronal [Fe X] and [Fe XIV] lines in a bright region of Cygnus, and measure a wide range of radial velocities (-110 to $+200$ km/s). Leahy et al. [1997] compare 1420 MHz continuum and polarization measurements with the X-ray emission from Cygnus. Again, they find that the southern portion of the remnant is highly polarized (up to 39%) compared to the north ($\sim$2.4%).

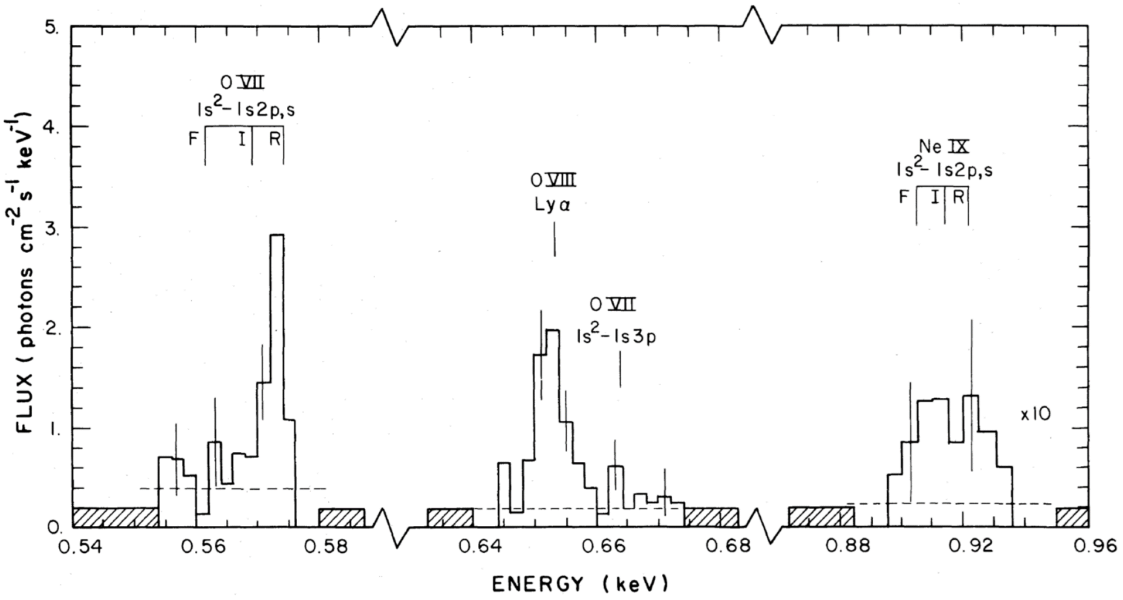

Figure 1.8: Soft X-ray Spectrum observed by Vedder et al. [1986] in the region shown in Figure 1.7. This plot remains the only high-resolution soft X-ray spectrum of Cygnus. The lack of O VII forbidden lines indicates nonequilibrium ionization conditions.

Comparison with X-ray emission shows a probable correlation between regions bright in X-rays (i.e. high electron density) and depolarization. The bright filaments are found to have magnetic fields aligned along their long dimension.

Levenson et al. [1997] used the *ROSAT* satellite to begin mapping Cygnus with 10" resolution. Using position-sensitive proportional counters, ROSAT mapped Cygnus in its entirety, as well as (nearly) the full sky in soft X-rays ($0.1 - 2$ keV). ROSAT split the emission from Cygnus into 7 different energy bands, allowing rudimentary spectra to be obtained. ROSAT created the first high resolution X-ray images of Cygnus. The X-ray images, combined with optical Hα data, provided definitive evidence that the Cygnus Loop was formed by an explosion within a preexisting cavity. Levenson et al. [1998] produced a high-resolution optical map of Cygnus (see Figs. 1.9 and 1.10). The optical emission traces the X-ray emission very well, particularly the Balmer-dominated shocks which indicate the presence of neutral material. These shocks represent regions where the SN ejecta is encountering the surrounding neutral ISM. Aschenbach and Leahy [1999] compare ROSAT X-

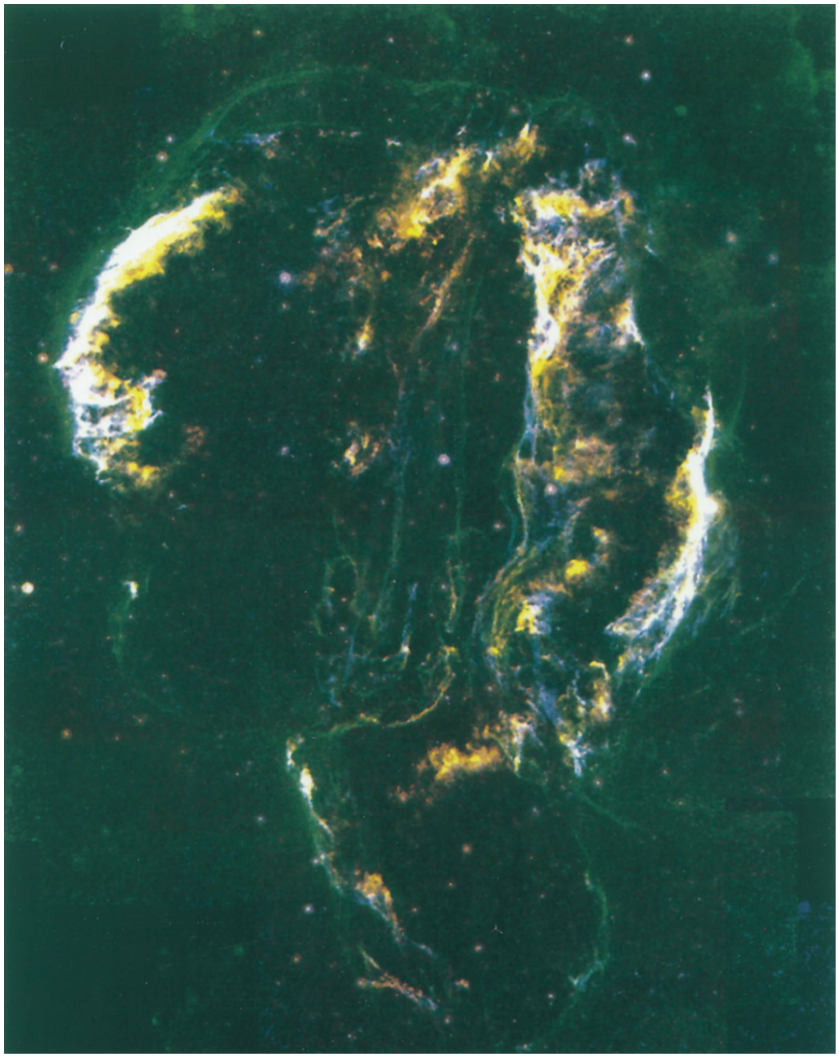

Figure 1.9: A false-color combination of [S II] in red, Hα in greed, and [O III] in blue. Blends of Hα and [S II] are yellow, [O III] and [S II] together are magenta, and Hα and [O III] together are cyan. Image taken from Levenson et al. [1998]

ray data with radio data. The ratio of X-ray to radio surface brightness varies strongly across the remnant, but bright X-ray and radio filaments do coincide in position. Levenson et al. [1999] map the softness (the relative contributions of high- and low-energy X-rays) of the Cygnus Loop by taking the ratio of the emission in *ROSAT*'s 0.25 keV and 1.25 keV bands (see Figs. 1.11 and 1.12).

They find that there is a very distinct boundary of maximum softness around the outer edge of the entire remnant. Further, this softness is noticeably exterior to regions of maximum brightness.

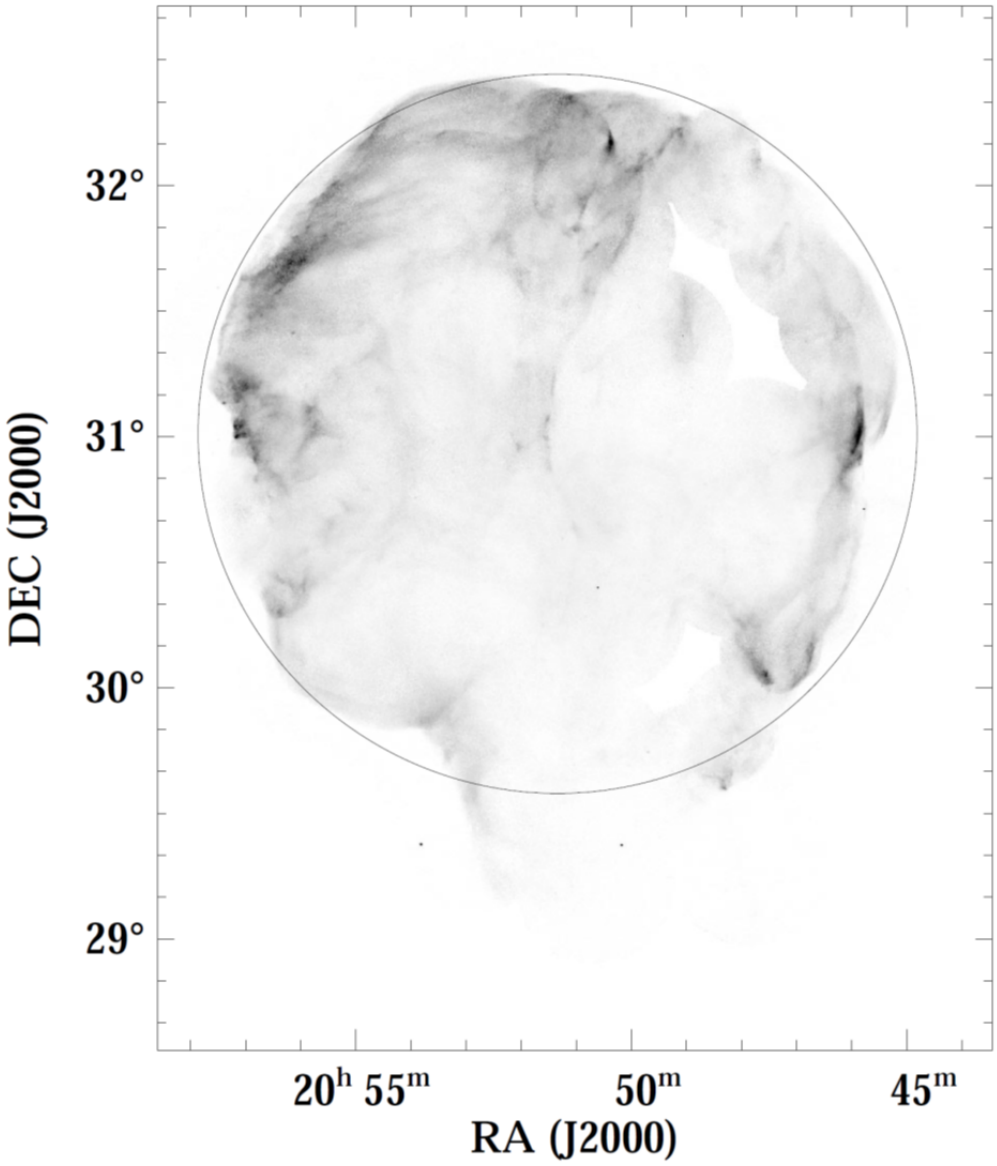

Figure 1.10: A *ROSAT* High Resolution Imager map of the Cygnus Loop. The circle represents the best fit to the optical emission displayed in Figure 1.9. Image taken from Levenson et al. [1998]

They conclude that bright regions are typically associated with reverse shocks originating from encounters between the blast wave and ISM clouds. Regions of maximum softness are associated with the forward blast wave which has been decelerated by the denser regions of the ISM.

Danforth et al. [2000] compare ultraviolet, optical, and X-ray emission from several fields within the Cygnus Loop. They find that Cygnus contains both thick radiative (phase III) filaments

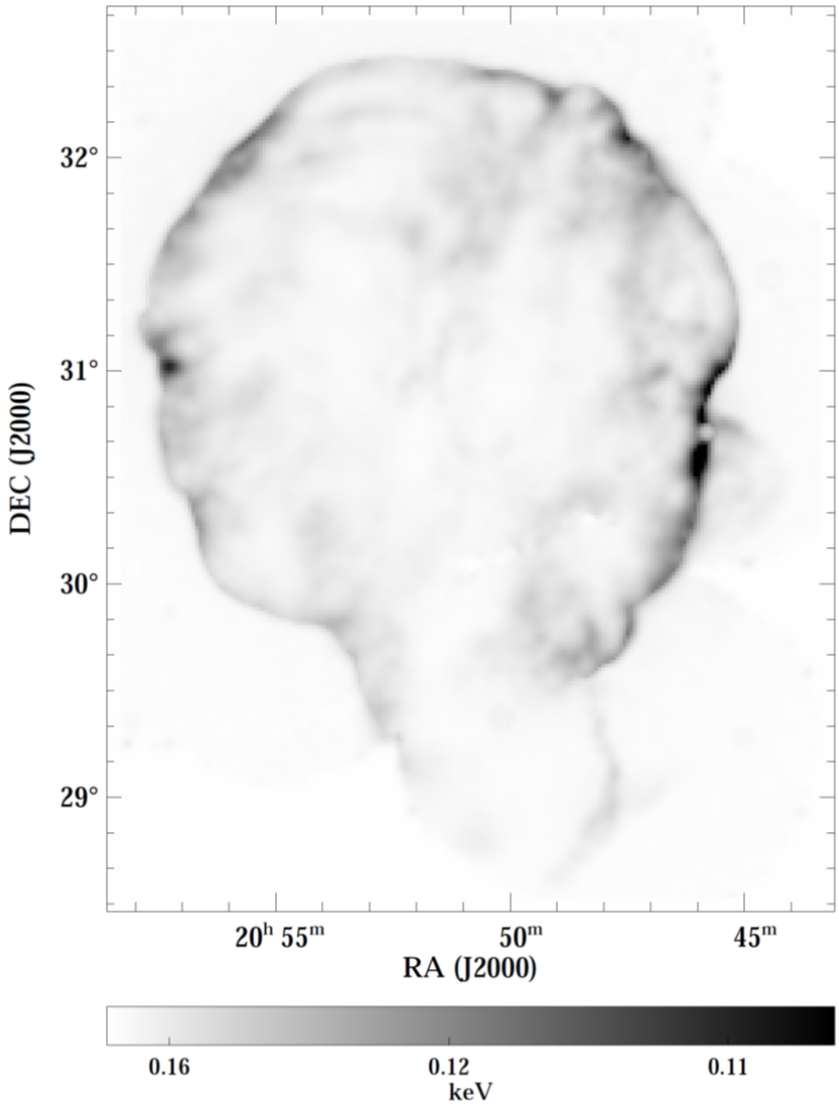

Figure 1.11: The ratio of emission in *ROSAT*'s 0.25 keV and 1.25 keV bands produces a softness map of the Cygnus Loop. Softness is quite distinct at the edges of the remnant where the blast wave is being decelerated by the surrounding ISM. Image taken from Levenson et al. [1999]

characterized by dense environments, high surface brightness, and low shock speeds, as well as thin nonradiative (phase II) shocks characterized by low-density environments, low surface brightness, and high shock speeds. In nonradiative filaments, UV flux comes from C IV as it becomes further ionized and from two-photon emission from preshock neutral hydrogen. Radiative filaments emit lines from a broad range of hot, intermediate, and low-temperature ions, depending on the effective

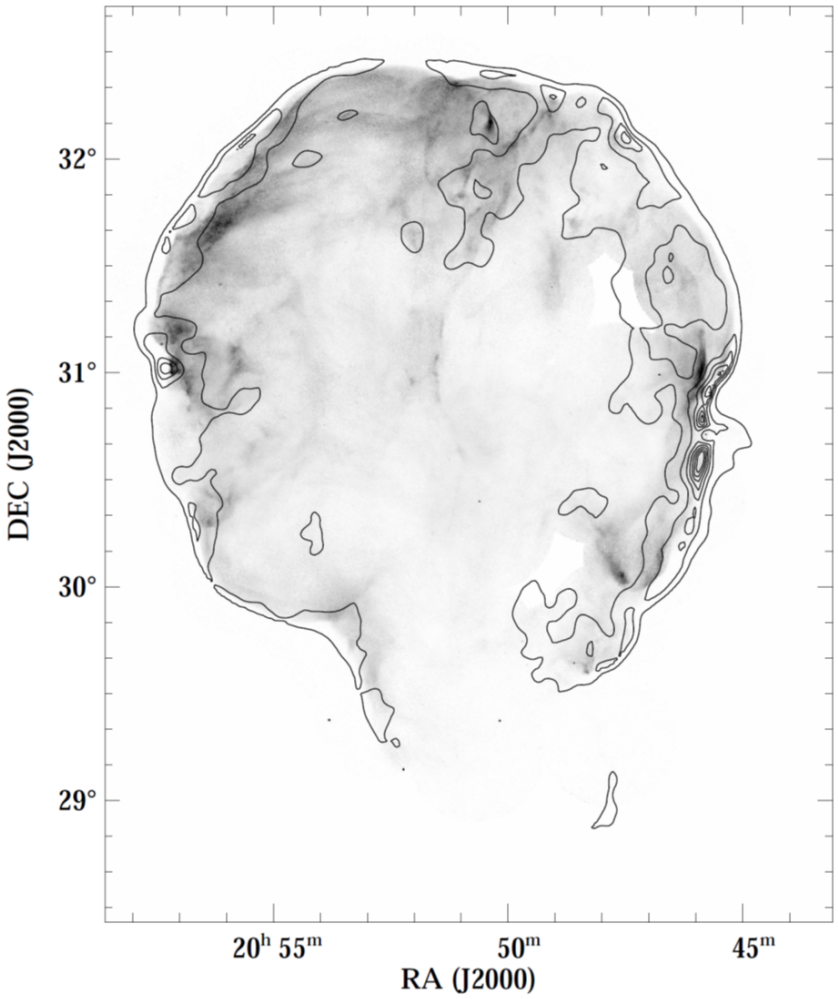

Figure 1.12: Softness contours overlaid with an X-ray image of the Cygnus Loop. Regions of maximum softness are distinctly ahead of regions of maximum brightness. This indicates that bright regions are due to reflected shocks following encounters with clouds and the blast wave, while the softest emission is associated with the forward decelerated shocks in the overdense material. Image taken from Levenson et al. [1999]

"age" of the shock at any given location. Miyata and Tsunemi [2001] observed several locations within Cygnus with the *Advanced Satellite for Cosmology and Astrophysics* (*ASCA*) and *ROSAT* satellites in order to study the reverse shock within the SNR. Within a relatively small region, they find that a one-temperature model is inadequate to fit the spectra, and that a 2-temperature NEI model is required. The best fit varies from $kT = 0.043 - 0.067$ keV for the low-temperature component and $kT = 0.27 - 0.34$ keV for the high-temperature component. Elemental abundances vary

by location, but are generally depleted from solar values. Density is also variable and ranges from $1.9 - 6$ cm^{-3} for the high-temperature component and from $10 - 40$ cm^{-3} for the low-temperature component.

The new millennium has produced another advance in X-ray spectroscopy with the launch of the *Chandra, XMM-Newton*, and *Suzaku*. Levenson et al. [2002] used the *Chandra X-Ray Observatory* to analyze interactions of the blast wave and the inhomogeneous ISM on the western limb of Cygnus. Their chosen field of view (see Fig. 1.13) includes an initial interaction between

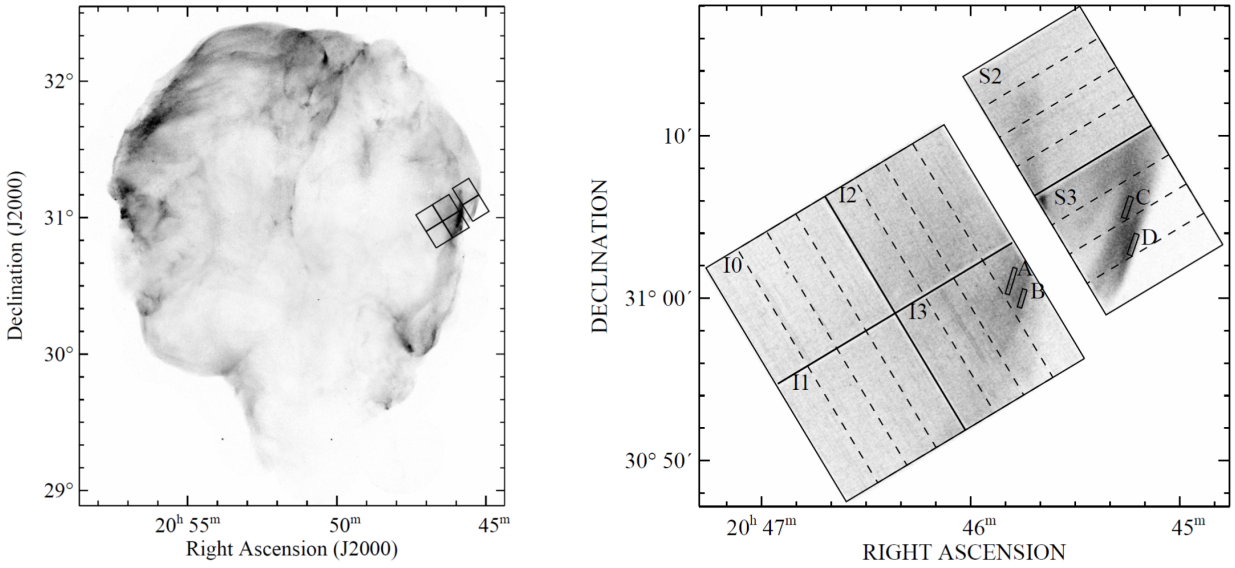

Figure 1.13: *Left*: Image of Cygnus from Levenson et al. [1997] overlaid with the field of view and position of Chandra ACIS observations taken by Levenson et al. [2002]. *Right*: A zoom-in of Chandra's field of view with regions A-D identified for spectral analysis. The field of view contains a site of initial interaction between the blast wave and a large cloud as well as the encounter of the shock front and the surrounding cavity shell.

the blast wave and a large cloud as well as the encounter of the shock front and the shell that surrounds the cavity of the supernova progenitor. The obtained spectra (shown in Fig. 1.14) show obvious variations. The shock front in the dense clouds is fit with $kT = 0.03$ keV, and regions where reflected shocks further heat the material are fit with $kT \approx 0.2$ keV. The authors find no evidence for instabilities or nonequilibrium conditions, nor do they find substantial variations in elemental abundances. The original blast-wave velocity is determined to be $v \approx 330$ km/s in the

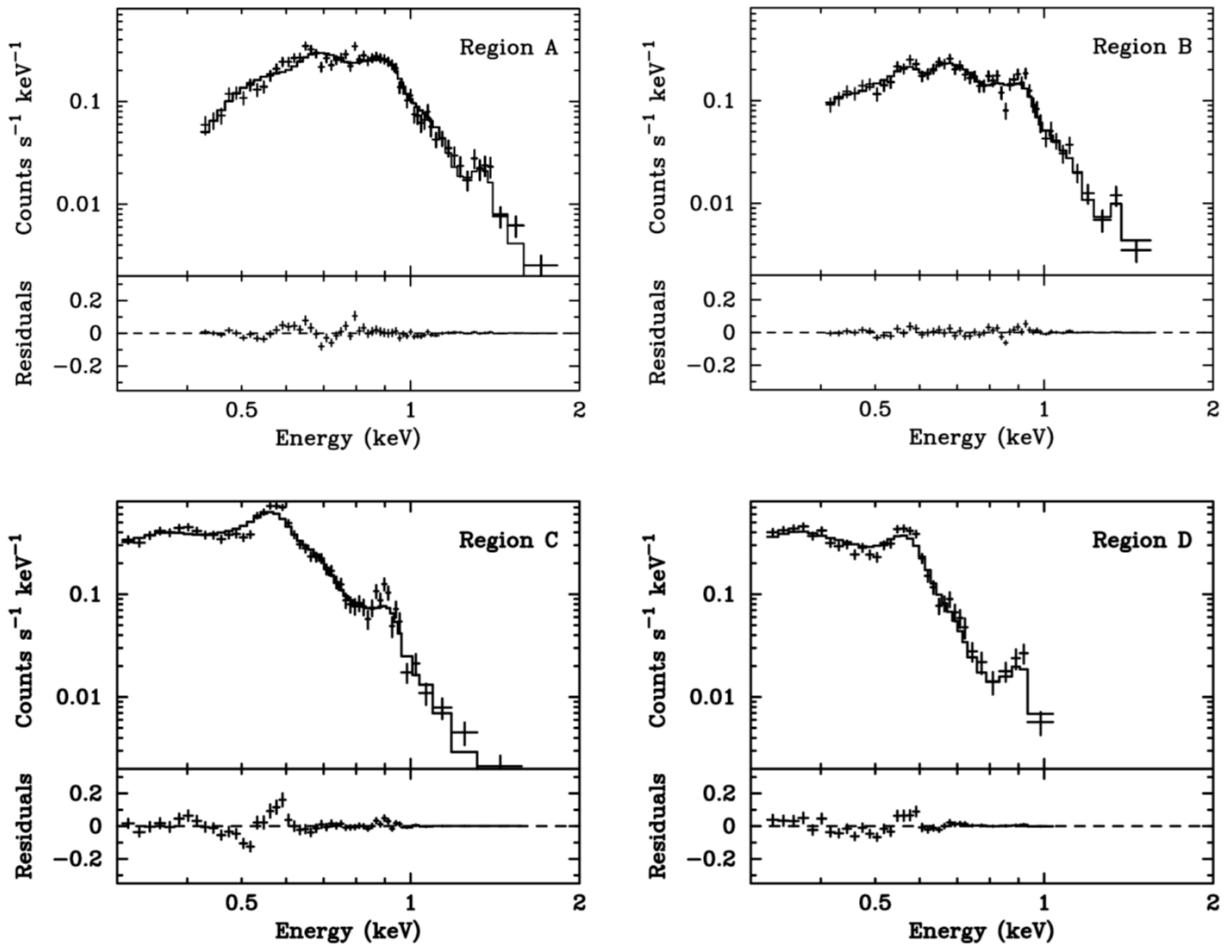

Figure 1.14: Spectra from regions A-D as identified in Fig. 1.13. These spectra are characterized by equilibrium plasma models with significant temperature variation between regions.

ambient medium. Leahy [2004] carry out a similar experiment in a different region and also find wide variation in best-fit parameters. They find that temperature varies from $kT = 0.170 - 0.254$ keV. O group elemental abundance varies from 0.06 - 0.7, Ne group abundance from 0.18 - 1.52, and Fe group abundance from 0.14 - 1.93. Notably, the Ne group to O group and the Fe group to O group ratio remain nearly constant between regions. This is taken to be evidence that the elements are due to a supernova explosion from an $\sim 18 M_{\odot}$ star.

Miyata et al. [2007] used *Suzaku* to make the first detection of highly ionized carbon and nitrogen lines in the Northeast portion of Cygnus (see Fig. 1.15). They find that their spectrum

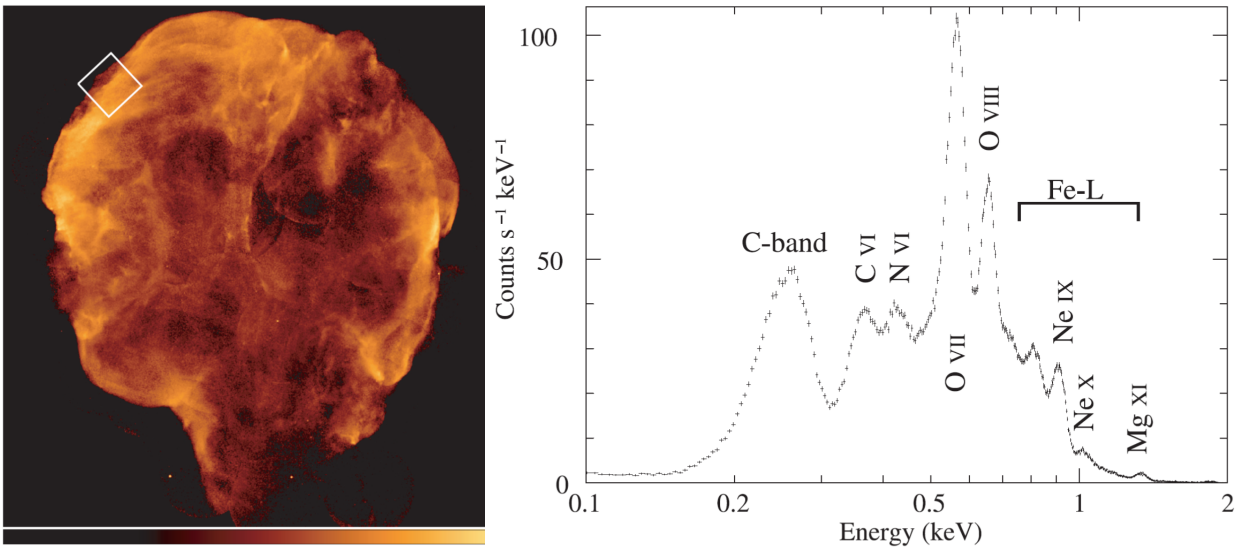

Figure 1.15: *Left*: Image of Cygnus from Levenson et al. [1997] overlaid with the field of view and position of Suzaku observations taken by Miyata et al. [2007]. *Right*: The spectrum acquired shows distinct emission from ionized C and N. The carbon band contains a large amount of flux but remains unresolved.

can be fit with a two-component NEI model. They find elemental abundances to be depleted relative to solar values to a level of ~ 0.1. Once again, parameters are seen to vary substantially over the field of view ($kT = 0.18 - 0.34$ keV for the high-temperature component and $kT = 0.09 - 0.16$ keV for the low-temperature component). They also find a large amount of emission in the "C-band", or 1/4 keV bandpass which is not resolved by *Suzaku's* energy-sensitive detectors. Katsuda et al. [2008] confirm these results in the same region with *Chandra*.

Tsunemi et al. [2007] use *XMM-Newton* to take multiple observations across Cygnus from the northeast to the southwest edges (see Fig. 1.16). They split their observations into annular regions and study the radial variation in spectral parameters. Similarly to Miyata et al. [2007], they find that most areas require a two-component NEI model, with the exception of the rim regions which only require a one-component NEI model, and that parameters vary substantially. A major finding is that the interior of the remnant appears to have high metal abundances. This had not been observed before, in part because most observations had focused on the brighter edge regions of the remnant.

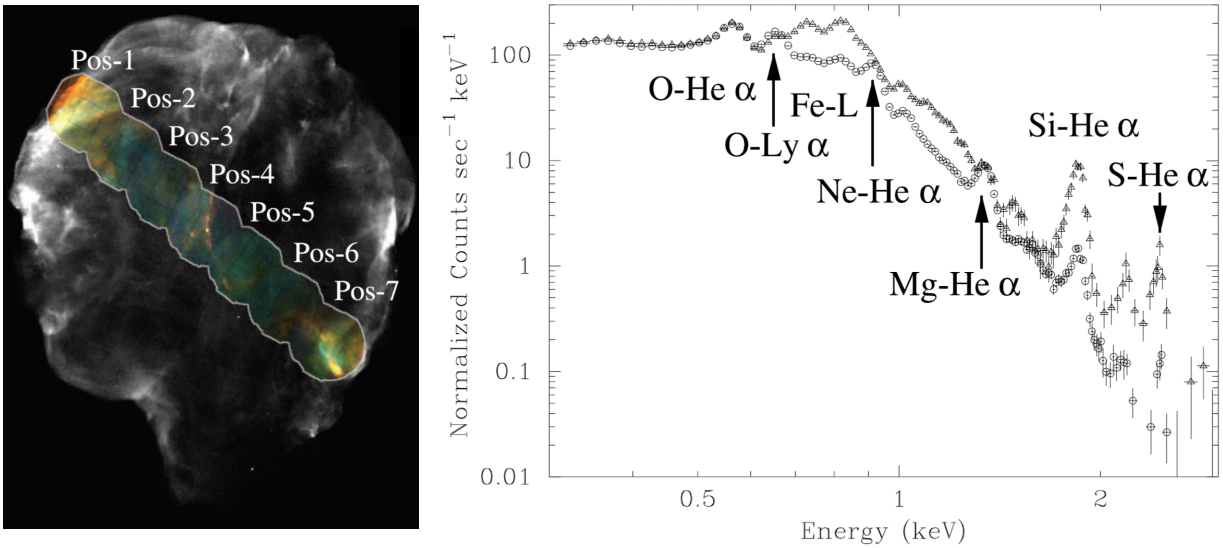

Figure 1.16: *Left*: Image of Cygnus from Levenson et al. [1997] overlaid with the fields of view and positions of XMM observations taken by Tsunemi et al. [2007]. *Right*: The spectra vary substantially between the rim (circles) and central regions (triangles) of the remnant.

Uchida et al. [2009a] and Uchida et al. [2009b] mapped the heavy-element distribution and shell structure along the edge and interior of the remnant using both *Suzaku* and *XMM-Newton* (see Fig. 1.17). Again, they find the edge regions to be consistent with a single-component (low-temperature) NEI model, whereas the central regions require two components (both high- and low-temperature) to achieve an acceptable fit. Figure 1.18 displays the flux profiles of the low- and high-temperature components from the northeast to the southwest of the Cygnus Loop. The low-temperature component is associated with the forward blast wave and is brightest at the edges of the remnant due to projection effects. The high-temperature component is associated with the reshocked interior ejecta and is brightest in the central region, also due to projection effects.

Katsuda et al. [2011] present evidence of possible charge-exchange occurring within Cygnus. They examine 21 *Suzaku* pointings and 1 *XMM* pointing covering nearly the entire outer edge of the remnant (see Fig. 1.19) and find certain areas with anomalously enhanced abundances. They show that the presence of charge-exchange between neutral atoms and He-like oxygen could lead to the inference of apparently enhanced abundances using pure thermal emission models. Accounting

for charge-emission could reveal that actual metal abundances are low throughout the rim. This assessment is confirmed by analyses made by Cumbee et al. [2014] and Roberts and Wang [2015]. Additional regions with possible charge exchange were found by Uchida et al. [2012]. These results demonstrate the need to model the charge-exchange contribution to the X-ray emission of Cygnus (and SNRs, in general), as this will be important to the correct measurements of the ionization, thermal, and chemical properties.

Although thought to be the result of a core-collape supernova of a 15—20 $M_{\odot}$ star, there has been no reliable evidence for a stellar remnant until relatively recently (Kaplan et al. [2006]). Katsuda et al. [2012] report the discovery of a diffuse nebula containing a pointlike source in the southern region of the Cygnus Loop, based on *Suzaku* and *XMM* observations. The neutron star

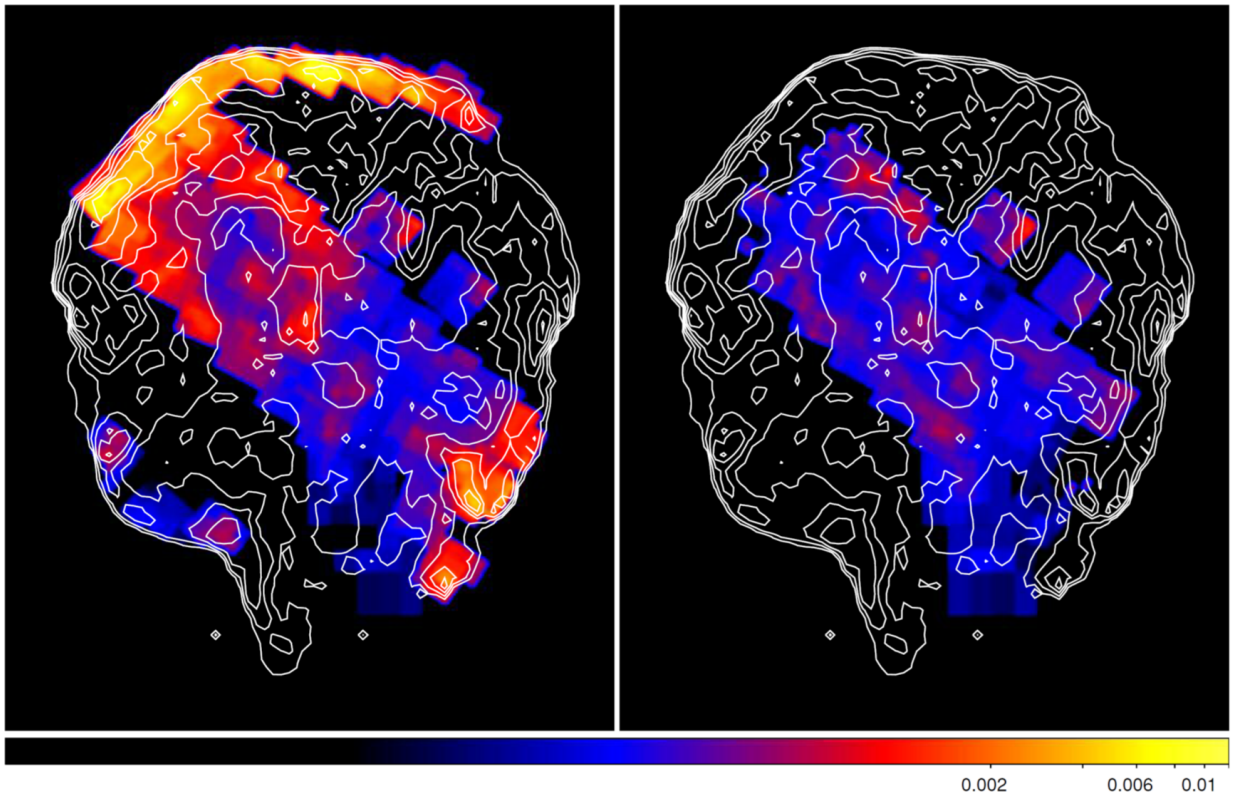

Figure 1.17: Low-kT (left) and high-kT (right) components, as observed by Uchida et al. [2009b] overlaid with contours of the *ROSAT* HRI image. The low-kT component is apparent in every pointing. The high-kT component, in contrast, is only seen in the interior of the remnant.

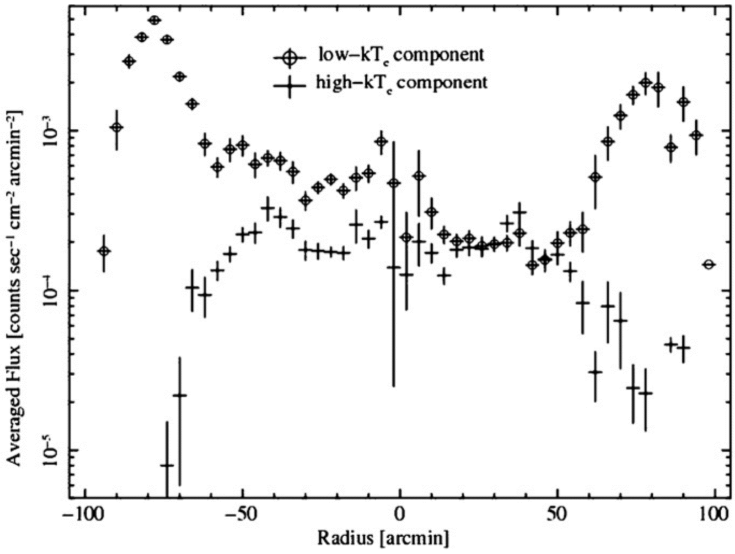

Figure 1.18: The averaged flux profiles as a function of radius. The circles and triangles represent the flux of low-kT and high-kT components, respectively. The high-kT component exists only in the center of the remnant. In contrast, the low-kT component exists in the center as well as at the edges, where it is brightest.

candidate is located $\sim 2^\circ$ away from the geometric center of the loop, implying a high transverse velocity of $\sim$ 1850 km/s, assuming a distance of 540 pc and age of $\sim 10,000$ years (Blair et al. [2005]).

1.3.1 Summary of Cygnus' Spectral Parameters

As the previous text shows, Cygnus has been extensively studied for over 60 years. The present view of Cygnus is still incomplete and there are many unanswered questions. We will summarize Cygnus' current range of spectral parameters, as determined by the *Chandra, XMM-Newton*, and *Suzaku* spacecraft. In the following section, we will use these parameters to produce the theoretical spectrum that we expect to be incident on our instrument. The results are summarized in Table 1.1.

The interior of Cygnus is only well-explained by a two-temperature model, representing the cooler ISM interacting with the forward blast wave and the interior ejecta which have been reheated by the reverse shock wave. The temperatures for each component vary substantially by region, and

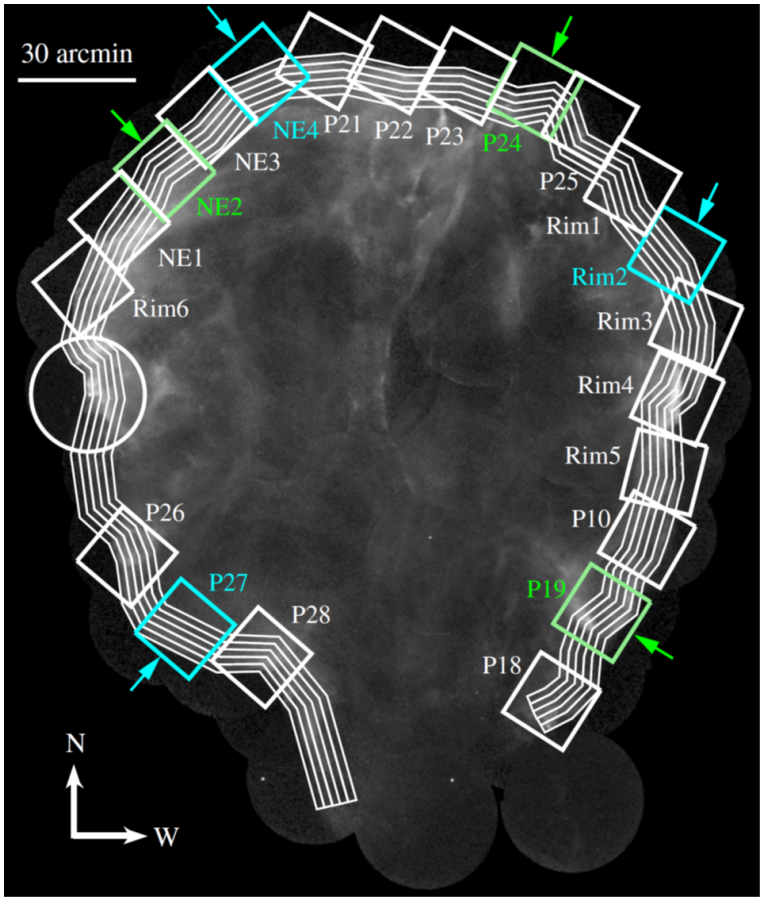

Figure 1.19: The *ROSAT* HRI image with pointing locations marked for Katsuda et al. [2011]. Squares represent the field of view of *Suzaku*. The circle shows the single pointing made by *XMM*.

fall within the range $kT = 0.03-0.254$ keV for the low-temperature component and $kT = 0.18-0.88$ keV for the high-temperature component. Elemental abundances are also seen to vary substantially by location, but are generally depleted from solar abundances. Many observations indicate that the Cygnus Loop is in conditions of nonequilibrium ionization, also varying by location. Magnetic field strength has not been observed to be a significant factor in X-ray spectra. Thus, we do not list magnetic field strength in Table 1.1.

Table 1.1: Physical Parameters of Cygnus

Reference	Instrument	Region	kT_{low}	kT_{high}	$O/O_{\odot}$	$\log(n_e t)$
Levenson, 2002	*Chandra*	W Rim	0.03–0.18	···	0.44–0.53	···
Leahy, 2004	*Chandra*	SW Rim	0.17–0.254	···	0.06–0.70	···
Miyata, 2007	*Suzaku*	NE Rim	0.09–0.16	0.18–0.34	0.07–0.11	11.31–11.99
Tsunemi, 2007	*XMM*	NE to SW	0.20–0.23	0.48	0.07–0.11	11.12–11.31
Katsuda, 2008	*Chandra*	NEt Rim	0.19–0.32	···	0.10–1.4	10.58–11.8
Uchida, 2009a	*Suzaku*	N Rim	0.32–0.43	···	0.10–0.45	10.52–10.79
Uchida, 2009b	*Suzaku/XMM*	Interior	0.12–0.24	0.43–0.88	0.11–0.23	10.42–11.32

1.3.2 Limitations of Current Observations

Cygnus' large size makes it an excellent (and one of the only) target for spatial investigations of a SNR interacting with its surrounding environment. *ROSAT* has provided a full spatial map of the remnant and *Chandra* and *XMM-Newton* have provided images with improved spatial resolution in targeted areas. Unfortunately, the large size also makes spectral investigations of Cygnus very difficult. *Chandra* and *XMM* are capable of exquisite point-source spectroscopy, with resolving power up to $E/\Delta E > 1000$ in the < 2 keV band. As slitless spectrographs, *Chandra* and *XMM* disperse spectral images of their targets across the focal plane. Thus, their excellent resolution is determined by the line-spread function of the focusing optics aboard both satellites, but only when observing point-like objects. If the observed target is extended (subtends an angle greater than the spatial resolution of the telescope), the achievable spectral resolution is determined by the size of the target on the sky. Figure 1.20 demonstrates the effect on *Chandra's* High-Energy Transmission Grating Spectrometer (*HETGS*) for several extended SNR of increasing size. Eventually, no spectral features can be distinguished by the dispersive spectrometer. The case of Cygnus is, in fact, even worse than that displayed in Figure 1.20, as it extends far beyond the full field of view of *Chandra* or *XMM*. In this case, spectroscopy must be carried out using the intrinsic energy resolution of the detectors (ACIS for *Chandra* or EPIC for *XMM*).

Because nearly all spectroscopic investigations of Cygnus have relied on energy resolution, the best spectral resolving power occurs at higher energies (> 0.5 keV) , where $E/\Delta D$ naturally

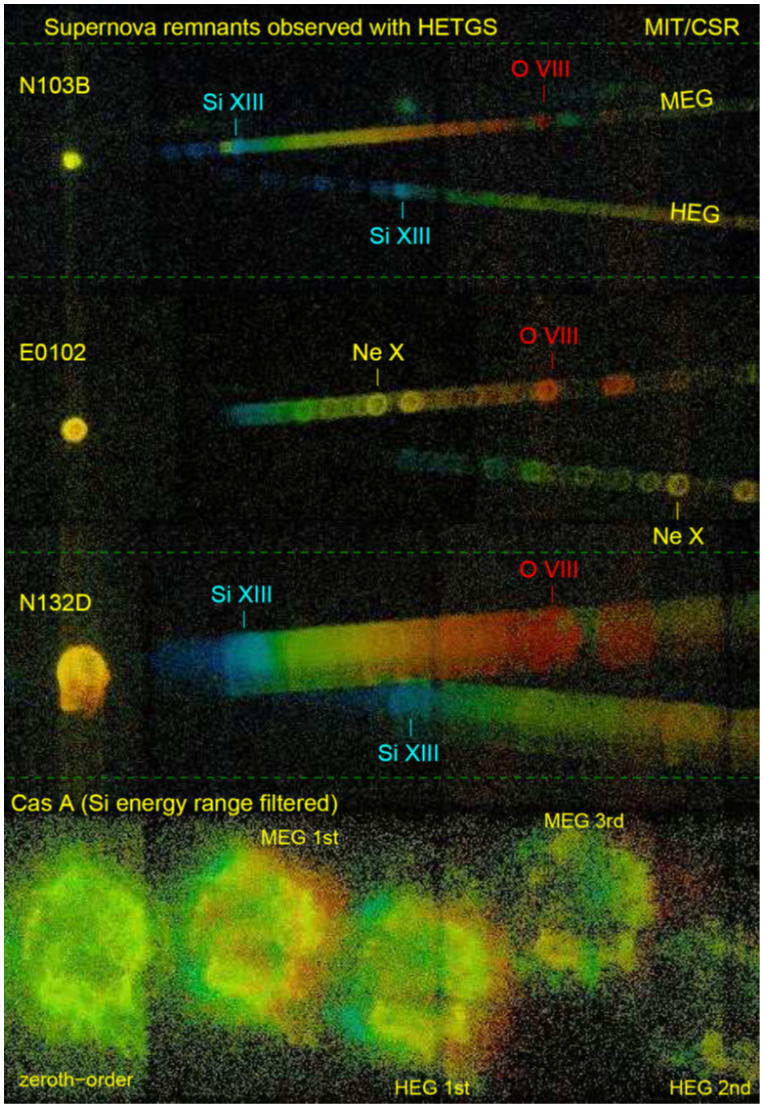

Figure 1.20: Spectra as seen by *Chandra-HETGS* of several extended sources. As the size of the source increases, the spectral resolution drops.

rises. A very large amount of Cygnus's flux, however, is emitted below these energies in the 1/4 keV bandpass where resolving power is very poor. This makes it impossible to resolve spectral features associated with lighter elements (such as carbon) and lower temperature regions of Cygnus.

The large size of Cygnus also makes it difficult to obtain global spectral parameters for the remnant. Spectral parameters within different areas of the remnant have been shown to vary substantially, even with the relatively low resolving power of current instruments. Specific pointings

are often chosen for their brightness relative to the rest of the remnant, meaning the regions are not a typical representation of the remnant as a whole. It is known that supernova explosions do not distribute their ejecta evenly (Vink [2012]), leading to substantial variation in metallicity throughout remnants, in general. This makes it very difficult to get a good estimate of the total elemental abundances within Cygnus. There have been a number of observing campaigns dedicated to targeting multiple regions (Tsunemi et al. [2007] and Uchida et al. [2009b], for instance), but it is difficult to build up a comprehensive picture of the remnant when comparing multiple observations taken at different times with different instruments. A single observation encompassing the remnant in its entirety would lead to substantial improvement in global abundance estimates.

Thus, current observations of Cygnus are typically of very localized regions with poor spectral resolution. The latest manual for the X-ray spectral fitting package, XSPEC (Arnaud et al. [2015]) sums up the basic situation very astutely:

> "...if the data used in the fit are not particularly good, one may be able to find many different models for which adequate fits can be found. In such a case, the choice of the correct model to fit is a matter of scientific judgement."

The point, of course, is that improved observations of Cygnus are required to substantially improve our understanding of the remnant. Individual shock waves have been studied and characterized, but an overall characterization of the remnant remains illusive.

1.4 The OGRESS Sounding Rocket

The Off-plane Grating Rocket for Extended Source Spectroscopy (OGRESS) has been designed to specifically address the inadequacies in spectral resolution and field of view suffered by the current suite of state-of-the-art X-ray instruments. OGRESS has a field of view that spans $3.25^\circ \times 3.25^\circ$, allowing it to view the Cygnus Loop in its entirety. As OGRESS has no spatial resolution, this will produce a spatially integrated global spectrum of the remnant, integrating over all spatial variations, determining the dominant state of the plasma and overall elemental abundances throughout the remnant. As will be discussed, OGRESSs novel optical system allows the

use of dispersive optics. OGRESS utilizes an array of off-plane gratings, allowing resolutions of ∼2-5 times those of *Chandra*, *XMM-Newton*, and *Suzaku* to be achieved (when observing diffuse sources). Because dispersive optics increase their resolving power at longer wavelengths (rather than high energies), OGRESS will particularly improve spectral resolution in the low-energy 1/4 keV bandpass where the resolution of *Chandra*, *XMM-Newton*, and *Suzaku* are at their worst. Figures 1.15 and 1.16, for instance, show that at low energies (the C-band, in Fig. 1.15) the spectrum is unresolved, despite having a high flux.

Figure 1.21 shows a simulated spectrum of Cygnus created using an absorbed two-component NEI model in XSPEC ($wabs * (vnei + vnei)$, in XSPEC syntax). The spectrum shown was created somewhat arbitrarily using temperatures and abundances which fall within the range of values listed in Table 1.1. Care was taken to ensure the simulated spectrum produced a similar proportion of counts in the 1/4 keV bandpass as Cygnus, based on *ROSAT* All-Sky Survey data. Certain lines have been labeled, and can be compared to the spectrum shown in Figure 1.15. The same spectrum is also shown with resolution similar to *Chandra/XMM/Suzaku* and OGRESS. The resolving power of *Chandra/XMM/Suzaku* improves as wavelength decreases (and energy increases), and degrades as wavelength increases. OGRESS, in contrast, has relatively poor resolving power at short wavelengths and cannot distinguish most of the high energy lines below 20 Å. OGRESS can, however, resolve many long wavelength lines in the C-band above 30 Å which are indistinguishable to *Chandra/XMM/Suzaku*. Thus, OGRESS will provide the first global spectrum of the Cygnus loop with the highest spectral resolution ever achieved below 0.5 keV. This spectrum will help answer the question of global elemental abundances, and begin to resolve the mysterious C-band, which composes roughly one third of Cygnus' total emission.

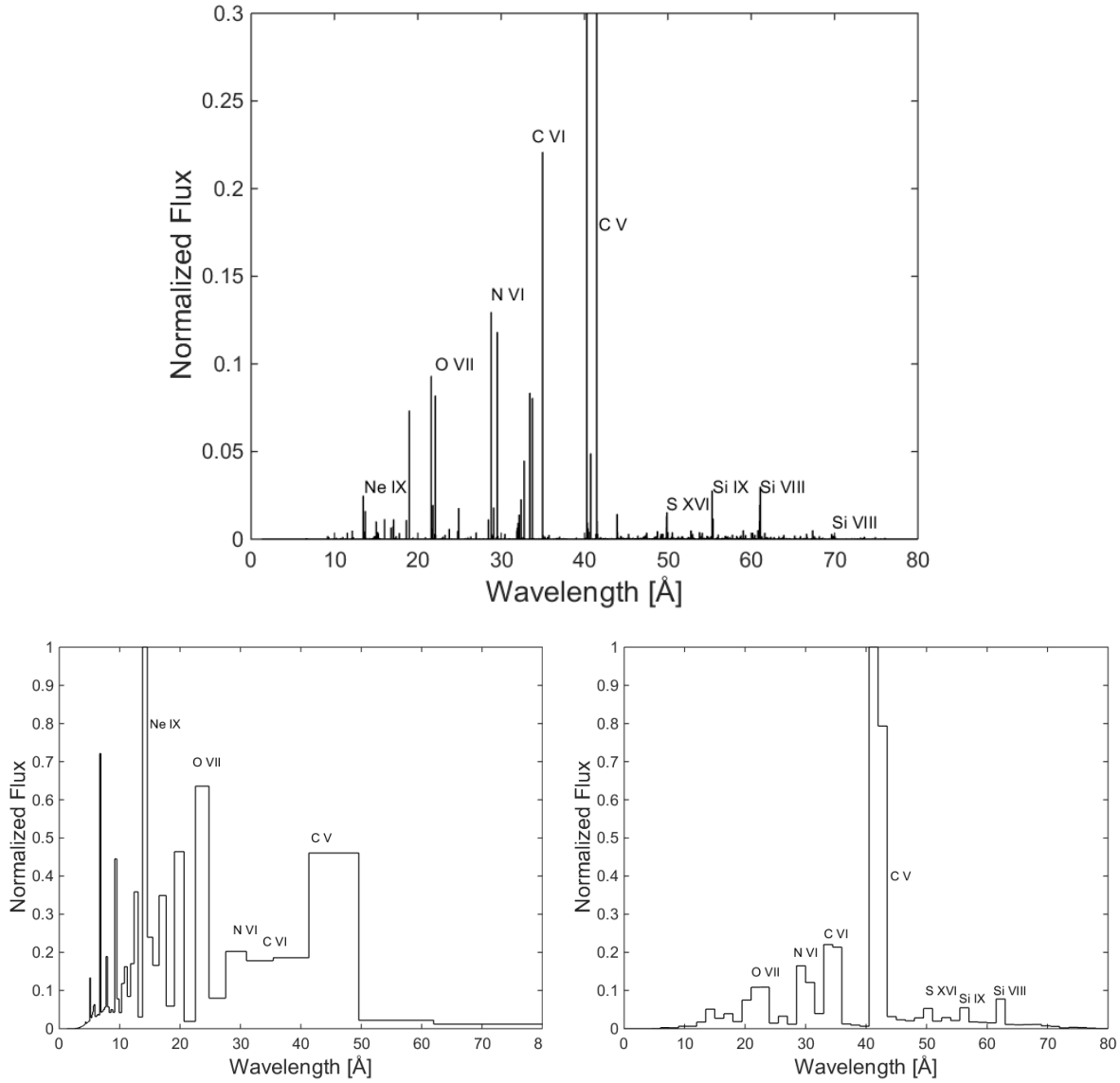

Figure 1.21: *Top*: Simulated spectrum of Cygnus (XSPEC). *Bottom-Left*: The same spectrum seen with energy resolution comparable to *Chandra/XMM/Suzaku*. Resolving power improves at higher energys, and thus the wavelength bin size decreases at short wavelengths. Spectral lines become indistinguishable above 30 Å. *Bottom-Right*: The same spectrum seen with wavelength resolution comparable to OGRESS. At this resolution, lines above 30 Å are resolvable.

Chapter 2

The OGRESS Sounding Rocket

OGRESS is a soft X-ray spectrograph consisting of two nearly identical optical channels. Figure 2.1 shows a basic diagram representing the main components of the payload. Each optical channel has three main components: passive focuser modules (to create a focus), off-plane grating arrays (to diffract the light), and Gaseous Electron Multiplier (GEM) detectors (to collect and measure the light). The different positioning of the detectors relative to the incident spectrum (resulting in different bandpasses) is the only distinguishing characteristic between the two channels.

OGRESS is the fourth generation of a series of similar payloads launch by the University of Colorado, beginning in 2006. The three main components of the soft x-ray spectrograph (the focusers, gratings, and detectors) were inherited from these previous payloads, and will be discussed briefly here.

2.1 Wire-Grid Passive Focusers

Typical X-ray telescopes use nested grazing incidence mirrors to collect and focus their light. This has the obvious advantage that the geometric collecting area of the instrument can be made arbitrarily large (within budget, space, and weight limitations), and thus can observe arbitrarily dim targets. A sounding rocket budget is more inclined to find a cheaper alternative, as X-ray mirrors are typically very expensive. More importantly, it is very difficult to perform dispersive spectroscopy on diffuse sources using a typical imaging system, as discussed in section 1.3.2 (see Fig. 1.20). The Cygnus X-ray Emission Spectroscopic Survey (CyXESS) payload was originally

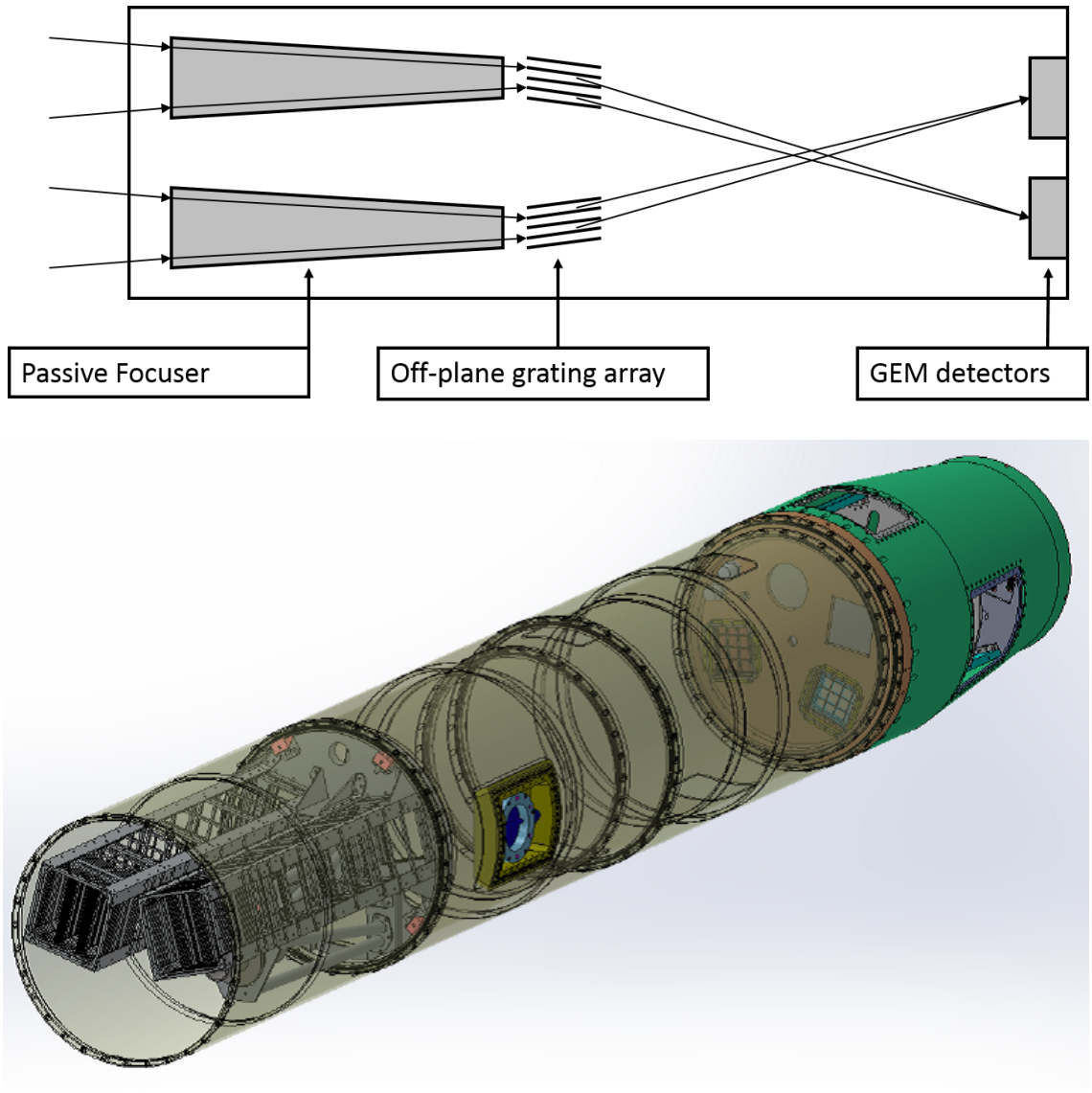

Figure 2.1: A very basic diagram showing the main components of the OGRESS Spectrograph.

designed to use a wire-grid passive focuser to sculpt a converging beam (shown in Figure 2.2). The terminology for these optics has been the subject of mild debate since their creation. Their primary function is to produce a focus, but they accomplish this without modifying the path of any light rays. They operate in very similar fashion to standard wire-grid collimators and have been referred to as such. I will refer to them as "passive focusers", or simply "focusers", as this is their intended function in the OGRESS telescope.

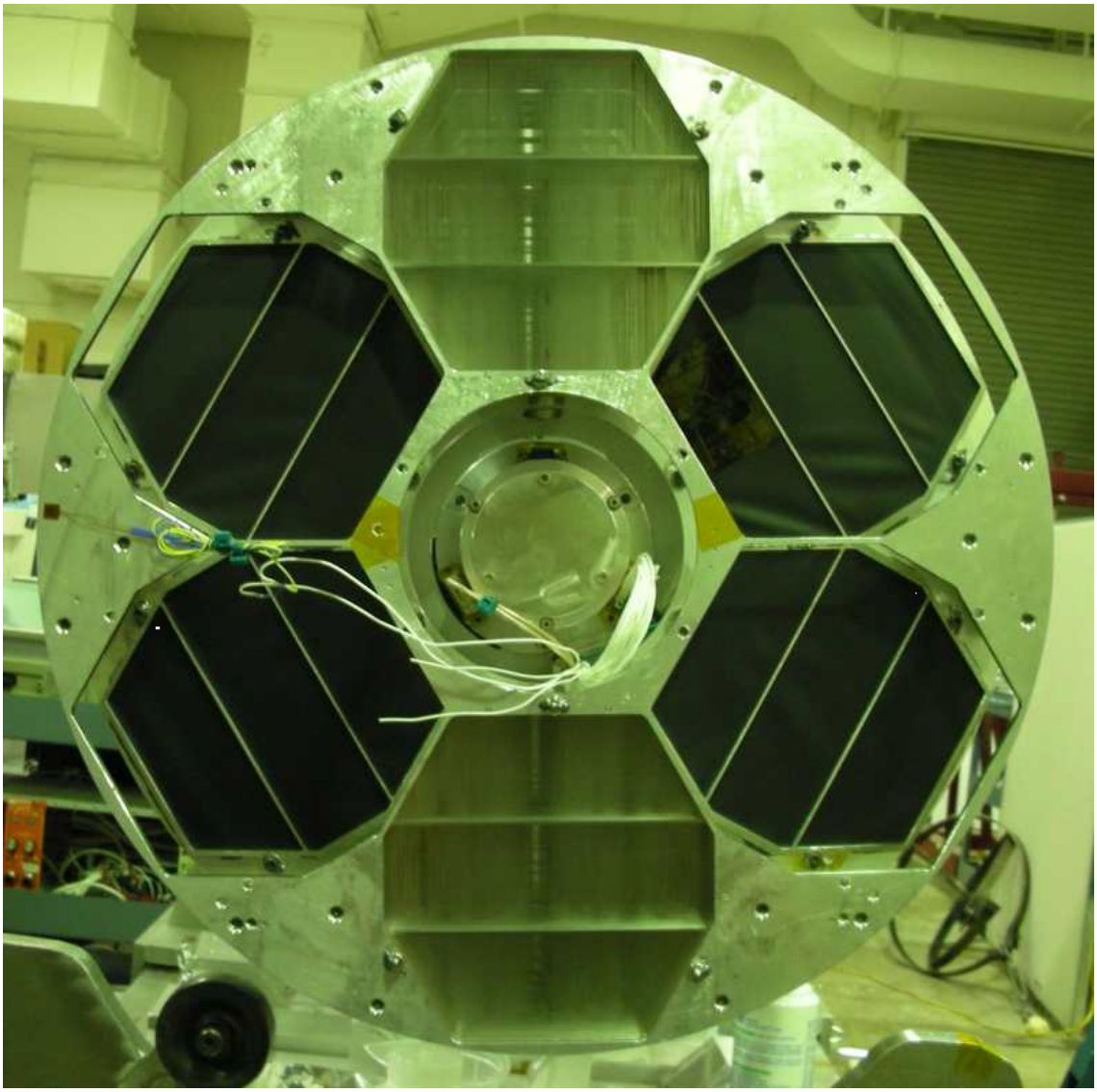

Figure 2.2: The wire-grid focusers flown on the CyXESS payload.

Because of repeated damage to the payload in past launches, this focuser structure has been rebuilt several times, but the basic design has remained the same. These focusers have been discussed in great detail in three previous theses. Since I inherited these focusers and did not modify them in any way, I will only discuss them briefly. See McEntaffer [2007] and Oakley [2011] for the original design process, and Zeiger [2013] for the design and implementation of the second generation used here.

24 wire-grid plates are stacked sequentially at varying positions over roughly 1 meter. See Figure 2.3 for an image of a single wire-grid plate. As can be seen in the figure, each plate has a

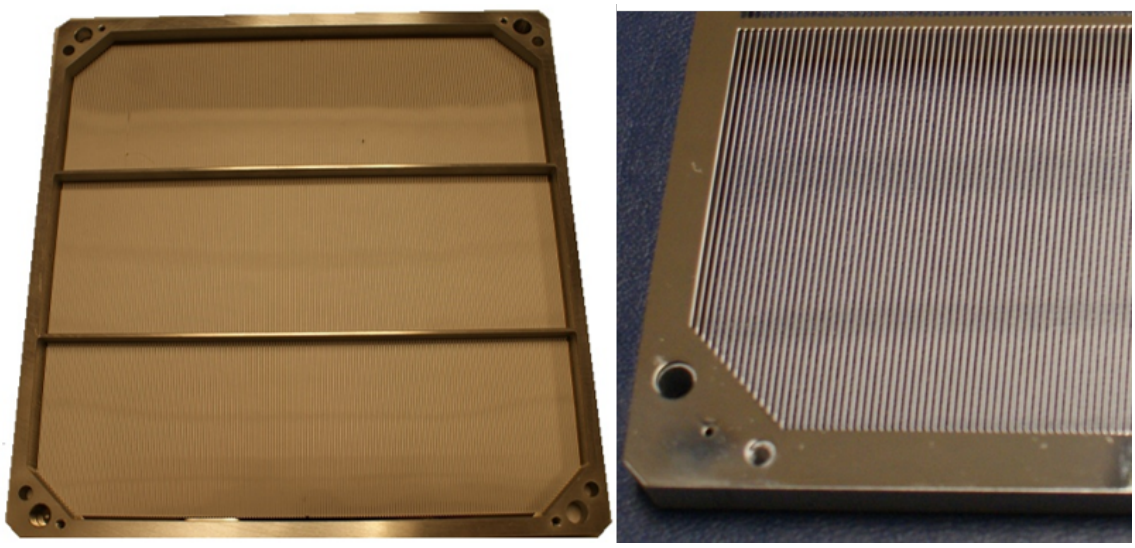

Figure 2.3: A single wire-grid plate. A total of 24 plates are stacked sequentially to create a passive focuser module.

series of vertical wires, effectively creating a series of slits which each collect light from a different portion of the FOV. As the plates approach the back of the stack, the slits become narrower and closer together. This arrangement only allows light converging from the desired directions to pass all the way through the focuser, as shown in Figure 2.4. Light coming from alternate directions is vignetted by the wires and absorbed. Because the slits only converge along one axis, a line focus is created at the focal plane, and the spectrum will appear as a series of long lines (as shown in Figure 2.5), rather than discrete points, as in *Chandra* or *XMM-Newton*. Figure 2.6 shows a view down the OGRESS focuser modules. The dark lines across the focuser faces show areas where light (from the observer's position) can travel a significant distance down the focusers. Only the largest, most distinct line on each focuser allows light to pass through completely.

OGRESS inherited its focusing optics from the CODEX payload (Zeiger [2013]), the only payload within the CyXESS heritage that did not suffer significant damage on landing, making OGRESS the only payload that did not require a significant rebuild of the focuser structures. Since

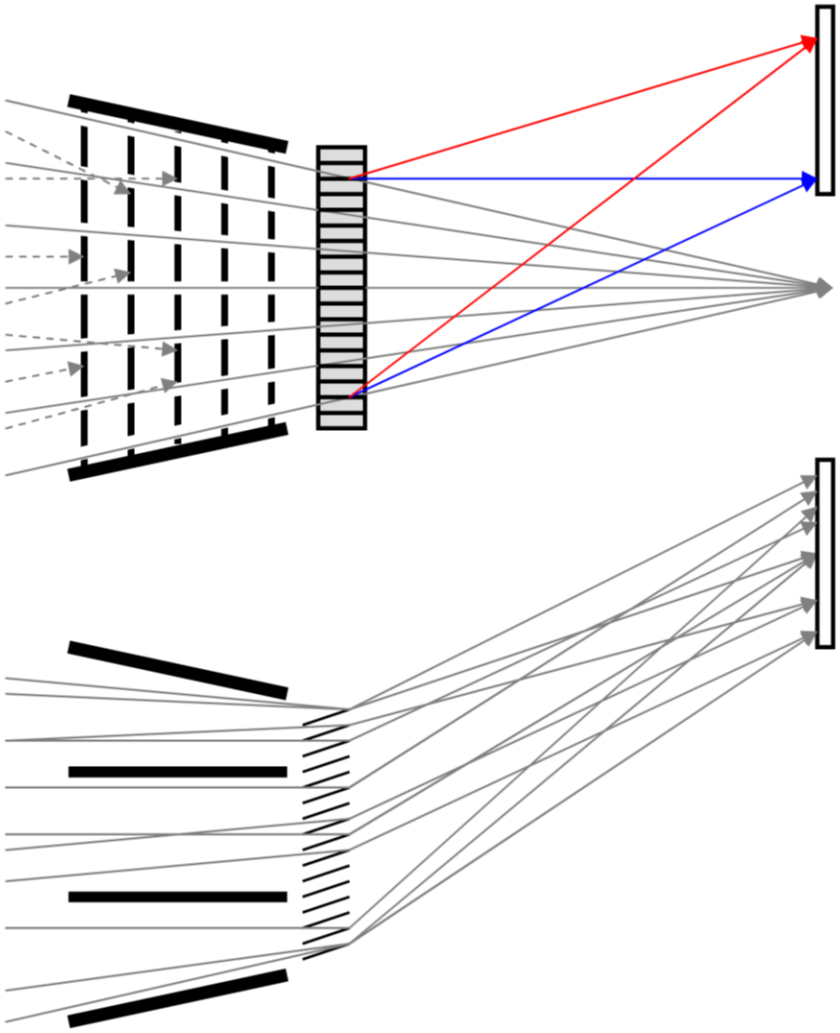

Figure 2.4: Incident light on a focuser module followed by the grating array and detector. *Top*: A view parallel to the slits. Light can travel through the slits and form a focus. Light from undesired angles is vignetted and destroyed. *Bottom*: A view perpendicular to the slits. Light is only focused in one dimension leading to long lines at the focal plane.

the focusers had already been thoroughly tested and calibrated for the CODEX launch, I was able to save a significant amount of testing time and turn my attention to the more relevant problem, the detectors. These focusers are designed to accept light from a $3.25^\circ \times 3.25^\circ$ FOV and form a line focus of $\sim$1.7 mm, as shown in the ray-trace of Figure 2.7.

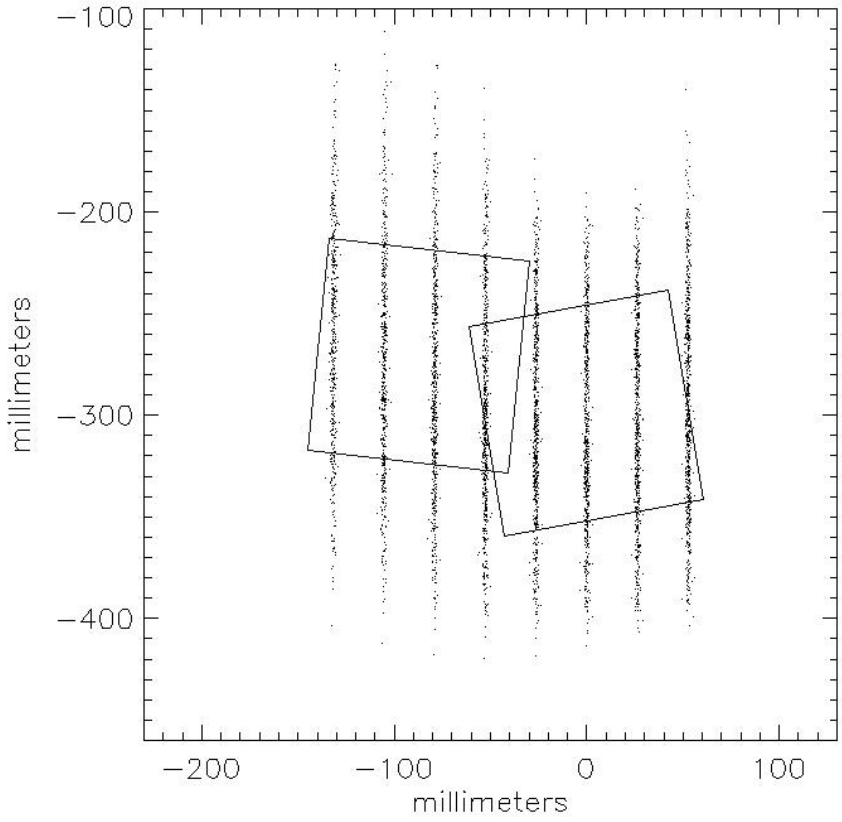

Figure 2.5: A spot diagram of incident light at the focal plane for one optical chain. The long spectral lines generated by the focuser modules require large-format detectors in order to maintain acceptable effective area. The squares represent the active areas of the detectors relative to the incident spectrum. Because each detector collects light from its own optics chain, the detectors do not overlap in the real instrument. The spectral lines represent different orders of Oxygen K-α (spanning order -5 through +2).

2.2 Off-plane Grating Arrays

Our dispersive optics were also inherited and unmodified from previous payloads and will thus also be discussed only briefly. Once the incident light from our science target has been collected and directed into a converging beam, it is split up into its constituent colors to produce a spectrum with an array of off-plane gratings.

Spectrometers typically employ gratings in the in-plane mount, as shown in Figure 2.8. In this configuration, incident light approaches the grating perpendicular to the grooves and diffracts

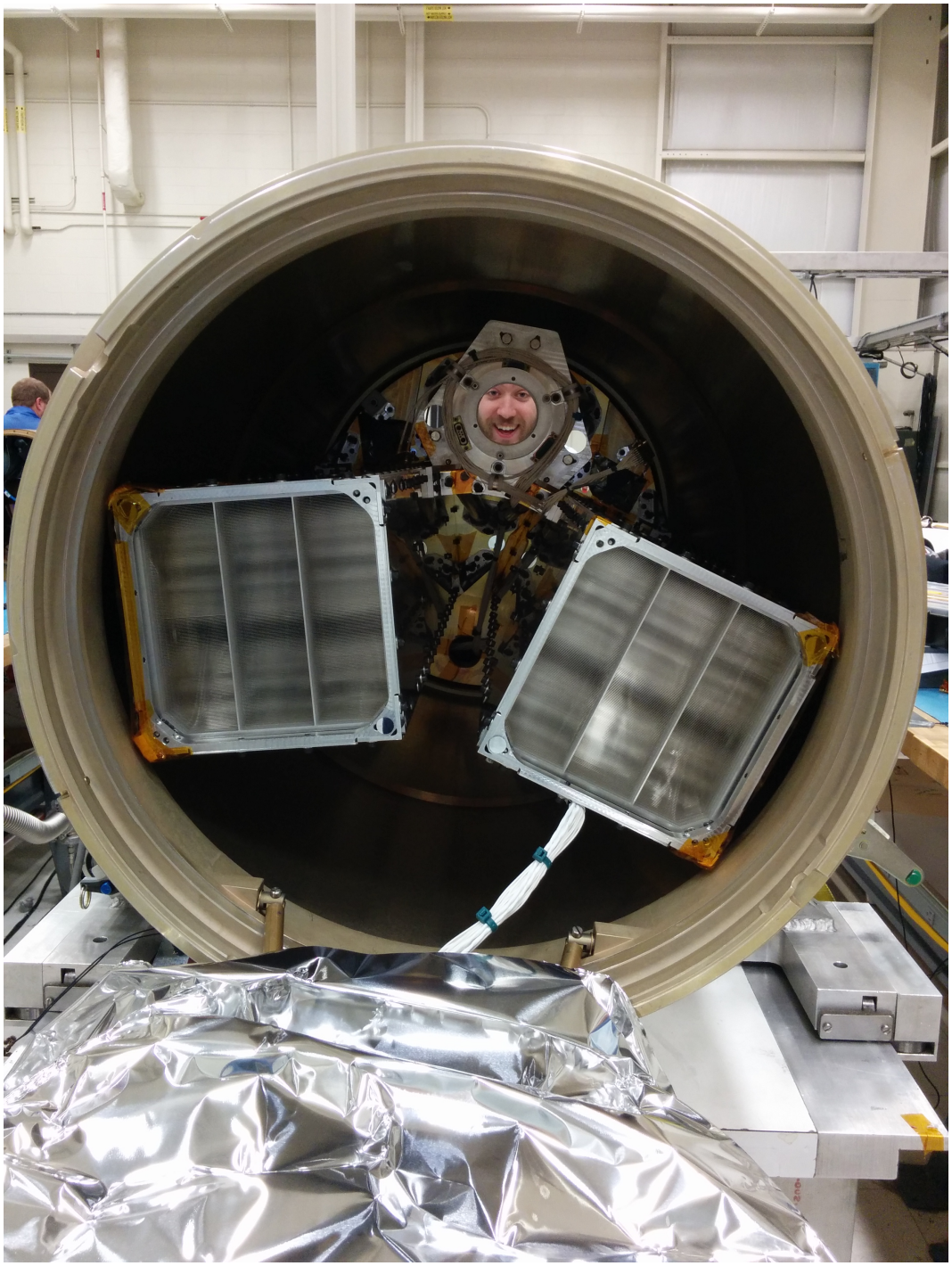

Figure 2.6: A view down the OGRESS focuser modules. The dark areas in the modules show areas where an observer can see relatively deeply into the modules before the line of site is blocked by a wire. The darkest regions show where the line of site can pass through the entire module. The authors face is seen reflected in the star tracker alignment flat.

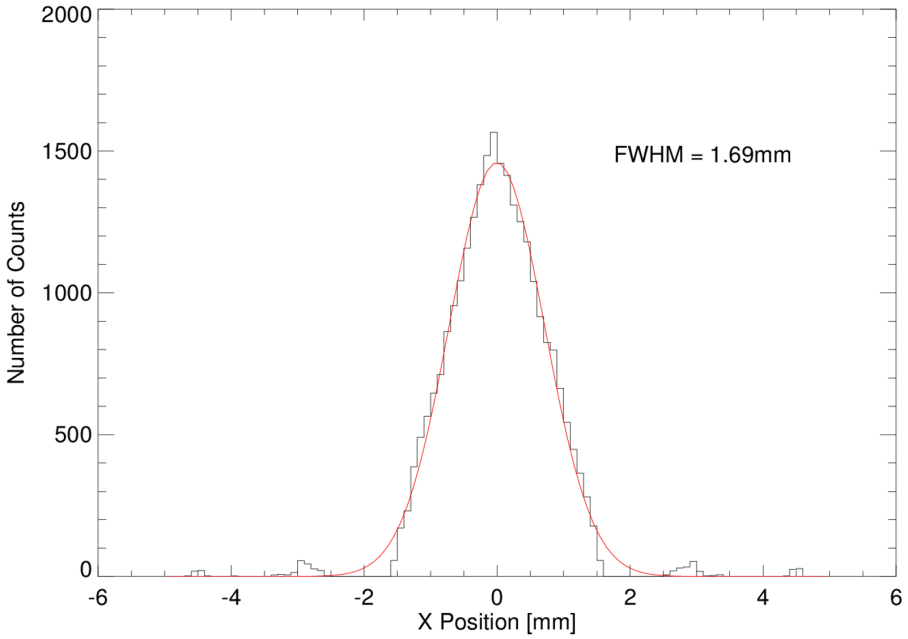

Figure 2.7: A simulation of the line-focus created by the focuser modules. $< 1\%$ of light from undesired angles is able to pass through the modules.

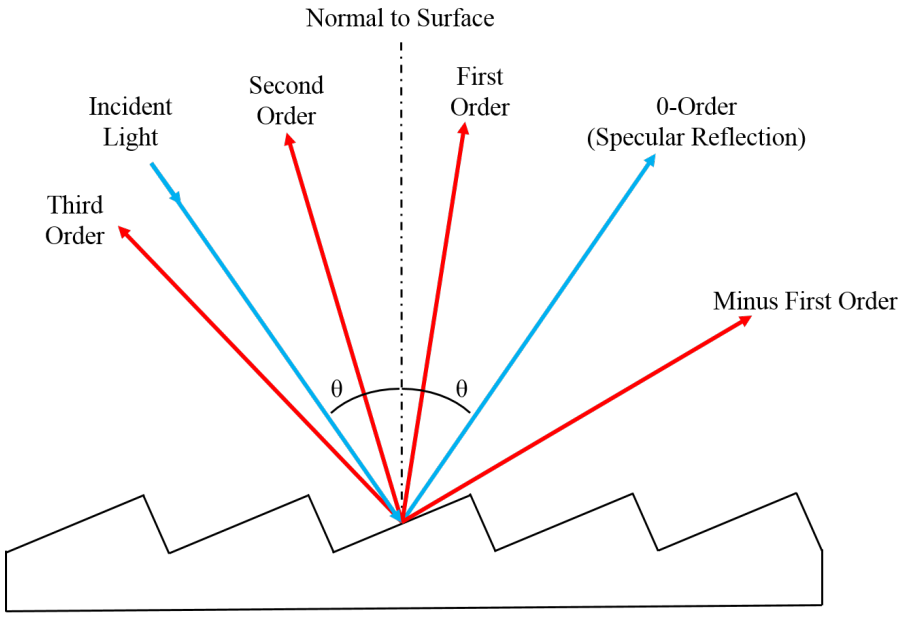

Figure 2.8: A single grating in the in-plane configuration. This configuration produces low diffraction efficiency in systems requiring grazing incidence.

in an arc, such that the incident and diffracted light lies within the same plane. When working with optical or UV light, this configuration can be used at near-normal incidence requiring only one grating. As the wavelength of incident light decreases, the reflection angle must become shallower to maintain reflection efficiency, and gratings must be stacked in arrays to maintain adequate collecting area. The groove density must also become higher to maintain high dispersion. This is made easier in the in-plane configuration, as the incident light "sees" the grating grooves in profile, increasing their effective density. Unfortunately, high spectral orders are lost because they are vignetted by adjacent gratings, leading to lower spectral resolution and throughput for the instrument.

Recent advances in nanofabrication techniques now allow gratings to be constructed with very high groove density (5670 lines/mm for OGRESS), removing the primary advantage of in-plane, grazing incidence gratings. The problems of degraded resolution and throughput can be solved by using gratings in the off-plane configuration. In this configuration (shown in Figure 2.9), incident light approaches the grating quasi-parallel to the grooves. The light, once again, diffracts in an arc, but the incident and diffracted light are in orthogonal planes, hence the "off-plane" designation. In the off-plane configuration high spectral orders are no longer vignetted by adjacent gratings in the array. This provides higher throughput (since light is not being lost) and higher spectral resolving power (at higher spectral orders).

The gratings are mounted at the back end of the focuser structures where the converging beam is still quite large, and the grating array must be matched in size in order to diffract the full beam. Since each grating must be mounted at grazing incidence (4.4° for OGRESS) an array of 67 gratings is required to capture the beam from an individual focuser module. These gratings are held in a titanium flexture mount (shown in Figure 2.10) which holds each grating in tension. This keeps the gratings flat and prevents them from contacting each other during launch vibrations. At the focal plane, the gratings produce a dispersion of 0.89 Å/mm (see Oakley [2011] for a derivation). Because the optical path length will change depending on wavelength, spectral lines increase in width as wavelength increases from 1.7 mm at 0-order to $\sim$ 2.1 mm at 120 Å. Thus, our spectral resolution will vary from $\sim 1.5 - 1.8$ Å across the face of the detectors, and the resolving power

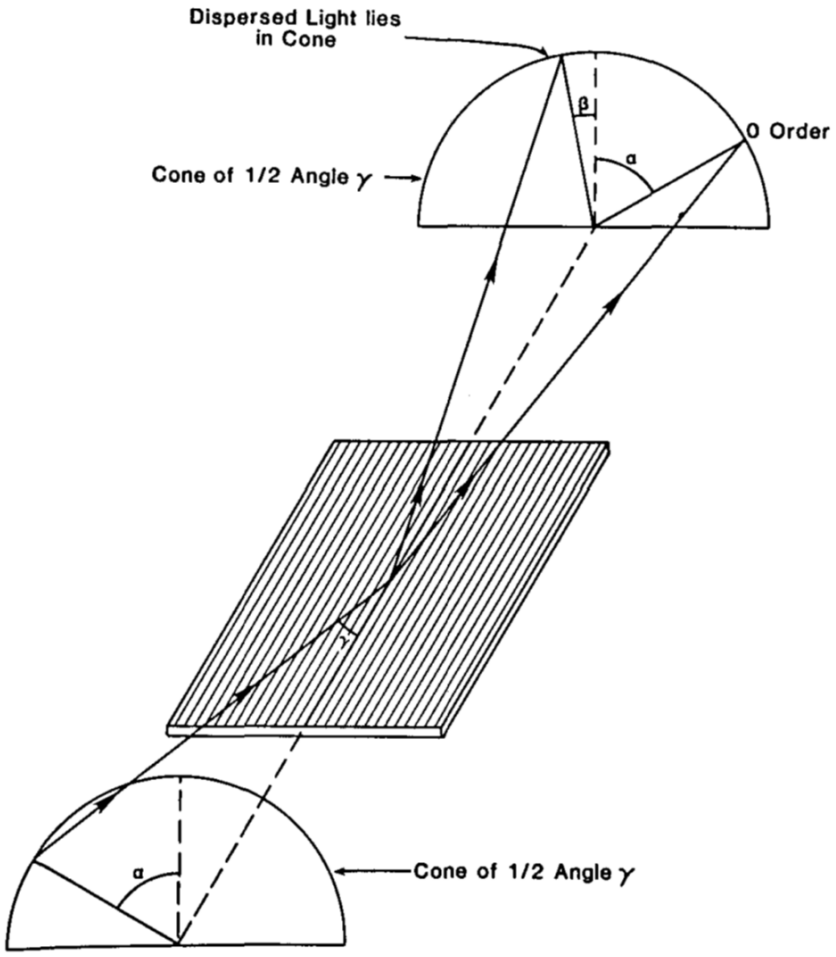

Figure 2.9: A single grating in the off-plane configuration. The spectrum is no longer in the same plane as the incident beam, allowing tighter packing of grating modules. The image is taken from Cash [1982].

$(\lambda/\Delta\lambda)$ will be $\sim 10 - 60$.

The diffraction efficiency of our gratings is shown in Figure 2.11 Because our gratings have symmetric sinusoidal groove profiles, efficiency in negative spectral orders will be identical to the positive orders. The grating efficiency was calibrated for the CyXESS payload at 277 eV (C-Kα) and was found to agree with the theoretical efficiency curves (see McEntaffer [2007]). Unfortunately, the grating efficiency has not been recalibrated for subsequent payloads, including OGRESS.

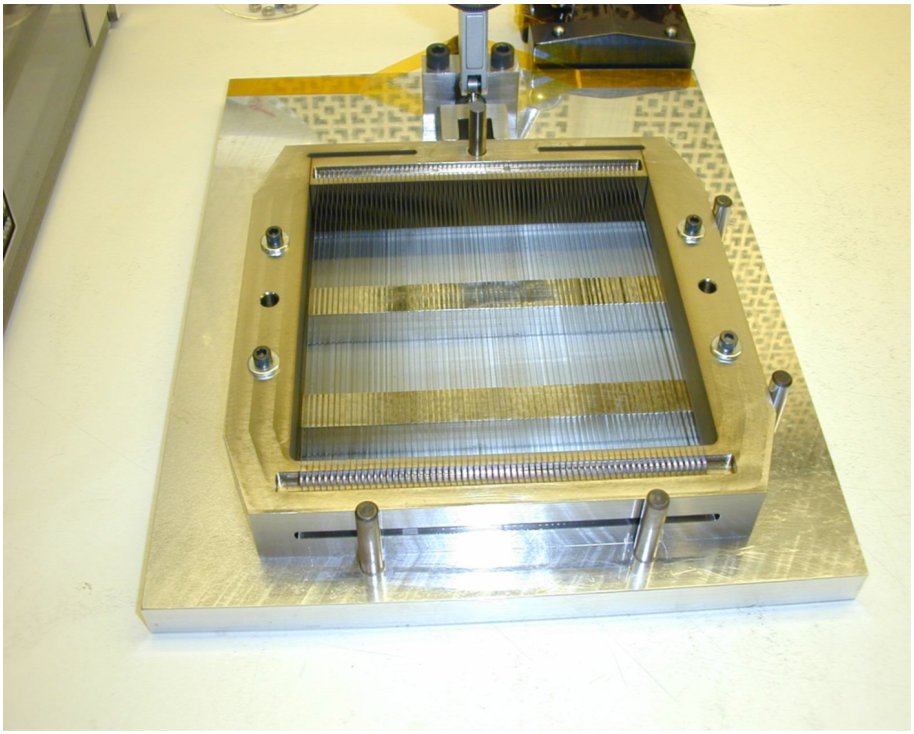

Figure 2.10: A titanium flexture mount holding 67 off-plane gratings. In this image, the mount is resting on a stage which can compress the mount, allowing the gratings to be inserted or removed. When the mount is released, the gratings are held in tension.

2.3 Gaseous Electron Multipliers

To collect the spectrum, OGRESS uses Gaseous Electron Multiplier (GEM) detectors. GEMs were initially developed at CERN to detect energetic particles and X-rays created in particle accelerator experiments (Sauli [1997]). Shortly thereafter, people began to consider the possibility of using GEMs on a space mission to detect X-rays (Costa et al. [2001], Jahoda [2010], Soffitta and Team [2013]). The CyXESS payload lineage is thus far the only attempt to utilize GEMs in a space environment.

A basic schematic of a GEM detector is shown in Figure 2.12. Incident light is transmitted through a thin window into a gas-filled chamber and ionizes the detector gas, creating a population of photoelectrons. Due to an applied voltage, the photoelectrons find themselves in an electric field, causing them to drift toward the back of the detector. An electron cascade is produced

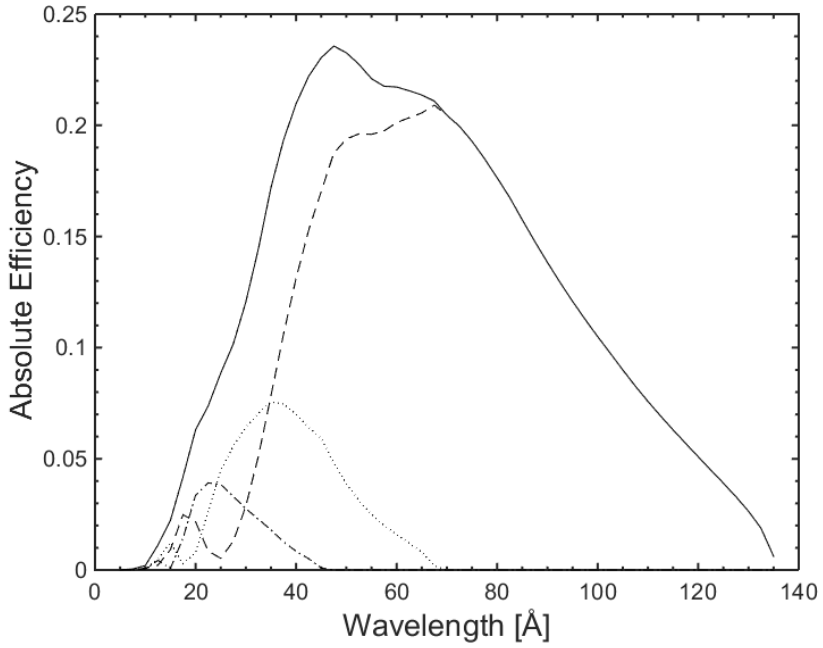

Figure 2.11: The theoretical grating efficiency curves for first order (dashed), second order, (dotted), and third order (dash-dotted). The solid line represents a sum over all orders (except 0-order). McEntaffer [2007] confirmed these efficiencies at the carbon K-α line (first and second order).

when the photoelectrons encounter a series of GEM foils. Each GEM foil consists of a layer of perforated dielectric material coated with a thin layer of copper on each side. By applying a voltage difference between the copper layers, a very strong electric field can be produced within the pores. When photoelectrons drift into the pores, shown in Figure 2.13, they are accelerated into other gas molecules, causing further ionizations and resulting in a Townsend Avalanche. The resulting pulse of electrons is deposited onto an anode at the back of the detector and subsequently read out by the electronics.

The advantages of GEMs for OGRESS are two-fold. First, they can be made in large format, allowing us to capture a large portion of the long spectral lines at the focal plane, mentioned before. Thus, the size of the detector directly translates to both effective area and increased bandpass. The second advantage of GEMs is that they can be made inexpensively, and are thus attractive to a sounding rocket budget.

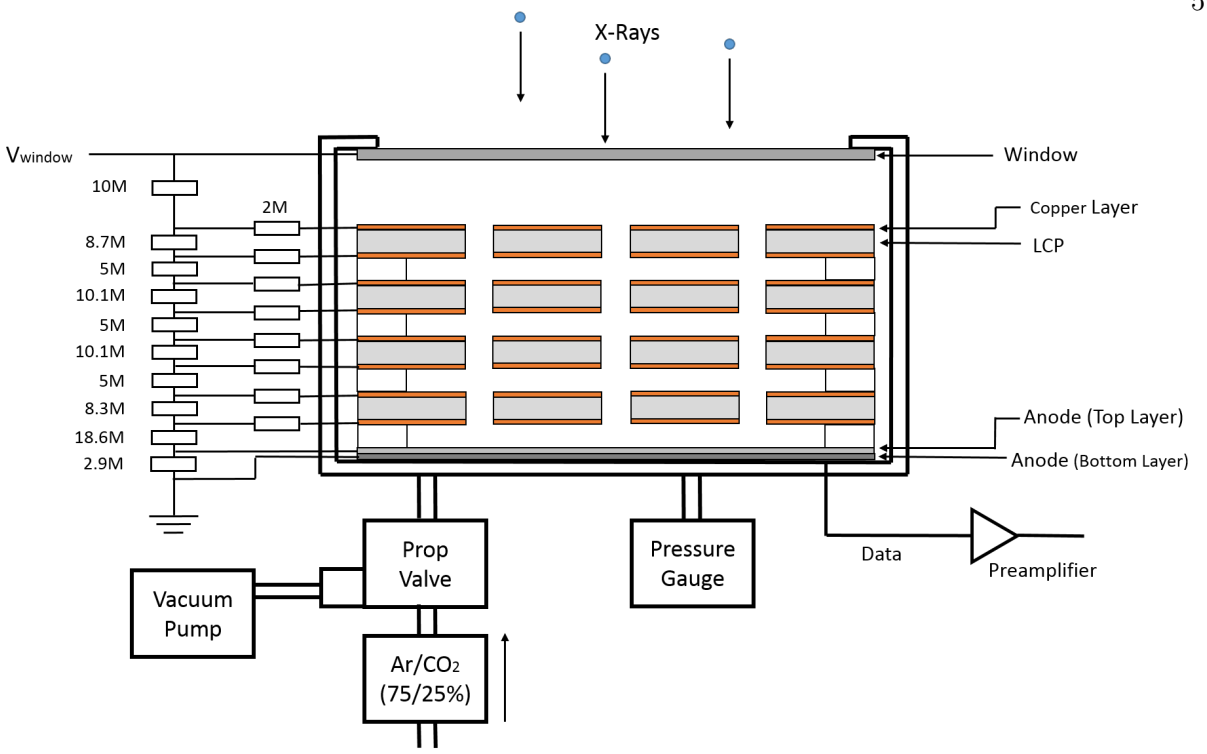

Figure 2.12: A basic schematic of a GEM detector. X-rays enter the detector through the thin window and generate photoelectrons by ionizing the detector gas. The electrons are accelerated and amplified by the GEM foils, and the resulting charge pulse is deposited on the anode.

We will now discuss the specific characteristics of OGRESS' detectors. Pictures of one of these are shown in Figures 2.14 and 2.15. The detector windows are made of 5000 Å thick polyimide coated with a 300 Å layer of carbon. The carbon layer allows a voltage to be applied, supplying the initial drift electric field for the photoelectrons. The GEMs are filled with a mixture of Argon (75% by volume) and CO_2 (25% by volume). The argon is easily ionized by the incident X-rays, while the CO_2 acts as a quencher gas to collisionally resupply electrons to the ionized argon atoms. Using a quencher gas leads to a steady gain over extended periods of integration. To achieve appropriate gain for soft X-rays, each detector uses 4 GEM foils to amplify the signal from the original photoelectrons. Roughly -3600 volts is applied to the window. This voltage is steadily reduced at each copper layer and finally reaches ground at the detector anode. The anode is a two-layer serpentine cross delay-line (one layer for X, one layer for Y). The raw signal from a

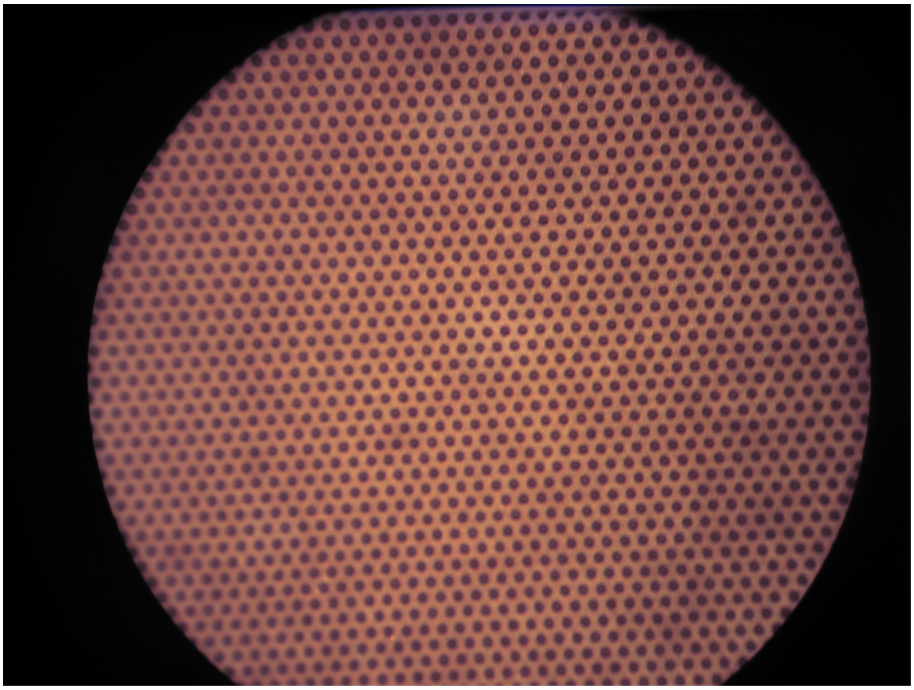

Figure 2.13: A GEM foils seen through a microscope. The holes are each 70 μm wide.

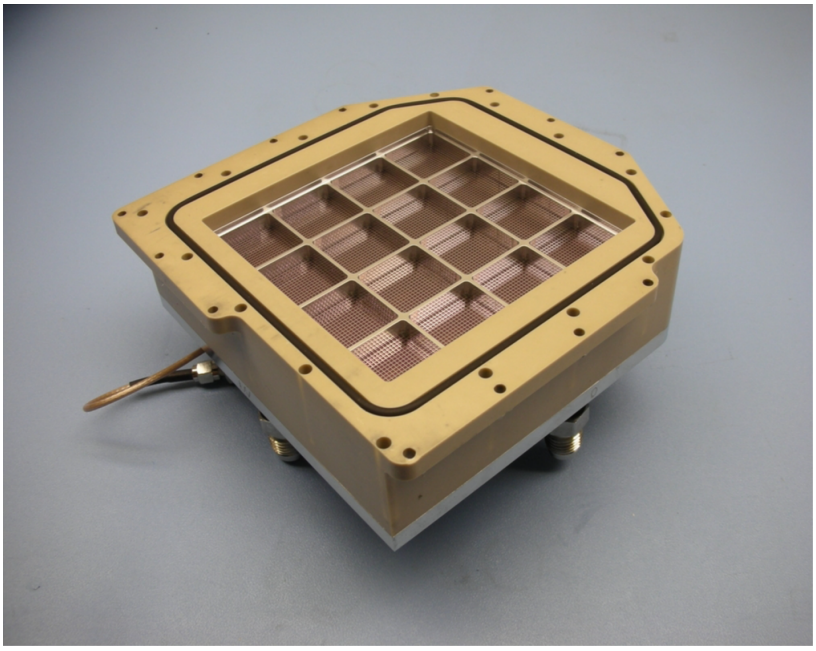

Figure 2.14: An image of a GEM detector. The O-ring seals the detector against the payload bulkhead. The thin polyimide window is visible, along with the 4x4 aluminum grid which supports the window against the interior pressure.

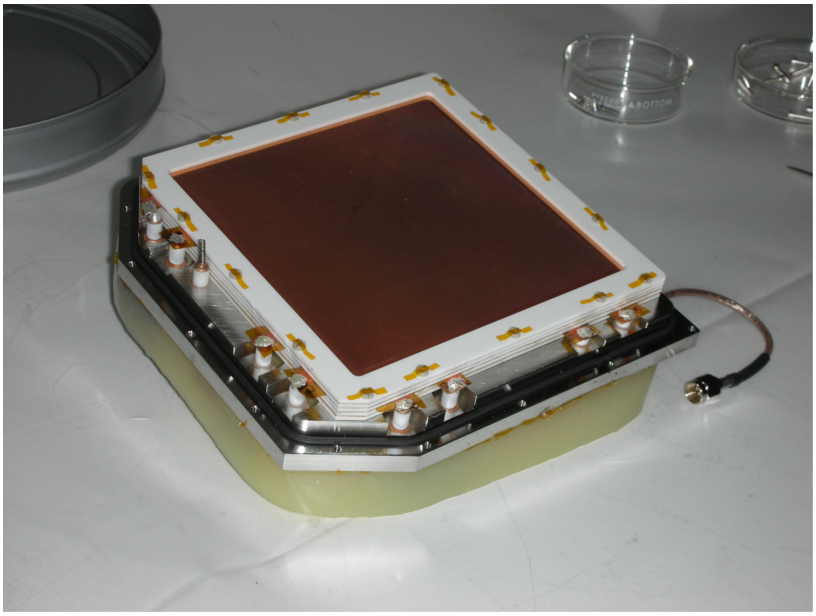

Figure 2.15: A GEM detector with the window and housing removed. The GEM foils connect to the resistor chain through the white cylindrical terminals. Copper traces to each foil are connected to the terminals using conductive epoxy.

photon is 4 voltage pulses (designated fast pulses) which run to both ends of each delay line. The relative timing of these pulses provides the spatial information of the incident photon. The total charge deposited is also measured, theoretically giving the GEMs an intrinsic energy resolution which can be used to separate spectral orders.

CyXESS and EXOS used the first generation of GEM detectors constructed at Sensor Sciences, LLC., and shown in Figure 2.14. These detectors have an asymmetric shape based on the hope that six detectors would eventually fit together on the detector bulkhead. A high voltage is applied to the carbon-coated detector window, which is connected through a high-volts resistor chain to the top and bottom layers of each GEM foil, as well as the anode. A schematic of the first generation resistor chain is shown in Figure 2.16. Because the charge pulse falls preferentially on the top layer of the delay line, a voltage must be applied between the two layers to direct more of the charge onto the bottom layer, ideally resulting in an equal amount of charge falling on each layer. An image of an anode is shown in Figure 2.17, and the reduced geometrical area of the bot-

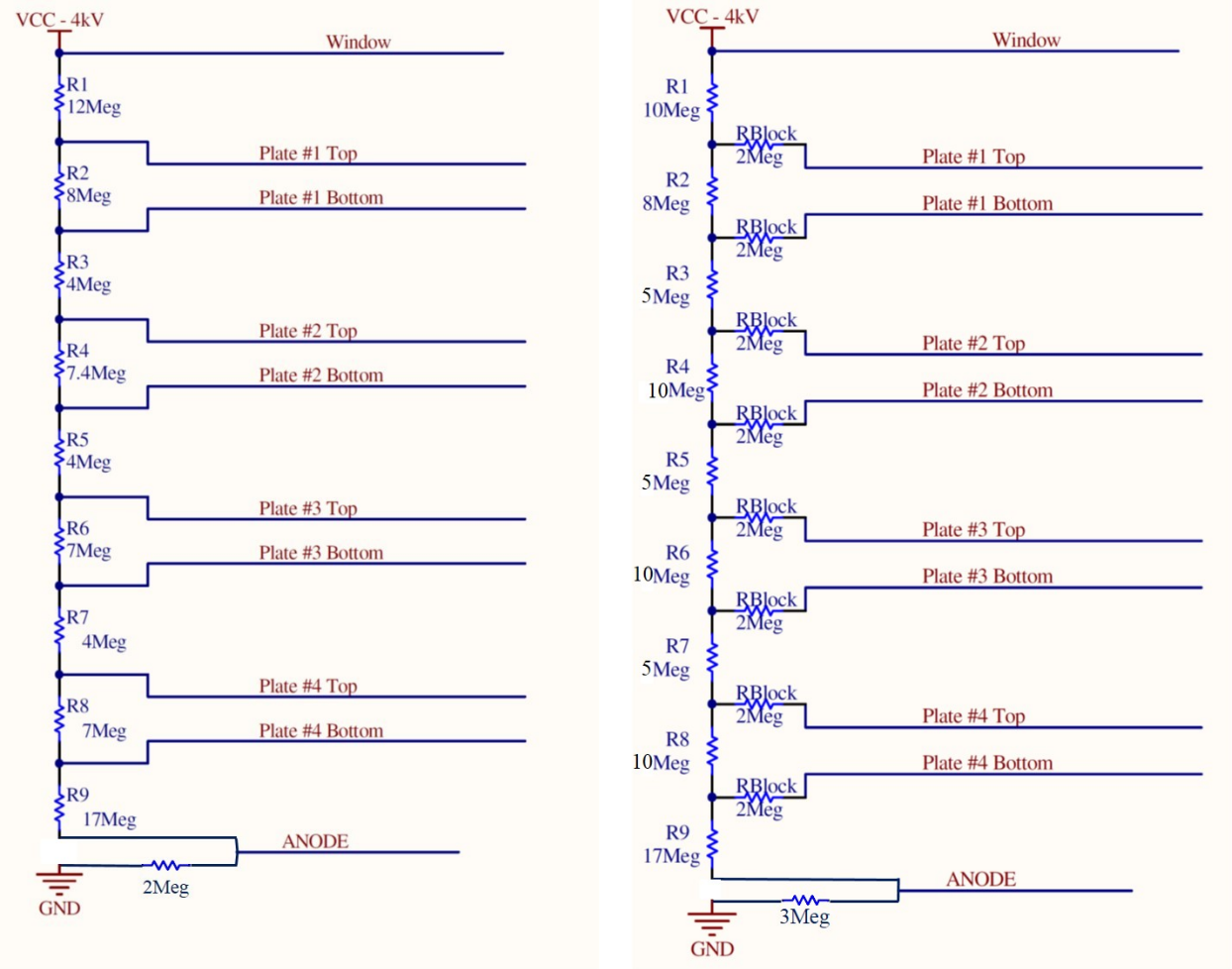

Figure 2.16: A schematic of the first- and second-generation GEM resistor chains. The anode label refers specifically to the Y trace, which is voltage-biased to counteract its larger geometric area.

tom layer is clearly apparent. The optimal voltage drops for each GEM foil and for the anode were determined during the CyXESS mission for a specific set of polyimide foils at a specific pressure (14.5 PSI). This in turn led to the total voltage applied to the detector window and to the values of each HV resistor. Although EXOS upgraded to the newer LCP foils, the budget did not allow for the HV resistor chain to be reoptimized. This was also not considered necessary, since the newer foils had substantially higher gain, fewer hotspots, and were generally easier to operate. Optimizing the chains for a specific set of foils is, in some ways, foolhardy. Foils can be destroyed by arcing events and, in practice, are regularly changed. For these reasons, EXOS flew the first-generation

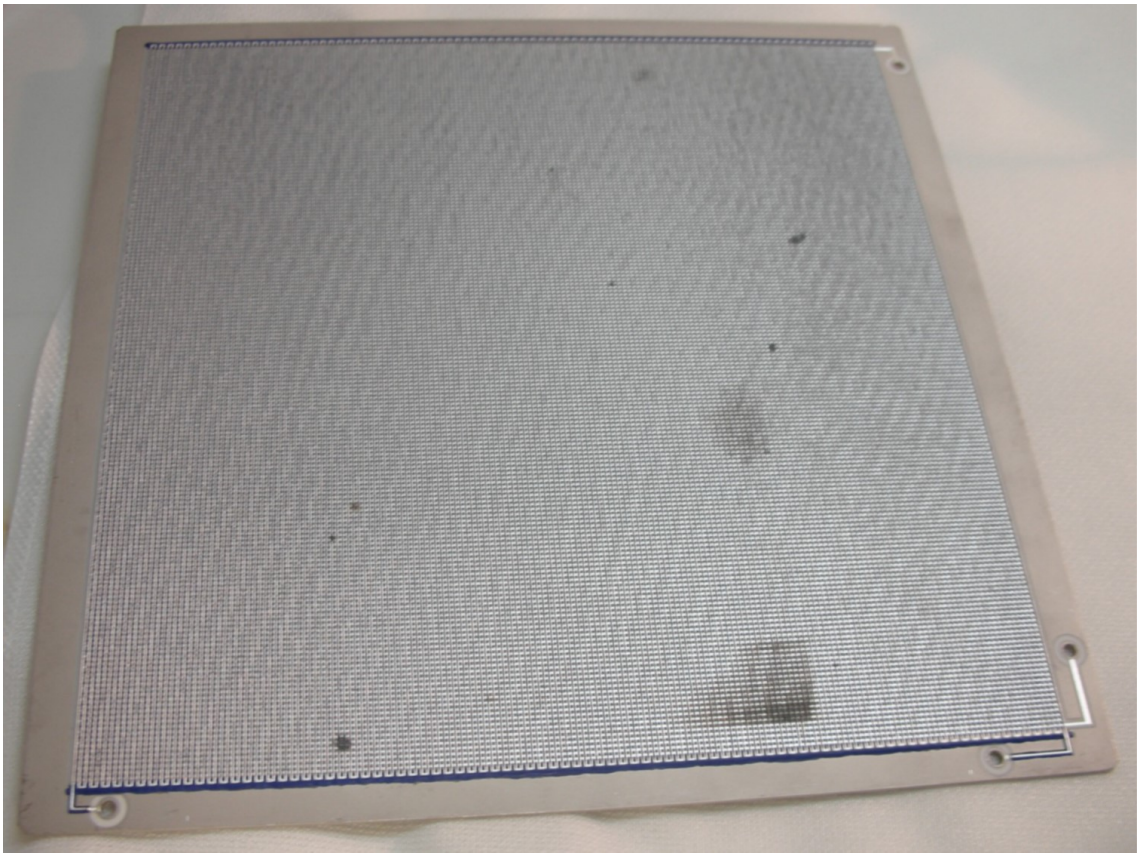

Figure 2.17: A cross delay-line detector anode. A photon generates an electron cloud which deposits charge on both traces of the anode. One trace runs in the X direction, and one runs in the Y direction. The deposited charge cloud runs to both ends of each anode and exits via the terminals seen at the corners. Because the Y anode trace sits on top, it receives a larger share of the charge cloud, unless a bias voltage is induced to make charge favor the bottom X anode trace.

detector heads with the second-generation foils.

During the CODEX mission, the idea of a 6-detector instrument was let go, and the opportunity was taken to fabricate new larger and sturdier detector heads. The new heads had many small changes which made them easier to work with in a laboratory situation. An image of the second-generation detectors is shown in Figure 2.18. The new heads were thicker, removing the risk of housing cracking, which occurred several times with the first-generation version. Mounting screws between the insulating PEEK housing and the back aluminum layer were made larger and mounted on the back side of the detectors, making assembly and disassembly more convenient.

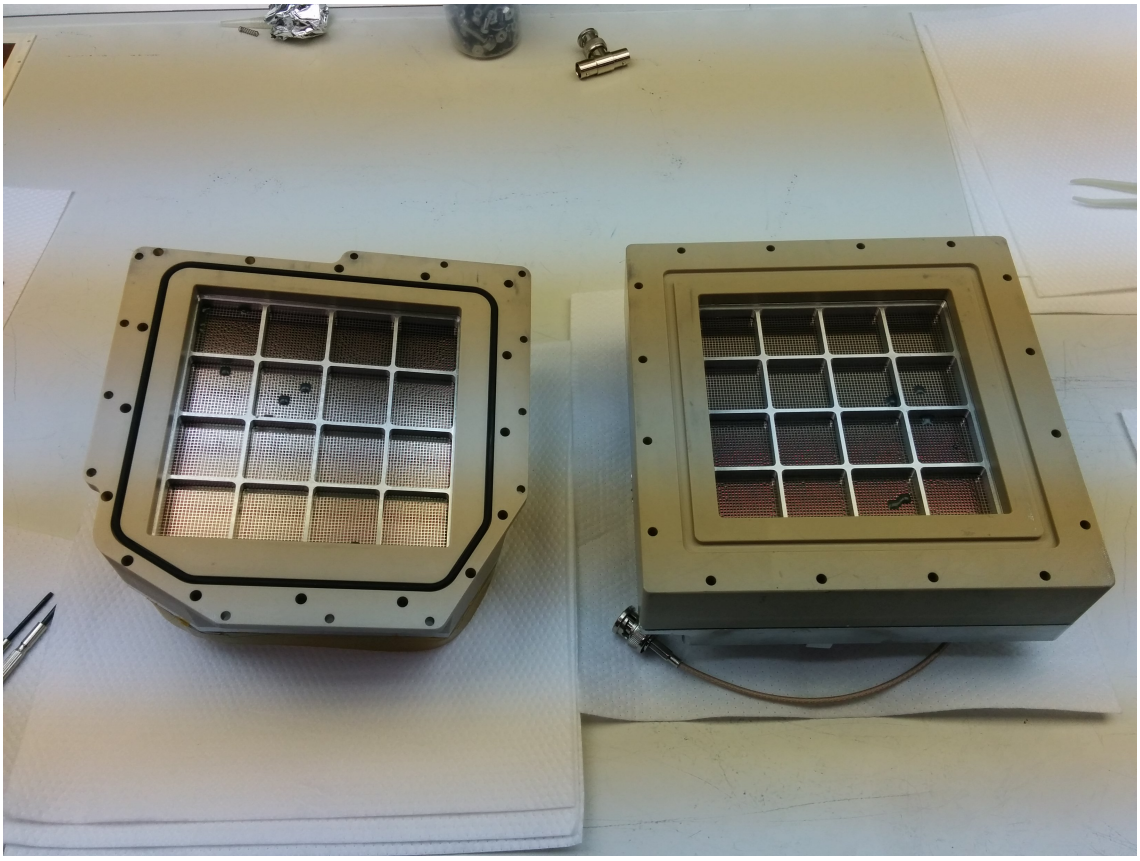

Figure 2.18: A first-generation GEM head seen on the left, and a second-generation GEM head seen on the right. Each detector window has been epoxied in several places to repair holes.

The electrical connections were also switched from SMA to BNC. The SMA connections of the first-generation heads maintained excellent signal integrity, but often became loose and only allow a finite number of tightenings before becoming unreliable. The HV resistor chains for the second-generation detector heads were also reoptimized for the second-generation foils. A schematic of the new resistor chain is shown in Figure 2.16. Unfortunately, the new detector heads did not produce reliable signal, and scheduling constraints did not allow adequate time to troubleshoot them during the CODEX mission. Ultimately, CODEX also flew two first-generation detector heads, just like EXOS.

OGRESS flew one old detector head and one new detector head. The new head was used because they are easier to work with. The old head was used because the form factor was smaller

and it could thus fit closer to the edge of the detector bulkhead, allowing a more optimal positioning relative to the dispersed spectral lines from its optics chain. Each detector was run at 10 PSI and $\sim$ -3600 V (I discuss this decision in more detail in section 2.6.3). Lower voltage applied to the detector window results in lower voltage differences at each part of the resistor chain. Because the voltage drop within each GEM foil lowers by the same factor there was no need to reoptimize most of the resistor chain. However, the anode bias voltage must remain unchanged, in order to maintain an equal distribution of charge on each layer. This required me to modify the end of the resistor chain. We cut away the insulating potting and replaced the anode bias resistor with a trimpot, allowing us to experiment with different resistance values and maintain an acceptable ratio of charge deposition on each layer, as measured by the size of the fast pulses on an oscilloscope.

2.4 Expected Performance

2.4.1 Count Rate

To form a rough estimate of the expected count rate when observing Cygnus with OGRESS, we may use data from the *ROSAT* All Sky Survey (*RASS*) to determine Cygnus' intrinsic brightness. *ROSAT* has 5 spectral bands between 0.1–1 keV, labelled R1, R2, R4, R5, and R6. Figure 2.19 and Table 2.1 show the shape and extent *ROSAT*'s spectral bands. Note that the bands largely overlap with each other. We first determine the number of counts *ROSAT* would see if it observed a $3.25^\circ \times 3.25^\circ$ FOV centered on Cygnus. The two bands of interest are R1 and R4 which effectively cover the 1/4 keV bandpass and the > 0.5 keV bandpass, respectively. The R2 band is also relevant, but it overlaps completely with R1. Thus, R2 does not contribute substantial information to our count rate estimate. An analysis of the *RASS* data shows that *ROSAT* sees ~ 209 Hz in R1 and ~ 276 Hz in R4. This translates to ~ 3.5 Hz/cm^2 in R1 and ~ 11 Hz/cm^2 in R4.

Now we must calculate OGRESS' effective area in these two bands. We begin with the geometrical effective area. For most X-ray telescopes, this will be the collecting area of the primary

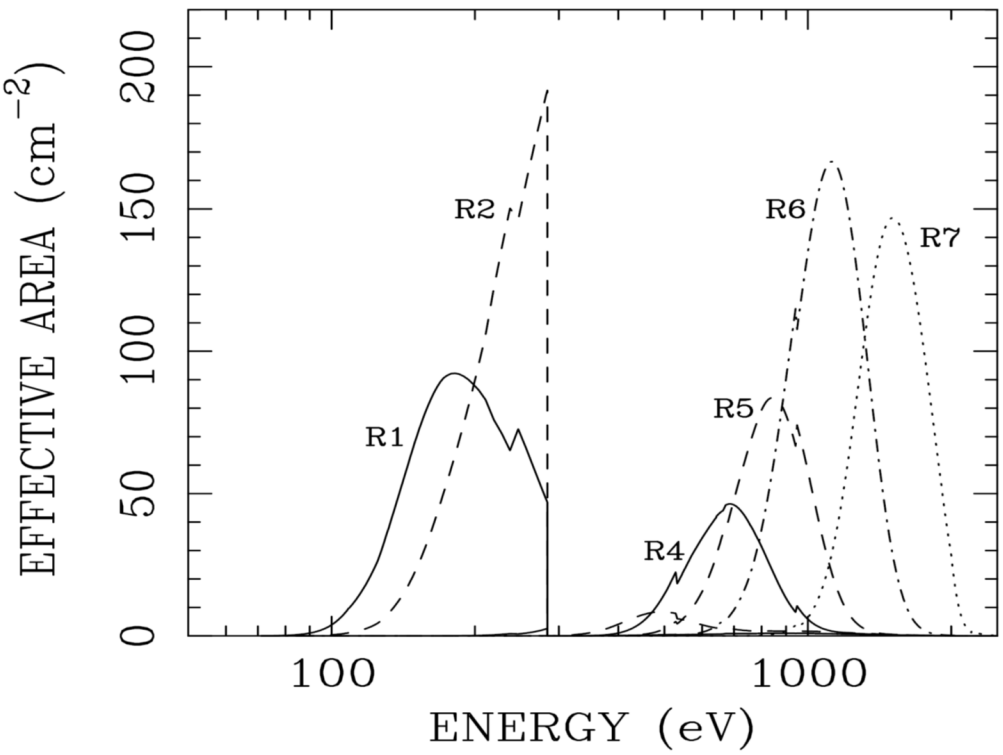

Figure 2.19: On-axis band response curves for the *ROSAT* bands.

Band Name	PI Channels	Energy[a] (keV)
R1	8–19	0.11–0.284
R2	20–41	0.14–0.284
R4	52–69	0.44–1.01
R5	70–90	0.56–1.21
R6	91–131	0.73–1.56
R7	132–201	1.05–2.04

[a] 10% of peak response. The R1 and R2 bands share the same upper energy limit because they are bounded by the carbon Kα absorption edge of the PSPC entrance window.

Table 2.1: Pulse channels and energy range definitions for for *ROSAT*'s spectral bands.

mirror. Because OGRESS does not have optics to actively collect and focus light, its geometric area is equal to the size of the line-focus created by the wire-grid focusers. A 1.7 mm FWHM (see Figure 2.7) combined with the detector width of 10 cm, leads to a geometric area of 1.7 cm^2. This is then multiplied by the transmission of each component of the telescope, which includes the losses from the wire-grid focusers (~ 0.7), the gratings (~ 0.2 for R2 and ~ 0.06 for R4, see Fig. 2.11), the ion repeller grid (0.92), the GEM window support structure (0.578), and the polyimide detector window (~ 0.5 in both bands). The R4 estimate is then multiplied by 2, since OGRESS will observe both positive and negative spectral orders in that bandpass. This leads to an estimate of ~ 0.4 Hz in R2 and ~ 0.13 Hz in R4, as seen by OGRESS. With an estimated time on target of ~ 200 seconds, OGRESS is therefore expected to collect ~ 100 counts between 10–120 Å. This is, of course, quite a small number of counts and will lead to a low S/N spectrum. In practice, OGRESS will see somewhat more counts than this from Cygnus. We expect to see several times as many counts in the 0-order line corresponding to specular reflection, most of which will be long wavelength (even down to the FUV). Additionally, *ROSAT* suffers a large gap in sensitivity between 0.284 keV (at the carbon edge of their windows) and ~ 0.44 keV, which is not as severe for OGRESS. OGRESS, will therefore, be able to observe emission in this range which *ROSAT* is effectively blind to. We will also be aided by the fact that Cygnus is expected to produce a line spectrum and that most of the flux will fall within just a few strong lines (mostly CV, CVI, NVI, and OVII lines, see Fig. 1.21).

2.4.2 Grasp

One of the classic measures of efficacy for any spectrograph is the grasp, corresponding to the product of effective area and FOV. OGRESS' grasp, as a function of wavelength, is slightly different from its predecessors due to the different placement of the detectors relative to the incident spectrum. Thus, we will carry out a derivation of OGRESS' theoretical grasp as a function of wavelength.

When estimating the count rate seen by OGRESS from Cygnus, we assumed that the effi-

ciencies of each component of the spectrograph were roughly independent of wavelength. This is acceptable when making a rough estimate, particularly since the *ROSAT* spectrum is low resolution (i.e. the bright vs. dim areas of the spectrum are not well-known). Here, however, we will take into account wavelength dependence for the diffraction gratings, the detector window transmission, and the geometric area of the detectors. The grating efficiency is already shown in Figure 2.11. The transmission of the 5000 Å polyimide detector windows is shown in Figure 2.20. Calculating the

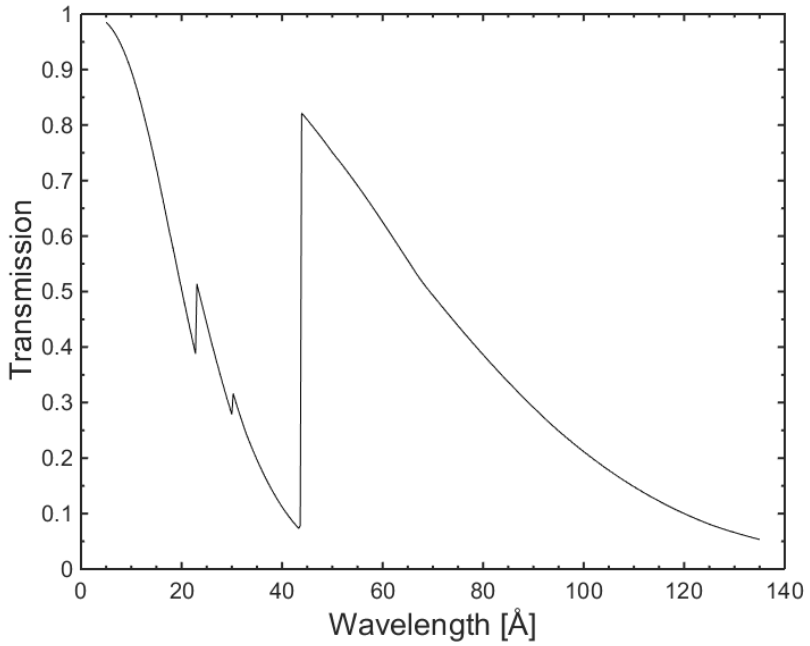

Figure 2.20: The transmission function of OGRESS' 5000 Å polyimide detector windows.

geometric area of the detectors is slightly more complicated, since certain areas of the spectrum are seen by both detectors, and the regions around 0-order are seen in both positive and negative spectral orders. The geometric collecting area of the detectors is shown in Figure 2.21.

To calculate the grasp for OGRESS, we multiply these three functions (collecting area, diffraction efficiency, and window transmission) together with the FOV of the instrument (0.0032 sr) and the geometric transmissions associated with the wire-grid focusers (0.7), the window support mesh (0.578), and the ion repeller grid (0.92). The resulting grasp of the instrument is shown in Figure

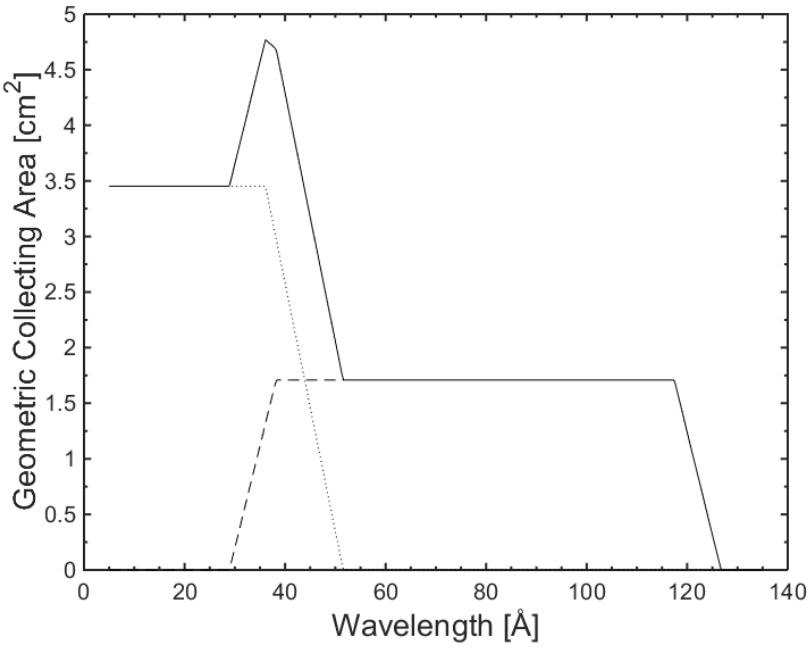

Figure 2.21: The total geometric collecting area of OGRESS' detectors is shown as the solid line. The geometric areas of detector 1 and 2 are shown by the dashed and dotted lines, respectively.

2.22.

2.4.3 Spectral Resolution

Spectral resolution is the key to better understanding the Cygnus Loop, and it is here that OGRESS will significantly outperform other instruments. OGRESS' spectral resolution is compared to that of *Chandra* and *XMM* in Figure 2.23. OGRESS begins outperforming these instruments in first-order diffraction around 20 Å, and has over twice their resolving power for wavelengths over 40 Å. Second and third order diffraction have twice and thrice the resolving power of first order, so OGRESS will outperform *Chandra* and *XMM* at shorter wavelengths, as well. As shown in Figure 1.21, OGRESS' improved spectral resolution will begin to separate lines within the 1/4 keV band, which contains a significant portion of Cygnus' flux.

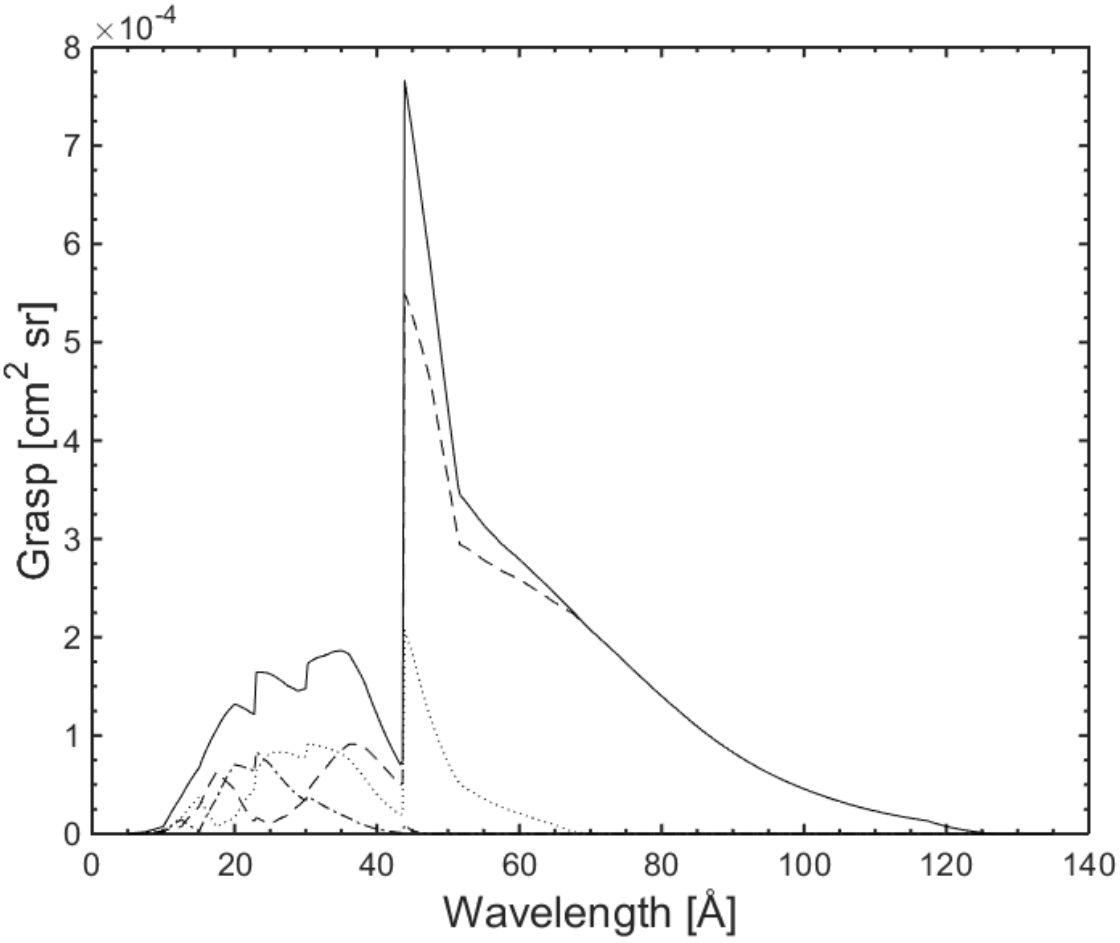

Figure 2.22: The grasp of the OGRESS spectrograph. The solid line shows the sum over all spectral orders. First, second, and third order grasps are displayed by the dashed, dotted, and dash-dotted lines, respectively.

2.5 Previous Flights and Background Noise

As mentioned previously, OGRESS is the fourth generation in a line of similar payloads launched by the University of Colorado. These previous payloads were designated CyXESS, EXOS, and CODEX (McEntaffer [2007], Oakley [2011], & Zeiger [2013]), and targeted Cygnus (CyXESS & EXOS) and Vela (CODEX). The original goal of the program was to measure Solar Wind Charge Exchange (SWCX) in the 1/4 keV band with high resolution. The original payload layout was designed to allow additional optical chains (focuser, gratings, detector) to be added within the 22”

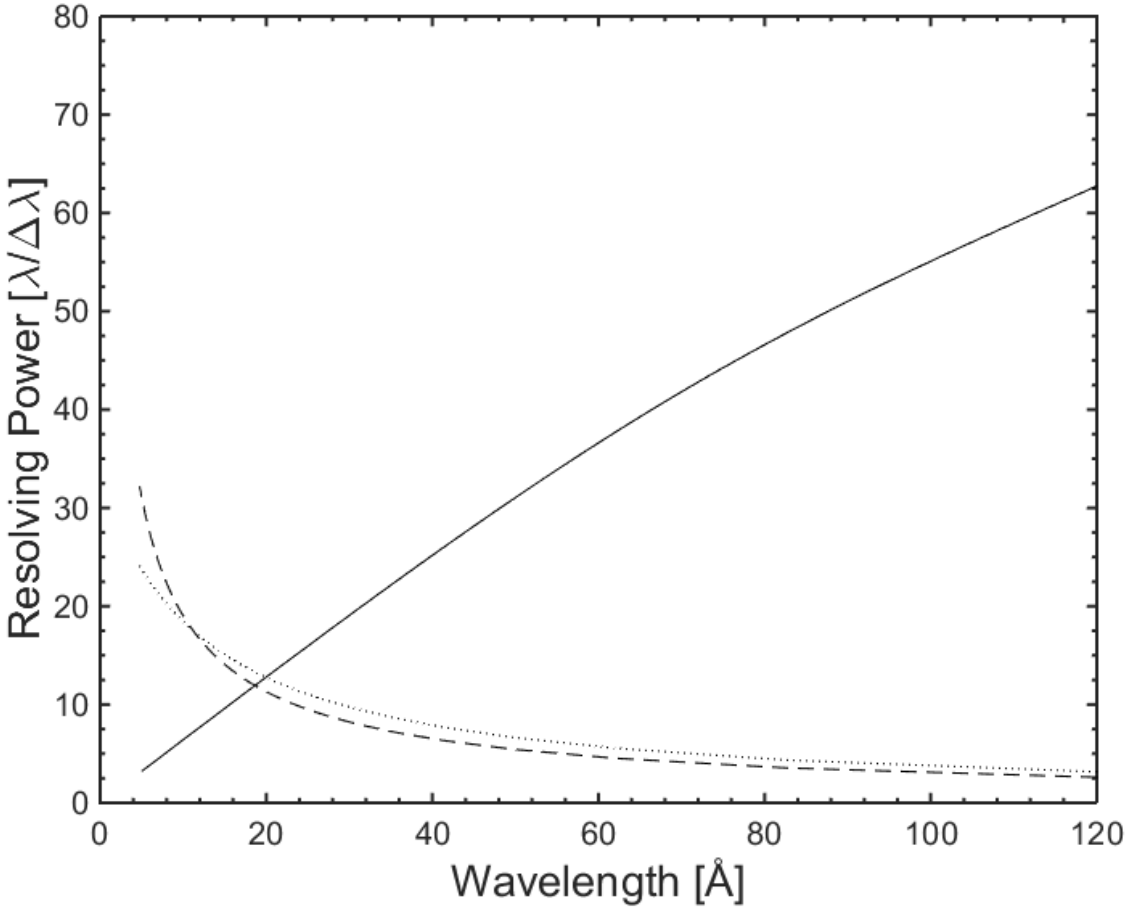

Figure 2.23: OGRESS' spectral resolving power (for first-order diffraction) is shown by the solid line. The dashed and dotted lines represent the resolving power of *XMM-Newton* and *Chandra*, respectively.

payload diameter, allowing the sensitivity of the instrument to increase with each launch. This plan was ultimately discarded during the CODEX redesign of the focusers, permanently settling for 2 optics modules. The loss in potential sensitivity is partially offset by our ability to sample each spectrum on both sides of 0-order, an option not considered for CyXESS and EXOS. Because our gratings are unblazed, we can double our effective area by simply adding more detectors to collect both positive and negative spectral orders. Each payload in this campaign has experienced unforeseen (and largely different) problems during launch, despite largely successful efforts to solve the problems of the predecessors. We will now discuss each previous payload, their modifications,

and their flight results.

2.5.1 CyXESS

The Cygnus X-ray Emission Spectroscopic Survey (CyXESS) was plagued by electronics noise, due to the use of switch-mode power supplies, which caused confusion between the two detectors. One of the detector windows tore during flight, causing gas to be emptied into the payload and rendering the detector unusable. Finally, CyXESS' detectors experienced sustained coronal discharge which began at initial turn-on and lasted for ~ 20 seconds. This ionized most of the detector gas leading to a sustained period of low gain and noisy signal while the detector gas was refreshed by the gas system. The discharge also led to numerous hotspots on the detectors. Ultimately, CyXESS collected only 65 seconds of usable data, which were low-quality.

2.5.2 EXOS

The Extreme X-ray Off-plane Spectrograph (EXOS) was heavily modified from CyXESS to address each of these problems. The switch-mode power supplies were replaced with standard voltage-dividing power supplies which produced more heat, but far less noise on the electronic lines. The detector windows were also thickened from 3600 Å to 5000 Å to reduce the risk of a window tear. Thickening the windows reduced their transmission by $\sim 15\%$ in exchange for a $\sim 100\%$ increase in burst pressure. EXOS' flight plan was modified from that of CyXESS such that the detector high voltage (HV) was not turned on until 30 seconds after the shutter door opened to allow the payload pressure to fall below the coronal discharge regime, reducing the risk for immediate arcing at turn-on. Finally, EXOS utilized a new type of GEM foil to improve the detector performance. The CyXESS GEM foils used polyimide as the dielectric and etched the holes with an acid bath. The EXOS GEM foils used Liquid Crystal Polymer (LCP) for the dielectric and had their holes laser drilled. LCP has a much lower hygroscopicity than polyimide, leading to lower absorption of water, and thus reducing the risk of arcing. Laser drilled holes have been shown to be shaped much more consistently and cleanly (Tamagawa et al. [2006]). This modification resulted

in far fewer hotspots during operation and a near-immediate ramp to full gain across the entire face of the detector (compared to a $\sim$ 5 minute warm-up period for the CyXESS GEMs). As suborbital flight time is $\sim$ 300 seconds, this would substantially increase the quantum efficiency of the detectors during flight, as there would be no wait for the detectors to fully warm up.

Ultimately, EXOS was just as disappointing as CyXESS, and perhaps more so. The 30 second delay between shutter door open and HV turn-on, was clearly beneficial, but EXOS still experienced a more minor version of the CyXESS event. The count rate spiked to $\sim$ 104 Hz at turn-on for $\sim$ 20 seconds, at which point the detectors settled and began operating nominally. For the remainder of the flight, EXOS experienced a much higher count rate than expected. The signal had some peculiarities. First, and most notably, the signal did not display the standard window bar shadows. Under normal conditions, the GEMs will display shadowing effects from both the fine stainless steel window mesh and the large 4×4 aluminum grid, as shown in Figure 2.14. Figure 2.24 shows the raw EXOS flight data both during the arcing event and during the remainder of the flight. When external arcing was occurring, the windows bar features were clearly apparent, but are strangely absent for the remainder of the flight. Another peculiarity is that the signal appears to be rather uniform on detector 1, whereas the signal clearly increases in strength from one side of detector 0 to the other. This is an odd effect, but it is easy to speculate that this is due to a gain variation across detector 0. Detector 0 also showed a steady increase in counts throughout the flight, consistent with the idea that the gain was ramping up in a similar fashion to the old-style GEM foils. The flight data from EXOS proved very difficult to interpret due to the lack of spectral features, lack of window bars, and the difference in appearance to the CyXESS data. Due to high winds, EXOS experienced a rough landing such that the crush bumper was fully compressed and torn off of the payload. The damage altered the optical path and quality of the instrument, making post-flight calibrations impossible.

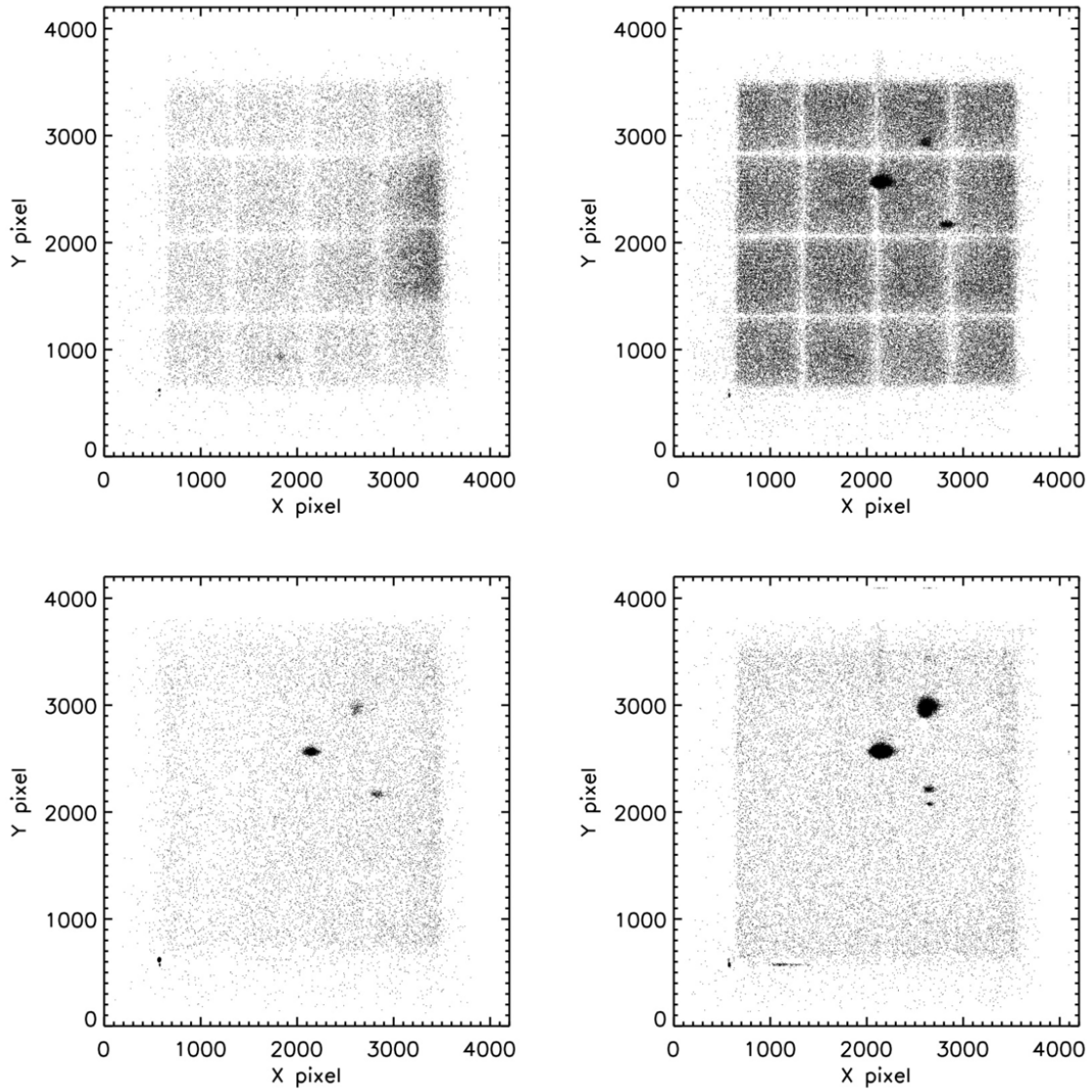

Figure 2.24: EXOS flight data. Detector 0 is shown on the left, and detector 1 is on the right. During EXOSs minor arcing event (top) the window bar shadows were clearly visible. For the remainder of the flight, however, the shadows were strangely absent.

2.5.3 CODEX

Much of the work for CODEX involved redesigning and rebuilding the focuser structures and replacing the majority of the payload's mechanical structure, due to EXOS' rough landing. Ultimately, the focuser structure for CODEX was vastly improved from the CyXESS/EXOS version, and provided much better positioning tolerances for the wire-grid plates. This led to a significant

increase in focuser efficiency. In addition to improving the focusers, CODEX had its detectors repositioned such that 0-order light would now be captured. This would give a much better indication of payload functionality during flight, since 0-order light should be the strongest spectral feature in any object we observe. Also, the CODEX detectors were rotated relative to their incident spectra. This decision was made because hotspots on the GEMs often bleed in the X and Y directions (see Figure 2.25), causing confusion between noise and spectral lines. With the detectors rotated,

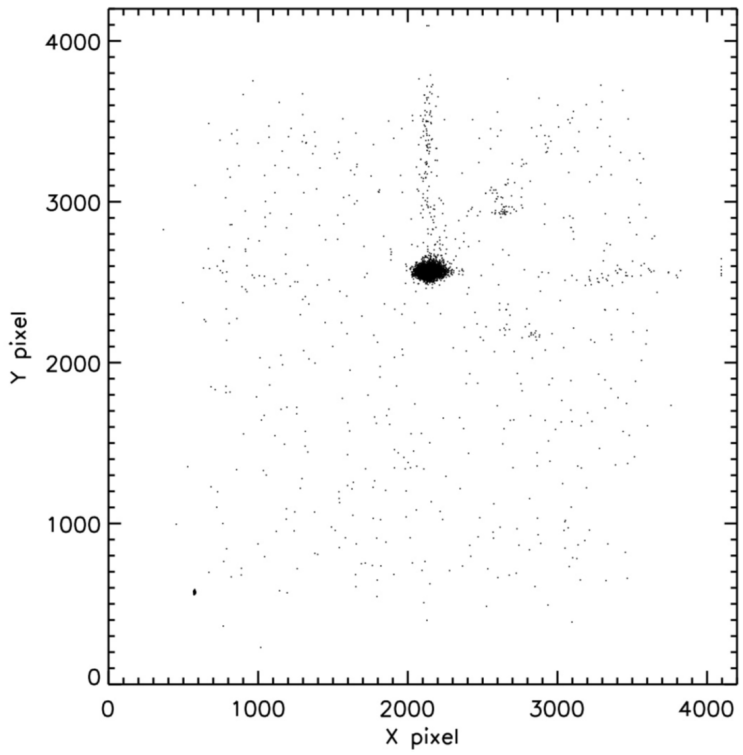

Figure 2.25: Laboratory data taken with the EXOS payload. The distinct hotspot near the center is seen to bleed along X and Y, as well as at a 45° angle. Counts bleeding from hotspots can masquerade as spectral features.

hotspot noise bleeds at an angle relative to spectral lines, allowing an easy distinction between the two.

It was decided that CODEX would observe the Vela SNR, rather than Cygnus. This was deliberately done so that the flight data would appear different from EXOS'. If the flight data looked the same, it would be known that both flights were having the same problem. If the flight data

were different, then there would be two distinct scientific results. Finally, CODEX used a different observing plan than EXOS and CyXESS. Rather than slewing directly to the science target and turning on, CODEX alternated between a dark patch of sky and its science target, as shown in Figure 2.26. Although this technique would significantly reduce the time spent on-target, it was

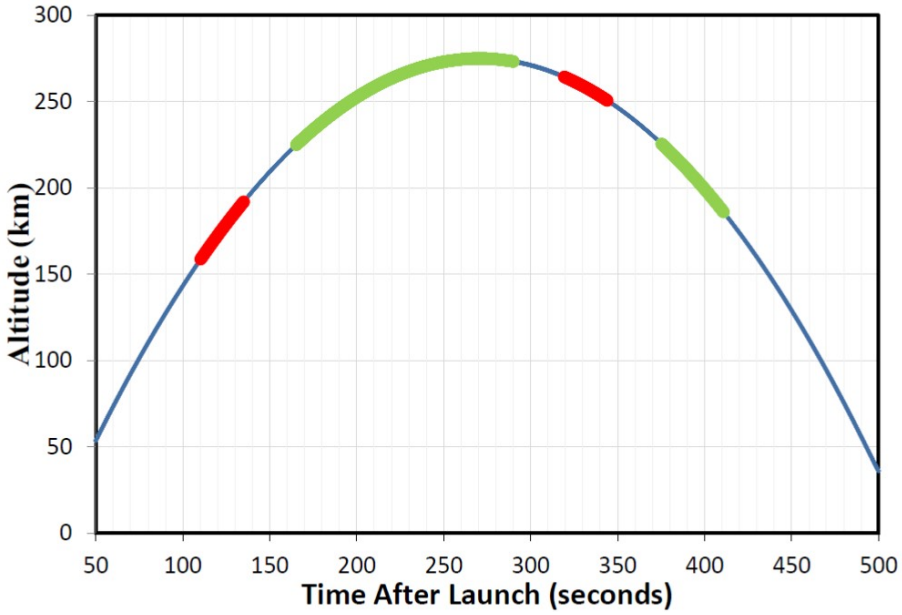

Figure 2.26: CODEX's revised observing plan. Red areas denote time spent observing a dark area of sky, as a calibration reference. Green areas denote time spent observing Vela. There is substantial slew time between targets.

deemed invaluable to have a dark-sky calibration to compare to the on-target data. The patch of dark sky was observed twice, to provide calibrations at different altitudes, as well as different times, to demonstrate whether the background was changing with altitude or time. In addition to the dark sky calibration, CODEX kept its detectors turned on for an additional 10 seconds after closing the shutter door to provide a true dark calibration in the absence of sky signal.

CODEX had distinct malfunctions in flight. For reasons that remain unknown, one of CODEX's detectors failed during flight and produced no counts. After the shutter door was closed, CODEX experienced an immediate arcing event, requiring the detectors to be turned off, and undoing the end-of-flight dark calibration exposure. Despite these setbacks, CODEX had one detector

which functioned without any apparent problems and produced good data throughout the flight. In the end, CODEX's results were much more definitive than those of CyXESS or EXOS, but not in an encouraging way. The raw data were virtually identical to those of EXOS, despite targeting a different object with a different bandpass and with a detector rotated differently relative to the spectrum. Adding additional consternation was the fact that the signal also did not change between the dark sky and Vela. Thus, CODEX succeeded in removing any doubt about the data quality of the preceding flights, and firmly established that there was an unidentified, but significant, source of noise overwhelming the signal from the science targets.

2.6 Payload Upgrades and Modifications

Many changes were made to OGRESS to account for the newly (but not fully) understood problems with the previous payloads. These changes focused on the gas and electronics systems, the detectors, and the addition of an ion repeller grid; all to be discussed individually below.

2.6.1 Gas System

Because the GEMs are gas-filled detectors, a system is required to maintain appropriate pressure. This is required even under optimal conditions due to gas diffusion through the 5000 Å polyimide windows. Under realistic conditions, we must also deal with gas leaks through various fittings, as well as potential tears in the detector windows. Previous payloads, particularly CODEX, commonly suffered from holes in the thin windows. Window tears vent detector gas into the payload, increasing the pressure to the coronal regime. This often leads to arcing events. A schematic of the CODEX and OGRESS systems are shown in Figures 2.27 and 2.28, respectively. CODEX used a large high-pressure gas bottle as a reservoir which was followed by a high pressure regulator which then split off to two proportional valves (one for each detector) which maintained the desired pressure within each detector.

For OGRESS, it was decided that the large high-pressure gas reservoir was unnecessary. For such a volume of gas to be needed during flight, something catastrophically wrong would have

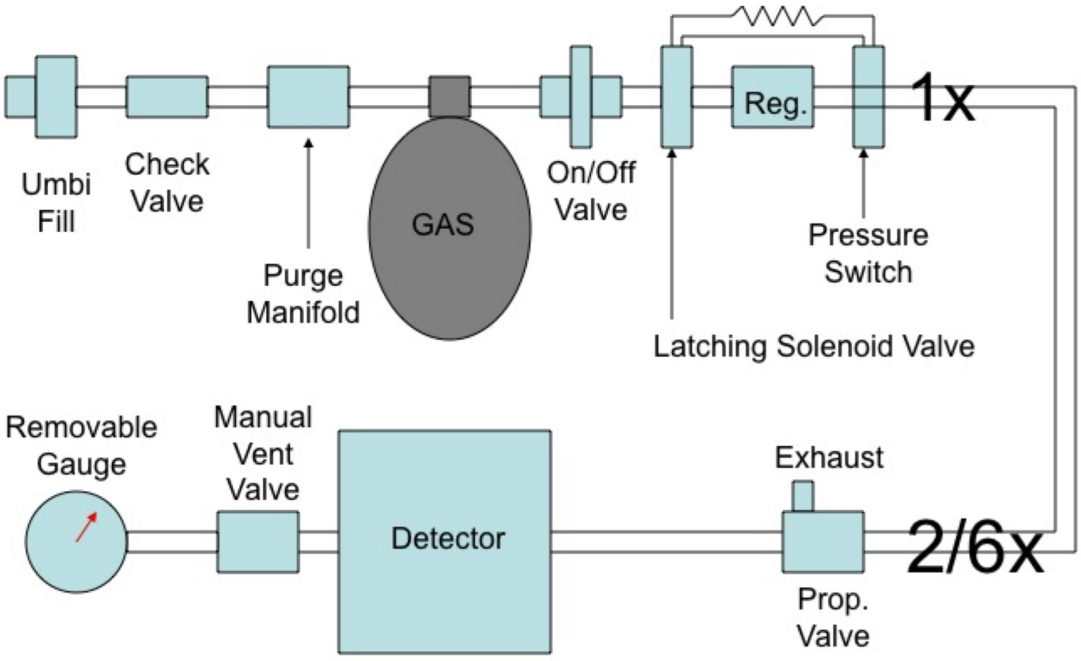

Figure 2.27: The gas system used by CyXESS, EXOS, and CODEX.

to happen to the detectors. Since the CODEX flight, Wallops Flight Facility (WFF) has also introduced more stringent regulations concerning high-pressure gas which would have complicated field operations. For these reasons, a smaller, lower-pressure gas bottle was used for OGRESS, allowing us to switch from high-pressure metal gas tubing to more standard polyethylene plastic tubing, which is far easier to work with. Without the need for an additional regulator, the gas bottle was fed directly to each proportional valve and finally to the detectors. For OGRESS, the off-the-shelf proportional valves were modified so that a current shunt monitor was installed to measure the current being drawn by each valve. The current draw on the proportional valves translates directly to how wide the inlet orifice is being held and therefore tells us if a leak has developed in the detector window. Prior to OGRESS, the presence of a window hole was not generally known, since the proportional valves will widen their orifices to maintain the detector pressure, making the leak difficult to detect. This is a particular issue during flight, where a window leak will not necessarily cause a noticeable spike in payload pressure, due to the instantaneous pump-out to

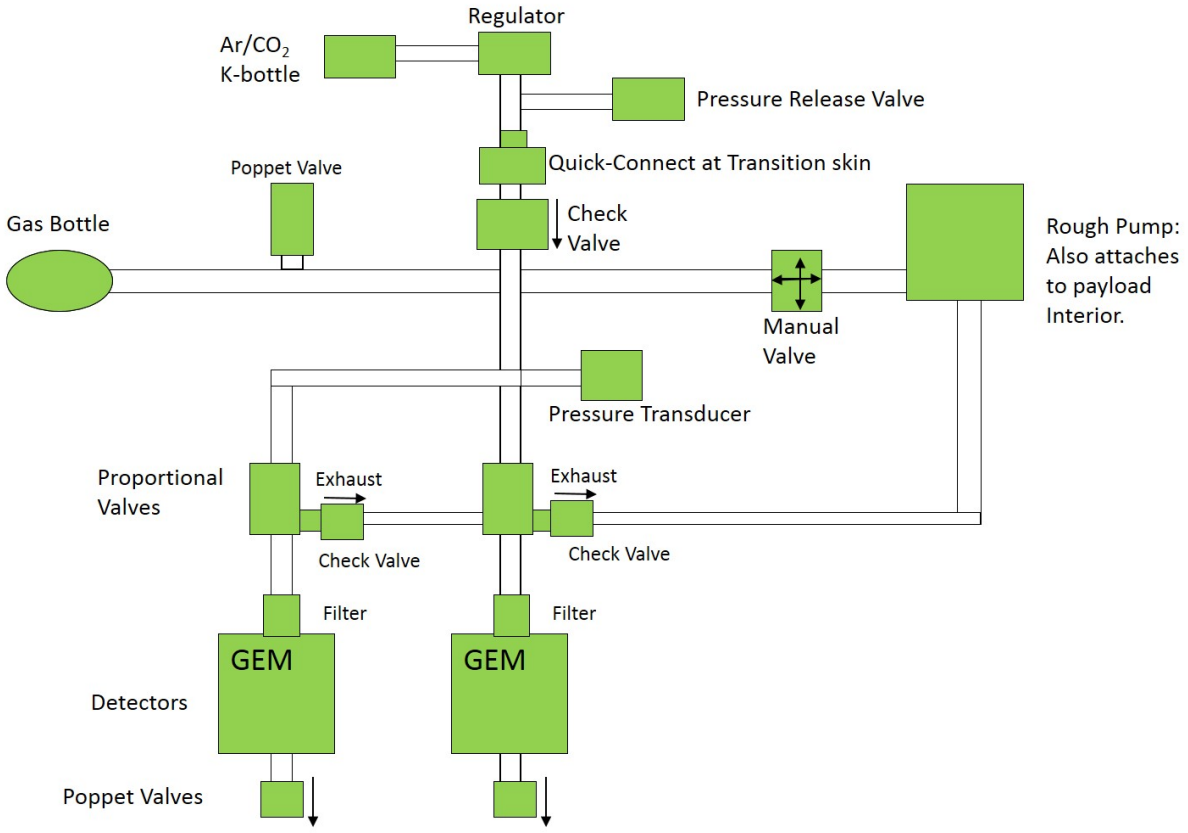

Figure 2.28: The gas system used on OGRESS. Many check valves and poppet valves have been added. These prevent overpressurization and ensure gas flows in the preferred direction. Also displayed is the pumping system which allows us to operate the GEMs below atmospheric pressure.

space. Having a measure of gas flow-rate gave us much higher confidence in the functionality of the gas system.

In addition to the prop valve modifications, particulate filters were installed at the detector inlets to keep the interiors clean and prevent internal arcing. Check valves were also installed at the detector outlets, reducing the risk of a detector overpressurizing.

2.6.2 Electronic Section

OGRESS' electronics system was rebuilt from scratch (see Figures 2.29 and 2.30). This was long overdue, as the original system inherited by CyXESS was built in the 1980s. Although steady additions, upgrades, and modifications had been made to the original system over time, we decided

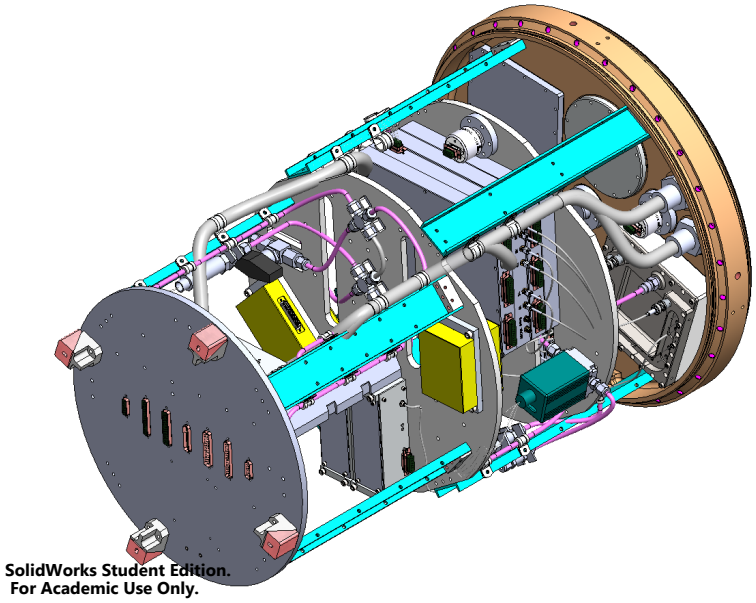

Figure 2.29: A CAD model of the new electronics deck.

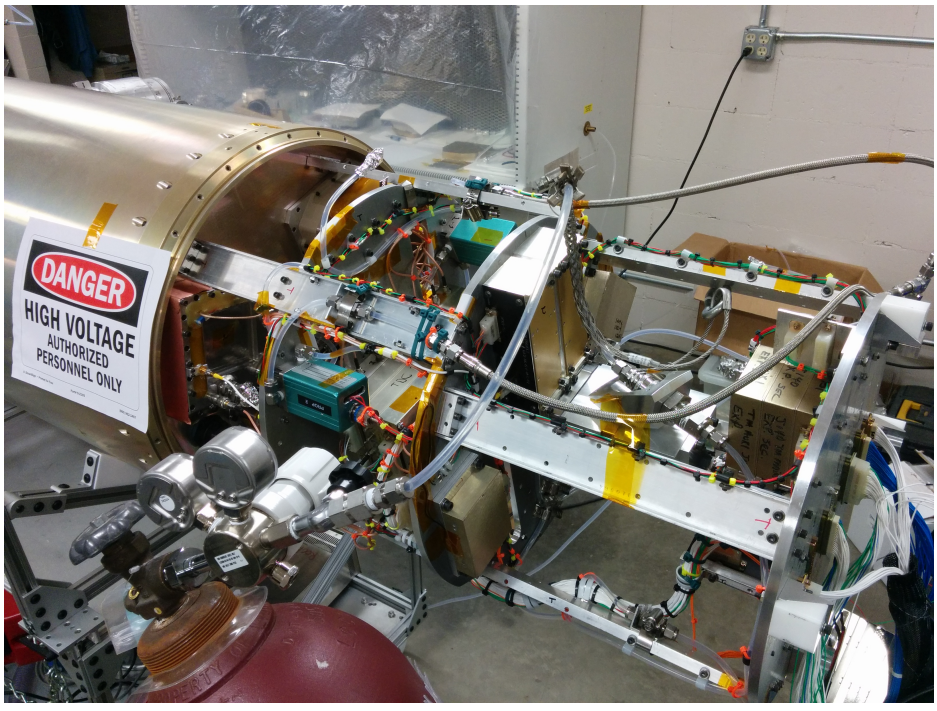

Figure 2.30: The new electronics section attached to OGRESS.

to overhaul OGRESS' electronics system with modern components. Several notable changes were made to the redesigned electronics system which we will note here.

First, each detector was built with its own independent set of electronic components, sharing only the telemetry system. This was done partly to reduce the chance for catastrophic failure, so that if a single electronic component failed during flight, only one detector would be lost. This also addressed a serious problem which was never fully resolved on the previous payloads. For CyXESS, EXOS, and CODEX, the analog detector data were mixed together into the same data chain prior to digitization. Data from different detectors was distinguished using the Least Significant Bit (LSB) of the Pulse Height Distribution (PHD) which was always set to 0 or 1 depending on which detector was sending the data. Unfortunately, electronic noise often led to this bit being randomized such that data from each detector would often become confused. Under normal circumstances, roughly 10% of the data would bleed from one detector to the other. Under conditions of high count rates, this confusion would become complete, resulting in 50% of the data bleeding to the wrong detector. This was not a serious problem for CyXESS or EXOS, as the detectors from these payloads sampled the same bandpass with the same orientation relative to the spectral lines. This proved a much more serious problem for CODEX, however, since those detectors sampled different bandpasses, leading to spectral confusion. With the parallelization of the electronics chains, OGRESS never experienced the detector confusion that CODEX did.

Due to the many indications that previous payloads had not functioned appropriately, we decided to add a large number of diagnostic monitor signals to our data stream to show general health of the payload. These signals included voltage and current levels drawn by each electronic component. Pressure in the gas bottle and detectors were also monitors, as was gas flow rate through each detector (to be discussed in greater detail below).

A simple, but important change to OGRESS' electronics section was to install new current limiting HV power supplies allowing a slow ramp up to full flight voltage. This small change led to vastly improved detector performance. For all previous payloads, HV turn-on was always a period of intense anxiety, due to the detectors tendency to immediately arc, as happened to CyXESS and

EXOS during flight. The reason for the arcing was fairly simple. When immediately turning on to full voltage, the HV power supplies would initially overshoot the target voltage for a brief time before settling to the desired voltage. Since the detectors are run close to their breakdown limit (out of the necessity to produce high gain), this overshoot was very often enough to cause arcing. Although the anxiety never fully disappeared, we found that OGRESS was far less likely to arc during turn-on.

Another notable change to the electronics was the installation of a Field Programmable Gate Array (FPGA) to convert the data to WFF1993 preferred format (see McCoy et al. [2016]). The primary function of the FPGA was to interface the asynchronous detector data with the synchronously clocked telemetry (TM) stream. We found that FPGAs provided a simple, low-cost alternative to an on-board computer and required little custom hardware to implement. The great strength of FPGAs is their adaptability, essentially functioning as programmable hardware. Thus, all troubleshooting can be carried out via software.

Another long-overdue upgrade was the development of GUI software to enable high quality real-time display of collected data during laboratory testing and flight. During previous launches, flight data were read out real-time onto an oscilloscope. This setup allowed the scientists to know if data were coming in, but it was impossible to tell if the data were high quality. For OGRESS, a DEWESoft card and software was purchased, which uses WFF's preferred data format. This enabled us to perform electronic hand-shake testing prior to integration, greatly reducing the risk for scheduling overruns in the field. Having access to the DEWESoft software also enabled us to create and test a GUI to display payload data during flight. Figure 2.31 shows an image of this GUI. The GUI showed all of the monitor signals which had been added, a TMIF heartbeat pulse, as well as images of the incoming x and y detector data.

2.6.3 Detector Optimization

The basic parameters of interest for any detector are quantum efficiency (QE), energy resolution, and gain. For gas detectors, QE tends to be quite high and corresponds to the absorption

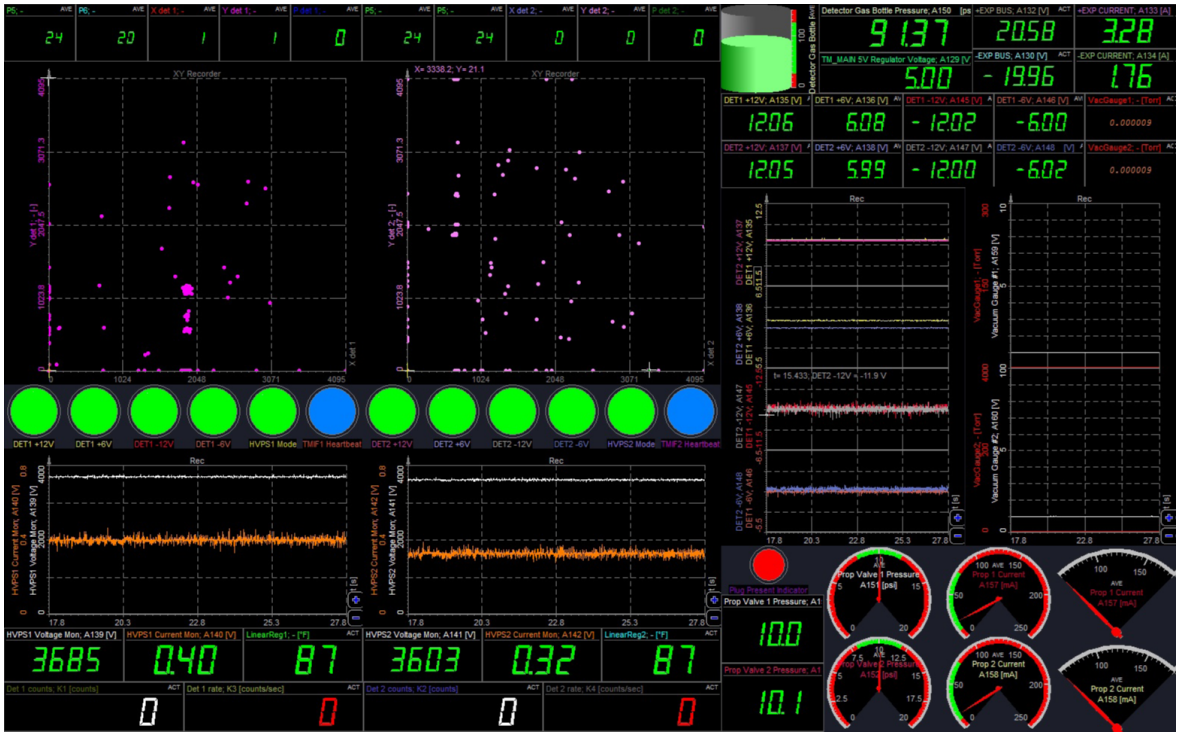

Figure 2.31: The data monitoring GUI developed with DeweSoft. The top left portion displays data from each GEM detector. The top left row of boxes show these data as continuously updating numerical values while extracted x and y data are plotted cumulatively on two-dimensional scatter plots. Below, lamp icons indicate whether low volt supplies for each detector are nominal (green) or out of range (red). Additionally, a blue lamp icon flashes with the heartbeat signal generated by each TMIF module. The bottom left portion shows detector high volts data in the form of recorder plots and as continuously updating numerical values. Below, data from the counter deck of the encoder are displayed. The top right portion shows data for the detector gas bottle pressure, bus power supplies, detector low volts supplies and payload pressure. The bottom right portion shows the GEM detector pressures and proportional valve currents.

coefficient of the gas (see Figure 2.32). The energy resolution of the GEMs is also not a large concern, as it is only needed for spectral order separation, and can thus be of moderate quality. The largest concern for the GEM detectors is their gain.

Gain is a measure of the detectors' ability to amplify the incident X-ray signal into a measurable quantity. When an X-ray enters the gas-filled chamber of a GEM detector (or any gas detector), the X-ray will ionize the gas and create a number of photoelectrons equal to

$$n_T = \frac{\Delta E}{W_i} \tag{2.1}$$

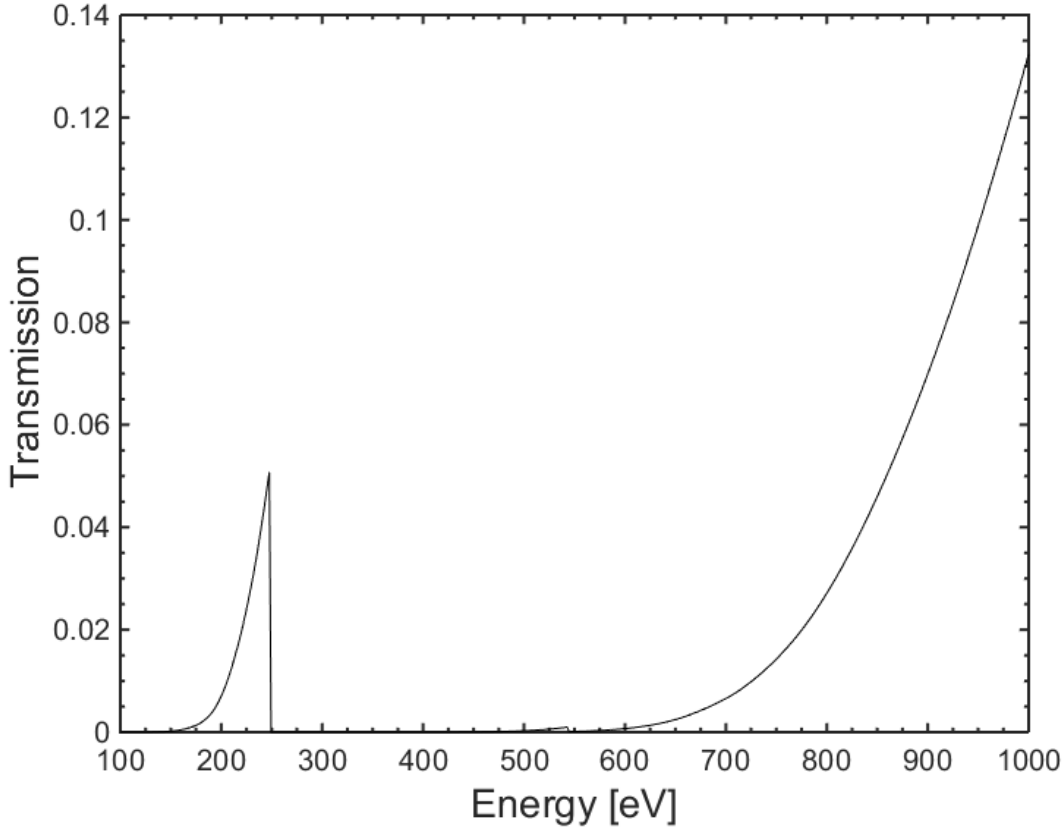

Figure 2.32: Gas Transmission through a mixture of 75% Ar and 25% CO_2. Gas pressure is set to 10 PSI with a depth of 5 mm.

where ΔE is the total energy loss in the gas (the energy of the photon), and W_i is the effective average energy to produce one photoelectron. Values for W_i have been measured by Sauli [1977] for many different gases, including Ar (26 eV) and CO_2 (33 eV). (2.1) can be easily extended to gas mixtures by weighting each component by its volume fraction. Thus, for our mixture of 75%Ar/25%CO_2, a 1/4 keV photon will produce

$$n_T = \frac{250}{26}0.75 + \frac{250}{33}0.25 = 9.1 \text{ electrons.} \tag{2.2}$$

This is an exceedingly small number of initial electrons, and the signal must be amplified as much as possible to produce a measurable signal. If the output signal is too small, it will not be distinguishable over the natural fluctuations in the electronics. This can directly effect the QE of the

detector, as small charge pulses can be ignored by the electronics. Thus, it is imperative that we maximize our detector gain to the highest possible extent.

As mentioned earlier, GEMs produce their gain by accelerating the photoelectrons through the porous GEM foils to create a Townsend avalanche. The effective gain of the detectors is

$$G_{eff} = C \times \frac{S_{mean}}{q_e n_e} \tag{2.3}$$

where S_{mean} is the average measured pulse height channel, q_e is the electron charge (1.602×10^{-19} Coulombs), and n_e is the number of initial photoelectrons. The constant, C, simply acts to convert S_{mean} to units of charge. Thus, C will have units of [Coulombs/Pulse Height Channel]. This equation includes the effects of both amplification and loss processes, by simply comparing the input signal to the output signal. Because our detector anodes have two layers, we effectively feed charge into two separate electronic channels, which may have different gain. We will thus extend (2.3) to include two layers, giving it the form

$$G_{eff} = C_1 \times \frac{S_{1mean}}{q_e n_e} + C_2 \times \frac{S_{2mean}}{q_e n_e} \tag{2.4}$$

where the numbered subscripts refer to the different charge channels. We determined C_1 and C_2 for our detectors and electronics by putting a known signal through our electronics and measuring the resulting pulse height. To do this, we used a pulse generator (HP 8112A) to create a square voltage pulse of 1V. This was sent through a 1 pF capacitor to put 1 pC of charge directly into the preamplifiers to measure the pulse height.

The parameters which determine detector gain are voltage (between the top and bottom of each GEM foil), number of foils, gas pressure, and temperature. OGRESS' detectors use four GEM foils. To our knowledge, no other research group has used this many foils (other groups stop at three). This reduces the voltage required across each plate, but leads to dispersion of the charge cloud. Utilizing more than four foils would begin to affect the spatial resolution of the detectors, directly impacting the spectral resolution of the instrument. Thus, four foils is the highest number we can use without significantly reducing instrument performance in other areas. A temperature

control system for the detectors could potentially lead to higher or more stable gain, but this was beyond the capabilities of OGRESS' budget and launch schedule. Instead, temperature was merely monitored so that its effect on gain could be accounted for. Thus, our customizable parameters affecting gain are voltage and gas pressure.

Detector Gain is primarily determined by the average energy acquired by an electron between collisions with gas molecules. Voltage determines the energy an electron gains after traveling a certain distance. Higher voltage therefore provides higher gain. If the voltage is set too high, however, electrical breakdown will occur (as happened during CyXESS' and EXOS' flights) which can sometimes have devastating consequences for the detectors. During arcing, X-ray signals are masked by the huge amounts of charge being deposited on the anode. In the worst cases, electrical arcs can melt the dielectric material between the foil pores and short the top and bottom copper layers together. When this occurs, the GEM foil is unable to hold a voltage difference across the pores and must be replaced. Laser-etched foils are quite expensive, so there are typically only a few spares available. Thus, catastrophic arcing events must be minimized. Because we require as high a gain as possible, our GEMs are typically operated close to the breakdown limit, making arcing events an unfortunately common occurence.

The final parameter affecting gain is detector gas pressure. CyXESS and EXOS flew their detectors at 14.5 PSI and $\sim$ -4000 V. CODEX found that gain was increased with lower gas pressure. Lowering the gas pressure increases the mean free path of electrons within the gas, thus allowing them to gain higher energies between collisions. Close to atmospheric pressures, this results in more collisional ionizations per electron. This eventually reverses at low pressures, as the reduced number of collisions outpaces the improvement in ionization efficiency. CODEX's detectors were flown at $\sim$13.6 PSI, slightly above the typical ambient atmospheric pressure of Boulder, CO and Las Cruces, NM. The pressure was not reduced from this level, since there was no way for the prop valves to exhaust the detectors lower than ambient pressure. For OGRESS, we implemented a vacuum system which was attached to the prop valve exhausts and allowed us to use the detectors at pressures below ambient atmospheric conditions. This had to be done carefully, as the GEM windows cannot

maintain an inward pressure differential and readily implode under such conditions. Thus, the detectors were only run under vacuum conditions, maintaining the outward pressure differential on the detector windows. This allowed us to explore a much wider range of potential pressures and voltages than previous payloads.

The gain characteristics of GEM detectors has been investigated in many papers (e.g. Bondar et al. [1998], Bondar et al. [2002], and Tamagawa et al. [2008]) and varies as a function of temperature, pressure, and applied voltage. We ran many tests at 7.5, 10.0, 12.5, and 15.0 PSI and increased voltage until arcing occured. We also attempted these tests at 2.5 and 5.0 PSI, but found that the detector arced before good data could be taken. The results are shown in Figure 2.33. At a fixed pressure, a higher applied voltage led to higher gain. At a fixed voltage, a lower pressure led to a higher gain. Sweeping through both pressure and voltage allowed us to put the GEMs in a more optimal configuration which yielded many benefits. A notable feature of Figure 2.33 is that the maximum achievable gain does not substantially change between different pressures. For a given voltage, the gain will increase as pressure is lowered, but arcing also occurs more easily. Thus, lowering the pressure does not allow us to run the GEMs at a higher gain.

Nevertheless, we found that operating the GEMs below atmospheric pressure produced a number of benefits. At lower pressures, less strain is put on the thin detector windows lowering the risk of tearing. Additionally, experience suggests that arcing events become less dangerous at lower voltages. Unlike the previous payloads, OGRESS did not fuse a single plate during the entirety of pre- and post-flight testing, as well as the actual flight. The likely explanation for this reduced risk is that less energy is dissipated between foils during an arcing event at lower applied voltage. GEM foils are essentially parallel plate capacitors. The amount of charge transferred between plates during an arcing event is $Q = CV$, where C is the capacitance and V is the voltage difference. Decreasing the voltage difference results in less charge being transferred. Also, each electron that is transferred gains less energy in the jump between the plates, further reducing the total energy of the event. This likely accounts for the reduced (or eliminated) incidence of fused plates achieved by OGRESS.

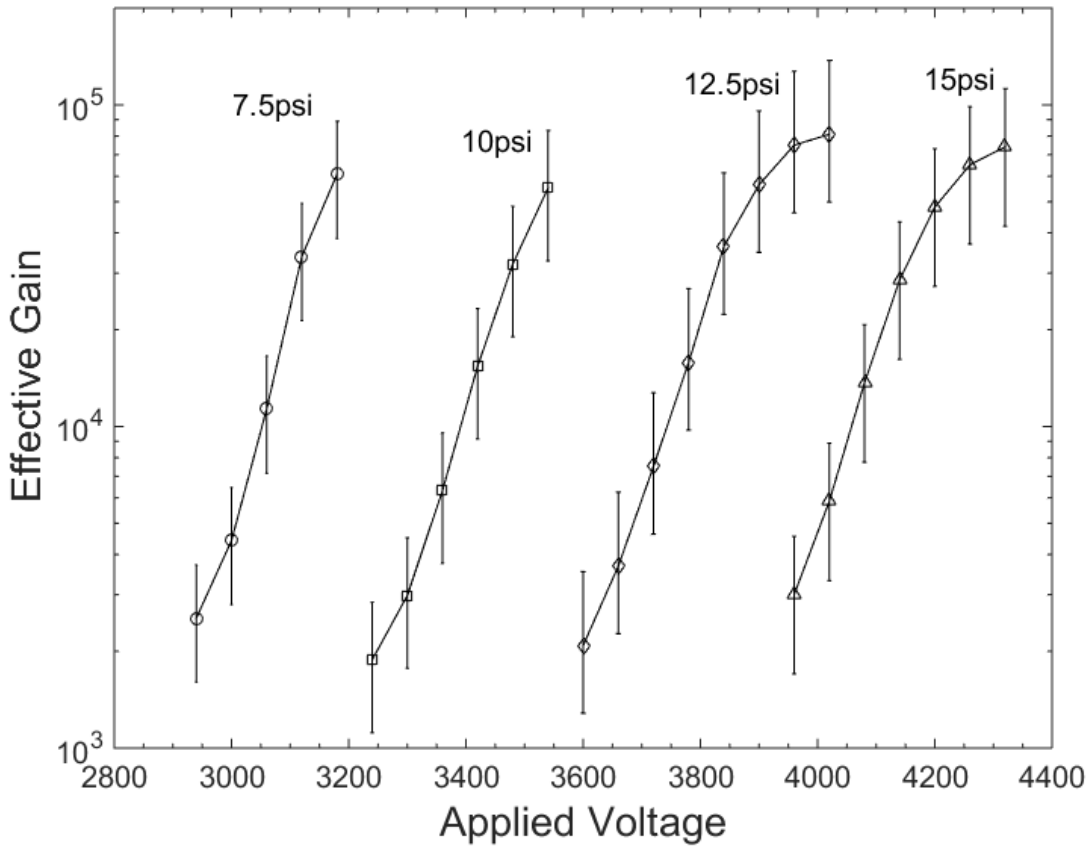

Figure 2.33: Effective gain of detector 2 at various pressures and voltages. Gain varies substantially by location on the detector. The error bars enclose 68.2% of this natural variation. For a fixed pressure, higher voltage leads to higher gain. For a fixed voltage, lower pressure leads to higher gain. We find, however, that the maximum gain that can be reached at a given pressure (or voltage) is nearly constant.

We also tested the gain stability over time (see Figure 2.34). We found that the gain of our detectors was quite stable over the course of 1 hour. Most importantly, the detectors reached full gain immediately upon turn-on, giving us confidence that they would operate at full gain during flight.

Finally, we produced gain maps of one detector at several different pressures to see if there were any effects. These tests were carried out using a radioactive Fe-55 X-ray source. Gain maps were taken at 7.5, 10.0, 12.5, and 15.0 PSI. At each pressure, the voltage was set to an appropriate

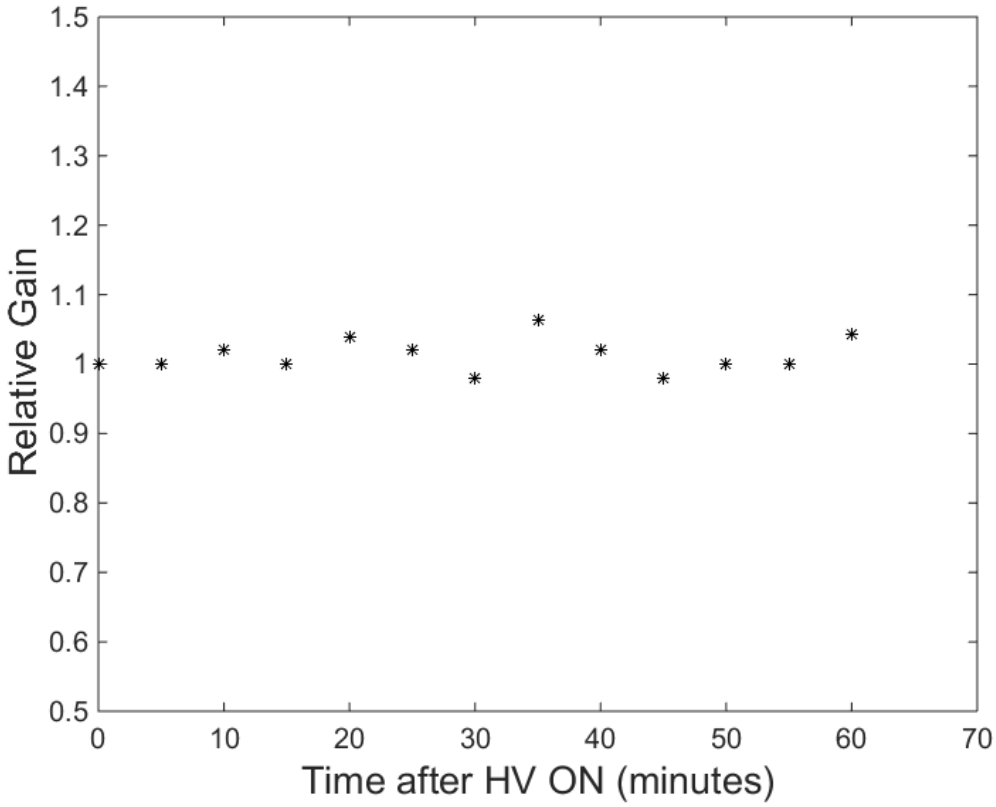

Figure 2.34: Gain stability of detector 2. The detector reaches full gain immediately upon turn-on. Within the span of 1 hour, the fluctuations in gain remain below ±5%.

level such that the average gain fell near pulse channel number 128 (out of 256). The gain maps are shown in Figure 2.35.

Several features are apparent when viewing the gain maps. First, there is a substantial amount of variation in gain across the face of the detector. The cause of the variation is unclear, but it could occur due to variations in either the GEM foils or the detector anode. Rotating the GEM foils relative to the anode would determine whether the foils are at fault. Unfortunately, the mounting structure of the foils is not symmetric and thus cannot be rotated. The second notable feature of the gain maps is the consistency of their appearance at different pressures. Changing the detector pressure appears to have no effect on the spatial variations in gain. This is very good news, as it allows us to run the detectors at any pressure without concern for the gain distribution.

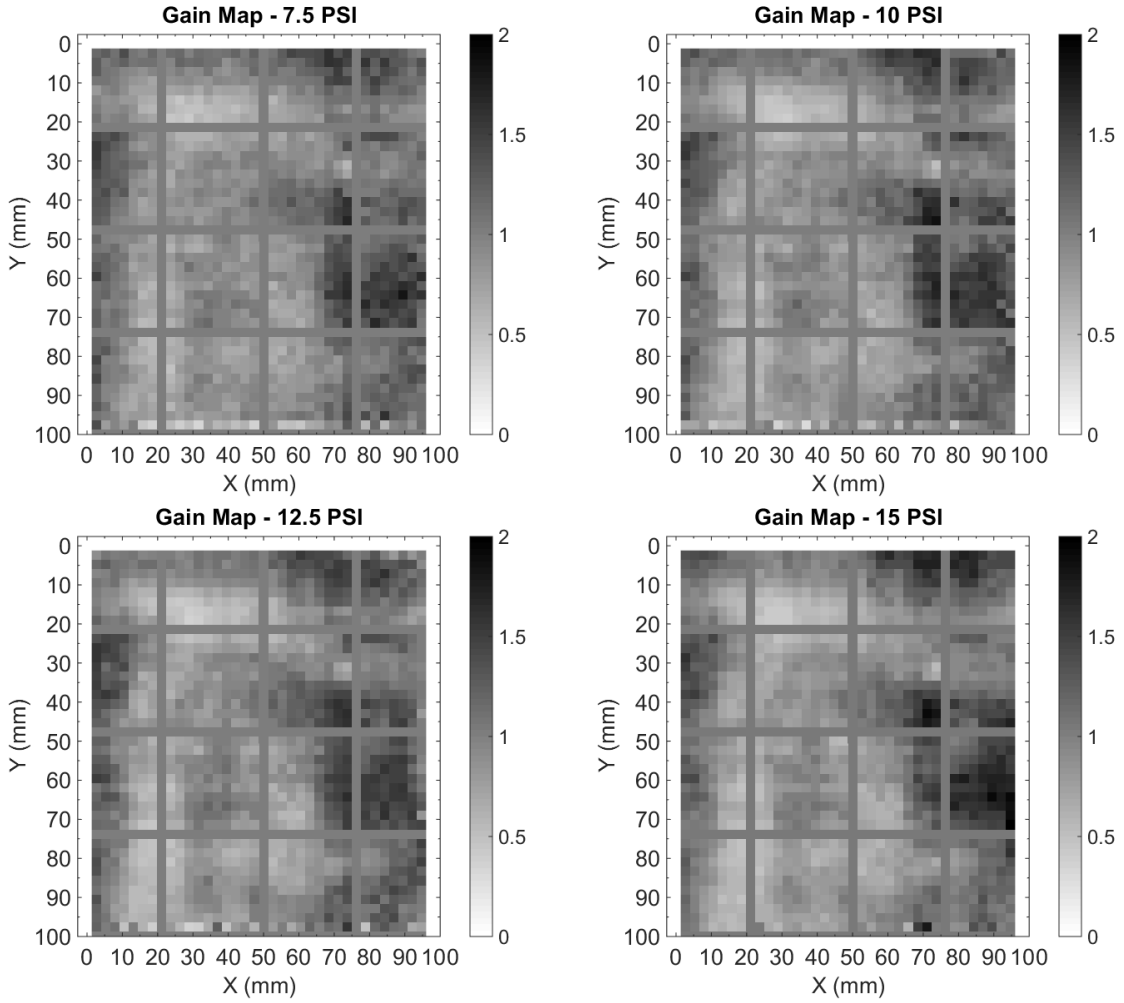

Figure 2.35: Gain maps at 7.5, 10, 12.5, and 15 PSI, with darker color corresponding to higher gain. Data has been scaled such that the average value of each map has a value of 1. Substantial gain variation over the detector is apparent, but this variation is consistent between different pressures. Areas behind the detector's window support structure (the 4 x 4 grid) have been masked due to the low count rate – and thus low reliability – of data in these areas.

2.6.3.1 Additional Detector Upgrades/Changes

Several additional changes were made to the detectors relative to previous payloads. As was touched upon in section 2.4, the detectors were repositioned to cover the area around 0-order. Although the throughput and resolution of the instrument are not at their best in this region, it was deemed wise to measure 0-order light to provide a rigorous wavelength calibration.

The electrical connections between the GEM foils and the resistor chain were also modified.

For previous flights, traces to each copper layer were connected directly to each terminal in the resistor chain using conductive epoxy (see Figure 2.15). This method made an excellent connection, but required substantial effort to disassemble, as epoxy had to be cut away manually. Ideally, it would never be necessary to disassemble a detector. In practice, however, it is often necessary to replace foils which have fused or damaged in some other way. To ease the process of disassembly and reassembly, we soldered wires to each copper trace. Each wire had an appropriately sized socket crimped to the other end, which fit snugly over each terminal. Thus, assembly and disassembly no longer required carefully cutting away epoxy. This sped up the process considerably, and removed the wait time (typically overnight) for the epoxy to cure.

2.6.4 Ion Repeller Grid

It has been known since CyXESS that the GEMs generate counts in the presence of charged particles. Ion pressure gauges, for instance, must be shut off prior to taking laboratory calibration data. The possibility of seeing a large number of charged particles during flight was not appreciated until CODEX demonstrated that the high background during flight was almost certainly not celestial X-rays. OGRESS and its predecessors acquired data at altitudes between 150 250 km. At these altitudes, there is a large population of ionized species consisting mostly of O+, O2+, and NO+ (Istomin [1962]), as well as many electrons. Positive ions inside the payload will be attracted to and impact the detector windows, since they are held at a high negative voltage. The attracted ions will acquire enough energy (roughly 3600 eV) to excite or ionize inner shell electrons in the detector window, leading to X-ray fluorescence. This will subsequently ionize the detector gas, leading to signal on the detectors.

Ion Repeller grids are flown commonly on rockets and have become standard for orbiting observatories – although the particle background will be different at those altitudes. Ions at 150 – 250 km are thermalized with the neutral particles at $\sim$ 500–800 K (Hedin and Nier [1966]). In the absence of solar radiation (at night), electrons will also be equilibrated to the temperature of the neutral particles (Bauer and Bourdeau [1962]). Thus, the typical energy of an ion or electron will

be $\sim$ 0.07 eV. One must remember that many ions in the thermal distribution will have energies higher than this and that the high-energy tail of the Maxwellian distribution must be taken into account. At $\sim$800 K (0.07 eV), the factor of particles exceeding 100 V is reduced (from the 0.07 eV level) by $e^{-100/0.07} \simeq e^{-1429}$. With a density of $10^4 - 10^5$ cm^{-3} (Seward et al. [1973a]), we expect the number of thermal particles overcoming the repeller grid to be extremely negligible. Thus, a +100 V repeller grid should be very effective at removing ion signal from the detectors.

OGRESS flew an electroformed nickel mesh with 92% mechanical transmission. +100 V was applied to the mesh to repel positive ions within the payload. An image of the mesh is shown in Figure 2.36. Laboratory tests were run to prove the concept of the repeller grid and to demonstrate

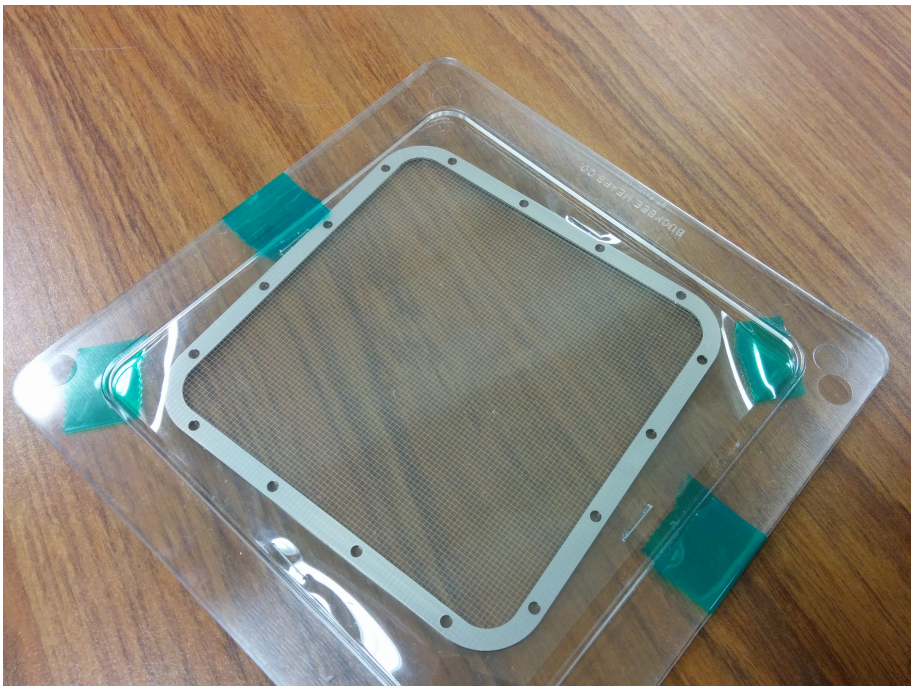

Figure 2.36: Repeller grid mesh, prior to being mounted in front of a detector window.

its feasibility. Figure 2.37 shows two 1-minute exposures demonstrating the signal generated by the micro-ion gauge, with several different voltages applied to the repeller grid. Although the ions produced by the pressure gauge will be more energetic than ions in the atmosphere, the signal was suppressed by $>$ 99% with an applied voltage of $\sim$10 volts or higher. These tests gave us confidence

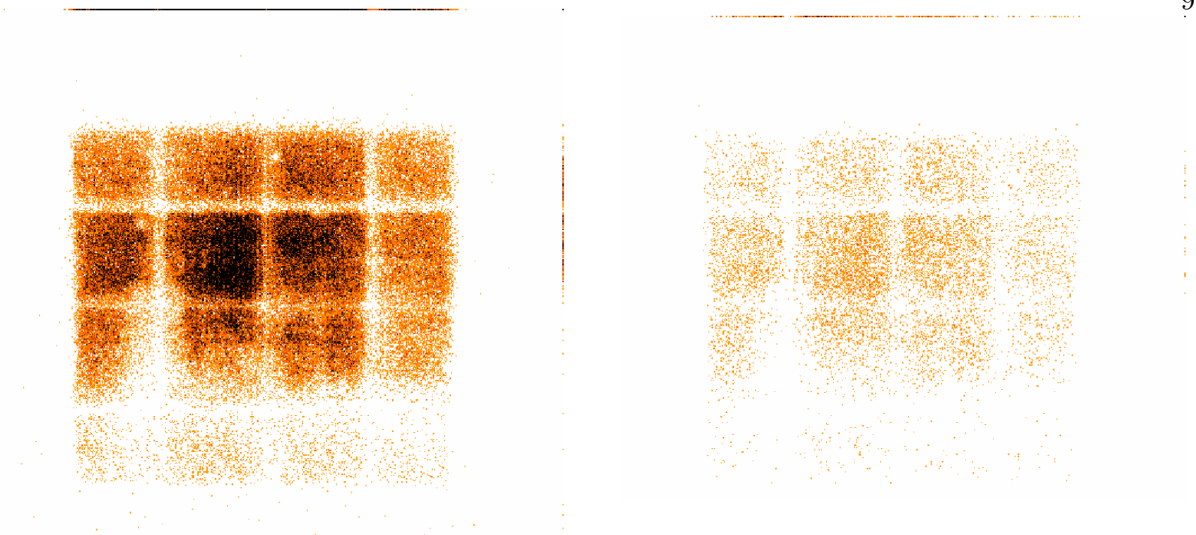

Figure 2.37: *Left*: Signal from the ion gauge with no voltage applied to the repeller grid. *Right*: Reduced ion gauge signal resulting from 5V being applied to the repeller grid. When >10V is applied, the signal is consistent with zero.

that +100 volts would fully remove the noise seen by positive ions.

2.6.5 Mechanical Structure

Although the focuser modules and gratings remained unchanged from previous flights, OGRESS did undergo some changes to the optical setup and mechanical structure. One of CODEX's skins was thinner than intended due to over-machining. Despite experiencing a relatively soft landing, CODEX suffered a severe kink in one of the outer skins (shown in Figure 2.38). This required us to replace the outer skins of the payload. Additionally, the bandpass of OGRESS was modified so that the high-energy spectrum surrounding 0-order could also be adequately observed, requiring a new detector bulkhead to be fabricated (shown in Figure 2.39). The change in bandpass also changed the path traveled by the collected light. This led us to shorten the interior optics bench by 1.4 cm to provide a better focus.

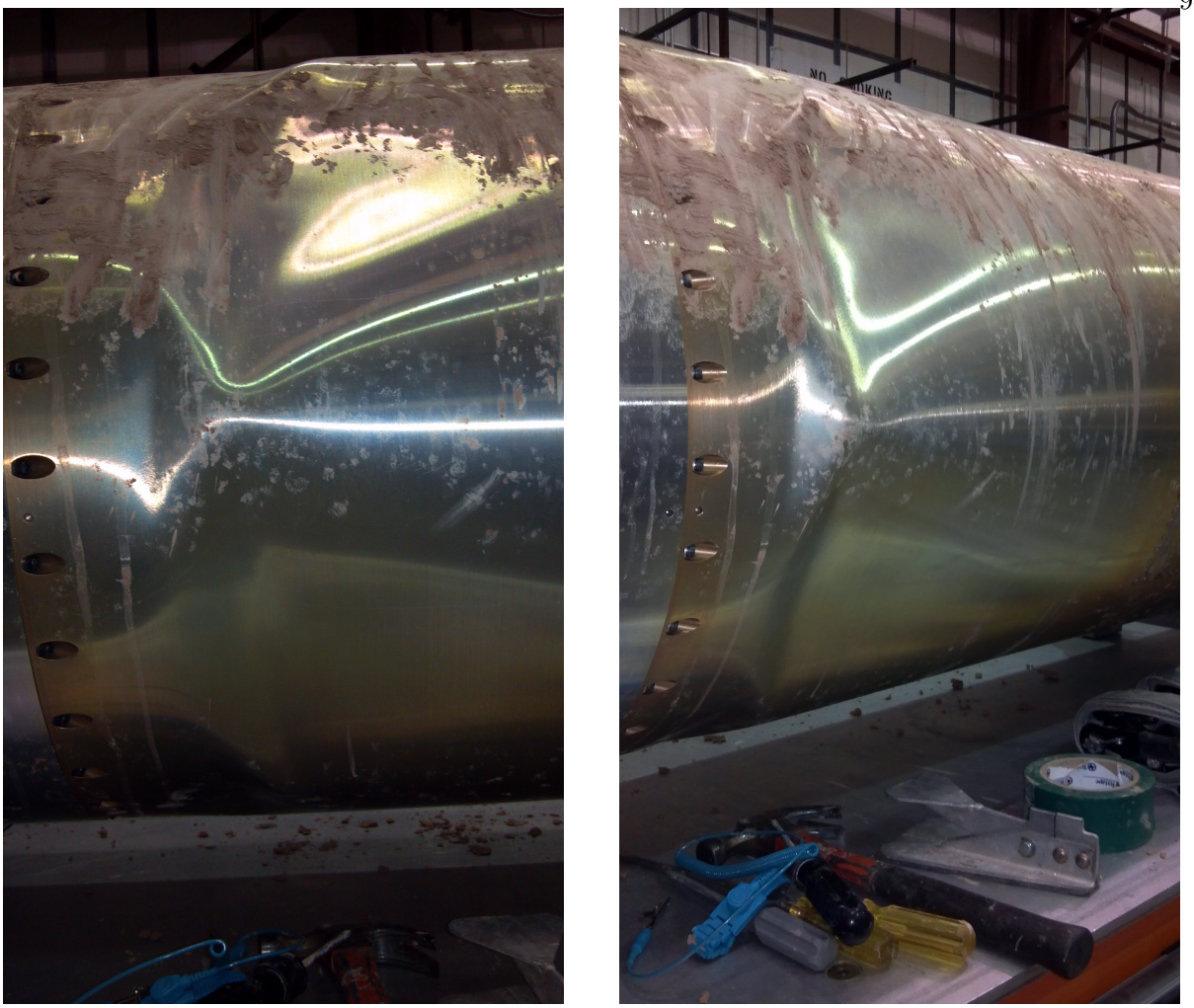

Figure 2.38: Two views of the severe kink in the CODEX skins, resulting due to an overmachined skin.

2.7 Flight Plan

OGRESS' observing plan was essentially unchanged from that of CODEX, although the science target was Cygnus, rather than Vela. The targeting plan is shown in Figure 2.40. Using data from the ROSAT All-Sky Survey, an X-ray-dark patch of sky was found near Cygnus and used as a dark-sky calibration target. OGRESS observed this dark patch at both the beginning and middle of the flight, so that any variations with time or altitude would be noticed. An additional flight calibration measurement was made at the end of the flight by leaving the detectors turned on for an additional 10 seconds after the shutter door closed. Like CODEX, OGRESS would ideally

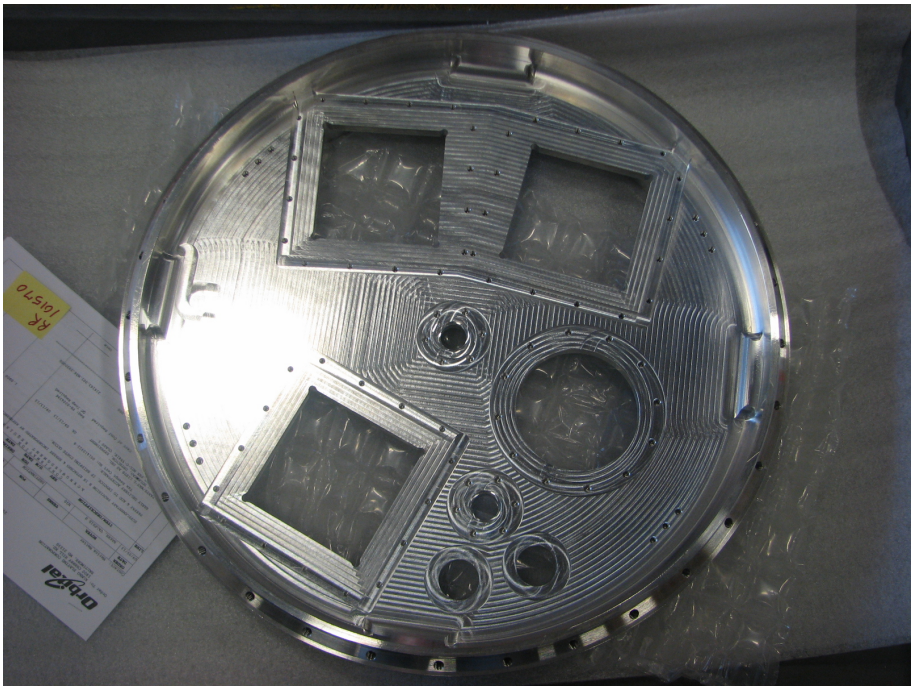

Figure 2.39: The OGRESS detector bulkhead.

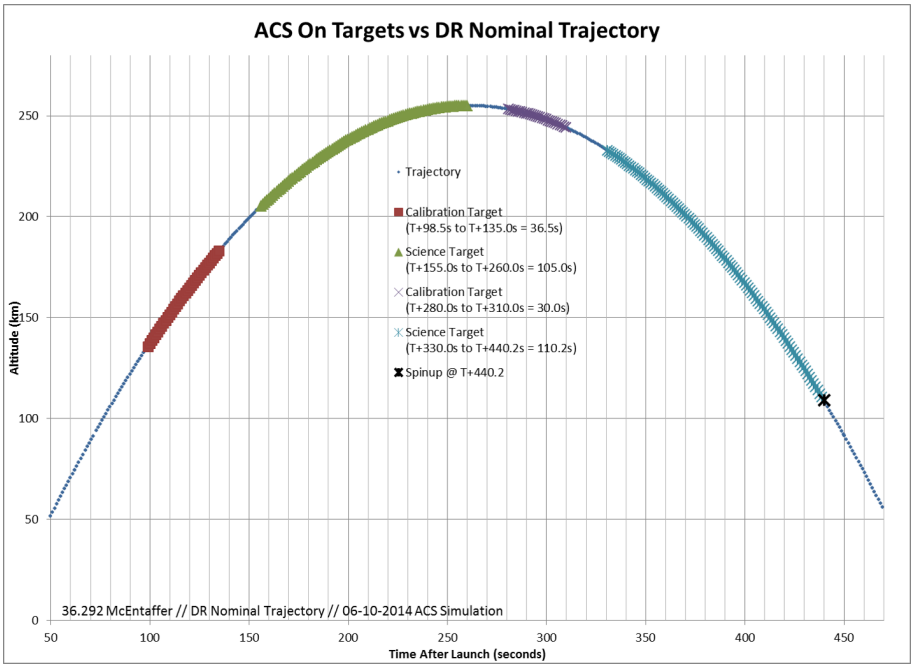

Figure 2.40: The observing plan followed by OGRESS. The plan is essentially unchanged from that of CODEX, but the science target has been changed to Cygnus. A new dark patch of sky was also targeted.

have both a detector background calibration and a sky calibration, making it easy to distinguish the signal from Cygnus from any background sources.

Because the detectors have a history of misbehaving during flight, a command uplink system (CUS) was implemented to allow some control of the instrument's functionality from the ground, under warranted conditions. The functions available to the experiment team for each detector were as follows:

1) HV Disable – enabling this command would turn off HV to the detectors. This would be done in the event of sustained detector arcing, as happened to CyXESS and EXOS. This command would also be used in the event of a window tear, as venting the detectors (see below) would result in arcing if the HV was not turned off.

2) Prop VENT – enabling this command would set the command pressure of the proportional valves to 0 PSI, and would compel the valves to close their inlets and open their exhausts. This would always follow HV Disable, either to change the detector gas after an arcing event (in which case this command would be disabled after a short time), or to empty a detector after a window tear to prevent the gas from leaking into the payload (in which case this command would remain on until HV turned off.

3) HV ON – enabling this command would turn on HV to the detectors. This command was intended for use in case the timer HV ON command failed to activate. This command overrides timer events and the HV Disable command, so it must be used carefully.

4) TMIF RESET – This command quickly turns off and on the telemetry system (TMIF). This command would be used to try to reset the TMIF in case it did not turn on, or in case it was behaving strangely.

5) Vac Gauge ON – This command turned on the micropirani pressure gauges. This command was activated during countdown so that the pressure could be monitored inside the payload throughout the flight.

6) Manual control of pointing via the startracker video feed. This functionality was to be

used extremely cautiously in the case that the star tracker failed to find the correct target.

The OGRESS team spent several days practicing uplinks for various potential failure scenarios. The most likely problems to arise during flight were considered to be an arcing event or a window tear event, which often occurred together in laboratory tests. Both types of events would be clearly visible on the DEWESoft GUI (Fig. 2.31) thanks to the modifications made to the electronics and gas systems. The course of action for either event would be similar. For a sustained arcing event, the detectors would be turned off via HV Disable, emptied via Prop VENT, refilled by deactivating Prop VENT, and turned back on by deactivating HV Disable. For a window tear, HV Disable and Prop VENT would both be activated and would remain so for the rest of the flight. This would prevent the leaking detector from increasing the payload pressure to the point that arcing would be induced on the well-behaved detector.

Chapter 3

Flight Data Analysis

OGRESS launched from White Sands Missile Range at ∼2:00am on May 2, 2015. OGRESS collected data with HV on for 388 seconds. The detectors did not arc at initial turn-on and behaved nominally for most of the flight. Each detector experienced small (independent) arcing events which immediately stabilized and did not affect the functionality of either detector. Although it would have been preferred to have no arcing events, it was gratifying to see that the detectors have finally achieved a level of stability and robustness to allow this kind of event to occur with no ill effects. Detector 2 also experienced a transient hotspot which occurred separately from its small arcing event and lasted for $\sim$ 15 seconds. While active, the count rate shot up to $\sim$ 26 kHz and then promptly returned to normal. Transient hotspots like this, although rare for OGRESS, were a common occurrence for CyXESS, EXOS, and CODEX. Happily, this event did not last long and did not result in a change in detector performance. Within the active areas, the detectors measured a very steady count rate between $\sim$ 30 and $\sim$ 40 Hz throughout the entire flight. All monitor signals were nominal for the entirety of the flight, indicating that the instrument functioned properly. Detector pressure was properly maintained, and no window tears developed. Payload pressure was also appropriately maintained (see Figure 3.1). OGRESS' detectors performed better than those of CyXESS, EXOS, or CODEX.

OGRESS experienced an anomaly in its Black Brant motor resulting in very intense vibrations during the second stage burn. This has become a frustratingly common event which occurs when a resonance mode builds up inside the motor. Post-flight discussions with WSMR personnel indicate

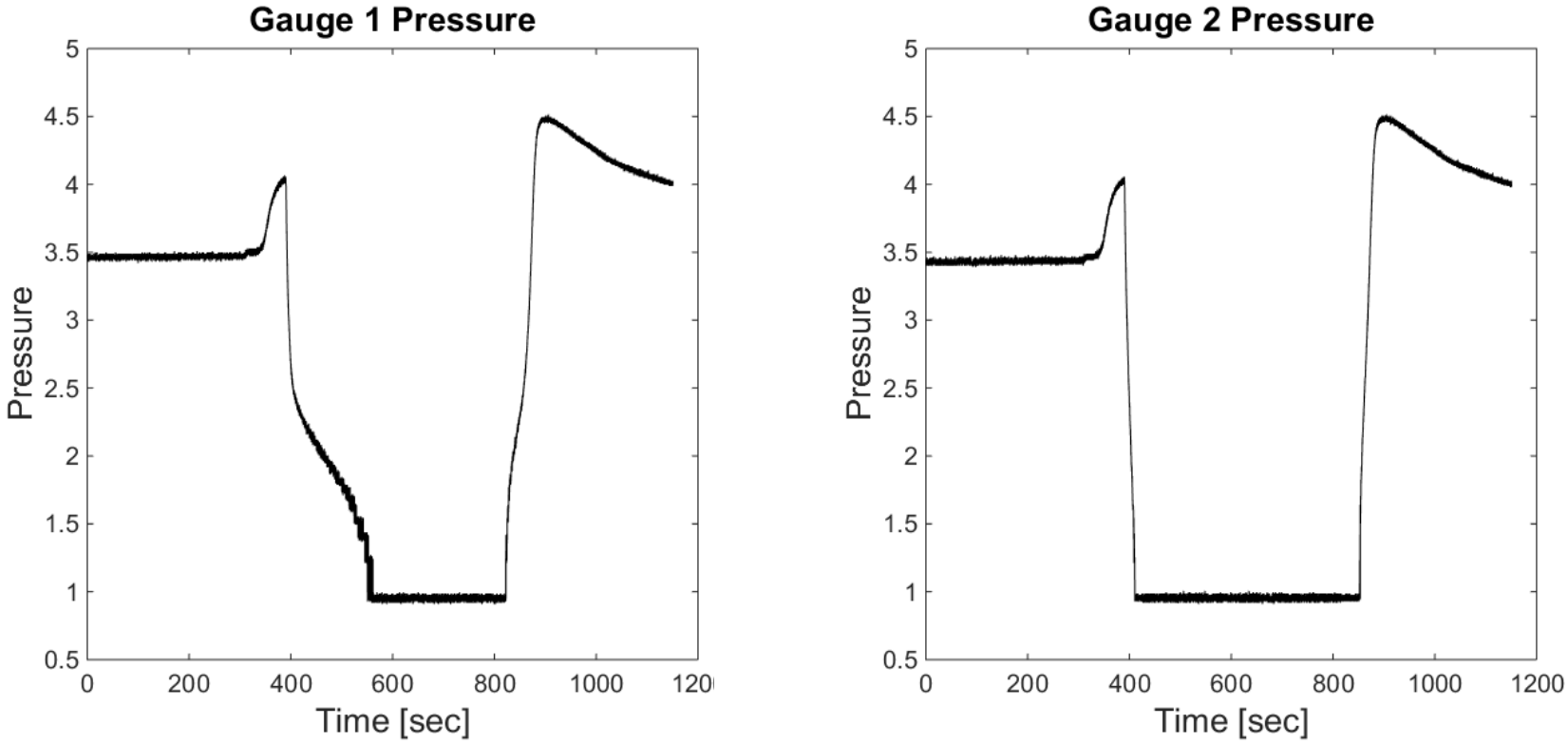

Figure 3.1: Payload pressure measured by Gauge 1 (*left*) and Gauge 2 (*right*), in units of voltage (the raw output from the gauges). The gauges bottom out at 10^{-6} Torr, indicating that payload pressure was below this level during flight. The gauges are mounted next to each other on the detector bulkead, so differences in measured pressure are due to different gauge calibrations. The pressure dropped rapidly after the shutter door opened and began to rise again ~ 15 seconds after the shutter door closed. The rise in pressure may not be genuine, as the gauges are likely to read incorrectly during reentry vibrations.

that this effect only seems to occur when launching an astrophysics payload at night from WSMR. Payloads which are launched during the day, from other sites, or for different kinds of science do not seem to be affected. EXOS experienced a very similar anomaly. OGRESS weathered the intense vibrations, no hardware was damaged, and the instrument functioned nominally. Considering the amount of new hardware in the electronics section, it was very gratifying to see the instrument function properly in such conditions.

OGRESS was recovered via helicopter the morning after launch. The payload experienced a soft landing, and no damage occurred other than superficial scratches to the skins. This was considered quite a victory after the landings of EXOS and CODEX, which suffered substantial hardware damage.

3.1 Flight Data

The raw flight data are shown in Figure 3.2. Detector 1 has a hotspot which was sustained throughout the flight and was expected based on preflight testing. Detector 2 also shows a hotspot, but this one was not sustained and can be easily removed by eliminating the 15 seconds of data when it was active. Several serious issues with the data immediately present themselves:

1) There are no apparent spectral features. This is obviously disturbing since we expect to at least see 0-order light on Detector 2, as this will be the strongest signal regardless of the specific spectral characteristics of our target. Even the dark sky pointing is expected to show a weak 0-order feature due to the galactic soft X-ray background. The data shown in Figure 3.2 show the signal from the dark sky and from Cygnus.

2) There are no apparent shadows from the window bar structures. This is an odd effect which has now been seen on every flight but has never been successfully replicated in a laboratory setting. This indicates that the same problems plaguing CyXESS, EXOS, and CODEX have not disappeared for OGRESS.

3) The count rate in the detectors' active areas were $\sim 15 - 30$ times higher than expected based on count rate estimates for Cygnus plus dark noise. This is also sadly consistent with the

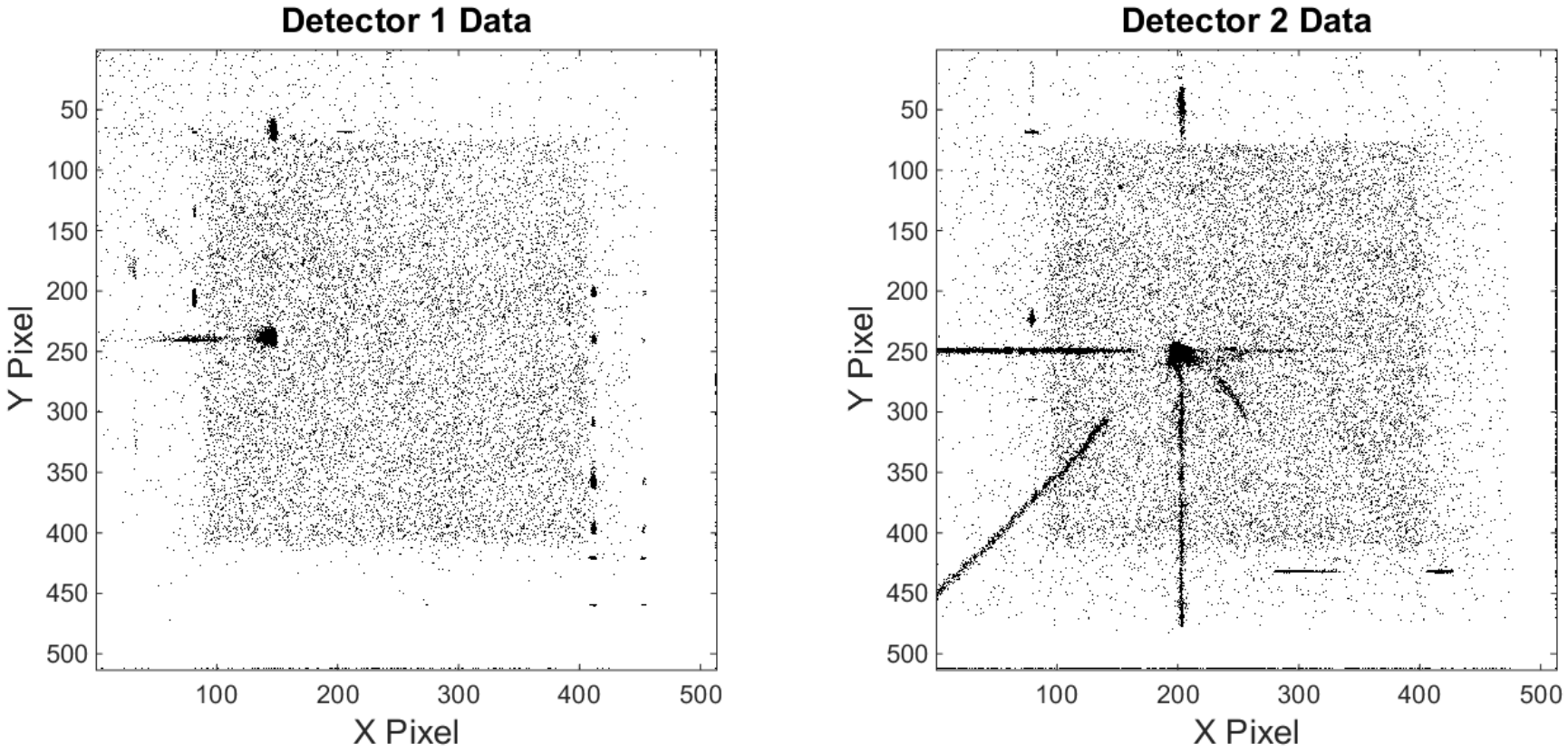

Figure 3.2: Raw flight data for each detector.

results of EXOS and CODEX.

Unfortunately, there appears to be very little qualitative difference between OGRESS' flight results and those of EXOS and CODEX which both acquired good data over a significant portion of their flights.

3.1.1 Count Rate

An investigation of the data is warranted regardless of initial appearances. Before investigating the actual images, much information can be gleaned from investigating the count rates of each detector throughout flight. The raw count rates of each detector are shown in Figure 3.3. The arcing events are obvious on both detectors, as is the period of the transient hotspot on detector 2. Each detector also shows the consistent ~ 30 Hz background count rate associated with the stim pulses (electronic pulses which are intentionally sent through the detector anode and electronics section, seen outside the active area of the detectors). The times associated with arcing and the transient hotspot can be removed. Also, counts falling outside the active area of the detectors can be removed (eliminating counts from the stims and misanalysed counts). Detector 2 shows a very consistent count rate throughout the flight, whereas Detector 1 begins with a relatively high count rate which then declines throughout the flight. This variable count rate on Detector 1 is entirely associated with its sustained hotspot. Eliminating the pixels in Detector 1's hotspot results in a very stable count rate, similar to detector 2 (see Figure 3.4).

The most notable feature of the count rate is its apparent consistency. We expect to see an increased count rate associated with Cygnus relative to the dark sky. If we separate the data into four distinct time periods, we can compare the count rates during each pointing: Dark Sky 1, Cygnus 1, Dark Sky 2, and Cygnus 2. The times and average count rates associated with each pointing are displayed in Table 3.1. Sadly, the count rate associated with the Cygnus pointings is actually slightly lower than those associated with the dark sky. This indicates that the signal observed during flight is dominated by something other than Cygnus.

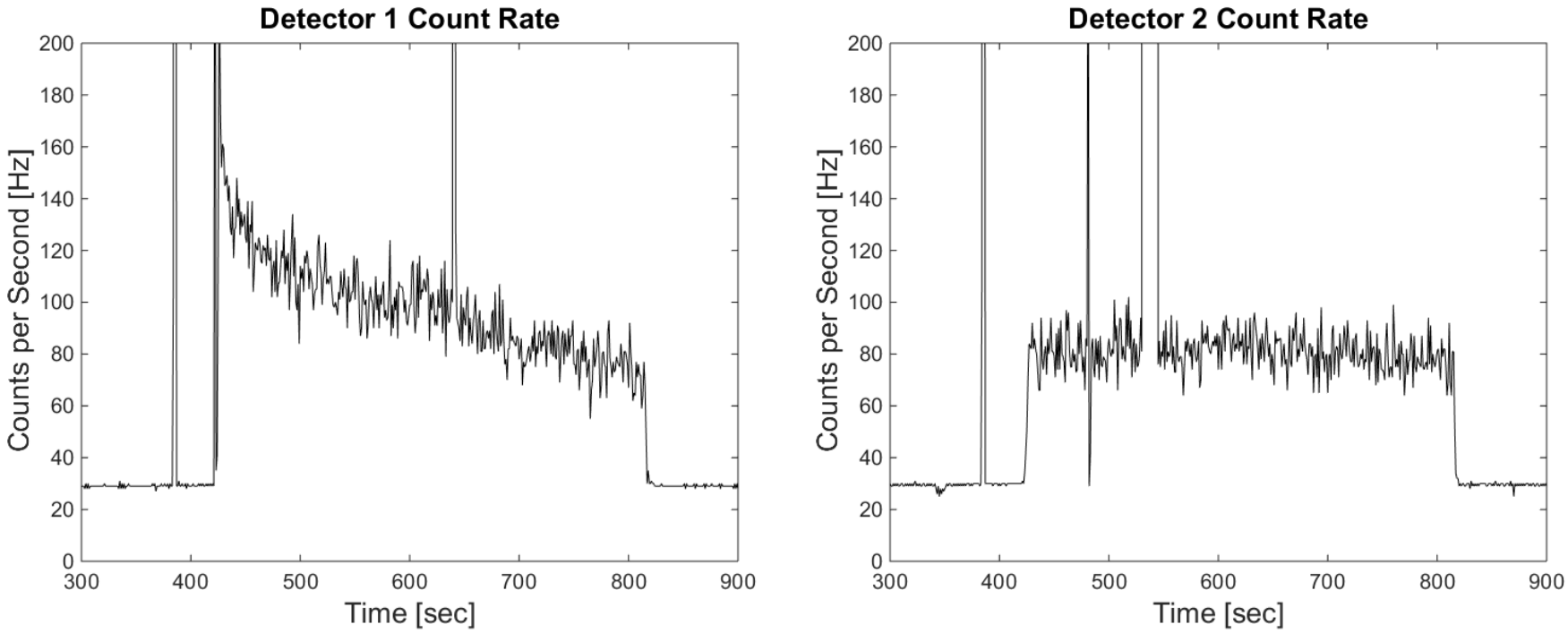

Figure 3.3: Raw count rate data for each detector.

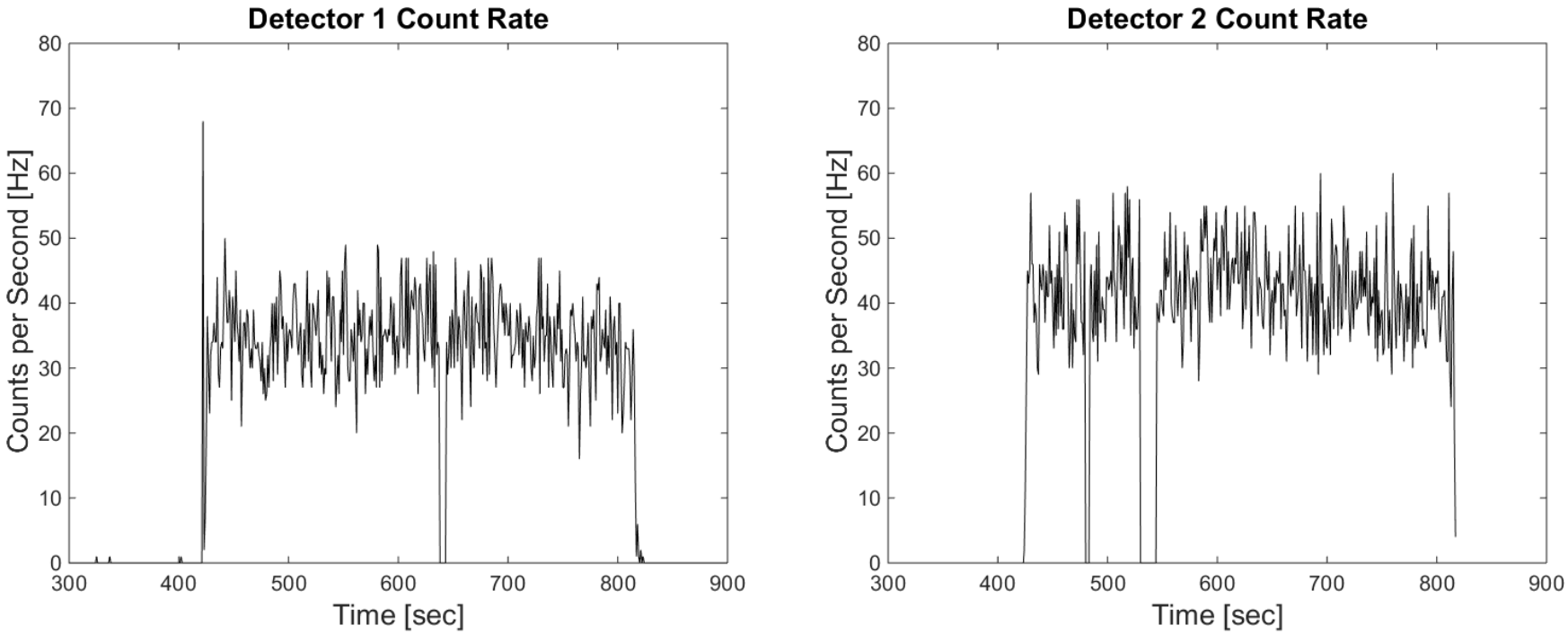

Figure 3.4: Count rate data in the active area of each detector. Hot spots and arcing events have been removed. The removal of the persistent hot spot from detector 1 leads to a count rate roughly as steady as detector 2's.

Table 3.1: Average Count Rate by Pointing

Target	Dark Sky 1	Cygnus 1	Dark Sky 2	Cygnus 2
Observing Time	31 sec	110 sec	39 sec	179 sec
Average Count Rate	75.7 Hz	75.7 Hz	82.8 Hz	75.3 Hz

3.1.2 Spectral Data

Now let us consider the X and Y data from each detector. The first step is to remove the $\sim$ 15 seconds of data from Detector 2 which experienced the transient hotspot. The data can then be separated depending on whether the payload was pointing at the dark sky or at Cygnus. The dark sky and Cygnus data are compared in Figure 3.5, with no obvious differences between the two sets (aside from fewer total counts on the dark sky, due to a lower observing time). For the Cygnus pointings, the active area data must be rotated and compressed to find counts as a function of wavelength. Figure 3.6 shows preflight data which display the orientation of the spectral lines on each detector. By rotating the images appropriately and summing counts perpendicular to the dispersion axis, we generate raw spectra for each detector, shown in Figure 3.7. Due to the rotations of the detectors relative to the spectral lines, the effective areas of each detector do not cut off sharply. Instead, they drop steadily near the edges of their respective bandpasses. Once again, the lack of spectral features and window bar shadows is immediately apparent. Figure 3.8 shows the number of counts acquired as a function of wavelength while observing Cygnus (the summation of the spectra shown in Figure 3.7). Also plotted is the geometric area of the detectors, which traces the data very well. This is an indication of how smoothly distributed the flight data are across the detector faces.

We now fit the flight data with various physical models using XSPEC, to see if an acceptable fit can be achieved with a realistic model. As stated in the introduction, the expected spectrum will follow an absorbed two-component NEI model with variable elemental abundances. We fit OGRESS' data to this model using initial parameters which fall within the values given in Table 1.1 from Chapter 1. The result is shown in Figure 3.9 and Table 3.2.

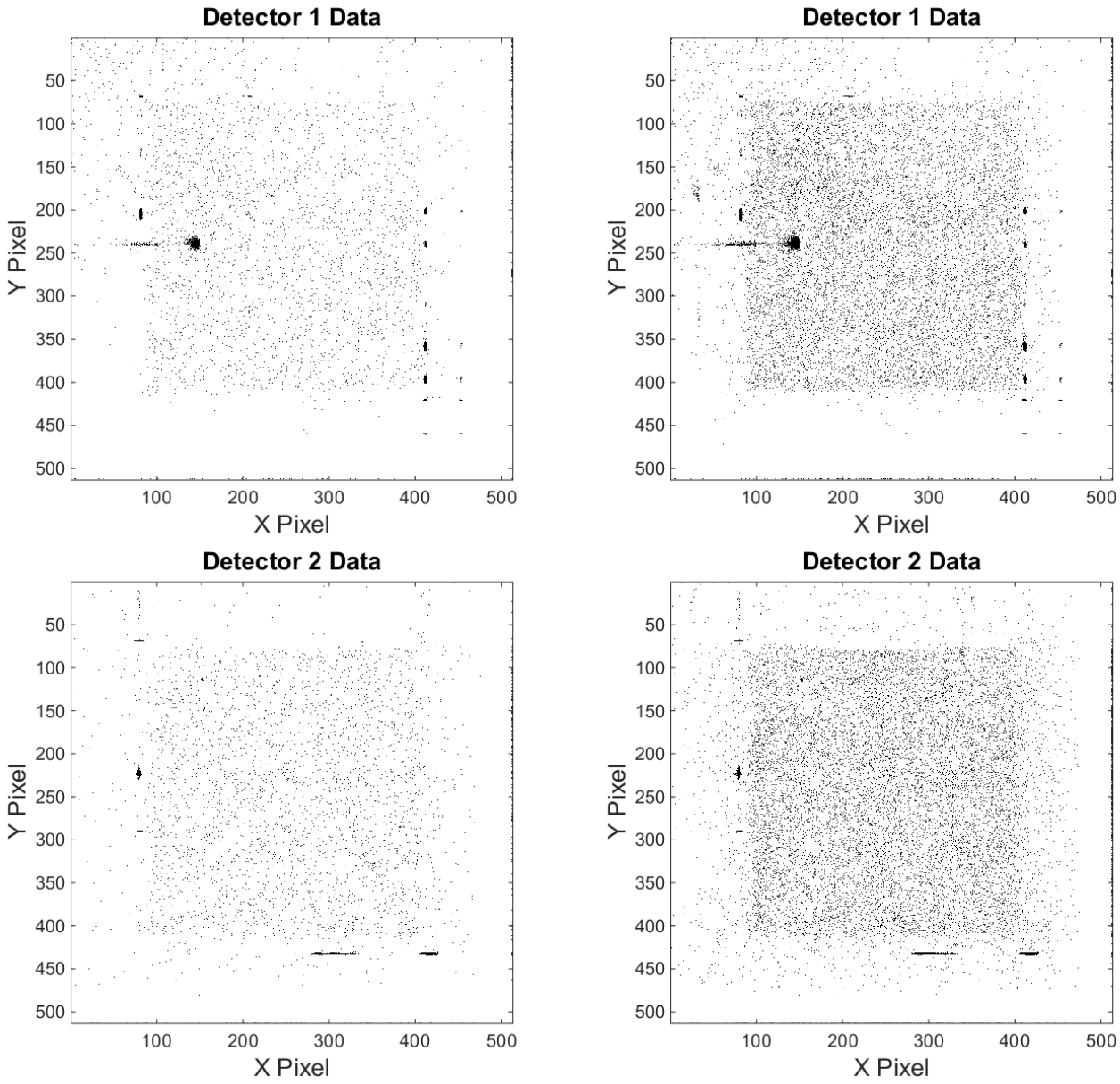

Figure 3.5: *Left*: Raw data when observing dark sky with each detector. *Right*: Raw data when observing Cygnus with each detector.

Using this model, a semi-acceptable fit can be achieved between 30–90 Å. At short and long wavelengths, however, the fit is exceedingly bad. The reduced chi-square value ($\Delta\chi^2$) of the fit is 8120/3579, the denominator noting the degrees of freedom. This $\Delta\chi^2$ is removed from the ideal value (3579) by $> 75\sigma$ (assuming Gaussian errors). Table 3.2 shows that the so-called "best-fit" of this model requires parameters which are highly unrealistic, particularly for the elemental

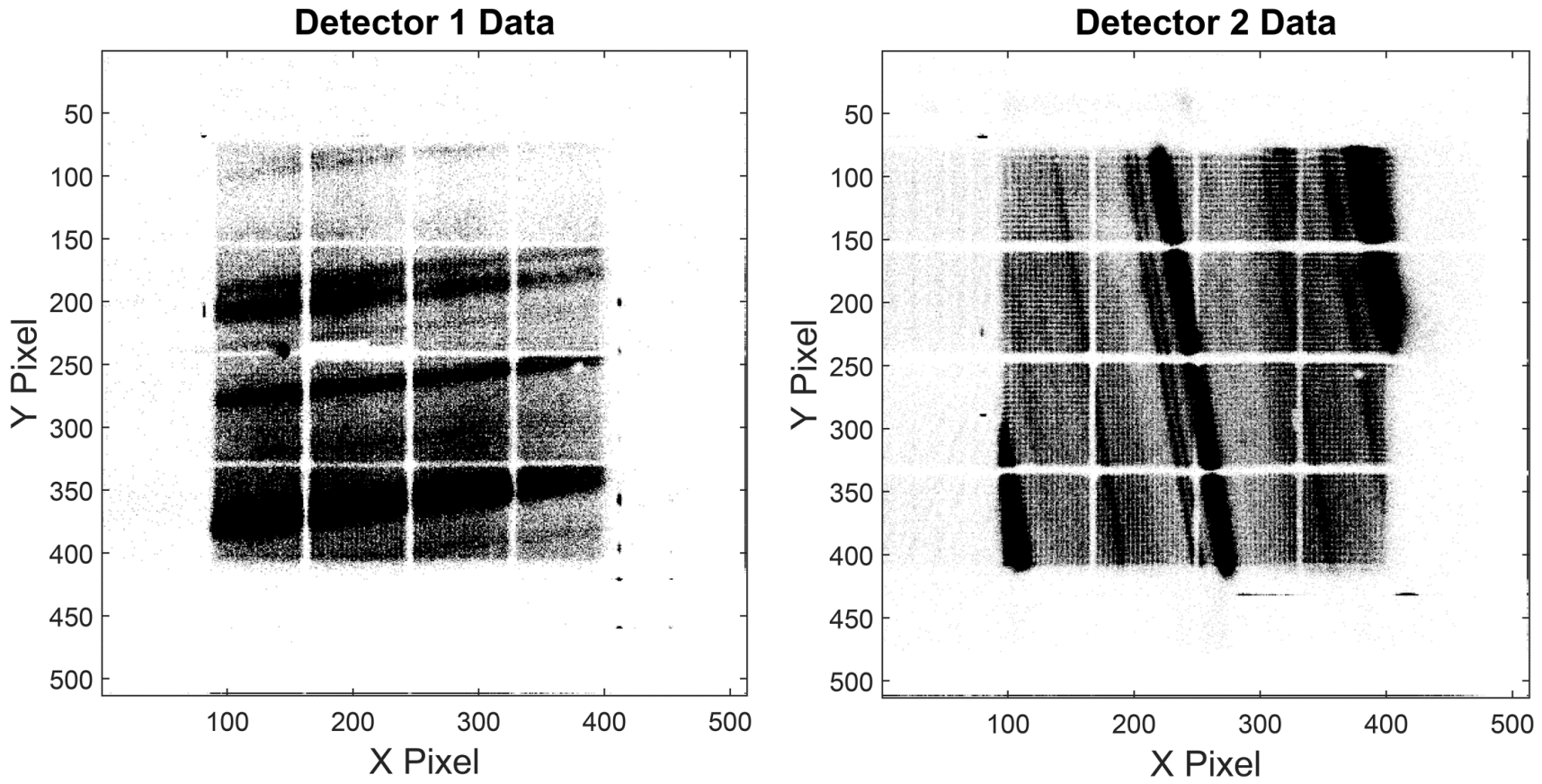

Figure 3.6: Preflight data for each detector illuminated with a Manson electon-impact X-ray source. Each detector is rotated relative to the incident spectral lines to help distinguish between spectral features and hot spot noise which bleeds in the X and Y directions.

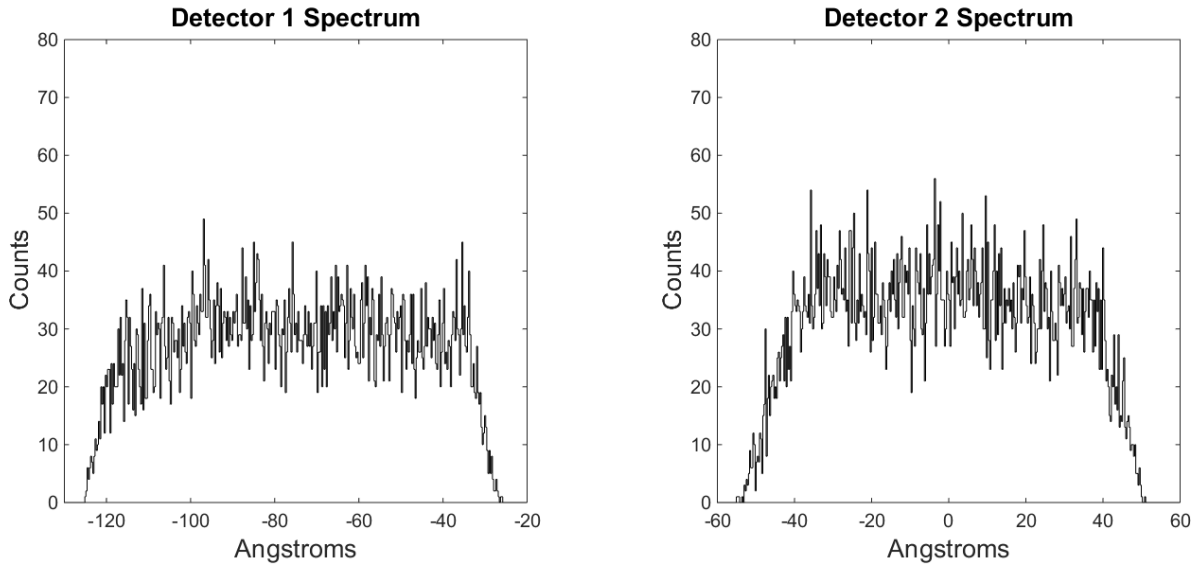

Figure 3.7: Raw spectra from each detector.

Table 3.2: Best-fit XSPEC parameters.

$\Delta\chi^2$	8120/3579	
n_H (cm^{-2})	0.0828e+22	
	Low-T Component	High-T Component
kT (keV)	0.114	0.768
H	1	1
He	1	1
C	0.22	0.00
N	0.00	0.00
O	0.00	0.00
Ne	0.00	14.9
Mg	0.00	0.18
Si	0.00	2.51
S	4.82	0.00
Ar	10.71	0.00
Ca	0.00	0.00
Fe	0.00	0.30
Ni	0.00	10.40
$n_e t$ (cm^{-3}s)	1.85e+11	6.49e+11
norm	2517	1.39e+4

abundances. The best-fit suggests that most metals have extremely low (even zero) abundances, but that a certain few are several times more abundant than solar values. Also, the uncertainties

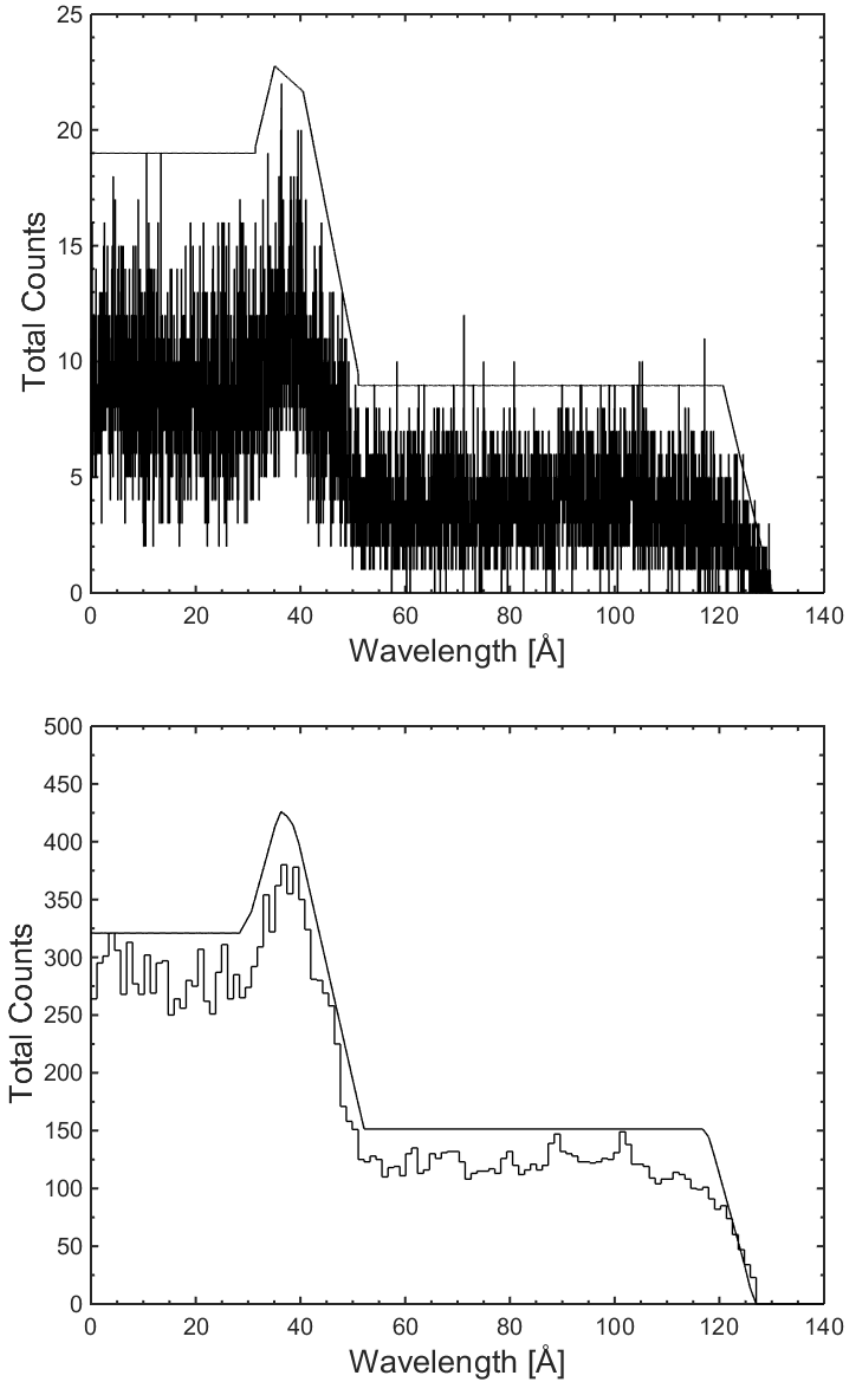

Figure 3.8: The histograms show the number of counts observed by OGRESS while observing Cygnus, as a function of wavelength. The solid lines shows the scaled geometric area of the detectors. The top image displays the raw unbinned data, whereas the bottom image displays the data binned by OGRESS' spectral resolution. The data closely follow the geometric area, indicating the smooth distribution of counts over the detector faces.

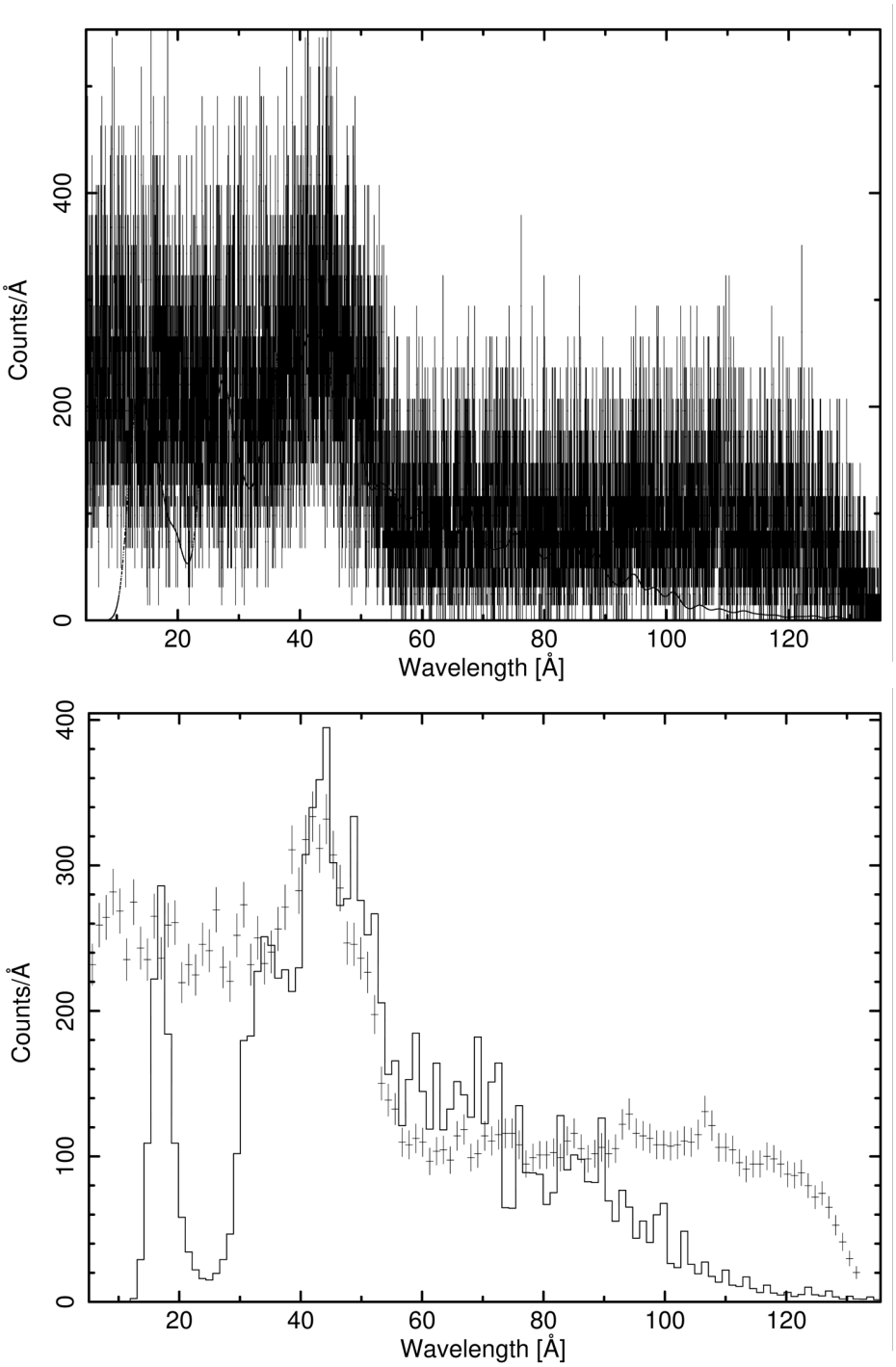

Figure 3.9: These images show OGRESS' observed spectrum as crosses. Cross length represents the Poisson errors associated with each bin. The histogram represents the best-fit spectrum created by an absorbed two-component NEI model. The top image shows the unbinned data. In the bottom image, the data have been binned to OGRESS' spectral resolution for easier comparison between the data and model.

associated with these "best-fit" parameters (not shown in Table 3.2) are typically larger than the values of the parameters themselves. Other absorbed, two-component XSPEC models (powerlaw, vbremss, vapec, vgnei, vpshock, see Arnaud et al. [2015]) give similarly bad fits. Thus, the spectrum which we expect from Cygnus is inconsistent with the data we observed. Along with the higher-than-expected count rate, this is strong evidence that OGRESS experienced some source of noise during flight that is inconsistent with the emission from Cygnus.

Although we do not have a good fit between the data and model, our data look qualitatively similar to the low-resolution plots containing data from *Chandra*, *XMM*, or *Suzaku* (see Chapter 1). It is worth considering the possibility that OGRESS successfully collected data from Cygnus, but at a substantially lower resolving power than anticipated. This would have the effect of smoothing Cygnus's spectrum, perhaps beyond the resolution of *Chandra/XMM/Suzaku*. We can test this theory by modifying the instrumental response function to expect much wider resolution when carrying out the spectral fits. Achieving an acceptable fit would indicate that OGRESS successfully collected data from Cygnus, but underperformed in resolving power. Pre- and post-flight testing show close agreement to the theoretical resolution. It is possible, however, that resolution is worse in flight conditions. One possible mechanism to degrade resolution in flight is scrambling of low-significance bits in the X and Y count data. This would spread counts out across the detector faces, effectively blurring the image. This could smear and suppress features such as spectral lines or window bar shadows.

Figure 3.10 shows the same data as Figure 3.9, but seen with degraded spectral resolution. The top image has had the resolution degraded to $\sim$ 13 Å. The bottom image has had the resolution degraded even further to $\sim$ 22.5 Å, the point at which the window bar shadows will begin to overlap. The fit is now substantially better – particularly at short wavelengths – because the modeled spectral lines are smoothed out. The fit, however, is still unacceptable especially at long wavelengths. For mildly degraded resolution (13 Å), $\Delta\chi^2 = 5756/3575$ for the absorbed two-component NEI model. When the resolution is further degraded (22.5 Å), the fit actually becomes worse and produces $\Delta\chi^2 = 5974/3575$. This occurs because the resolution is now too wide to agree with certain

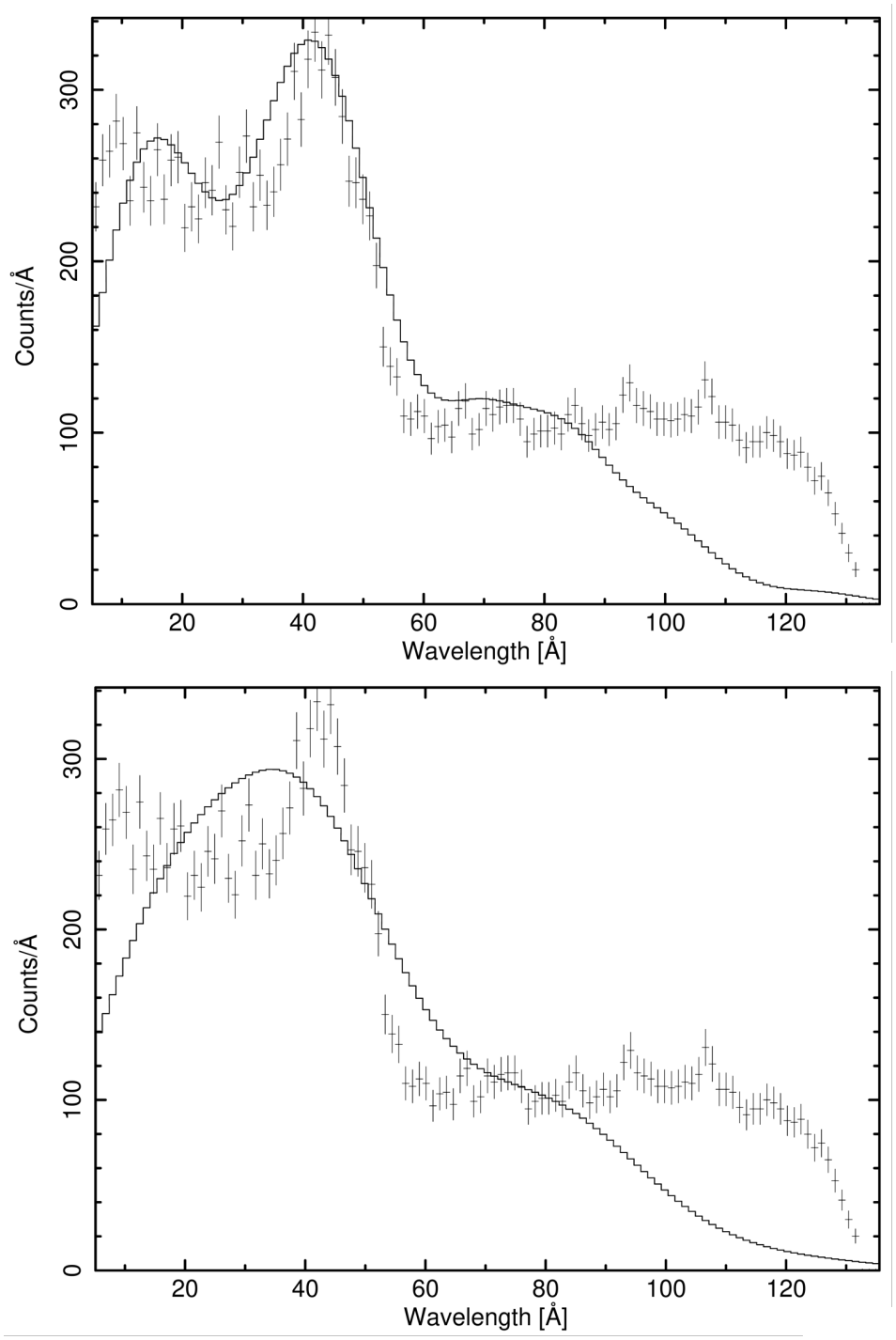

Figure 3.10: The data seen in Figure 3.9 is shown as crosses. The best-fit models are shown as the solid lines. *Top*: Spectral resolution has been degraded by a factor of 8 (to $\sim$13 $\mathring{A}$). *Bottom*: Spectral resolution has been degraded even further to 22.5 $\mathring{A}$. A good fit can still not be achieved at long wavelengths.

features in the spectrum. The $\Delta\chi^2$ values for the fits with degraded resolution are still $> 35\sigma$ above the ideal value (again assuming Gaussian errors). The poor fits indicate that OGRESS has not simply suffered a degradation to spectral resolution during flight. There is other evidence that the spatial resolution of the detectors (which contributes strongly to the spectral resolution) has not degraded in flight based on the sharp cutoff in signal at the edges of the effective areas of both detectors. If signal were to be spread out or randomized within the detector or electronics, this boundary would also be smoothed out. Additionally, the stim pulses are not spread out or blurred, indicating that the detectors functioned with optimal spatial resolution.

3.1.3 Pulse Height Data

Although the position data do not appear to make a usable spectrum, we can still attempt to extract a spectrum using the pulse height data. The raw Pulse Height Distributions (PHDs) of each detector are shown in Figure 3.11. Detector 1 and Detector 2 show somewhat different characteristics. Both detectors show spikes around channels 70 and 160 associated with the stim pulses. Both detectors also show a spike at maximum channel 255, indicating that a large number of the incoming counts are high-energy. Detector 1 also has a large number of counts in low charge channels. Hotspots almost always create counts with low pulse height, so the low-channel peak in detector 1's PHD is probably associated with the persistent hotspot (we cannot be completely certain for reasons discussed below). For Detector 2, the PHD changes dramatically depending on which portion of the detector is being sampled, as shown in Figure 3.12. The PH from each stim can be easily isolated and removed from that of the active area, as expected. Unfortunately, this is not the case for Detector 1 (see Figure 3.13), indicating that some sort of randomization has occurred in its PH data. This is difficult to understand, since the position data have no apparent problems, and the positions of the stim signals are consistent with pre- and post-flight testing. Also, the count rate is low enough that the read out system experiences a significant amount of down time between each count, making it difficult for count data to become confused during the write-out process. Even so, the PH data for detector 1 appear to have been randomly assigned between the

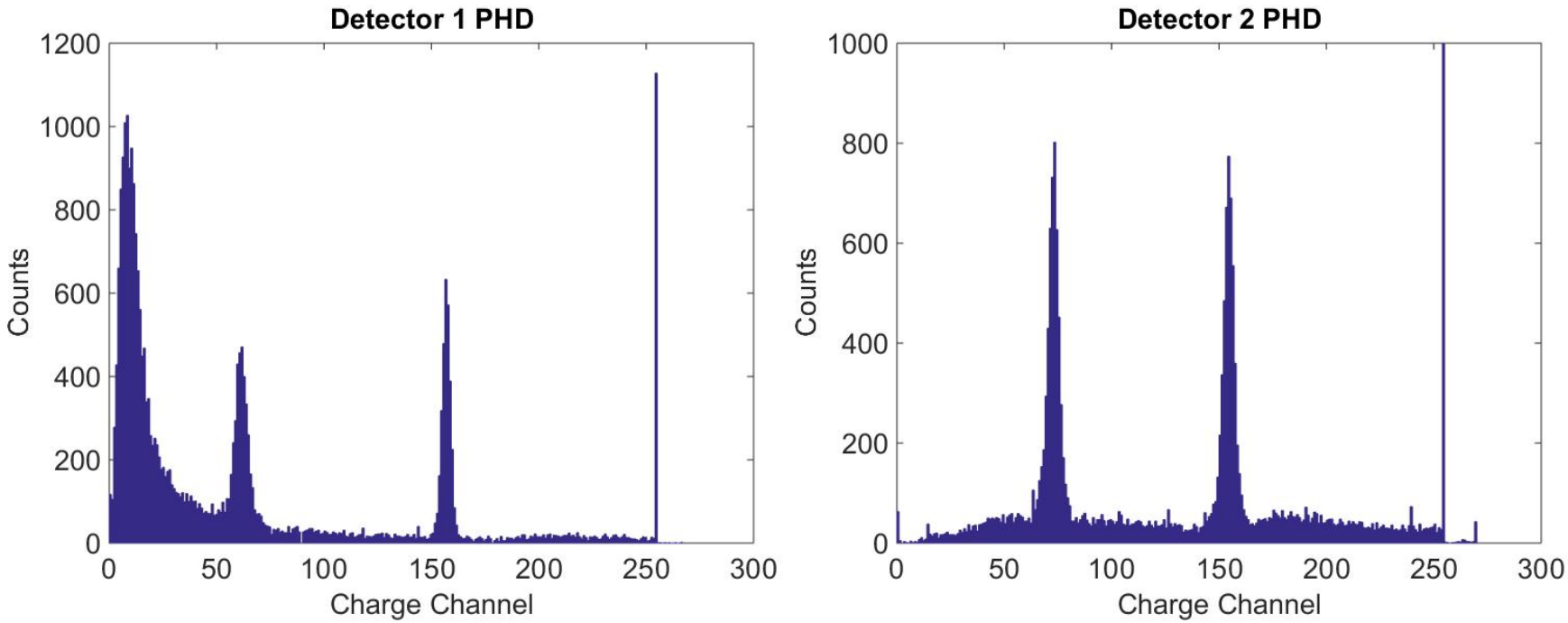

Figure 3.11: PHDs for each detector. The stim pulses are clearly visible near channels 70 and 160. Detector 1 also shows many counts at low pulse channels due to its persistent hotspot.

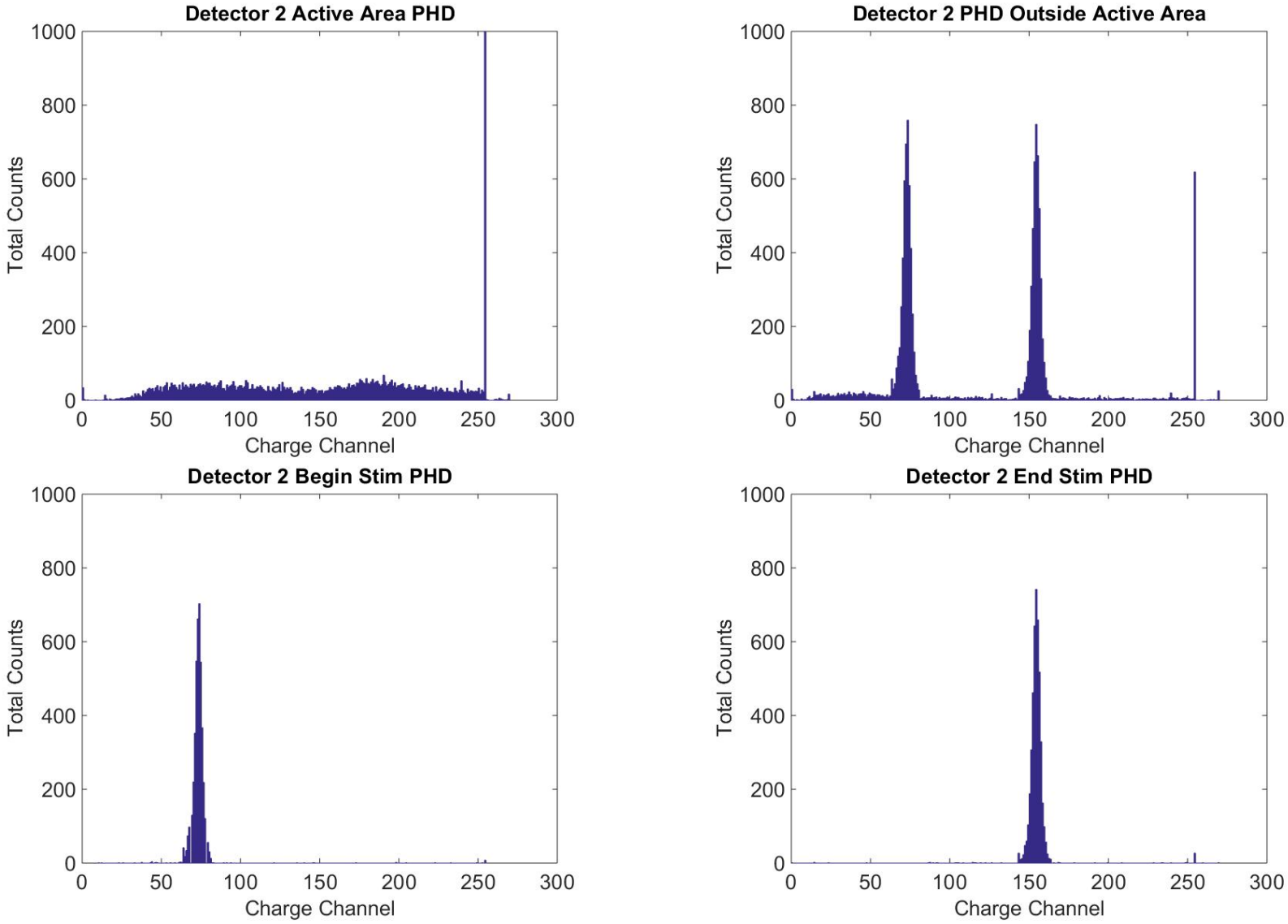

Figure 3.12: PHDs for different areas of detector 2. Features of the raw PHD (Figure 3.11) are easily separable.

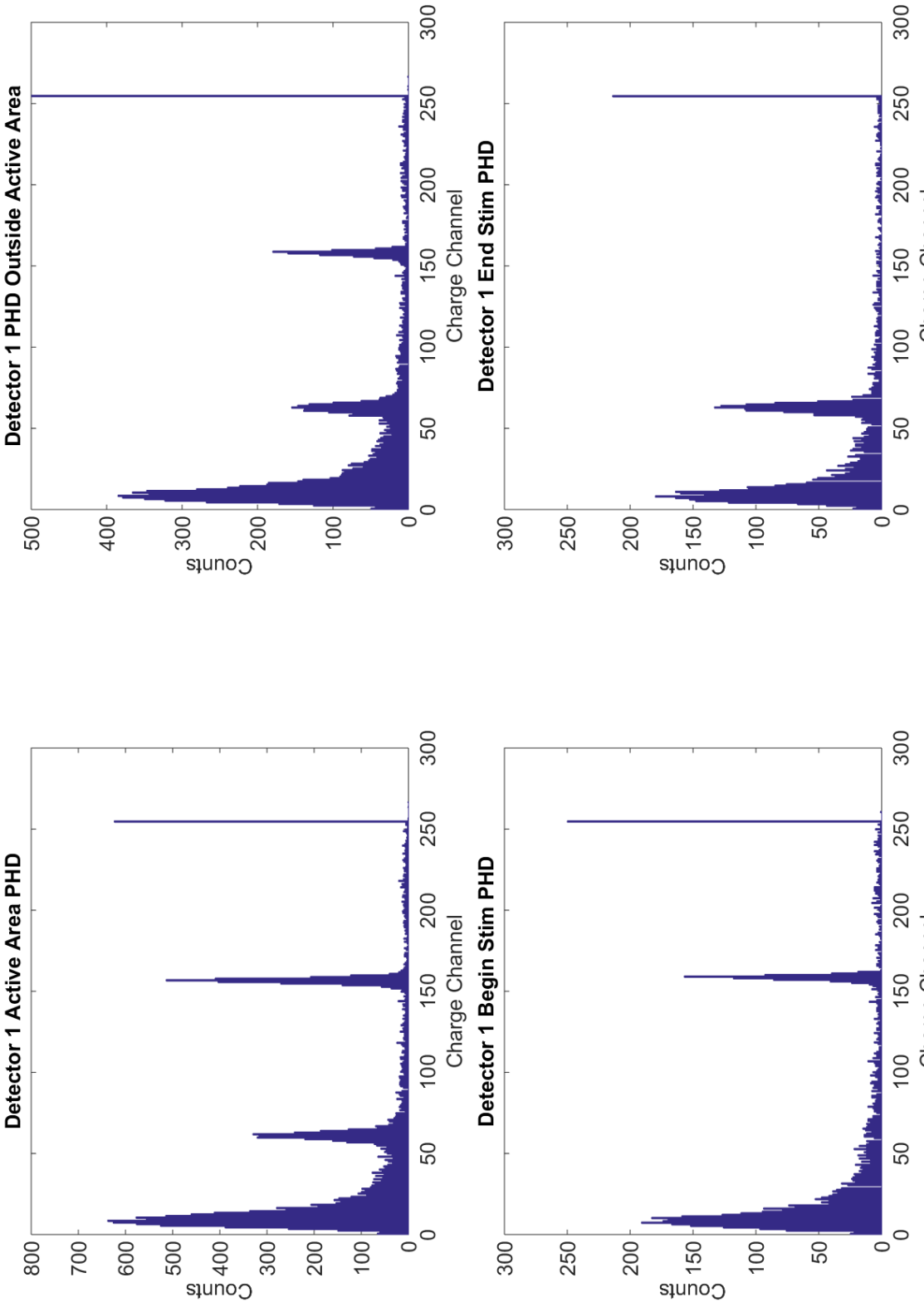

Figure 3.13: PHDs for different areas of detector 1. Features of the raw PHD (Figure 3.11) are not easily separable.

detected counts. Post-flight investigation into this issue revealed that the effect is also present in laboratory data taken both before and after flight. Unfortunately, this makes it impossible to use the PHD to analyze Detector 1, as the contaminating stim and hotspot signals cannot be removed from that of the active area. Luckily, this is not the case for Detector 2.

Using the PH data from detector 2, we can carry out a spectral analysis. This process is complementary to the analysis of the position data carried out in the previous section. Should the position data have been assigned incorrectly, the PH data may still allow us to extract a usable spectrum – though at lower resolving power than originally expected.

Figure 3.14 shows the PHD associated with the active area of Detector 2. With the stim pulses

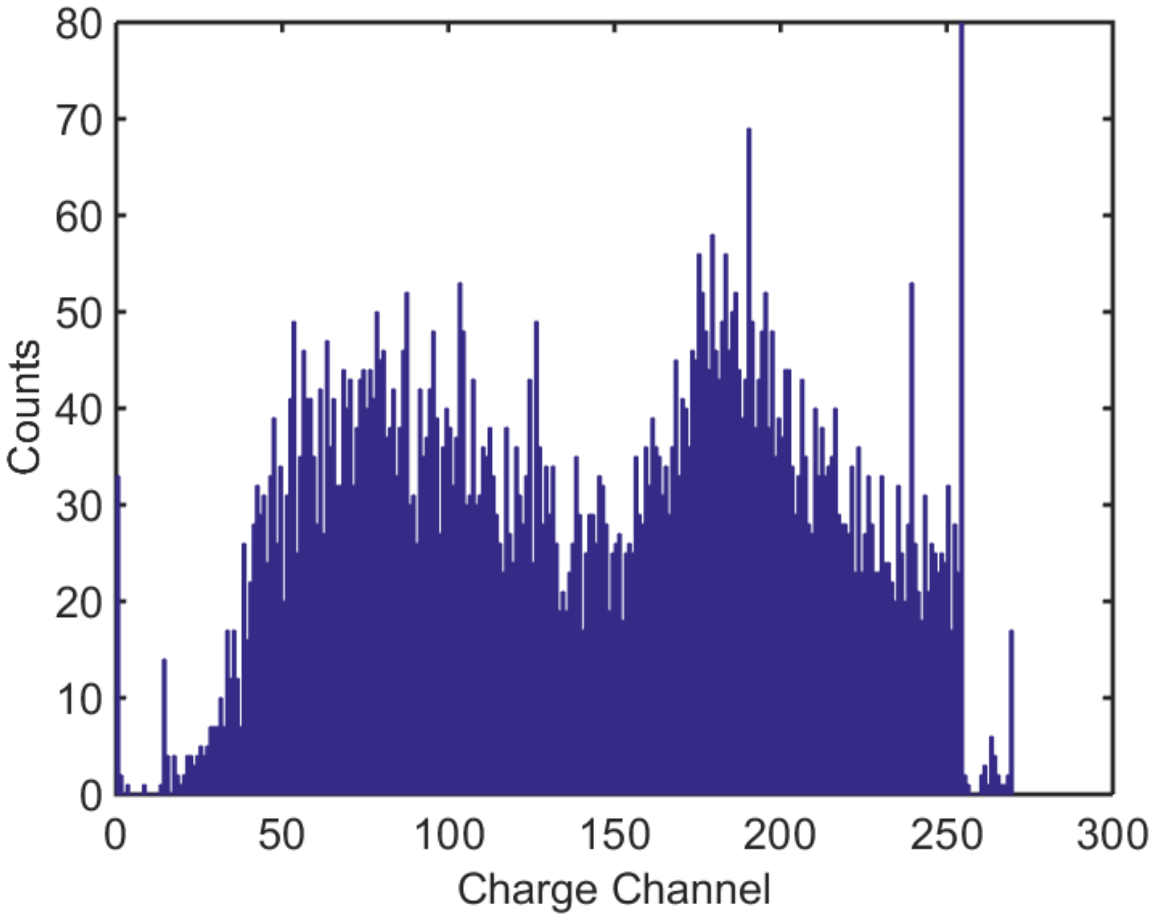

Figure 3.14: The PHD of detector 2's active area. The PHD shows some distinct structure.

removed, what once appeared as a low level of counts distributed evenly among charge channels now shows some very distinct structure. Before analyzing the PHD spectrum, we should consider correcting it using a gain map. Chapter 2 described the large spatial variations in gain which occur across the detector face during laboratory testing. However, the gain map for data acquired in flight (Fig. 3.15) looks considerably different than those acquired in the laboratory (see Fig. 2.35). The gain map acquired during flight is much smoother than those acquired in the laboratory and

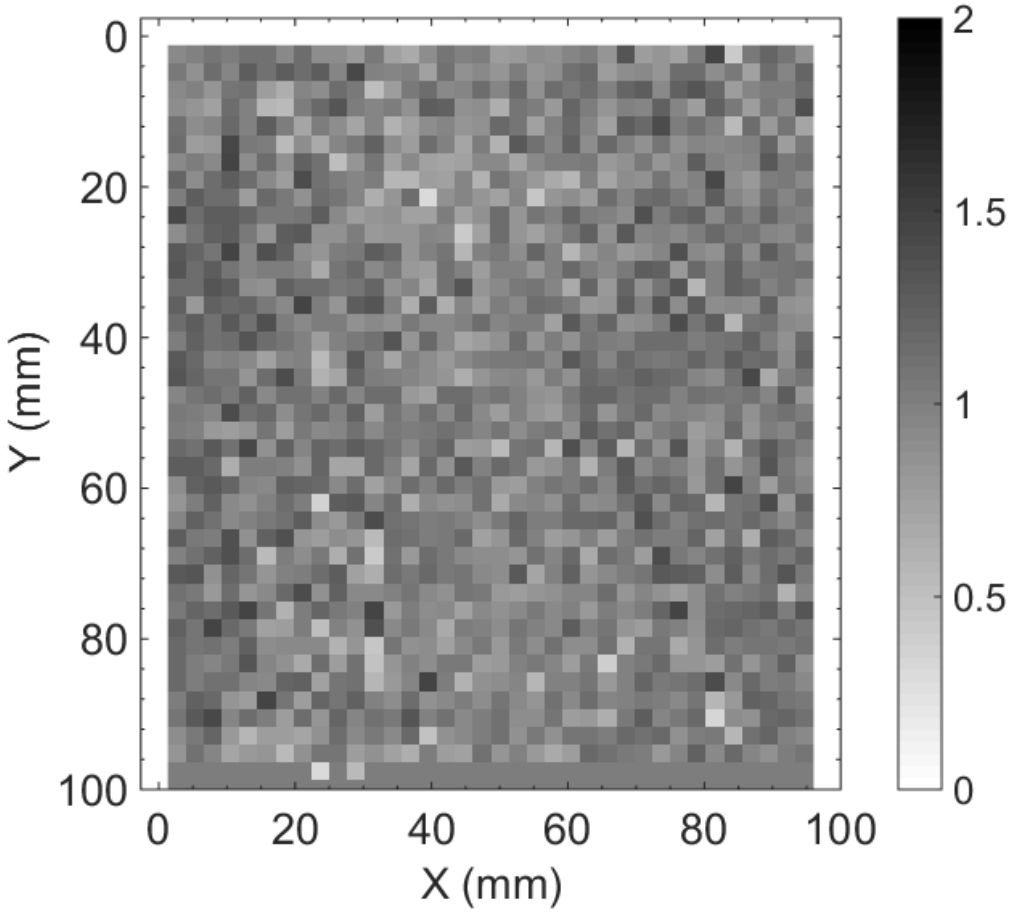

Figure 3.15: The gain map of detector 2's flight data. This gain map is much smoother than the ones produced with Fe-55 in the laboratory. As no window bars were apparent in the flight data, their locations have not been masked in this gain map.

shows little – if any – spatial variation. It is unclear why this discrepancy between laboratory and flight data should exist. One possibility is that the large penetration depth of 5.9 keV Fe-55 X-rays

causes different detector behavior than the short penetration depth of the < 1 keV X-rays we wish to observe from Cygnus. Fe-55 X-rays may produce most of their photoelectrons by ionizing the copper of the top GEM foil. If this is true, surface variations in the top foil (e.g. variations in oxidation or moisture absorption) could potentially lead to substantial gain variations. Regardless of the cause, the nature of the flight data appears to be distinct from that of laboratory data. Due to the lack of spatial variation in gain, we will not use the gain map to correct the flight PH data.

Figure 3.16 displays the raw spectrum based on the PH data. To analyze the spectrum, we

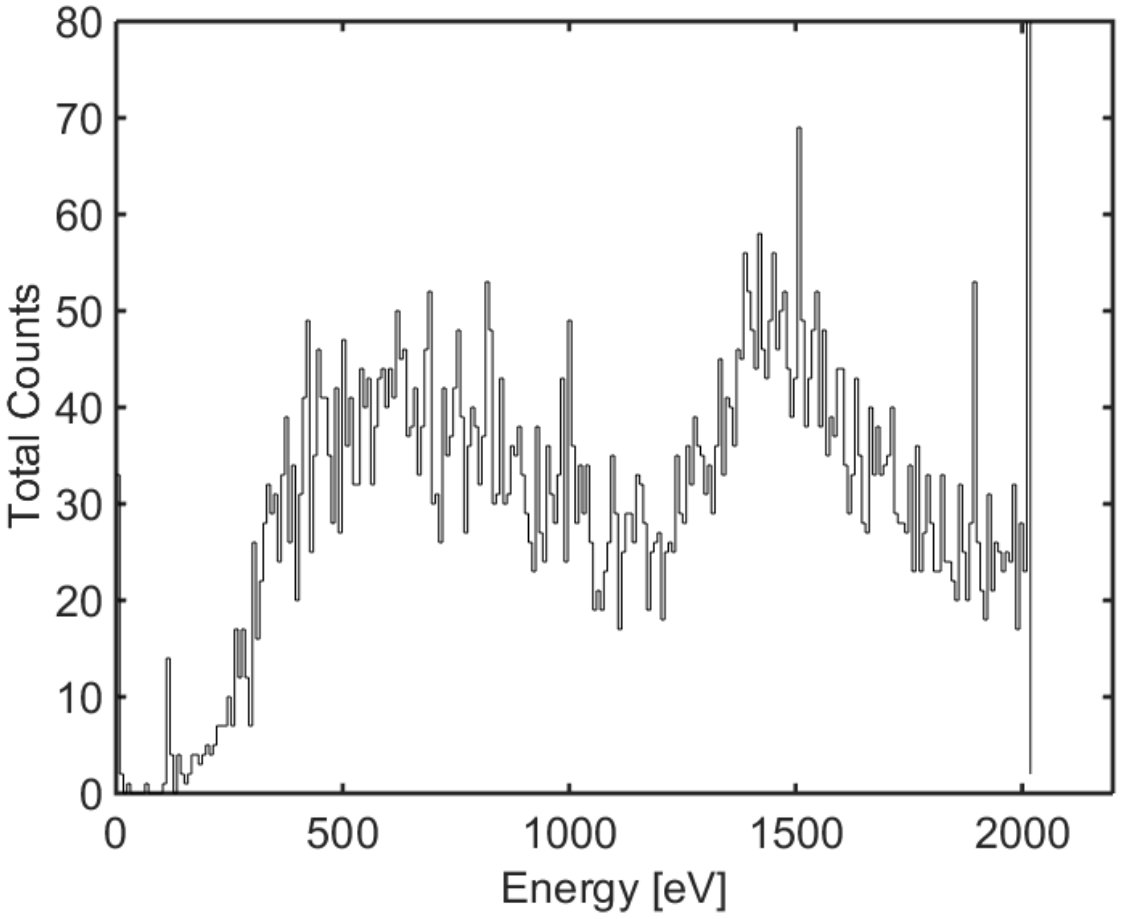

Figure 3.16: The raw spectrum, based on PH data.

must modify the theoretical spectral resolution and effective area of the instrument. The effective area will be different, since we will use the geometric area of detector 2 only. The spectral resolution

will, of course, be different when analyzing the PHD spectrum, as we are now relying on the energy resolution of the detectors rather than the dispersion of the gratings. Laboratory testing with an Fe-55 source has shown that the FWHM of detector 2 is very close to 100% of the central pulse channel (e.g. a spectral line centered in channel 83 will have a FWHM of 83 channels). This is substantially wider than the FWHM of CyXESS's detectors, which were able to achieve a FWHM of $< 30\%$. Careful measurements of detector energy resolution were not made for EXOS or CODEX, so it is not known whether this change in resolution is due to the LCP GEM foils, the new electronics, or some other effect.

Figure 3.17 shows the PHD spectrum now fitted with an absorbed two-component NEI model

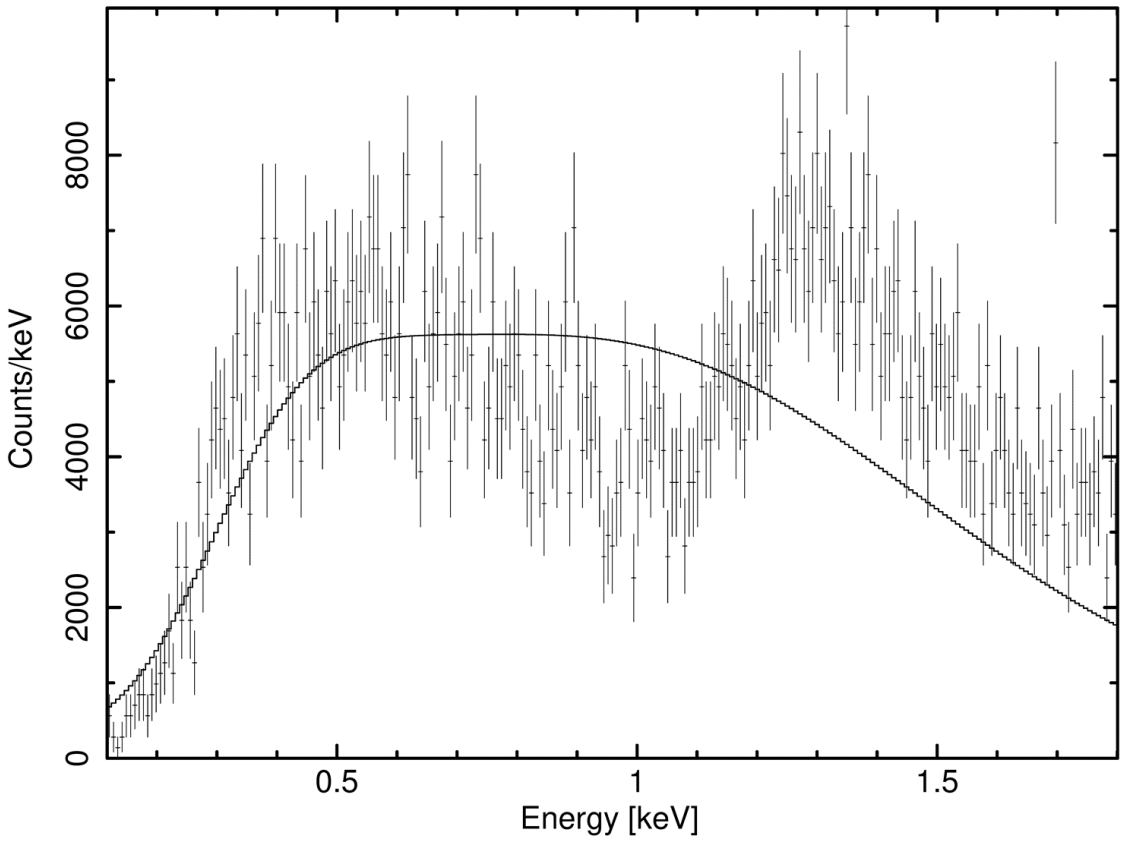

Figure 3.17: OGRESS' PHD spectrum (crosses) fitted with an absorbed two-component NEI model (solid line). The FWHM of the instrument is assumed to be 100% of the pulse channel. The high-energy bump is seen to be narrower than the assumed instrument resolution.

with the same initial parameters used for Table 3.2's fit. For this fit, we have ignored the lower PH channels (corresponding to < 100 eV), as pulses below these channels begin to be ignored by the electronics. Channel 255 has a large effect on our spectral fits, since it contains so many counts. However, a very large number of these counts are the result of minor malfunctions in the electronics (misanalysed bits). Therefore, we elect to ignore channel 255, as well. Table 3.3 displays the best-fit parameters. Once again, the best-fit for the PHD spectrum is quite bad

Table 3.3: Best-fit PHD parameters

$\Delta\chi^2$	870/208	
n_H (cm^{-2})	0.170	
	Low-T Component	High-T Component
kT (keV)	0.0808	1.781
H	1	1
He	1	1
C	0.00	0.00
N	0.00	0.00
O	0.00	0.00
Ne	0.00	0.00
Mg	0.00	247.1
Si	0.00	0.00
S	0.00	0.00
Ar	0.00	0.00
Ca	0.00	0.00
Fe	0.00	0.00
Ni	0.00	313.4
$n_e t$ (cm^{-3}s)	4.19e+13	2.09e+11
norm	0.00	45.98

with $\Delta\chi^2 = 870/208$ for this model, $\sim 32\sigma$ away from the ideal value. As with the dispersion spectrum, the best-fit parameters are highly unrealistic, requiring almost no metals. Also, the low-temperature component is effectively ignored (norm set to zero). A noticeable, and strange feature of this fit is that the PHD spectrum – particularly the high-energy bump – cannot be adequately modeled with our assumed detector resolution and response. The high-energy bump (centered at $\sim$1.3 keV) is narrower than the energy resolution of the detector, as measured with Fe-55 signal. Why this should occur is not clear. The high gas penetration depth of 5.9 keV Fe-55 X-rays relative

to 0.1 – 1.5 keV X-rays may explain the effect. At the lower penetration depths associated with low-energy X-rays, photoelectrons will always traverse roughly the same distance to the first GEM foil, experiencing a similar number of collisions with detector gas molecules. Photoelectrons from high-energy Fe-55 light, in contrast, will have a much wider range of distances to travel to reach the first GEM foil. This would result in a wide range in the number of collisions experienced along the way, which might translate to wider resolution at high energies.

We can attempt to model the data with narrower energy resolution, although we have no laboratory data to suggest that this is legitimate. Obviously, this new fit should not be taken very seriously, as we are effectively using the flight data as their own calibration.

Figure 3.18 shows the flight PHD spectrum fit with the same model parameters as in Figure 3.17 for an instrument with a FWHM of 45%. The best-fit parameters for the 100% FWHM produce a model which looks much different when passed through a 45% response function. It is immediately obvious from the plot that the same model has produced substantially more flux when used with a resolution of 45%. This is not a particularly intuitive effect. The reason it occurs is that most of this flux is spread out of the instrument's bandpass when applying a wider resolution. Clearly, different parameters are required to fit the data to a higher resolution instrument.

Figure 3.19 shows the flight spectrum with a new best-fit model using 45% energy resolution. The parameters of this new model are shown in Table 3.4. These new parameters provide a substantially better fit. $\Delta\chi^2 = 323/208$ for the new fit, only 5.6σ from the ideal. The $\Delta\chi^2$ for this fit is good enough to begin bordering on the edge of plausibility. The fit can be improved even further by ignoring several channels which contain a substantially different number of counts than their neighbors. Given the wide energy resolution of the detector (even the improved resolution assumed here) we never expect to see the counts spike (or drop) in a single channel. The fact that this is occurring suggests that the channels in question are not reliable. If we ignore the channels with the most substantial deviations from their neighbors (21, 174, & 223) we arrive at a new $\Delta\chi^2 = 279/205$. This value is now only 3.7σ away from its ideal. We also note that this fit assumes that the only noise present is from Poisson ($\sim$Gaussian) fluctuations. In reality, the

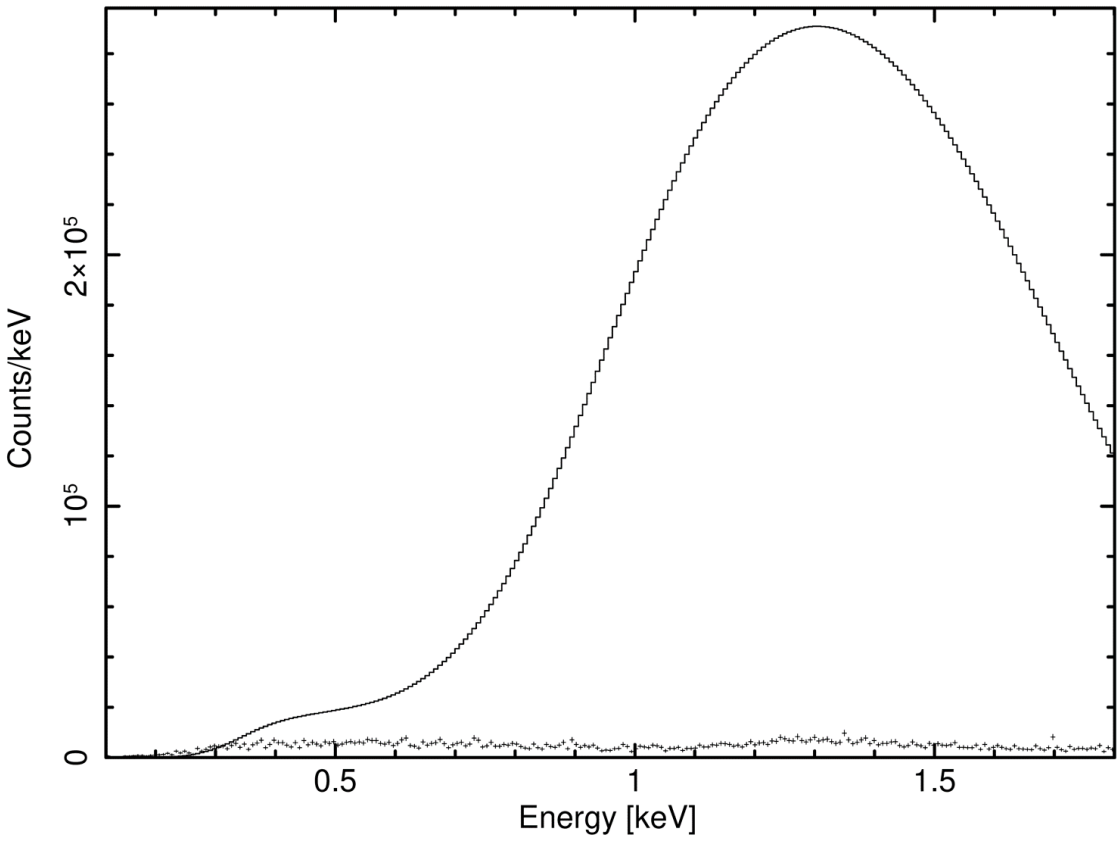

Figure 3.18: OGRESS' PHD spectrum (crosses) fitted with an absorbed two-component NEI model (solid line). The assumed spectral resolution of the instrument has now been reduced to match the width of the high-energy bump, with a FWHM of 45%. The spectral parameters from Table 3.3 have been used.

detector will experience dark counts, sky background X-rays, and possibly other unanticipated sources of noise. Recall that we have applied no background corrections to the spectrum. Thus, the true uncertainties associated with the data are likely to be significantly larger than the values assumed by the fit. Applying the true (larger) uncertainties would result in an even lower $\Delta\chi^2$ value. Based on these considerations and the low $\Delta\chi^2$ value, this fit seems plausible.

Our confidence in this model drops considerably when inspecting Table 3.4. The parameters required to produce the best-fit are, once again, highly unrealistic. The model calls for many metals to have zero abundance (including carbon) and for several others to have many times their solar values. The temperature of the hot component is questionably high. The low-temperature

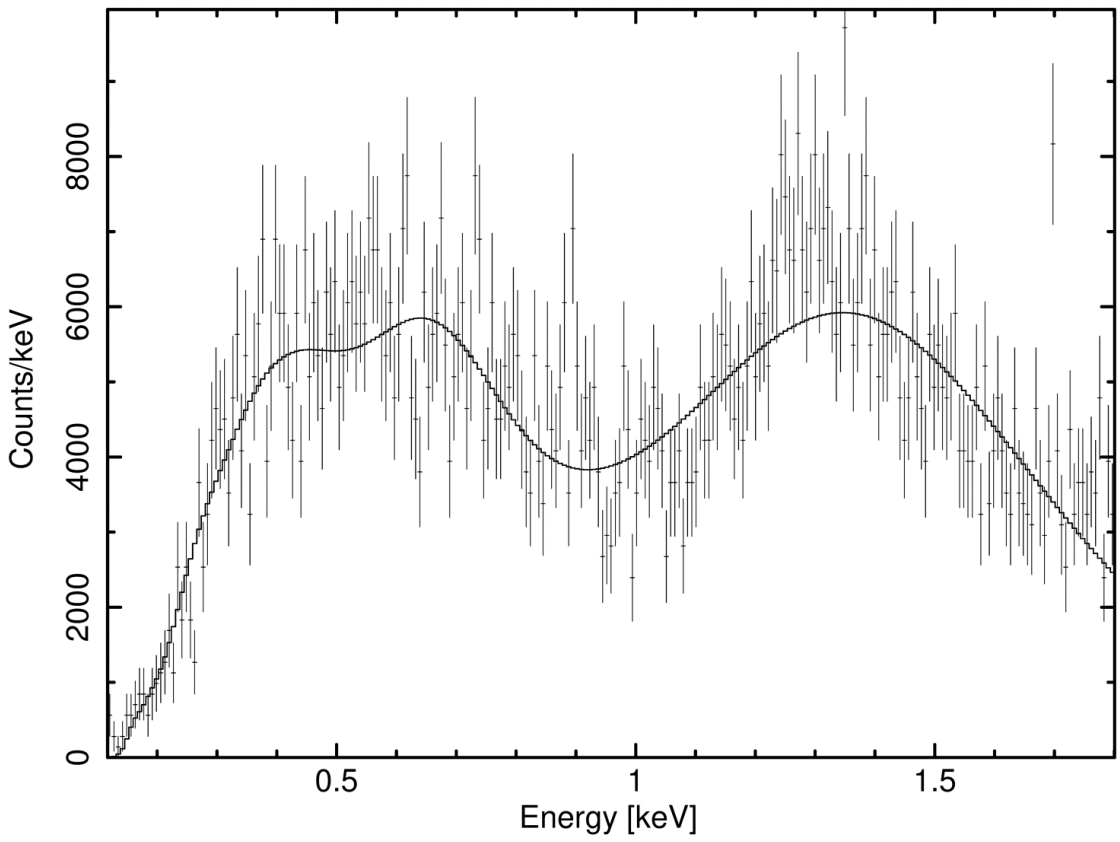

Figure 3.19: OGRESS' PHD spectrum (crosses) fitted with an absorbed two-component NEI model (solid line). The assumed spectral resolution of the instrument has now been reduced to match the width of the high-energy bump. New best-fit spectral parameters have been used (see Table 3.4).

component of the model requires a very high ionization age ($n_e t$), essentially resulting in CIE. In a realistic supernova, the low-temperature component will be associated with the outward-propagating shock wave which will still be underionized. Thus, we expect a substantially lower ionization age to be associated with the low-temperature component. The best-fit parameters are also highly inconsistent with measurements of Cygnus made with previous instruments (see Table 1.1).

It seems that the PHD spectrum cannot be adequately modeled with a realistic SNR spectrum. Before giving up, it is worth considering another possibility. The lack of prominent window bar shadows suggests that the signal seen by OGRESS is not coming directly down the optical

Table 3.4: Best-fit PHD parameters with improved resolution

$\Delta\chi^2$	323/208	
n_H (cm^{-2})	0.0432	
	Low-T Component	High-T Component
kT (keV)	0.0846	7.594
H	1	1
He	1	1
C	0.00	0.00
N	0.55	0.00
O	0.25	380.3
Ne	0.00	0.00
Mg	0.12	383.9
Si	0.00	0.00
S	0.00	0.00
Ar	0.00	0.00
Ca	5.01	0.00
Fe	19.4	0.00
Ni	0.00	1000.0
$n_e t$ (cm^{-3}s)	4.19e+13	2.07e+11
norm	4.34	1.66

chain (focusers, gratings, GEMs) as expected. Diffuse light coming from many different angles could suppress the window bar shadows. This behavior has not been seen in the laboratory, but that may simply be because OGRESS has only been tested with point sources. In the presence of a diffuse source such as Cygnus, it is possible that most of the signal scatters into the spectrograph from wide angles rather than traveling straight down the focusers. This is an unlikely scenario, but we will investigate it nonetheless.

If most light enters the payload without hitting the gratings (via scattering or unanticipated angles), then the effective area of the instrument will no longer be affected by the gratings or the geometric area of the detectors (as geometric area depends on wavelength). We will now model the PHD spectrum assuming the gratings and geometric area are not important. This may provide us with a good fit to a realistic model. Although we are ignoring the gratings, light hitting the detector from wide angles would probably require at least one reflection which we are not taking into account. Thus, the uncertainty associated with these fits will be high.

Figure 3.20 shows the fit to the data assuming the gratings and geometric area do not affect

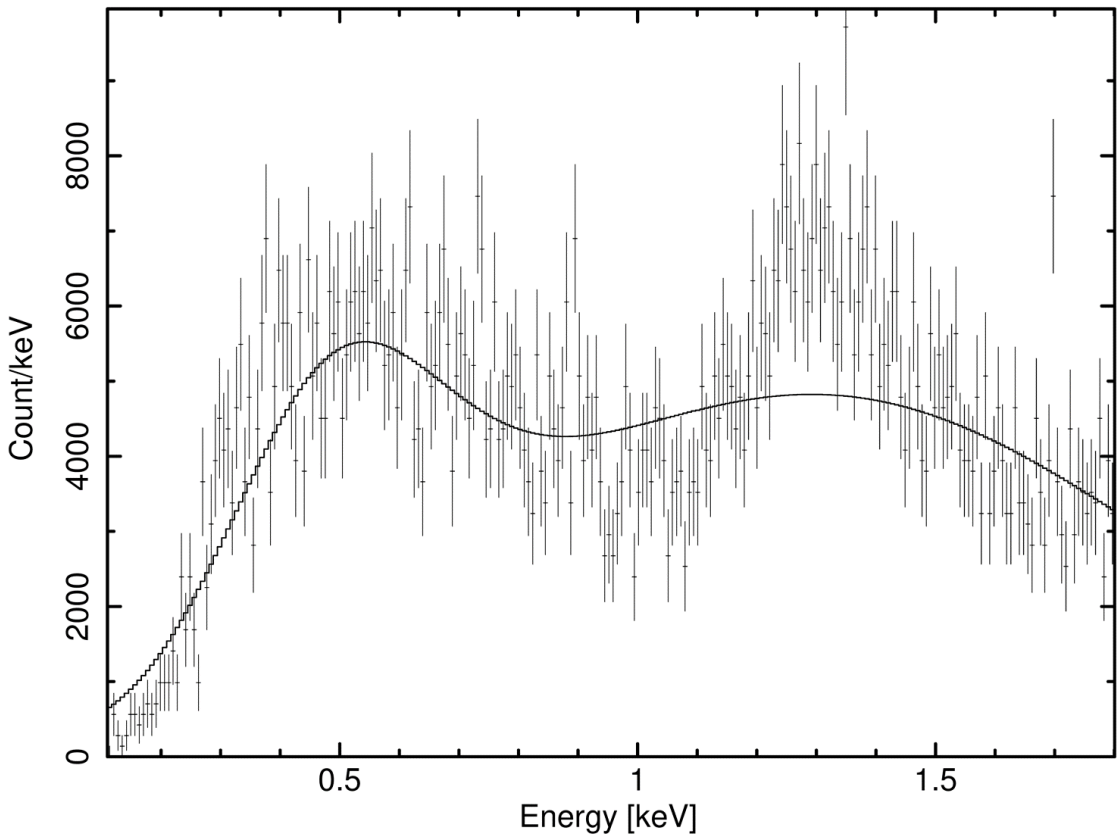

Figure 3.20: OGRESS' PHD spectrum (crosses) fitted with an absorbed two-component NEI model (solid line). The fit assumes that the light has not been affected by the gratings. The instrumental FWHM energy resolution is assumed to be 100%. Once again, the high-energy bump is not resolvable.

the instrument's response and a FWHM resolution of 100%. Table 3.5 shows the best-fit parameters. For this fit, $\Delta\chi^2 = 494/209$. Although better than Table 3.3, the fit is still unacceptable, being $\sim 14\sigma$ away from the ideal value. Once again, it is clear than the high-energy bump cannot be fit with this resolution.

As before, we can try using a FWHM resolution of 45%. This fit is shown in Figure 3.21. Table 3.6 displays the best-fit parameters. $\Delta\chi^2$ is now 411/209, 9.3σ from the idea value. This is one of the better fits we have produced, but it is significantly worse than the fit that takes the gratings into account (Table 3.4). It appears that removing the effect of the gratings and detector geometric

Table 3.5: Best-fit PHD parameters, no gratings

$\Delta\chi^2$	494/209	
$n_H(\mathrm{cm}^{-2})$	0.164	
	Low-T Component	High-T Component
kT (keV)	0.0808	0.417
H	1	1
He	1	1
C	0.00	0.00
N	0.00	13.64
O	0.00	0.00
Ne	0.00	0.00
Mg	0.00	69.25
Si	0.00	0.00
S	0.00	0.00
Ar	0.00	8.64
Ca	0.00	10.70
Fe	0.00	0.00
Ni	0.00	0.00
$n_e t$ ($\mathrm{cm}^{-3}\mathrm{s}$)	3.31e+13	1.63e+11
norm	2.19e-4	16.70

Table 3.6: Best-fit PHD parameters with improved resolution, no gratings

$\Delta\chi^2$	411/209	
n_H (cm^{-2})	0.0690	
	Low-T Component	High-T Component
kT (keV)	0.441	10.383
H	1	1
He	1	1
C	0.00	0.00
N	0.22	0.01
O	0.00	6.76
Ne	0.00	0.00
Mg	57.50	0.00
Si	0.00	0.00
S	0.00	0.00
Ar	0.00	0.00
Ca	2.59	0.00
Fe	0.00	0.00
Ni	0.00	0.00
$n_e t$ ($\mathrm{cm}^{-3}\mathrm{s}$)	3.33e+13	3.31e+13
norm	7.30	31.42

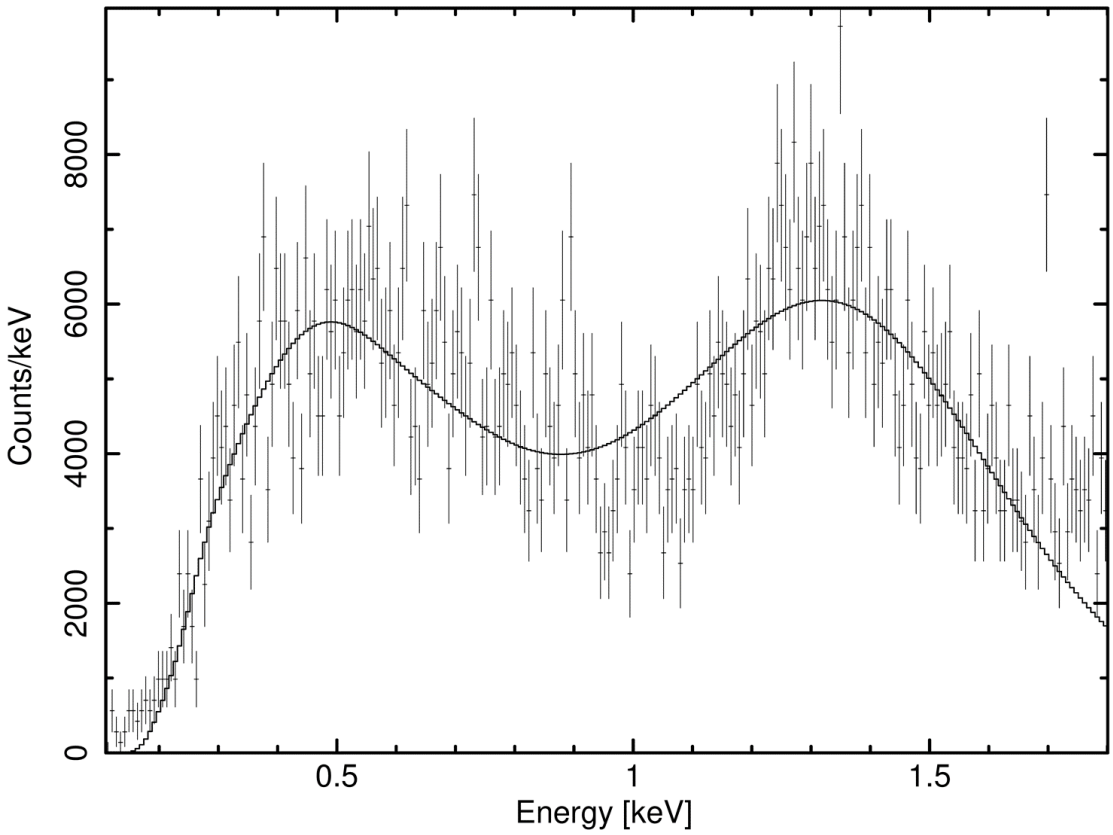

Figure 3.21: OGRESS' PHD spectrum (crosses) fitted with an absorbed two-component NEI model (solid line). The fit assumes that the light has not been affected by the gratings. The instrumental FWHM energy resolution is assumed to be 45%. A good fit is now achieved, but only with unrealistic parameters.

area has a mildly negative effect on our fits. Yet again, we find that the best-fit parameters are not easily believable. The high-temperature component is much hotter than expected, abundances tend to be either very high or very low, the ionization age is very high, and the parameters are not consistent with previous observations.

Neither the dispersion spectrum nor the PHD spectrum can be accurately fit using a realistic model for Cygnus. Combined with the elevated count rate, we have strong evidence that OGRESS experienced the same source of noise as CyXESS, EXOS, and CODEX, which effectively wiped out the signal from Cygnus.

3.2 Background Noise

Although we have not produced a usable spectrum of Cygnus, there is still more work to be done. If this payload is to fly again, the flight noise must be fully understood and removed in order to achieve a usable spectrum. If the noise can be successfully understood and removed, it may also generate a useful new tool (or warning) for the suborbital community.

3.2.1 Window Bar Shadows

We will begin our investigation of the flight noise by searching for evidence of window bar shadows in the flight data. In laboratory conditions, OGRESS always sees very distinct window bar shadows which block areas of the detector faces in a 4 x 4 pattern (see Fig. 3.6). Figure 3.22 shows X and Y profiles of the images from Figure 3.6. The shadows have been fit with gaussian curves to find the FWHM of each shadow. Figure 3.23 shows the X and Y profiles for the flight data. The expected locations of the window bar shadows (as determined by Figure 3.22) are marked. The shadows seen so distinctly in Figure 3.22 are not obviously apparent in Figure 3.23. Figure 3.24 shows the flight profiles once again but with wider bins to smooth out the signal. Again, the window bar shadows are not apparent.

It is important to remember that the positions of the window bar shadows depends strongly on the direction of incoming light. Figure 3.25 demonstrates the effect of illuminating a detector with two Fe-55 X-ray sources. The sources shine light from different angles, leading to two sets of window bar shadows. If the detector is illuminated by a truly diffuse source, the window bars will smear out according to the range of angles of incident light, becoming wider and shallower in the process. If the shadows begin to overlap, they may become indistinguishable. The window bar shadows are an important feature of the data, because they can provide evidence for whether or not the flight signal originates outside the detectors. If it does, then we may expect to find evidence of smeared window bar shadows.

We can test the hypothesis that the window shadows have been spread out by fitting the

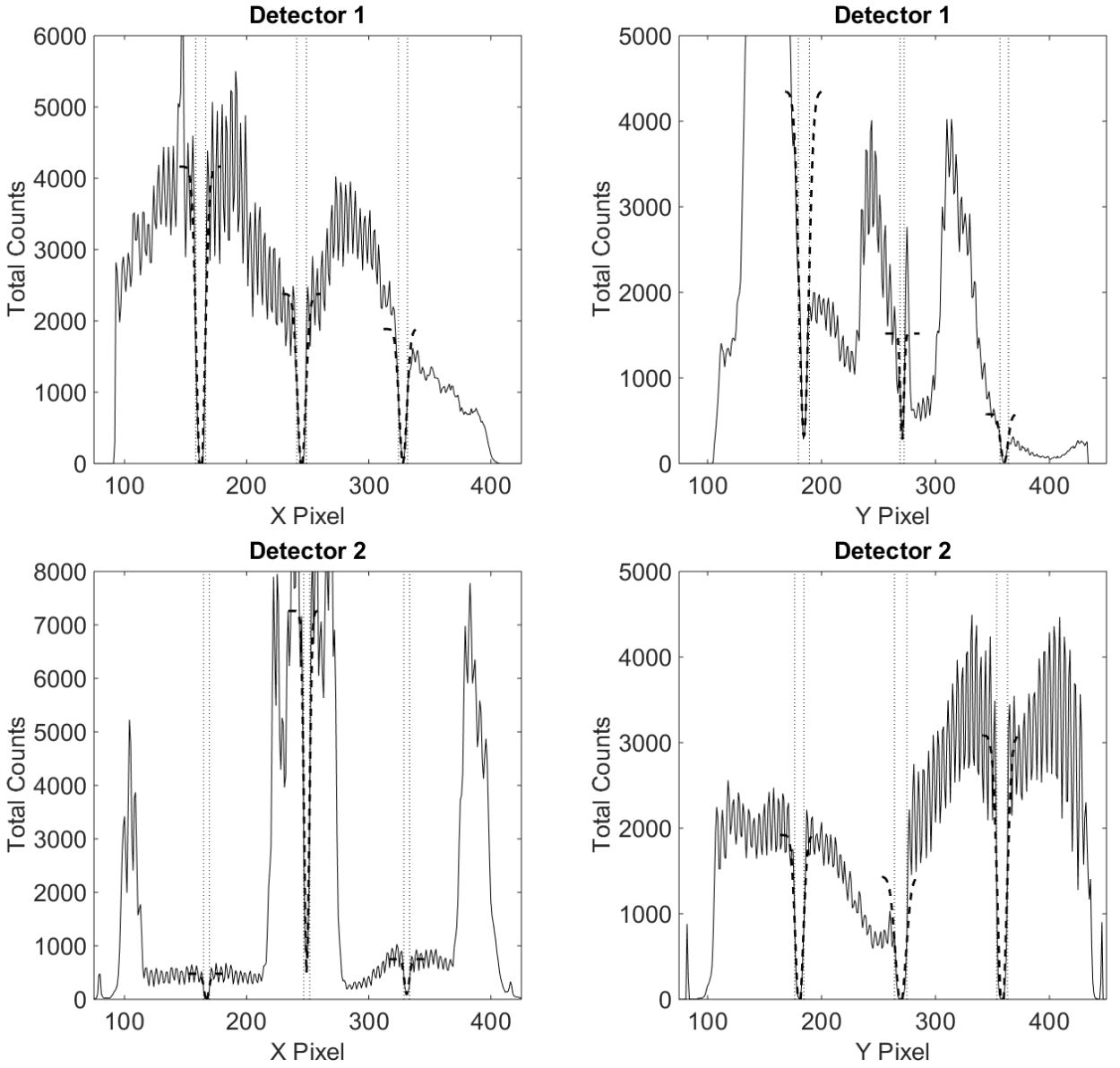

Figure 3.22: Histogram profiles in the X and Y directions for both detectors using the images from Figure 3.6. The dashed lines represent gaussian fits to the shadows. The dotted lines show the boundaries of the FWHM of each shadow. The shadows are deep, narrow, and very distinct.

flight data with a model for shadows of varying width and depth. The model has the form

$$M_{window}(x) = S(x) - \Sigma_i G(\mu_i, \sigma_{shadow}) \tag{3.1}$$

where $S(x)$ is a linear equation representing the average counts per bin at each location and $G(\mu_i, \sigma_{shadow})$ are negative Gaussian curves centered at the expected window bar locations. This

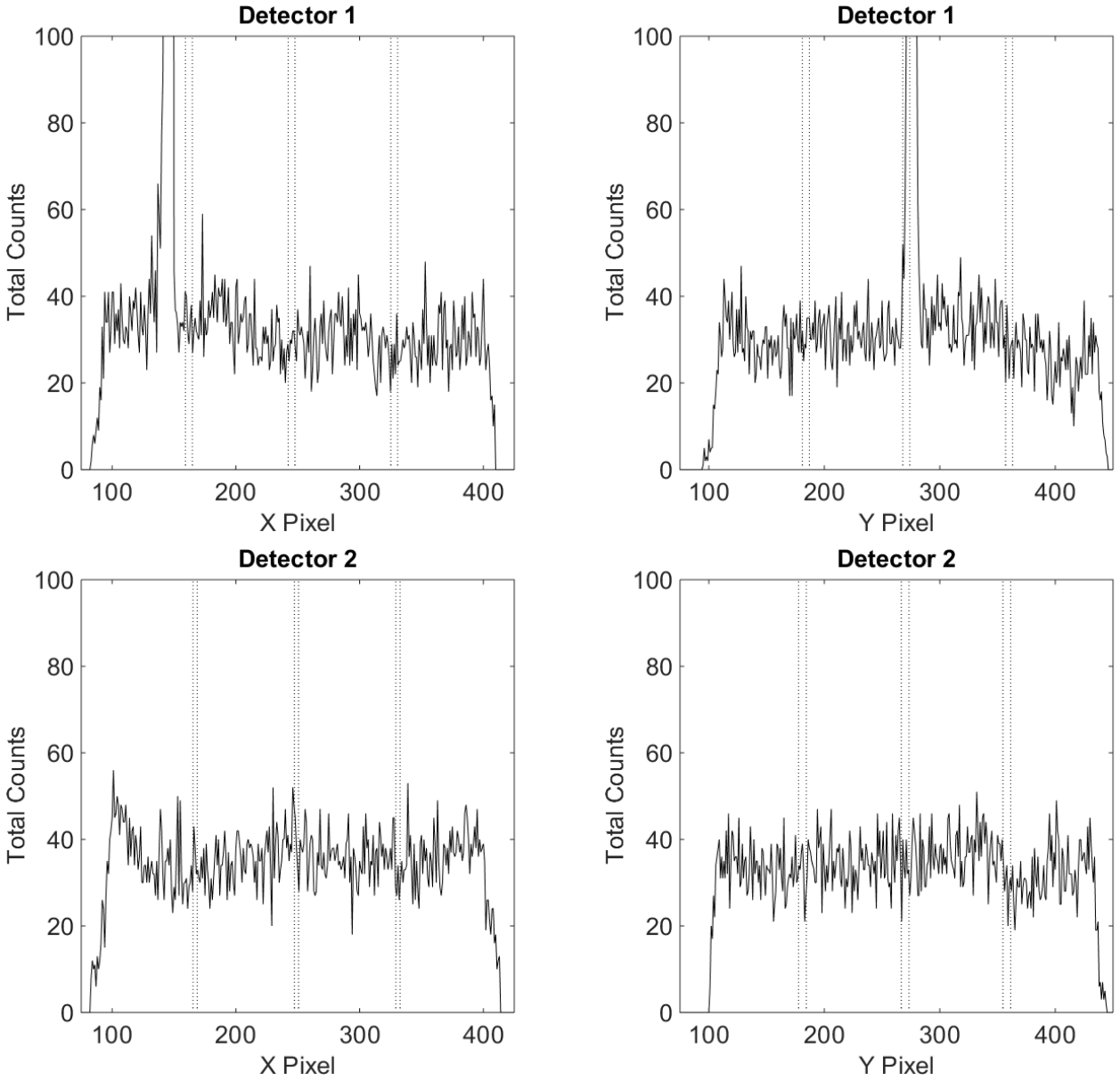

Figure 3.23: Histogram profiles in the X and Y directions for both detectors using the raw flight data (Fig. 3.2). The dotted lines show the expected locations of the window bar shadows. The spike on detector 1 shows the location of the persistent hotspot. Window bar shadows are not apparent.

corresponds to being illuminated by a single diffuse source which is Gaussian-shaped. We will assume that each shadow is equally wide. As σ_{shadow} widens, the Gaussians will naturally become shorter.

We will begin by fitting each profile with a straight line ($y = m \times x + b$) across the active area.

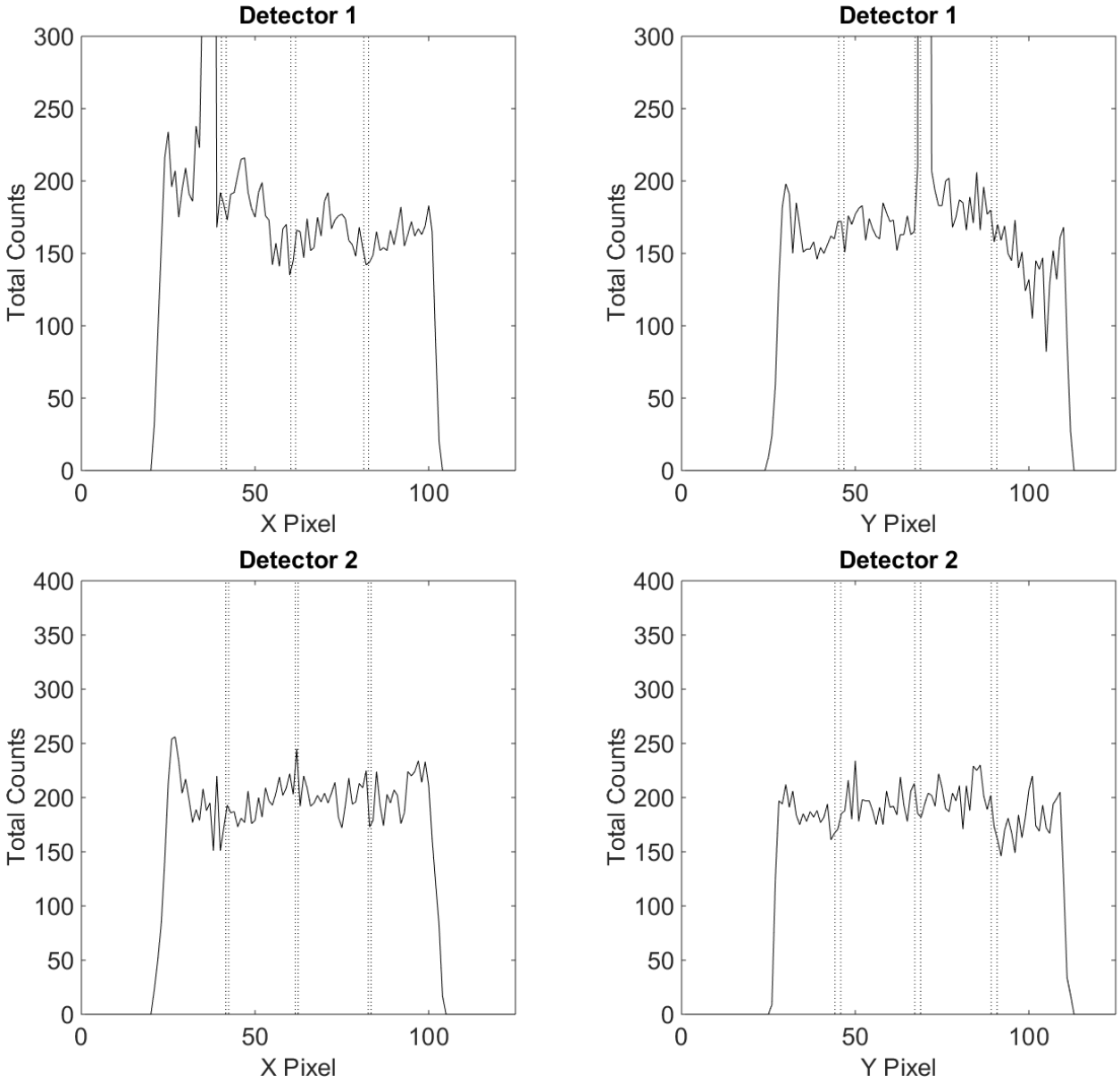

Figure 3.24: Histogram profiles in the X and Y directions for both detectors using the raw flight data (Fig. 3.2). The dotted lines show the expected locations of the window bar shadows. The spike on detector 1 shows the location of the persistent hotspot. Window bar shadows are not apparent.

This will give us a baseline goodness of fit which our model for window shadows (M_{window}) must improve upon to be taken seriously. We will use these fits to determine $S(x)$ for the X and Y profiles for each detector. The best-fit values for the slope (m) and y-intercept (b) are shown in Table 3.7. For these fits, the areas of the profiles which have been affected by the hotspot are ignored. The Y

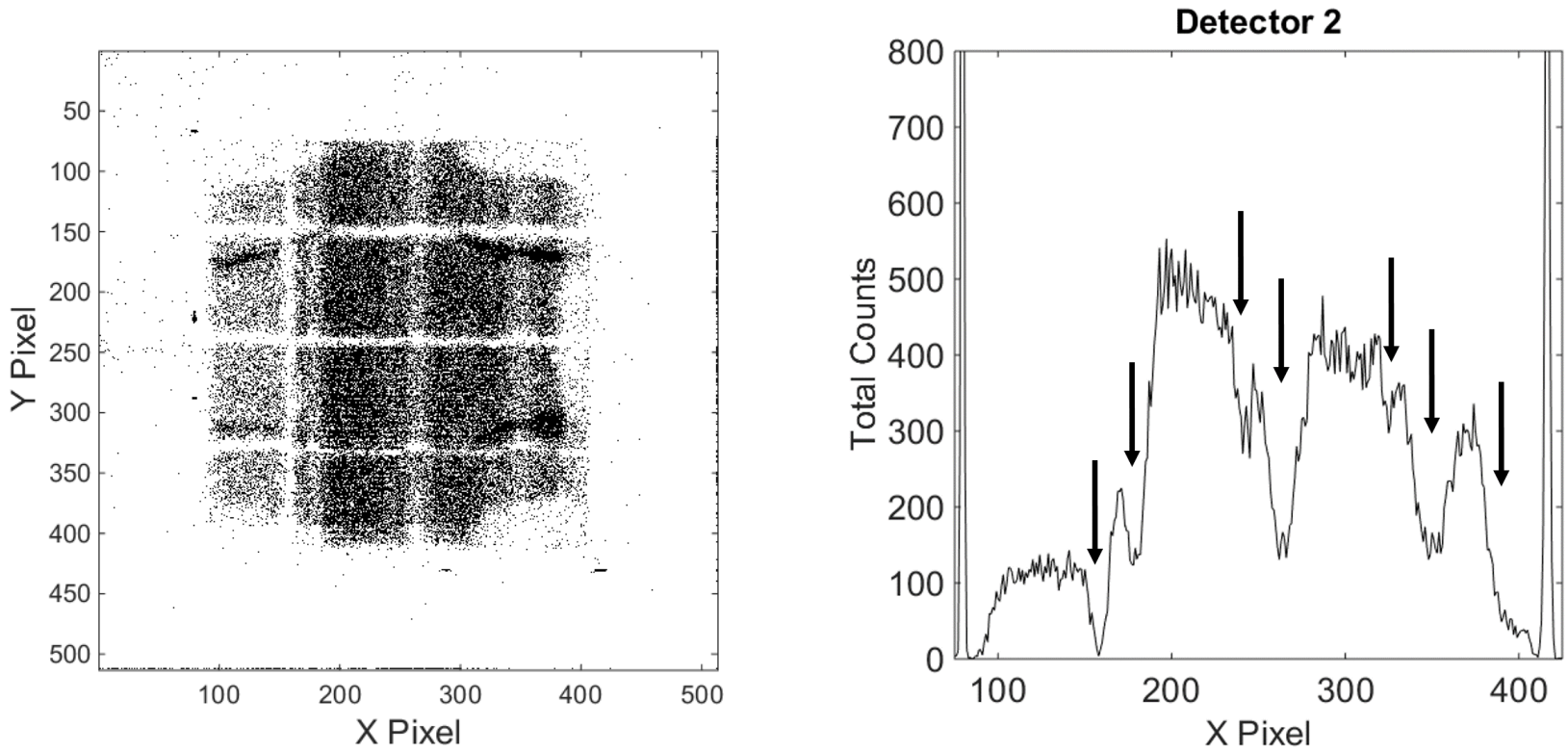

Figure 3.25: *Left*: An image taken using two Fe-55 X-ray sources. Ghosting effects are seen in the corners due to the very high pulse heights associated with Fe-55 signal. *Right*: The X profile of the image. When two sources are used, their light hits the detector from different angles and generates two sets of window bar shadows. The arrows note the locations of each shadow.

Table 3.7: Best Linear Fits

	Det 1 X Profile	Det 1 Y Profile	Det 2 X Profile	Det 2 Y Profile
$\Delta\chi^2$	337.3/290 (1.163)	496.4/308 (1.612)	369.1/297 (1.243)	315.4/325 (0.9704)
m	-0.02689	-0.01665	0.007056	-0.002022
b	49.75	45.7	48.37	48.18

profile for detector 2 is within 1σ of an ideal fit. For the other profiles, the distribution of counts varies more substantially and the fits are more marginal (though still quite good).

Now that we have simple line fits to each profile, we can add Gaussian window bar shadows to our model. The model follows the form of Eqn. (3.1) and is normalized such that the area under the curve equals that of the linear fit. The best-fit parameters for the shadow model are displayed in Table 3.8. The table displays the expected window shadow width, based on laboratory

Table 3.8: Fits to Window Bar Shadows

	Det 1 X Profile	Det 1 Y Profile	Det 2 X Profile	Det 2 Y Profile
1-σ Bar Width	2.34	2.566	1.436	2.843
$\Delta\chi^2$				
Width Factor 1	3661/291(12.582)	1981/309(6.411)	4788/298(16.068)	3397/326(10.421)
Width Factor 2	567.2/291(1.949)	757.1/309(2.450)	701.5/298(2.354)	691.5/326(2.121)
Width Factor 4	353.2/291(1.214)	592.3/309(1.917)	462.4/298(1.552)	401.6/326(1.232)
Width Factor 6	321.8/291(1.106)	530.4/309(1.717)	410.3/298(1.377)	329.3/326(1.010)
Width Factor 8	324.1/291(1.114)	505.1/309(1.635)	389.4/298(1.307)	314.7/326(0.9653)

measurements with a point source, as well as $\Delta\chi^2$ values for window bar shadows with widths that have been increased from this value by factors of 1, 2, 4, 6, and 8. The fits to the X and Y profiles are plotted in Figures 3.26 and 3.27. The modeled window bar shadows do not produce a substantially better fit, in most cases. Detector 1's X profile has the strongest evidence for shadows. When using shadows 6 times wider than those found with a point source (width factor 6), the shadowing model improves the fit (relative to the straight line) by $\sim 1\sigma$. The Y profile for detector 2 makes a very marginal improvement to the linear fit when the window bars are very wide. The other 2 profiles never produce better fits. Instead, they asymptotically approach the quality (and appearance) of the linear fit as the window bars approach infinite width.

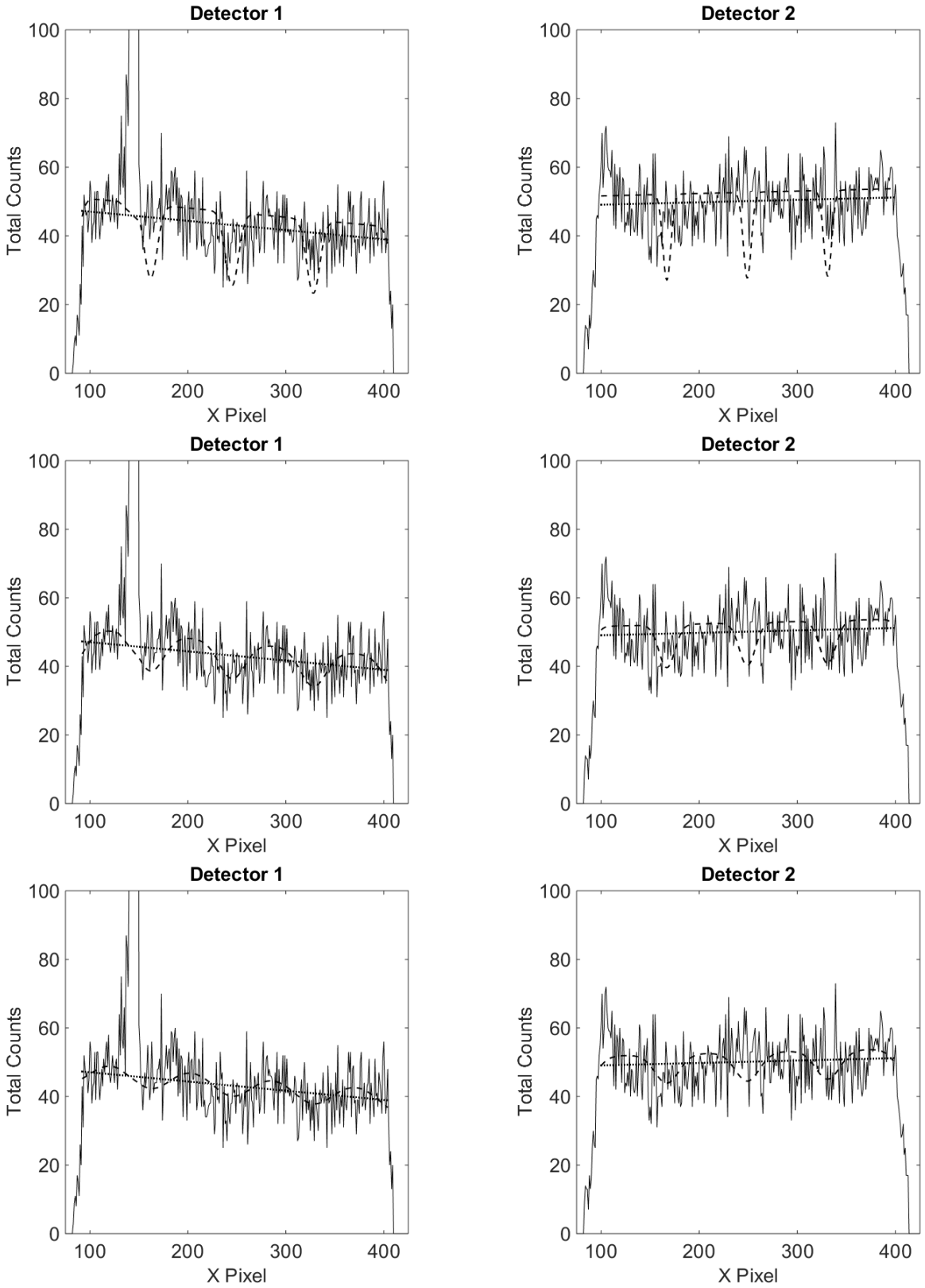

Figure 3.26: X profiles for the raw flight data (Fig. 3.2). The dotted lines trace the best linear fit to the data. From top to bottom, the dashed lines show modeled shadows that have been spread to 2, 4, and 6 times their expected widths.

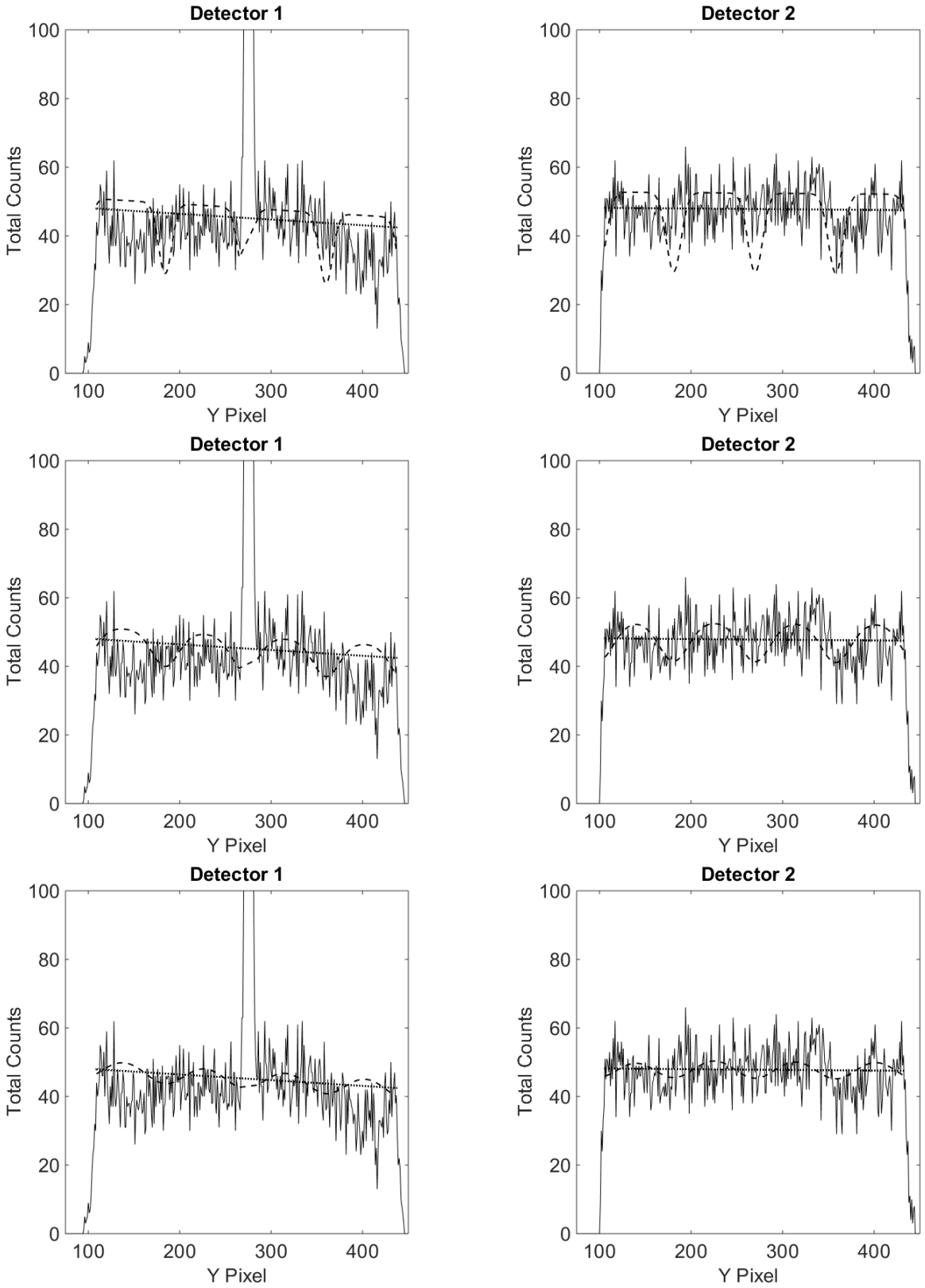

Figure 3.27: Y Profiles for the raw flight data (Fig. 3.2). The dotted lines trace the best linear fit to the data. From top to bottom, the dashed lines show modeled shadows that have been spread to 2, 4, and 6 times their expected widths.

The large variance of counts per bin leads to fairly good fits for both the straight line and window bar shadows. It seems clear by eye, however, that there are distinct systematic variations in count rate across each profile. This is an interesting effect, especially considering the smoothness of the flight gain map. The variations in counts per bin do not appear to be due to gain variation, so shadowing seems to be a plausible explanation. Figure 3.25 demonstrates that shadows can change their position in addition to their width. Thus, if the detectors are illuminated with a diffuse source that has spatial variations in brightness or that is simply not centered along the standard optical chain, the positions of the window bar shadows may change in addition to their width. Sources of signal which are close to the detectors will make the shadow positions spread out toward the edges. This might explain the dips in count which are apparent near the edges of the Y profiles for each detector (particularly detector 1). We will now expand our model to allow the shadows to change location as well as to widen.

Thus far, we have not performed a true chi-squared minimization. Rather, we have merely calculated chi-squared at a number of different parameter values and noted the trends. Because we are now dealing with line width and three centroid locations, varying parameters by hand would be overly tedious, and we will perform a true chi-squared minimization to find the best-fit parameters. Once again, the model will follow Equation (3.1), but the locations of the negative Gaussians will no longer be fixed. As before, the widths of each shadow (for each profile) are assumed to equal one another and are allowed to jointly vary.

Table 3.9 displays the best-fit parameters for each profile (X and Y for each detector). Figure

Table 3.9: Best-Fits for Window Bar Shadows.

	Det 1 X Profile	Det 1 Y Profile	Det 2 X Profile	Det 2 Y Profile
$\Delta\chi^2$	306/285 (1.076)	330/303 (1.090)	265/292 (0.909)	311/320 (0.972)
m	-0.0261	-0.0225	0.262	-0.00473
b	40.3	40.2	494.7	36.3
1-σ Bar Width	24.3	25.9	126.1	14.0
Centroid 1	124.5	147.8	96.5	160.0
Centroid 2	239.4	225.8	342.7	221.5
Centroid 3	329.4	406.1	569.3	373.0

3.28 displays each profile plotted along with their best-fit models. The expected locations of the

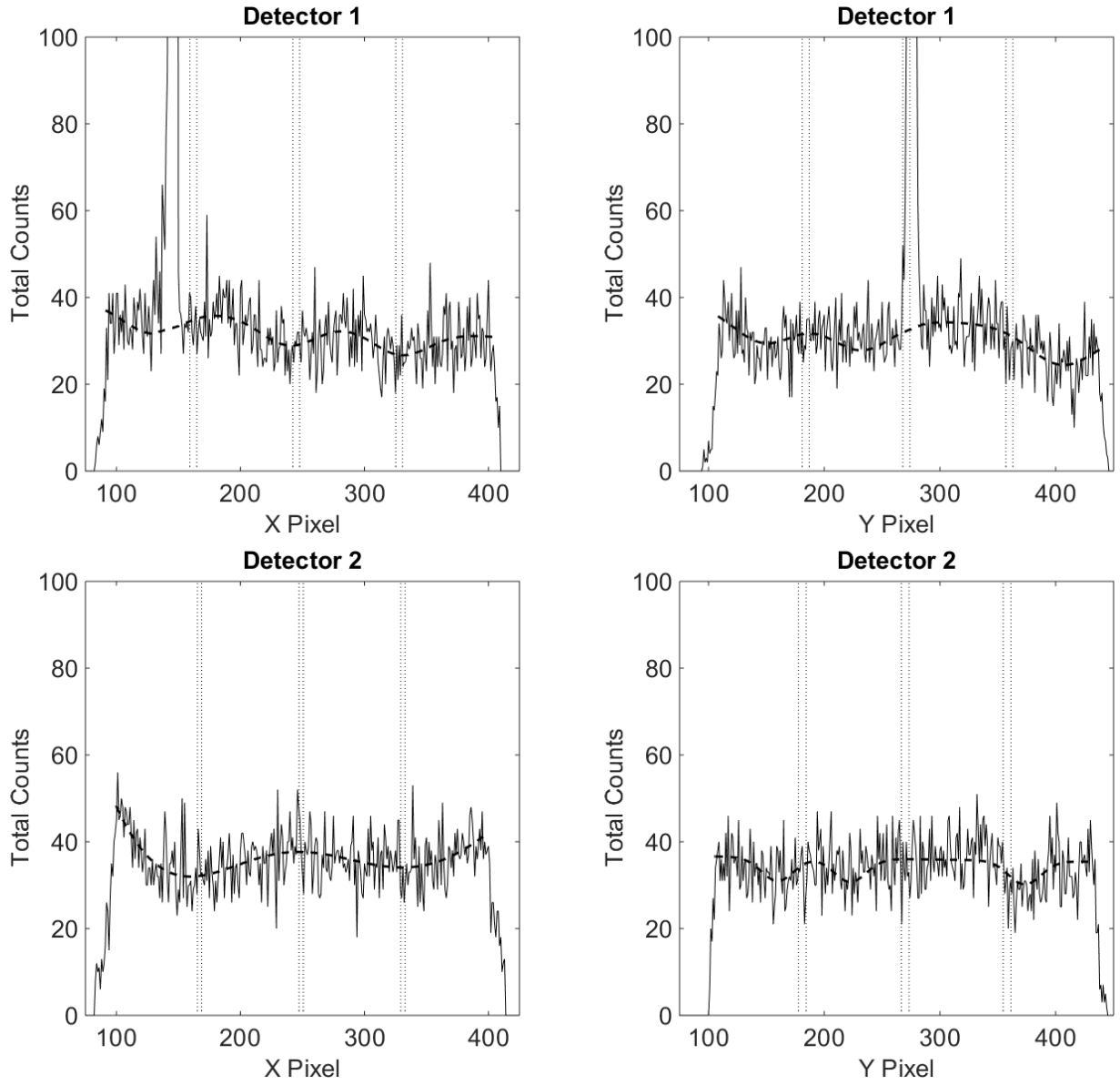

Figure 3.28: X and Y profiles for the flight data. The dashed lines represent the best-fit models listed in Table 3.9. The expected locations of the window bars, based on Figure 3.22, are shown with the dotted lines.

window bar shadows (based on Fig. 3.22) are also marked. All of the best-fits are very good. Detector 1's fits are within 0.88σ (X profile) and 1.10σ (Y profile) of their ideal values. Detector 2's fits both achieve $\Delta\chi^2 < 1$, suggesting that our uncertainties may be overestimated.

Once again, the most pleasing fit (though not the lowest chi-square value) is achieved by

the X profile for detector 1. The three shadows are evenly spaced and appear very close to their expected locations. The Y profile for detector 1 is also somewhat compelling. The shadows are not evenly spaced, but this may be due, in part, to the presence of the persistent hotspot which falls directly over an expected window bar shadow. This may also occur if the main source of signal is close to the detector. The width of the shadows for detector 1's Y profile match very well with its X profile, indicating that the shadows are formed from the same source of diffuse signal.

The fits to detector 2 are less convincing (despite having lower chi-square values), though still somewhat suggestive. Detector 2's Y profile shadows are noticeably narrower than any of the others. They do, however, fall in roughly the same places as those of detector 1's Y profile. This is not necessarily noteworthy, as the detectors have different orientations on the detector bulkhead, but it may reflect some directionality of the flight signal.

At first glance, the most displeasing fit (though not the highest chi-square value) occurs for the X profile of detector 2. This profile has been fit with only 2 Gaussians, the third being shifted far enough away that it has no effect on the shape of the best-fit curve. The two Gaussian components that remain are much wider than those of detector 1, raising suspicion as to whether or not they are real shadows. On the other hand, they lie very close to the expected locations of window bar shadows. Additionally, the missing window bar which we expect to see in the middle of the profile is where we also expect to see 0-order light from our dispersion spectrum. It is possible that we are seeing signal from Cygnus which is mostly buried underneath a much stronger contaminating diffuse signal. Figures 3.6 and 3.22 (lower left plot) show how 0-order light and the central window bar shadow are expected to overlap and how this affects the X profile. In Figure 3.22, the window bar shadows are very narrow and distinct due to the high count rate and the point-source which is being observed. The 0-order line is slightly rotated relative to the window bar shadows and enhances the count rate in a fairly wide range between pixels ~ 225 and ~ 275. In the flight data, both the shadow and 0-order light are expected to be substantially reduced from the levels seen in Figure 3.22. The count rate from Cygnus will, of course, be much lower than the count rate from the electron-impact X-ray lamp. If a diffuse source is present, the window bar shadow will

be shallower and wider. Thus, we expect 0-order and the central window bar shadow to fall in approximately the same place, and their basic effect will be to counteract one another. This, of course, requires that the light blocked by the window bar roughly equals the light contained in the 0-order line. Based on our low count-rate estimate for Cygnus made in Section 2.4, we might doubt that 0-order would contain enough signal to fully cancel out the window bar shadow. There are an average of 37.5 counts per bin between pixels 225–275. Pixels 135–185 and 305–355 (around the two Gaussians) have a joint average of 34.1 counts per bin. Thus, we require $\sim$ 170 counts from 0-order ($\sim$3.4 counts in 50 bins) to generate the difference. This number is somewhat higher than the total number of X-rays expected from Cygnus. We must remember, however, that our count rate estimate for Cygnus was considered to be slightly low (see Section 2.4), and 0-order is expected to be the strongest feature. More importantly, the estimate did not include low-energy photons outside OGRESS' bandpass, all of which are expected to fall in the 0-order line. Thus, this level of signal is plausible.

An obvious counter-argument to this hypothesis can be made based on the fact that 0-order is not apparent in the dispersion spectrum. We note, however, that the window bar shadow will mask some of the 0-order signal (as well as any contaminating signal in the same region), in the same way that 0-order masks the presence of the window bar shadow. The fraction of 0-order light blocked by the window bar will be quite low (see Fig. 3.6). A similar fraction of any diffuse contaminating signal should also be blocked. Because the total flux from the diffuse signal is much higher than that of 0-order, a proportionally larger number of counts are removed. Thus, the lack of an apparent 0-order signal in the dispersion spectrum may simply be due to a bit of bad luck. If the counts blocked by the middle window bar (from Cygnus plus contamination) is roughly the same as the total counts gained in 0-order (from Cygnus only), then the window bar shadow and the 0-order signal may effectively cancel each other. Admittedly, this scenario requires rather fine-tuned conditions. As we have seen, however, the signal required in 0-order to generate this scenario is plausible. Combined with the locations of the left-side and right-side best-fit Gaussians (very close to the expected locations of shadows), this scenario seems believable, if not entirely certain.

Ultimately, our best-fit models hint rather strongly at the presence of window bar shadows in the flight data. This suggests that OGRESS' flight signal originates from outside the detectors. With this information in mind, we will now consider possible sources of noise during flight.

3.2.2 Electronic

First, the noise may be electronic. This theory is supported by the lack of obvious window bar shadows (comparable to Fig. 3.6) which are expected from signal coming outside the detector. CyXESS, EXOS and CODEX all suffered from electronic noise, and steps were taken to solve these issues for OGRESS. CyXESS had electronic noise resulting from a switch-mode power supply. EXOS and CODEX had difficulty distinguishing which detector each count fell upon, resulting in data bleeding between detectors. OGRESS utilized voltage-dividing power supplies and separate data chains for each detector until post-digitization. We are confident that both issues were solved, as they were readily observable in a laboratory setting for previous payloads. OGRESS has had no evidence of these previous issues during laboratory testing or flight.

The hypothesis of electronic noise has difficulties, since we have never seen this kind of noise in the laboratory. We have witnessed plenty of electronic noise but have never seen effects similar to those seen in flight. Under all circumstances, previously observed electronics noise has resulted in counts bleeding directly in the x-direction, y-direction, or both (45 degrees). A demonstration of this effect is shown by Detector 2's transient hotspot in Figure 3.2. We have also induced RF noise during integration by leaving the electronic section's metal cover removed. These tests were not carried out with an X-ray source, so we do not have solid data on the possible effects to signal in the active area. However, we were able to see the effect this had on the stims. Per usual, noise on the electronic lines resulted in the stims bleeding in x and y. At any rate, any electronics noise should affect the stims as well as counts within the active area. A comparison of laboratory calibration data and Detector 2's flight data, shown in Figure 3.6, show no difference in the stim signal, indicating that the electronics do not function differently between flight and the laboratory. Additionally, all instrument monitor signals were nominal throughout the entirety of the flight. This rules out any

low-frequency deviations from optimal electronic conditions, although high frequency noise would not necessarily have been visible.

A final point against electronic noise is that nearly all of the counts during flight fell within the active area of the detector, which represents the physical size of the anode. Real counts deposit charge on the anode, and the timing of the charge pulses is then restricted by the time it takes to traverse the anode. A certain number of counts will always be misanalysed and fall outside the active area. The proportion of misanalysed counts is not noticeably different between the flight data and the laboratory calibration data. Any unforeseen source of noise being generated within the electronics section has no reason to favor the active area. We must then conclude that the observed flight signal is most likely not electronic in nature.

3.2.3 Internal Detector Noise

It is possible that OGRESS' detectors experienced some sort of noise that was generated within the detectors themselves, rather than from within the electronics. This type of noise would be consistent with counts mostly falling within the active area of the detector but making no window bar shadows.

This hypothesis has similar difficulties to the electronic noise scenario. We have successfully (though unintentionally) generated internal detector noise many times in the laboratory but have never generated signal similar to the flight data. The most common type of internal detector noise is the signal generated by hotspots (see the raw flight data in Figure 3.2). Hotspots occur due to manufacturing defects, damage to, or contamination on the GEM foils and result in a constant minor discharge between foils at a specific point. These counts occur in distinct locations and often dominate the overall count rate of the detector. The counts produced almost always fall into very low PH channels. Thus, hotspots can be easily separated from other signal based on their location or their PHD. Although there are hotspots present in the flight data, the smooth signal across the detector faces is clearly not of this nature.

Internal detector noise of another type was witnessed during the flight of the CyXESS payload.

After experiencing coronal discharge during HV turnon, CyXESS's detectors developed a large oval-shaped feature which dominated the count rate and blotted out the signal in the central regions of each detector (see Fig. 3.29). This oval feature steadily decayed with time and eventually

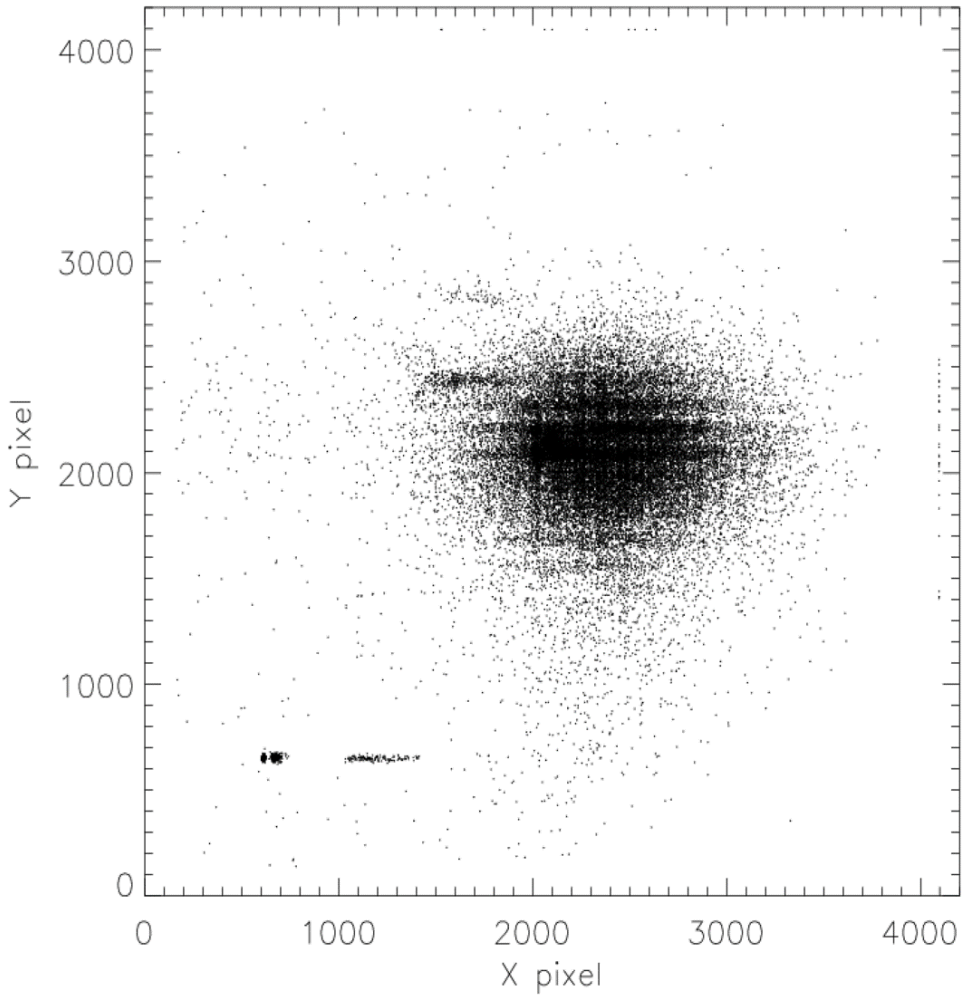

Figure 3.29: The oval hotspot witnessed during the flight of CyXESS. When the detector gas is fully ionized, a widely distributed background signal can occur during recombination.

disappeared, allowing spectral analysis of the final 65 seconds of flight data. The oval clearly showed the pattern of the fine window mesh but no window bar shadows. This spot was interpreted in the following way. Coronal discharge ionized the argon and dissociated the CO_2 inside the detectors. Ionized argon atoms then drifted toward the detector window, recombined on the window mesh,

and emitted photons which caused additional ionizations. As the gain increased over time (due to the nature of CyXESS's acid-etched GEM foils), the oval feature became visible. Eventually, the detector gas neutralized and was replenished by the gas system leading to the disappearance of the oval spot.

The signal seen by OGRESS is clearly not consistent with the interior detector noise witnessed by CyXESS. OGRESS did not experience significant discharges, so the detector gas would never have become substantially ionized. OGRESS' signal did not show window mesh features, filled the entire effective area, and remained very constant throughout the flight. Any sort of interior noise resulting from a discharge or large ionization event is expected to steadily decay as the detector gas neutralizes and to be generally more stochastic over time. Thus, OGRESS' signal does not appear to be caused by internal detector noise.

3.2.4 Scattered Light

Another possible source of noise is scattered light. Scattered light has posed severe problems for many payloads, particularly those observing in the ultraviolet. At sounding rocket altitudes, the atmosphere naturally produces UV signal, particularly Lyman-alpha, which can swamp the observed science signal without proper baffling. Scattered light would explain the lack of window bar shadows, as the light would come from multiple angles effectively washing out those features. OGRESS' detectors are not thought to be sensitive to UV light (based on the ionization energy of Argon), but this has not been thoroughly tested. Luckily, OGRESS' observing plan performed an in-flight test for the presence of scattered light by keeping the detectors turned on after closing the shutter door. The count rate during this time is shown in Figure 3.30, with times marked for shutter door close. The count rate, strangely, does not drop as would be expected in the presence of scattered light. This definitively demonstrates that scattered light is not the source of OGRESS' noise, but also produces a new set of problems which makes the noise difficult to explain. Any noise generated outside the payload should immediately vanish when the shutter door is closed. Electronic noise would normally be the natural explanation, but we have many reasons to think

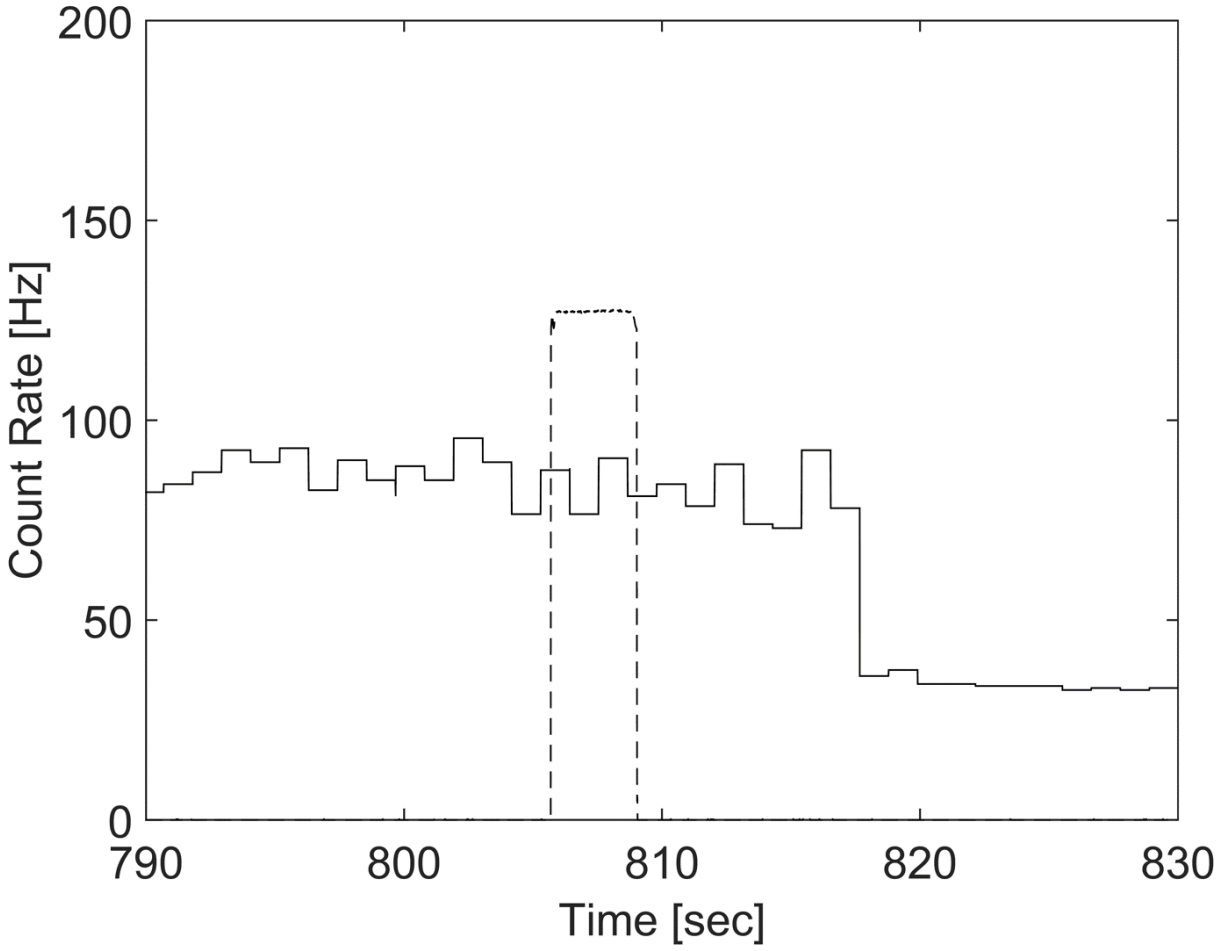

Figure 3.30: The solid line shows the average count rate between the two detectors. The dashed line shows a binary signal representing when the shutter door is activated. Prior to activation, the shutter door is open. During activation, the shutter door closes. After activation, the door is closed. The signal is unaffected by the closing of the shutter door and only ceases when the detectors are turned off.

that this has not occurred, as discussed in the previous section. There may, however, be other ways to generate noise internal to the payload.

3.2.5 Charged Particles

Originally, charged particles impacting the detector windows were thought to be the source of flight noise on previous instruments, and this may still be the case. The payload has ~ 30 seconds to

vent to space and fill with ambient ions between shutter door open and HV turn-on. These charged particles may stay inside the payload after the shutter door closes and continue to generate noise. This theory has been tested in a laboratory setting by observing the count rate when a powered ion gauge is suddenly turned off. On the ground, this immediately results in the signal vanishing, but this may simply not be an adequate representation of flight conditions. In a laboratory, the payload chassis is grounded, so any charged particles which impact it will neutralize. In flight, however, the chassis is ungrounded and the payload is likely to develop a net charge. According to Whipple [1981] this charge is likely to be negative. Figure 3.31 shows expected satellite potentials as a function of altitude of circular orbits for several different photoemission currents. The equilibration time to reach these potentials is measured in μs, so the true potential on the spacecraft should track the theoretical curves very closely, even when rapidly changing altitude. Because OGRESS launched at night, very low photoemission is expected. Regardless, photoemission is only important at altitudes above OGRESS' apogee of $\sim$ 250 km. Because electrons have a higher velocity than the heavy ions, the payload will experience a net current of electrons onto its surface. Thus, any positive particles inside the payload are still likely to neutralize when they hit the payload chassis. Also, the presence of the ion repeller grid makes it highly unlikely that positive ions will have the energy necessary to reach the windows, as discussed in section 2.6.4.

3.2.6 Internal X-Rays

An attractive possibility which seems consistent with the data is that X-rays are, in fact, being generated inside the payload. The two ingredients vital to this scenario are our high-voltage detector windows and the large number of thermal electrons available in the ionosphere. Electrons exposed to high voltage inside the payload can be accelerated into the interior walls and cause fluorescence radiation through electron-impact excitation of the payload interior. This is the same method often used to generate X-ray during laboratory testing. Figure 3.6, for instance, shows data acquired with an electron-impact X-ray lamp (also called a "Manson" source).

Internal fluorescence has actually been demonstrated inside a rocket payload. Seward et al.

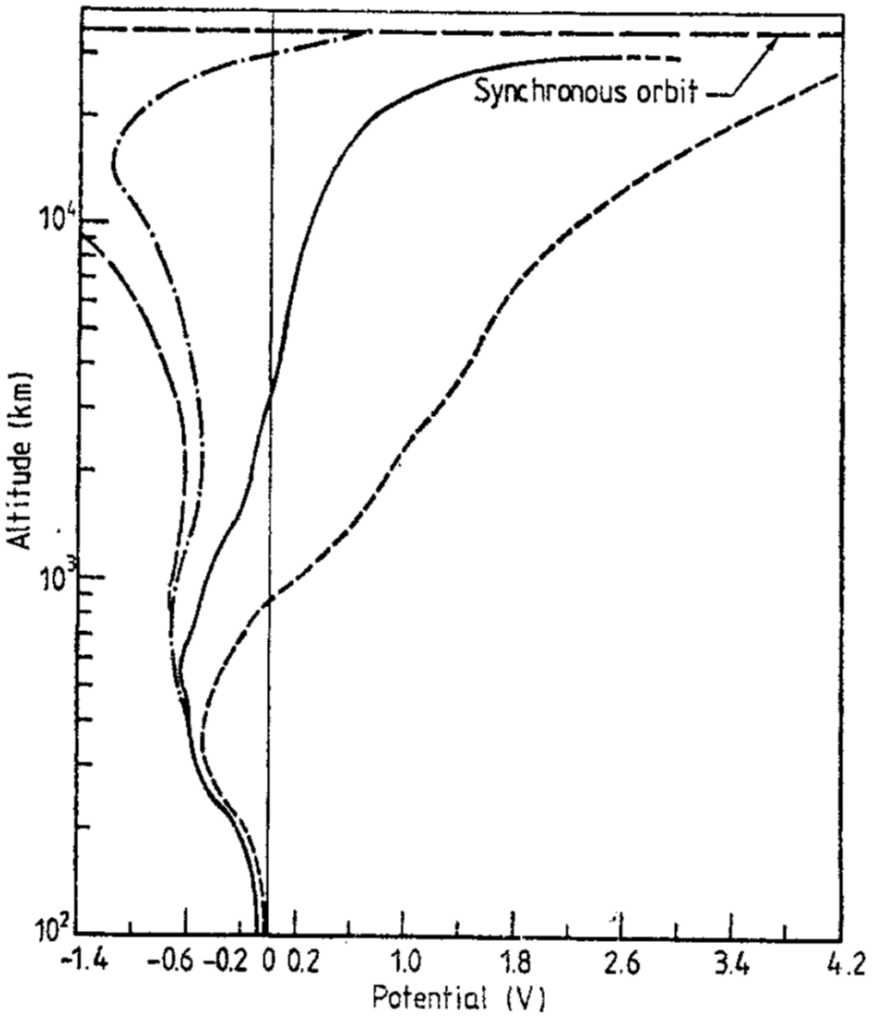

Figure 3.31: Satellite potentials as a function altitude of circular orbit for four values of photoemission current. The pertinent curve for OGRESS is the left-most curve of long dashes which represents no photoemission. The potential on the spacecraft chassis may have a large effect on contaminating signal from atmospheric ions and electrons. Image taken from Whipple [1981].

[1973a] demonstrated the use of an electrostatic sweeper to force high-energy electrons into the payload wall in an attempt to remove their contaminating signal. When switching from an applied voltage of 200 V to 700 V, they immediately witnessed a large increase in background count rate (see Figure 3.32). The increase in count rate can be explained by thermal ionospheric electrons gaining sufficient energy to cause fluorescence of the payload interior. At 700 eV, electrons have enough energy to excite C and O K-α lines. Inside OGRESS, electrons can be accelerated to as

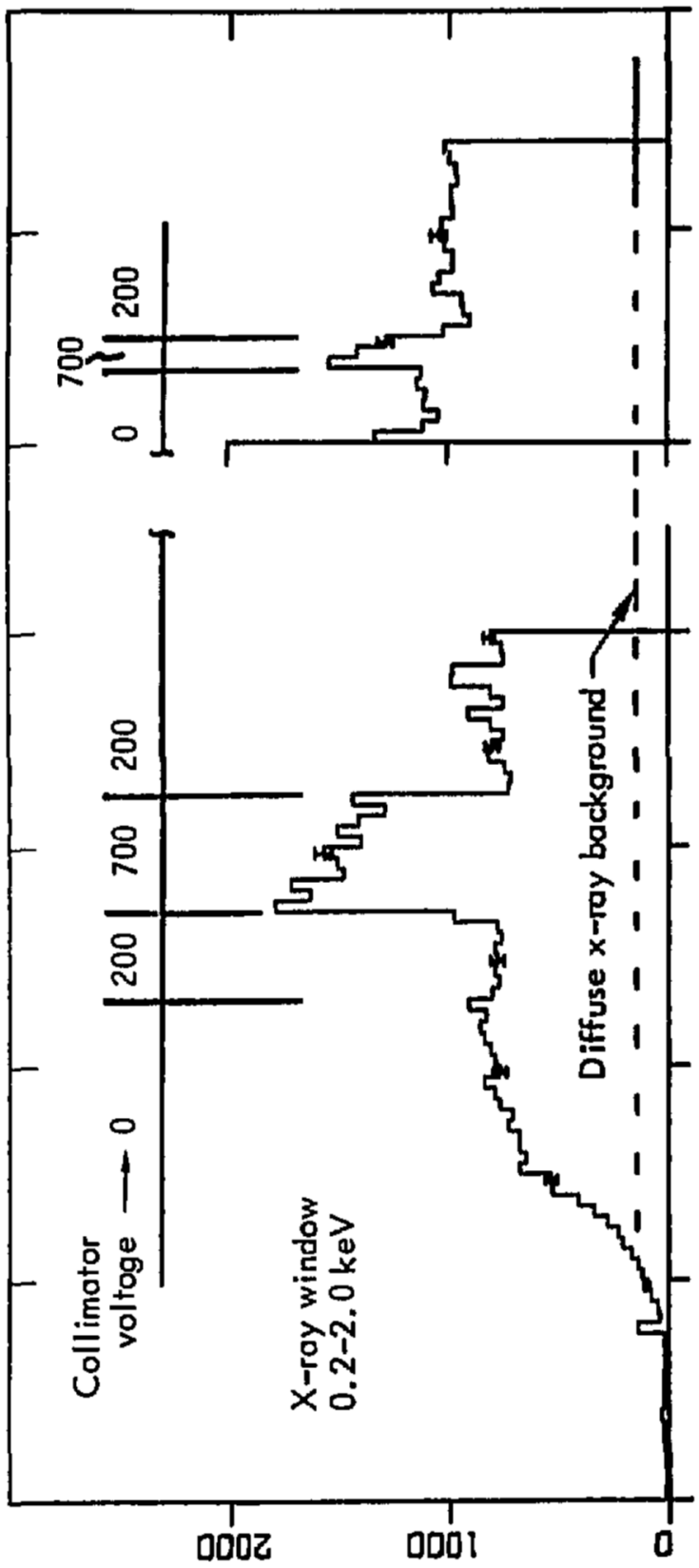

Figure 3.32: Count rate data collected from a sounding rocket in 1972 (Seward et al. [1973a]). When an exposed voltage of 700 V is applied inside the payload, the count rate increases substantially, indicating fluorescence of the payload interior.

much as 3600 eV by the detector windows.

An additional point in favor of internal fluorescence is that it relies on electrons, rather than positive ions, to produce the signal. Because the spacecraft will be negatively charged the thermal population of electrons inside the payload will not neutralize as easily as positive ions do. When the shutter door closed at $\sim$ 120 km, the payload would have had a negative potential of $\sim 0.1 - 0.2$ V. This is higher than the typical energy of the thermal electron population ($\sim$ 0.09 eV). This allows for the possibility of maintaining an internal electron population after the shutter door closed, as many/most of the electrons will not have enough kinetic energy to make contact with the payload walls. Electron-impact fluorescence may also cause collisional ionization of the payload walls, further maintaining the interior electron population after the shutter door closed. The ionization energy of electrons in the conduction band of chromium (the main component of the irridited surface) is $\leq$ 2.06 eV, so even lightly accelerated electrons can liberate new electrons – perhaps several at a time – from the payload walls. Thus, generation of internal X-rays seems to be a plausible – even likely – effect.

We present the following hypothesis to explain the flight signal:

1) During ascent and throughout flight, the payload acquires a negative potential which follows the long-dashed curve in Figure 3.31.

2) The shutter door opens, and the payload interior equilibrates with the ambient ionosphere. Thermal electrons diffuse into the payload interior and are supplied constantly until the shutter door closes.

3) Detectors and repeller grids turn on. Thermal electrons in the payload interior are now attracted toward the repeller grids. Electrons which pass through the grids are exposed to, and strongly repelled by, the high voltage detector window.

4) Repelled electrons will collide with either the repeller grid or the payload interior. This causes electron-impact excitation and fluorescence of the grids and payload interior. This emission dominates the observed signal, and Cygnus is lost in the noise.

5) The shutter door closes. Most of the electrons inside the payload are unable to contact the chassis due to its acquired negative potential, and the electron reservoir is maintained. Electron impacts result in ionization of the interior walls, further maintaining the electron reservoir. Electrons continue to be accelerated and fluorescence continues until the detectors turn off.

3.3 A search for Fluorescence Lines

We have already fit the flight spectra (dispersion and PHD) to SNR models and found that good fits require highly unrealistic conditions. Having hypothesized that the flight signal is generated from electron-impact excitation of the payload interior, we can fit the data to likely fluorescence lines. Because the signal is produced inside the payload, the gratings will have no effect on the signal, and we will once again rely on the PHD spectrum. For these fits, the geometric area of the instrument will not depend on wavelength.

The materials available to fluoresce in the payload interior are nickel (the repeller grid), chromium (the irridite layer), aluminum (the payload structure), oxygen (oxide layer on all surfaces), and possibly carbon. Carbon emission is always present when observing the electron-impact X-ray source, since a layer builds up on the anode due to the intense heat. As this level of heating has not occurred in the payload interior, the presence of carbon is less certain. C, O, and Al are likely to emit Kα radiation. The voltage of the detector windows (-3600 V) is insufficient to excite Cr- and Ni-Kα, but these elements can still have their L-shells excited and emit accordingly. Table 3.10 summarizes the emission components which we will fit to the flight PHD spectrum. We will

Table 3.10: Components of Interior Emission.

Emission Component	Energy (eV)
C-Kα	277
O-Kα	524.9
Al-Kα	1,486.7
Cr-Lα	572.8
Ni-Lα	851.5

carry out an analysis of the PHD spectrum in the same fashion as before. Table 3.11 shows the initial best-fit parameters. The values for energies and line widths are frozen and have been taken from (Haungs [1986]) and references therein. Thus, only the relative strengths of each line are allowed to change. The FWHM of the instrument is assumed to equal 100% of the line centroid, as before. Figure 3.33 compares the data to the best-fit model. For this initial fit, we see that carbon and chromium emission have been set to zero. This is sensible for carbon, as we do not expect

Table 3.11: Best-fit Fluorescence Parameters.

$\Delta\chi^2 = 1126/233$			
Emission Component	Energy (eV)	Line Width (eV)	norm
C-Kα	277	7.8	0.00
O-Kα	524.9	6.0	20.20
Al-Kα	1,486.7	0.43	22.78
Cr-Lα	572.8	4.0	0.00
Ni-Lα	851.5	2.7	4.60

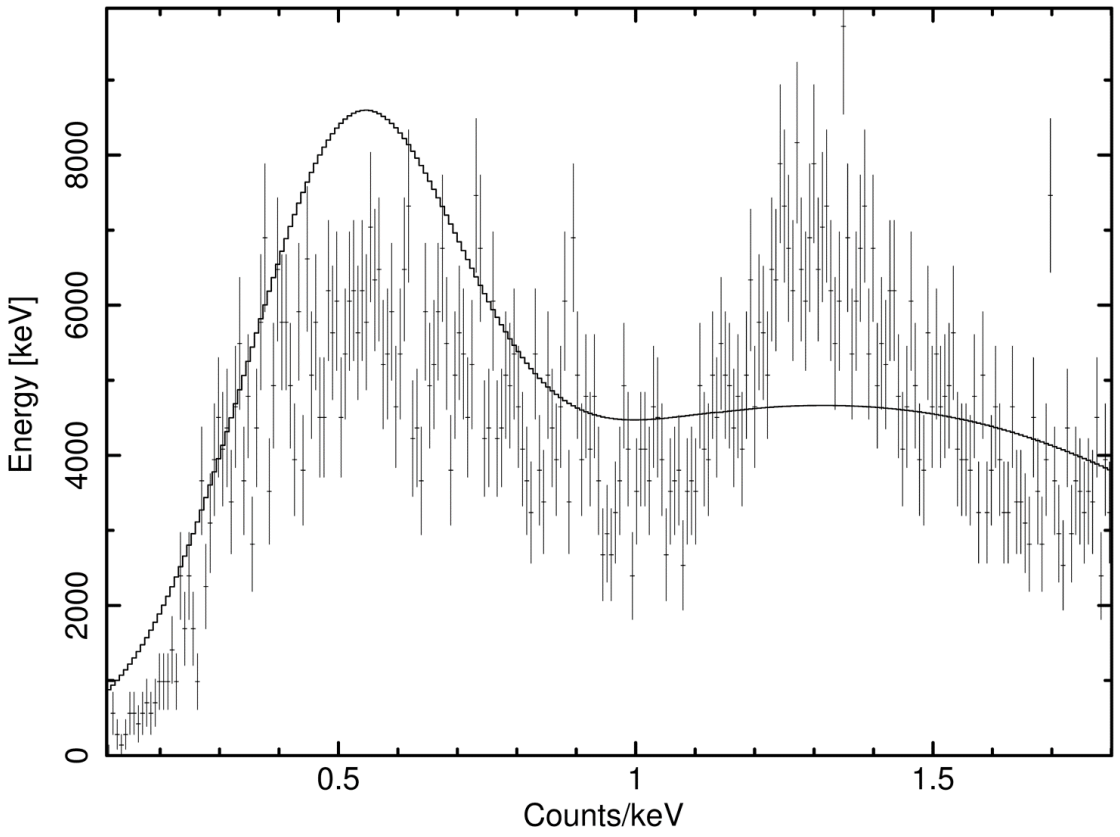

Figure 3.33: OGRESS' PHD spectrum (crosses) fitted with 5 fluorescence lines. The instrumental FWHM energy resolution is assumed to be 100%.

to have a significant coating in the payload interior (the opposite is true for the Manson source). The lack of chromium emission is somewhat suspect, as this is expected to exist in high amounts. The fit is not particularly good, with $\Delta\chi^2 = 1126/233$, $\sim 41\sigma$ removed from the ideal value. Once again, we see that the high-energy bump cannot be adequately modeled with our assumed energy

resolution, and we will try a new fit with tighter resolution (45%) in the same fashion as before.

When using a resolution of 45%, we find the best-fit parameters shown in Table 3.12. Figure

Table 3.12: Best-Fit Fluorescence Parameters with Improved Resolution.

$\Delta\chi^2 = 888/233$			
Emission Component	Energy (eV)	Line Width (eV)	norm
C-Kα	277	7.8	0.81
O-Kα	524.9	6.0	3.68
Al-Kα	1,486.7	0.43	12.54
Cr-Lα	572.8	4.0	1.11
Ni-Lα	851.5	2.7	5.48

3.34 compares the observed spectrum with this new best-fit model. At this resolution, carbon and

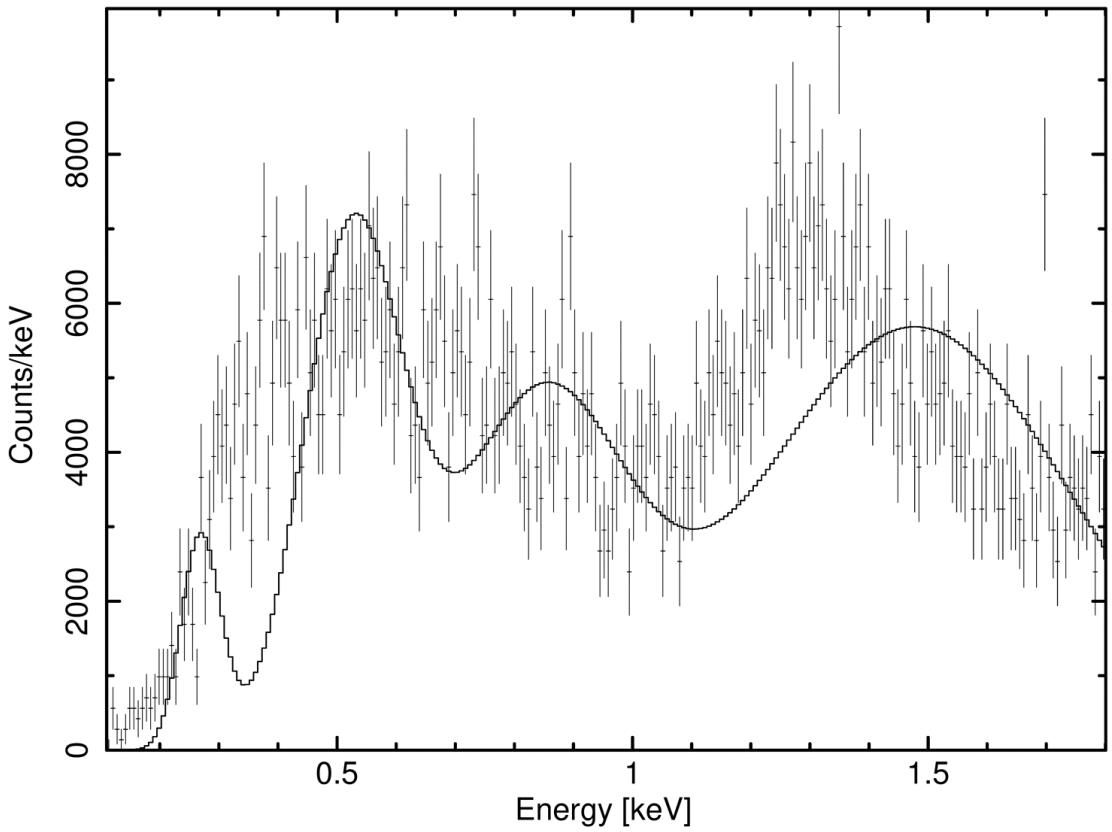

Figure 3.34: OGRESS' PHD spectrum (crosses) fitted with 5 fluorescence lines. The instrumental FWHM energy resolution is assumed to be 45%.

chromium emission are no longer set to zero. Now $\Delta\chi^2 = 888/233$, $\sim 30\sigma$ from the ideal value.

Two problems immediately present themselves when inspecting Figure 3.34. First, the peak of aluminum emission is distinctly removed from the center of the high-energy PHD bump. Based on our energy scale, the high-energy bump might be better fit with magnesium emission (1254 eV). This is not a huge problem, as their is considerable uncertainty in our PH–energy calibration. Uncertainty and actual variation in gain are not small, and these translate directly to uncertainty in our energy calibration. The error will be largest at high PH channels. An error of $\pm \sim 20\%$ is quite reasonable, and the shift in pulse peak is within this range.

The second problem seen in Figure 3.34 is that C- and O-Kα are distinctly separated at 45% resolution. Laboratory measurements (see Fig 3.35) make it clear that the detector does not

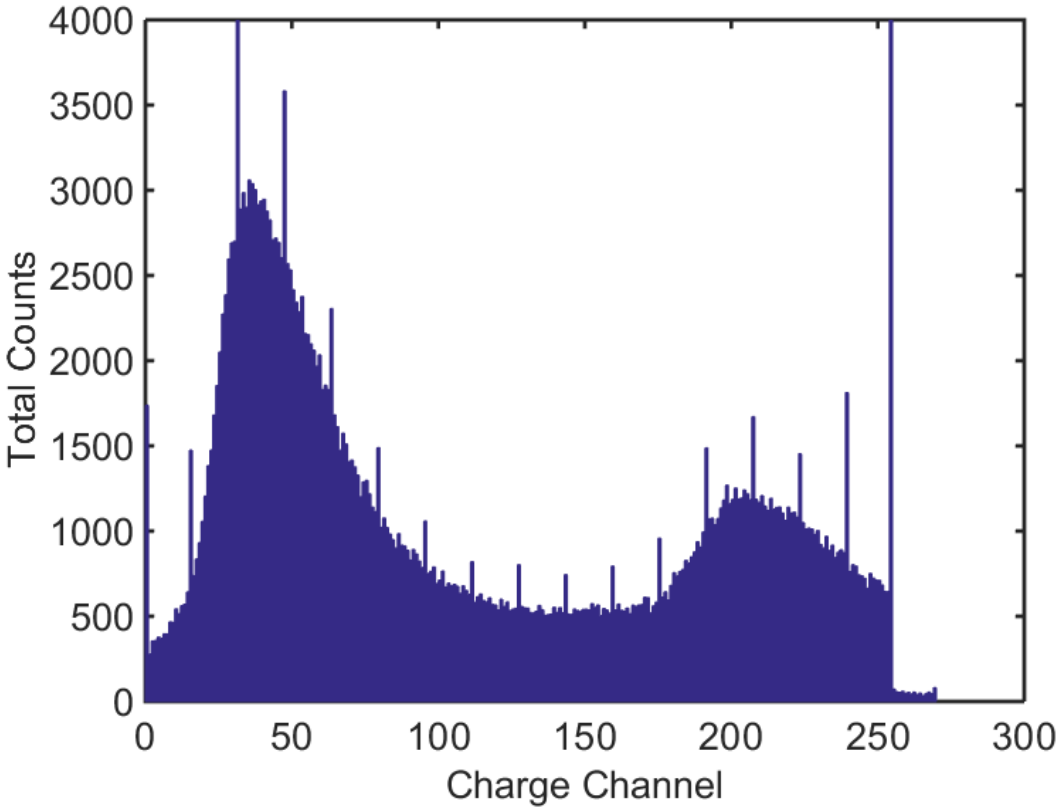

Figure 3.35: The PHD observed from the Manson source with an aluminum anode installed. The low-energy peak near channel 50 is a blend of C- and O-Kα. The high-energy peak near channel 200 is Al-Kα. The C- and O-Kα lines are not separable with our detector.

separate these lines. We are left with an apparent contradiction that the detector appears to have distinctly worse resolution at low photon energies. This not necessarily a surprise. As energy decreases, fewer photoelectrons are produced by each photon (~ 19 for O and ~ 10 for C), and the pulse height may be subject to proportionally larger variations.

To address the possibility of an error in our PH–energy calibration, we will allow the centroids of each line to shift as a group. This will likely shift down the energies of each line (or equivalently shift up our energy scale), resulting in a better match between the Al line and the high-energy PH bump. It will also likely require the "norm" value for the C line to become lower, which is more in line with our expectations. Addressing the resolution issue is more difficult. It seems that the detector resolution is energy dependent, with poor resolution at both low energies (near the C and O lines) and high energies (Fe-55 emission). Moderate energies (Al emission) appear to have the best resolving power. In attempt to capture the behavior of the detector's true energy resolution, we will modify our instrument response to have a FWHM of 100% near the C and O emission (in agreement with Fig. 3.35) which linearly decreases to 45% near Al emission (in agreement with Fig. 3.35 and the flight PHD spectra). This method is admittedly ad hoc, but it does appear to capture the true nature of the detector.

When using an instrumental response with linearly varying energy resolution and allowing the line centroids to jointly shift position, we find the best-fit parameters listed in Table 3.13. The line

Table 3.13: Best-Fit Parameters with Sliding Energy Resolution.

$\Delta\chi^2 = 424/232$			
Emission Component	Energy (eV)	Line Width (eV)	norm
C-Kα	264	7.8	0.00
O-Kα	500.0	6.0	4.42
Al-Kα	1416.5	0.43	13.07
Cr-Lα	545.6	4.0	2.22
Ni-Lα	811.2	2.7	5.17

widths have remained frozen for this fit. The line energies have been allowed to jointly shift, and the norms have been allowed to vary freely, as before. Figure 3.36 compares the flight PHD spectrum

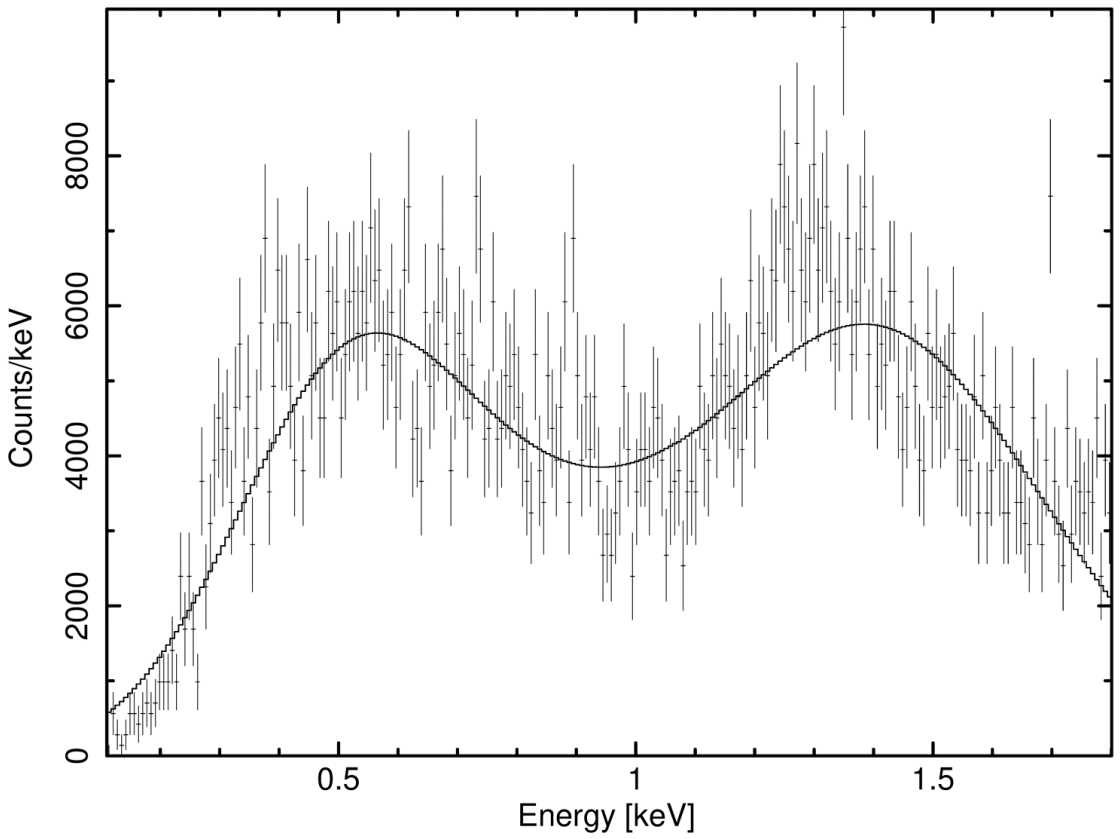

Figure 3.36: OGRESS' PHD spectrum (crosses) fitted with 5 fluorescence lines. The instrumental FWHM energy resolution is assumed to vary linearly from ∼100% at low PH channels to ∼45% at high PH channels.

to the best-fit model. The fit is now substantially improved, with $\Delta\chi^2 = 424/232$, now only $\sim 8.9\sigma$ removed from the ideal value. To achieve this fit, the energies of the line centroids have been shifted downward in energy (or the energy scale has been shifted up) by <5%. Carbon's emission is set to zero, in agreement with expectations. Each remaining component has a substantial contribution to the total emission. As shown before, $\Delta\chi^2$ can be improved even further by removing several channels which spike relative to their neighbors. Removing channels 1, 4, 22, 175, and 224 results in $\Delta\chi^2 = 346/227$, now only $\sim 5.6\sigma$ from the ideal value. Recall that the uncertainties associated with each data point are significantly higher than assumed by the chi-squared routine, so the fit (and all other fits we have made) are significantly better than might be thought based solely on the $\Delta\chi^2$ value. Thus, based on goodness of fit and the realistic nature of the best-fit parameters,

our model for internal X-ray fluorescence seems quite convincing.

To arrive at this good fit between the flight data and internal fluorescence, we have shifted our energy scale and modified the instrument response to provide energy-dependent resolution. Thus, we are obliged to fit the flight data with two-component NEI model one final time to ensure our improved fit to a fluorescence model is not merely a result of modifying more parameters. For this fit, we have adjusted the energy scale by 4.73% (the amount required to achieve the best fit to the fluorescence model). We have also modified the instrumental response to use a linearly changing energy resolution (FWHM) which begins at roughly 100% at low-energy channels and falls to 45% at high-energy channels.

Table 3.14 shows the best-fit parameters. Figure 3.37 compares the flight PHD spectrum

Table 3.14: Best-Fit NEI Parameters.

$\Delta\chi^2$	395/209	
n_H (cm^{-2})	0.210	
	Low-T Component	High-T Component
kT (keV)	0.178	0.463
H	1	1
He	1	1
C	0.00	0.00
N	0.00	0.00
O	3.28	0.00
Ne	0.00	0.00
Mg	0.00	45.05
Si	0.00	10.66
S	0.00	0.00
Ar	0.00	0.00
Ca	0.00	0.00
Fe	0.00	0.00
Ni	0.00	0.00
$n_e t$ ($\mathrm{cm}^{-3}\mathrm{s}$)	1.02e+10	2.40e+13
norm	60.37	39.61

with the best-fit model. This generates quite a good fit, with $\Delta\chi^2 = 395/209$. This is, in fact, one of the best fits we have yet achieved, and the chi-square value is even better than that of our fluorescence model. Modifying the instrumental response and energy scale appear to have had

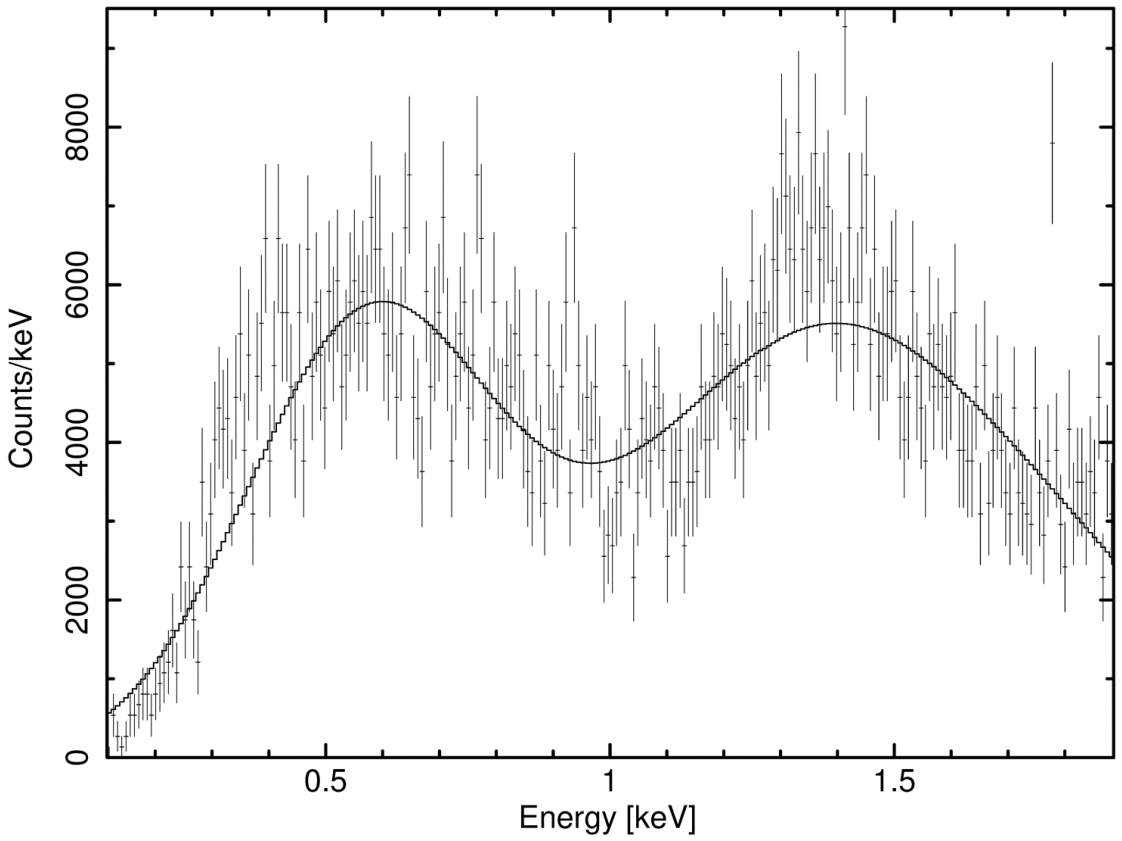

Figure 3.37: OGRESS' PHD spectrum (crosses) fitted with a two-component NEI model. The energy scale has been shifted to agree with that found from the fluorescence fit. The instrumental FWHM energy resolution is assumed to vary linearly from ∼100% at low PH channels to ∼45% at high PH channels.

a positive effect. Despite having a lower chi-square value than the fluorescence model, the two-component NEI model, once again, requires unrealistic parameters. In fact, the best-fit parameters in Table 3.14 (and the other NEI tables) look suspiciously like the fluorescence parameters. The best-fit NEI model has no metals at all other than oxygen, magnesium, and silicon. Oxygen, of course, is one of the primary ingredients in our fluorescence model and generates most of the flux in the low-PH bump. Aluminum is not a parameter in XSPEC's VNEI model, so XSPEC will always assume that its abundance is zero. Instead of using aluminum, XSPEC has used magnesium and silicon to generate the flux in the high-PH bump. These elements produce emission slightly below (Mg) and slightly above (Si) that of Al. It seems clear that if Al were an option, the XSPEC

model would likely have used it instead. Thus, the best-fit NEI model is one which mimics our fluorescence model very closely.

Although the chi-square values are comparable between the two-component NEI model and the internal fluorescence model, the parameters for the fluorescence model are far more realistic. As stated before, the parameters of the NEI model are inconsistent with previous observations of Cygnus. It is also simply difficult to imagine a SNR which has highly elevated abundances for 2-3 metals and zero abundance for the rest. The fluorescence model, on the other hand, has best-fit parameters which are highly believable considering the composition of the payload interior. The goodness-of-fit and realistic nature of the parameters provide compelling evidence that OGRESS witnessed X-ray fluorescence of the spectrograph interior.

Chapter 4

The Noise Problem

To successfully observe Cygnus in the future, the flight noise must be well-understood so that it can be suppressed during observation or removed during data analysis. To truly understand the source of the flight noise, we must be able to reproduce it in the laboratory. This is important both to confirm the origin of the flight noise and to test methods of suppression. The best way to do this is to put the payload in conditions that are as similar to flight as possible. This is not an easy task. During flight, the payload was subjected to launch vibrations, which were even stronger than expected due to the Black Brant anomaly. When the shutter door opened, the payload was subjected to vacuum conditions which were more extreme than we can make in the laboratory. The payload would have equilibrated with atmospheric conditions at > 150 km, filling with electrons and ionized atoms. Perhaps most importantly, the payload was ungrounded during flight and probably developed a net charge.

To reproduce the noise, we tested the instrument's response to a hot cathode ion gauge (an ion source) and a simple hot wire filament (an electron source), as these are the most likely sources for the flight signal. We applied a voltage to the chassis to simulate spacecraft charging. We also tested a prototype for a 2-layer repeller grid to attempt to suppress the flight noise.

4.1 Experimental Setup

4.1.1 Ion Gauge

To produce positively charged particles in the laboratory, we relied on a series 355 micro-ion gauge from MKS. The ion gauge functions by emitting an electron current from a heated filament. The filament is surrounded by a grid which attracts the electrons with a potential of +180 V. En route to the grid, the electrons collide with ambient gas atoms, causing some to be ionized. The ionized atoms are then attracted an ion collector wire which is held at a negative voltage. The ion current onto the collector wire is a function of gas pressure and is thus used often in high-vacuum applications. This gauge was our primary means of measuring payload pressure in the laboratory.

Not all ions are captured by the collector wire. Many escape the gauge completely and enter the payload. During laboratory testing of the CyXESS payload, it was discovered that the GEMs see a substantial amount of signal when the ion gauge was turned on, and care was taken to turn the gauge off during X-ray testing. Ions inside the payload are attracted to the negative detector windows and gain substantial kinetic energy ($\sim$ 3600 eV) in the process. This is enough energy to cause collisional ionization of inner shell electrons which can result in X-ray emission (and thus signal on the detectors).

For our tests, the ion gauge was mounted on the detector bulkead. This was done deliberately so that any ions entering the payload would be directed away from the detectors. This was done in an attempt to produce a more diffuse signal, as the ions could not travel from the gauge to GEMs in a straight line.

4.1.2 Hot Wire Filament

To produce electrons in the laboratory, we used the filament from a J.E. Manson CO., Inc. electron-impact soft X-ray source (normally dubbed the “Manson lamp” or “Manson source”). A current of 4–6 Amps flows through the filament. This serves to heat the filament to the point that electrons begin to bleed off by gaining enough energy to be ejected out of the tungsten conduction

band. Under normal operations, these electrons are attracted to a metal anode held at a high positive voltage ($\leq$ +5000 V). The electrons accelerate toward the metal anode and cause inner shell excitations, resulting in K-α emission corresponding to the impacted material (as well as C and O lines from contaminants). This is precisely the same process which was demonstrated by Seward et al. [1973a] (see Fig. 3.32) and which we suspect may have occurred during OGRESS' flight.

When performing electron testing, the filament was positioned inside the payload with a direct line-of-sight to the detectors. We found that other positions did not produce detectable count rates and that the signal dropped substantially as the distance between the detectors and filament increased. The filament was powered alone, without the metal anode normally used for X-ray generation. This produced a steady flow of thermal electrons into the payload.

4.1.3 Charged Skins

To charge the skins, the payload had to be electrically isolated. To do this, the electronics section was detached from the payload. Return signals and ground connections for all electronics (including components mounted to the detector bulkhead) are routed to the electronics deck. Thus, separating the Edeck from the detector bulkhead left the chassis isolated from the electronics. The one exception was the mid-volt power supply (MVPS) which supplies power to the ion repeller grids and is grounded directly to the detector bulkhead. To solve this issue, the MVPS was removed. The wiring for the MVPS was then modified such that the repeller grids received power directly from a HV power supply which was electrically isolated from the chassis.

The chassis also had to be isolated from the vacuum pumps. This was accomplished by installing an insulating ceramic adaptor between two vacuum connections (see Figure 4.1). During laboratory testing the chassis rests on teflon blocks on the rocket cart, so it is naturally ungrounded when detached from all electronic components.

After electrically isolating the payload, we attached a power supply and return resistor to apply a potential to the skins. In this way, we were able to experiment with different potentials to

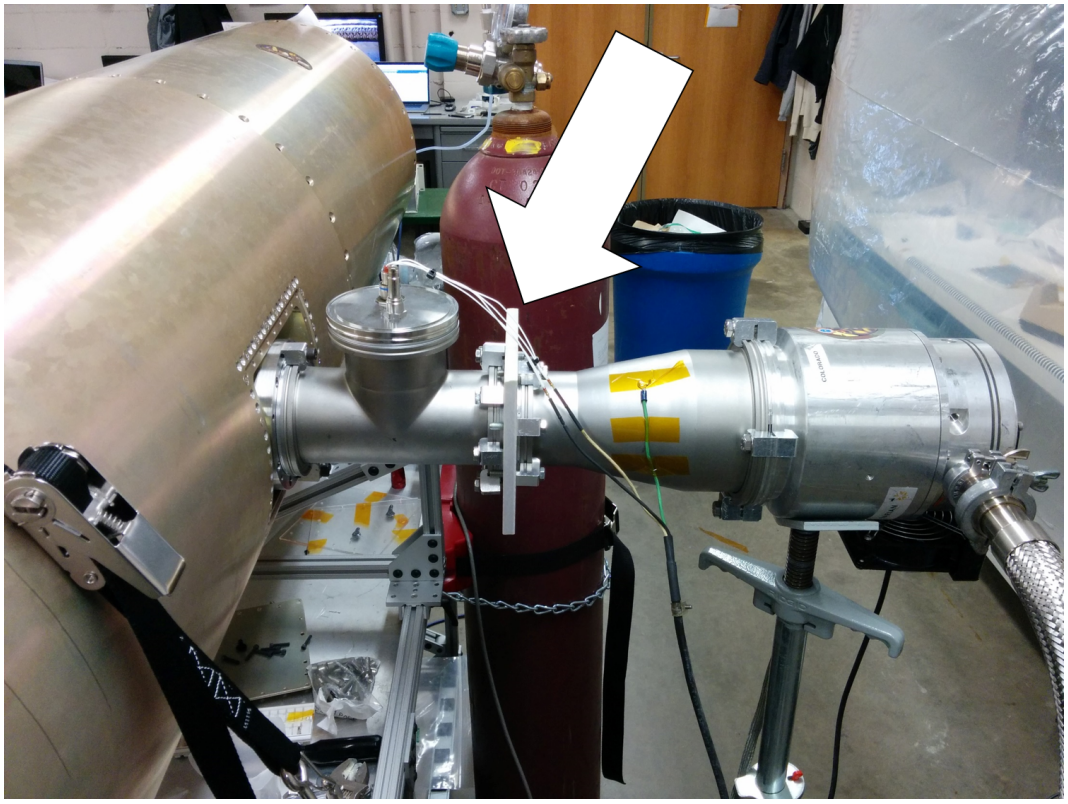

Figure 4.1: The arrow highlights the insulating ceramic adaptor installed between the payload and vacuum pump hardware. The white wiring is the supply and return for the hot filament. The green wire is the ground for the filament, carefully mounted away from payload chassis.

see the effect of spacecraft charging on observed signals.

4.1.4 Negative Repeller Grid

Based on the flights of CyXESS, EXOS, and CODEX, positive ions were originally suspected as the most likely cause of signal contamination. For this reason, OGRESS flew with ion repeller grids installed in front of each detector. While this is effective at shielding the detectors from ions, electrons can still pass through the grid and be exposed to the full voltage of the detector windows. If the HV windows are truly the source of the flight noise, shielding them with a much lower negative voltage may repel electrons more gently and prevent X-ray fluorescence.

The repeller grid was removed from one detector and modified such that both repeller grids

could be mounted over a single detector with separately applied voltages. The idea was to apply negative voltage (~ -50 V) to the top layer which would gently repel electrons from the detectors. The second grid layer would be held at +100 V to repel ions which would stream past the top layer. We tested the effect of this dual-layer repeller grid on signals generated from ions and electrons.

4.2 Ion Testing

Some ion gauge testing was carried out prior to flight. After witnessing the flight noise, we decided to carry out more extensive testing with the ion gauge and repeller grids to ensure our understanding of positive ions was correct. Ions are known to be abundant at > 150 km, and it is possible that our repeller grids either did not adequately shield the detectors or simply do not have the effect we anticipated. In particular, preflight testing never included the effects of charged or floating skins.

We ran ion gauge tests with many different voltages applied to the repeller grid(s) and skins. Figure 4.2 shows data acquired from the ion gauge with no repeller grid and grounded skins. The window bar shadows are very apparent, despite the fact that the ions do not have a direct path to the detectors. If the ions make only one reflection before hitting the detector, they will all come from roughly the same direction, so this is not necessarily surprising. Figure 4.3 shows the X and Y profiles of the image, and the window bars and fine mesh shadows are clearly visible. Figure 4.4 shows a comparison of shadow profiles from the ion gauge and the Manson source. The ion gauge shadow, although quite distinct, is significantly shallower than the Manson shadow. It also spans a wider range. This is good to see, as it is more evidence that diffuse sources can suppress the window bar shadows.

When the positive repeller grid is turned on, the ion gauge signal decreases by $> 99\%$. The signal is not decreased to a level consistent with the detector background, however, and there is typically a residual signal of 5-10 Hz remaining. The level of this residual signal is reached far below the operating voltage of the grids, so it probably originates from some mechanism other than ions hitting the detector window. The ion gauge is known to be a source of UV light, and it is possible

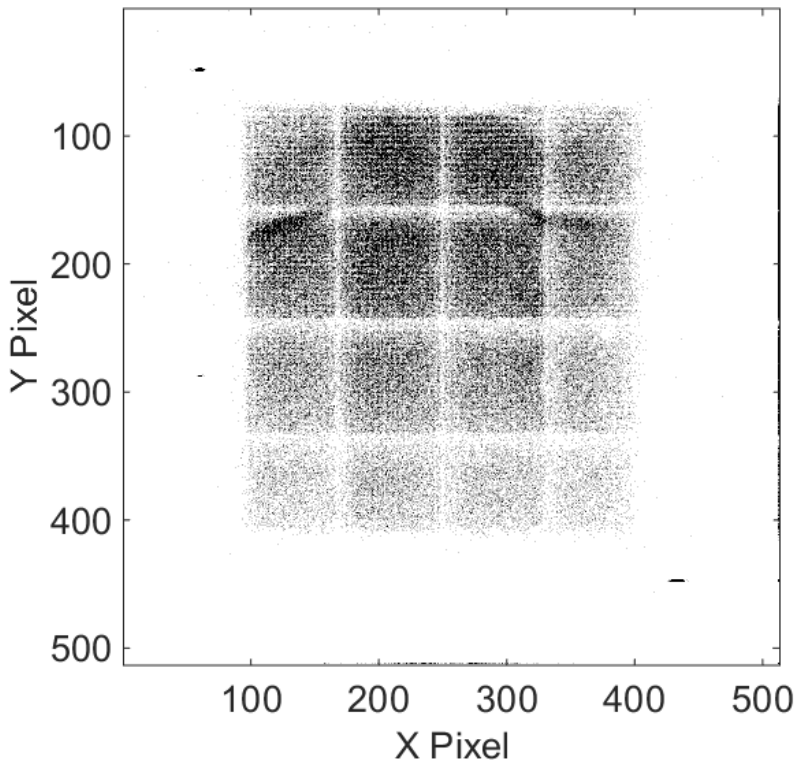

Figure 4.2: Signal from the ion gauge in the absence of a repeller grid.

that this creates a low level of signal on the detectors. The ion gauge also emits electrons in order to ionize the ambient gas. We may be witnessing signal from the small number of electrons which escape the collector grid.

Applying a voltage to the chassis has various effects on the ion gauge signal depending on the sign and magnitude, as shown in Table 4.1. When the chassis is electrically isolated, turning

Table 4.1: The Effect of Skin Voltage on Ion Signal

Chassis Voltage	Count Rate
-25 V	∼5 Hz
Ground	∼2700 Hz
Isolated (∼+2V)	∼10,400 Hz
+25 V	∼3700 Hz

on the ion gauge induces a positive voltage of ~ 2 V on the skins (this value will vary depending

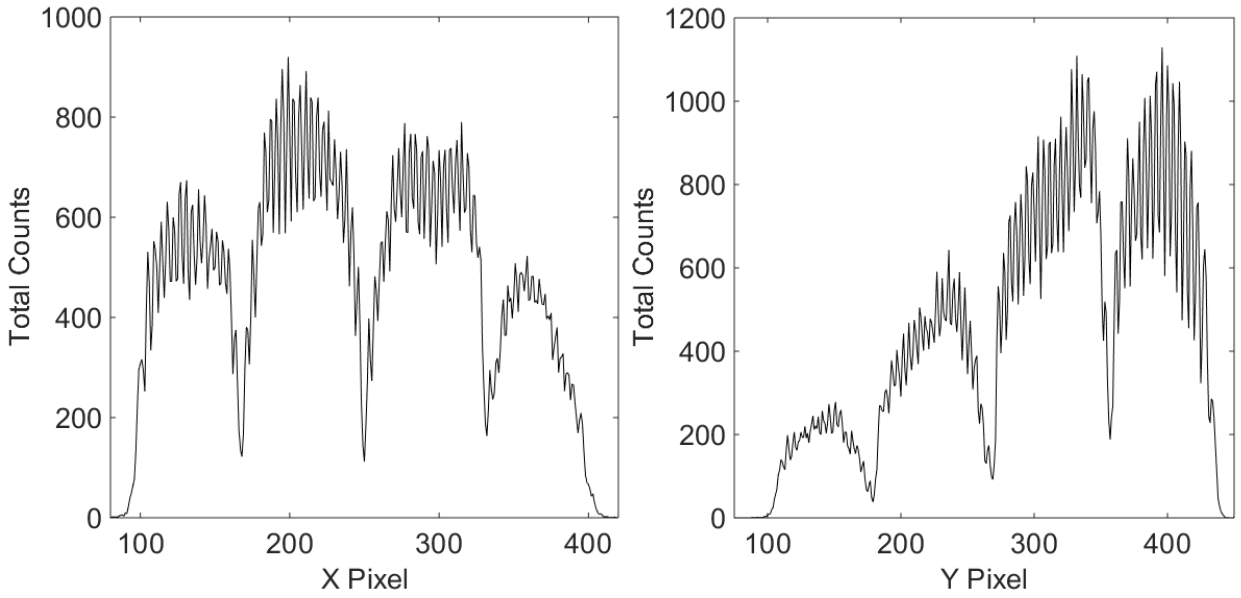

Figure 4.3: The images show the X and Y profiles of ion gauge signal. The ion gauge produces significantly wider window bar shadows than the Manson X-ray source.

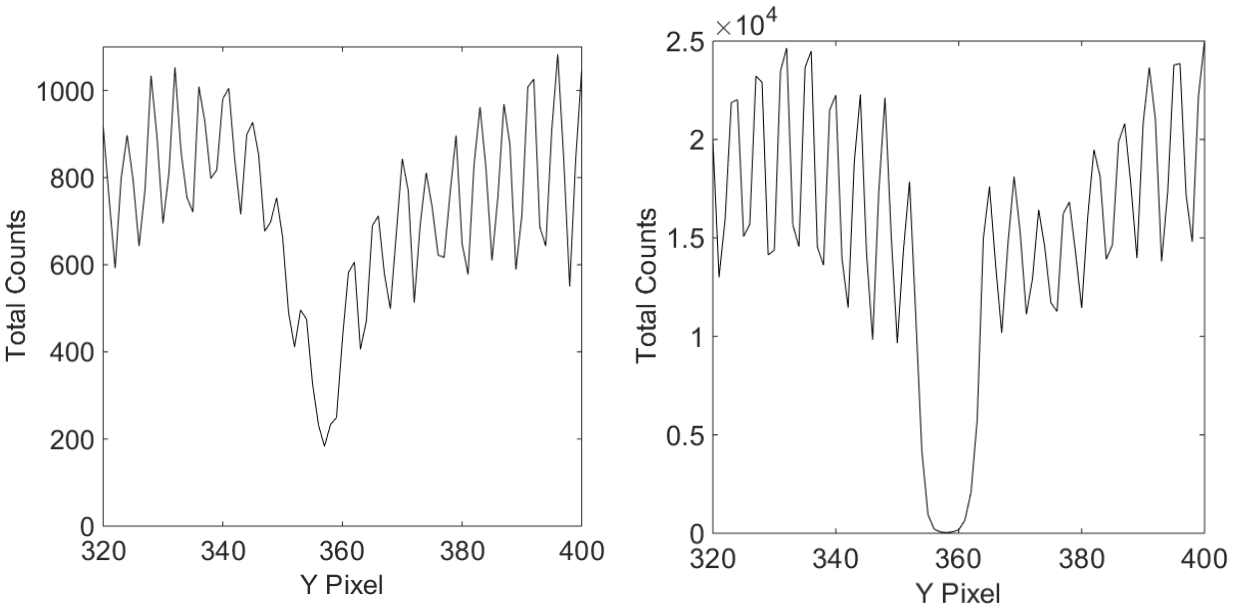

Figure 4.4: The profile of a single window bar shadow for the Manson (*left*) and ion gauge (*right*). The shadow produced by the ion gauge is noticeably shallower than the shadow produced by the Manson source.

on the resistance between chassis and ground). This is expected, as the gauge is an ion source

and produces an ion current onto the skins. Applying a low positive voltage ($\sim$ 2 V) to the skins increases the signal. This occurs because it becomes more difficult for the ions to impact and recombine at the skins, allowing more of them to impact the detector. When the chassis voltage becomes high enough, however, the signal begins to drop again. We believe this occurs because the ions experience a substantial repulsion away from the detector bulkhead, and thus from the detectors. Applying a negative voltage to the chassis expectedly causes a decrease in ion gauge signal. This, of course, occurs because ions will be attracted to – and recombine more easily at – the skins, reducing the number that have a chance to encounter the detector. These general effects appear to occur regardless of whether the positive grid is powered.

We also tested the effect of adding a negative-voltage grid above the positive ion repeller grid. The first tests were run with the positive grid off (see Table 4.2). The effect of the negative

Table 4.2: The Effect of the Negative Grid (Positive Grid OFF)

Chassis -25 V		Chassis Ground		Chassis Isolated (~+2 V)		Chassis +25 V	
Grid	Signal	Grid	Signal	Grid	Signal	Grid	Signal
Off	~4 Hz	Off	~6 Hz	Off	~13,000 Hz	Off	~1500 Hz
-50 V	~5 Hz	-50 V	~2700 Hz	-50 V	~10,000 Hz	-50 V	~3700 Hz
-400 V	~35 Hz	-400 V	~320 Hz	-400 V	~1600 Hz	-400 V	~640 Hz

grid varies greatly depending on the chassis voltage. There will be competing effects involved when the negative repeller grid is operational. The negative grid can attract ions closer to the detectors, increasing the signal. It can also remove ions (via recombination) that impact it, decreasing the signal. The chassis voltage also has competing effects, as it can determine the rate of ion recombination at the skins and can also attract/repel ions to/from the detector bulkhead. These effects appear to be of similar strength, and thus the net effect of the skins and negative grid can vary. With -25 V on the skins, the negative grid increases the ion gauge signal, presumably by attracting more ions away from the skins and toward the detector. With +25 V on the skins, mild voltages on the negative grid increase the gauge signal. At higher voltage, however, the negative grid begins to decrease the signal. Since few ions recombine at the +25 V skin, the dominant effect of

the negative grid becomes its ability to remove ions through recombination. When the skins are electrically isolated (at ∼+2 V), the negative grid serves only to decrease the signal. This occurs because the ions do not recombine easily at the skins, but are also not repelled strongly by the detector bulkhead, allowing many of them to travel close to the detector. In this scenario, the negative grid serves only to suck up and remove ions. When the skins are grounded, the effects are similar to a large positive skin voltage. The negative grid first increases the signal (by attracting ions toward the detector) and then decreases the signal (by removing ions via recombination).

When the positive grid is powered (at +100 V), the effect of the negative grid is far simpler (see Table 4.3). The negative grid appears to have no effect until its (negative) voltage becomes

Table 4.3: The Effect of the Negative Grid (Pos Grid ON)

Chassis -25 V		Chassis Ground		Chassis Isolated (∼+2 V)		Chassis +25 V	
Grid	Signal	Grid	Signal	Grid	Signal	Grid	Signal
Off	∼4 Hz	Off	∼3 Hz	Off	∼4 Hz	Off	∼3 Hz
-50 V	∼4 Hz	-50 V	∼4 Hz	-50 V	∼5 Hz	-50 V	∼3 Hz
-400 V	∼31 Hz	-400 V	∼4 Hz	-400 V	∼29 Hz	-400 V	∼22 Hz

comparable to the positive grid's (positive) voltage. At this point, increasing the negative voltage leads to a rapid increase in signal. Basically, the negative grid serves only to undo the effect of the positive grid. This is not necessarily a bad (or unexpected) thing. The ions still cannot pass through the positive grid unless the negative grid is powered to ∼ -100 V. A voltage of ∼ -50 V, however, is still likely to (gently) repel electrons without increasing the ion signal seen by the detectors.

The best conditions for removing ion signal are found to be: positive grid on (obviously), negatively charged skins, and no negative grid. This corresponds to our flight configuration, assuming spacecraft charging occurs as expected. Thus, no action is required to make the instrument less sensitive to ions. This is convincing evidence that positive ions are not the source of flight noise. It is gratifying to confirm that our ion repeller grid functions precisely as anticipated and does an excellent job of solving its intended problem, contaminating ion signal. The flight results

have shown, however, that the noise from previous flights was misidentified.

4.3 Electron Testing

Electrons provide a compelling explanation for the flight noise, via the mechanism of impact-induced fluorescence. We tested the detector response to the presence of electrons using a Manson filament, as described above. Again, tests were run with different voltages applied to the skins, and the effect of a negative repeller grid was investigated. The Manson filament proved far more difficult to work with than the ion gauge. The first issue was that the signal generated by the filament was generally low, producing lower signal to noise ratios despite longer integrations. Far worse, was the natural variability of the current provided by the power supply. This led to large variations in signal over relatively short time periods, sometimes noticeable over the course of a single exposure (see Figure 4.5). This makes the filament test data more difficult to interpret and less reliable than the ion gauge test data. This is unfortunate, as the behavior of the detectors in the presence of electrons is of greater interest to us. Despite these difficulties, inferences can still be made about the detectors' response to electrons, so we thoroughly discuss the results of the electron testing.

An image showing signal from the filament is displayed in Figure 4.6. Window bar shadow profiles are shown in Figure 4.7. As with the ion gauge, signal from the filament produces window bar shadows that are quite distinct, but still wider and shallower than signal from an X-ray source. Also, like the ion gauge, the filament induces a voltage on the payload skins when the chassis is electrically isolated. When using the filament, the induced skin voltage is negative at ~ -1 V. This confirms that the filament is a source of electrons and that the rate of particle emission is comparable to that of the ion gauge. Despite this, the count rate generated by the filament is substantially lower than that of the ion gauge, leading to the conclusion that electrons produce signal on the detectors less efficiently than ions do.

It should be noted that the most important result from the electron testing is the simple fact that electrons produce signal on the detectors. This confirms that electrons are a valid source of

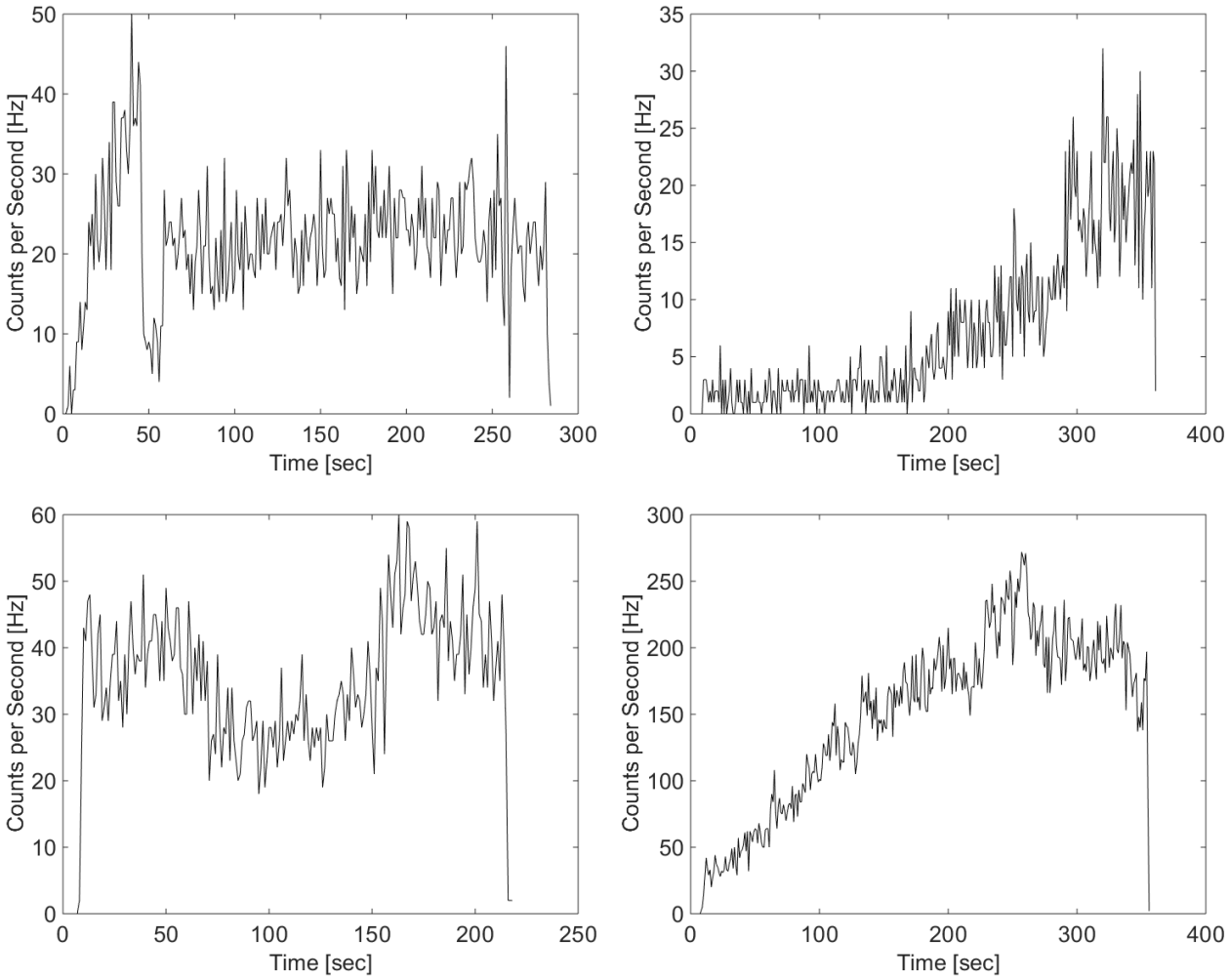

Figure 4.5: The plots demonstrate the intrinsic instability of signal from the filament. No settings were changed during any of the displayed exposures, so the changes in count rate represent instability in the source.

noise during flight. Considering the large number of electrons present in flight conditions, it is very likely that electrons were the primary source of noise during OGRESS' flight. After identifying electrons as the source of the noise, the next step is to understand the specific characteristics of electron signal and how it can be suppressed.

An important test for the electron source is to compare its PHD spectrum with the flight PHD spectrum to check if the emission is similar. Figure 4.8 shows the PHD acquired when observing the filament. The exposure was taken with the repeller grid turned on and the chassis ungrounded

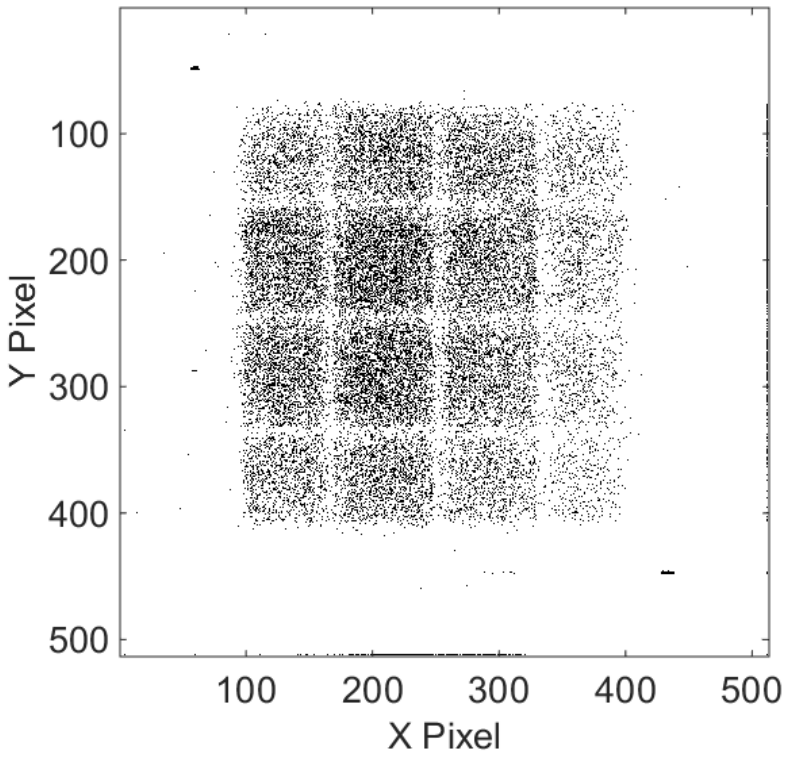

Figure 4.6: Signal from the Manson filament.

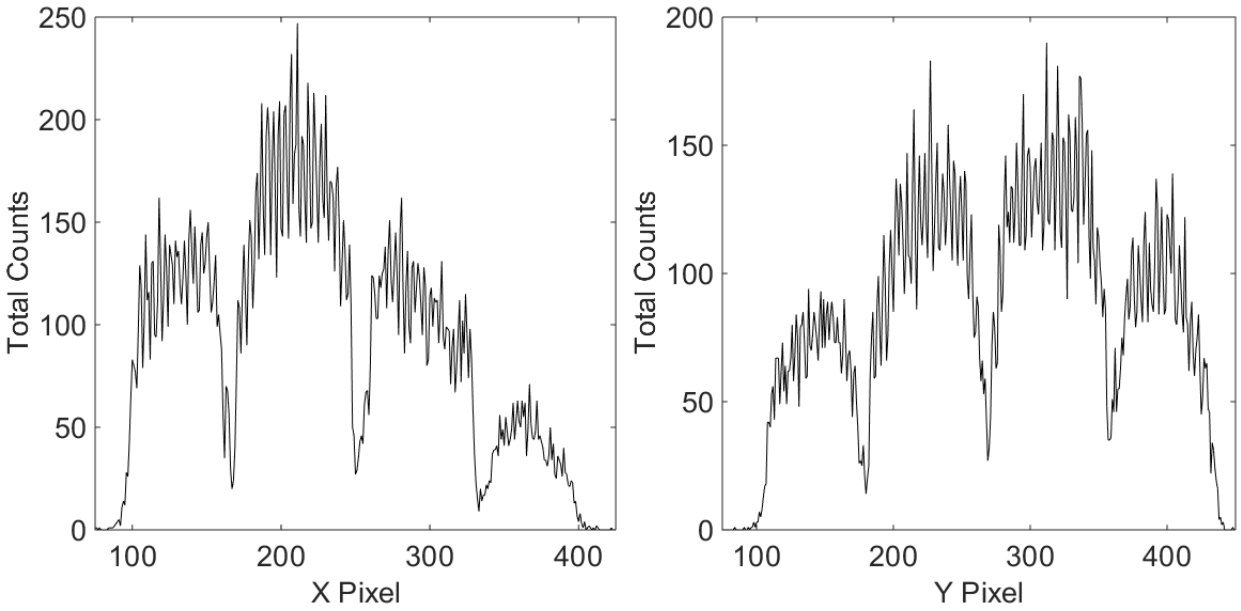

Figure 4.7: The X and Y profiles of the image shown in figure 4.6.

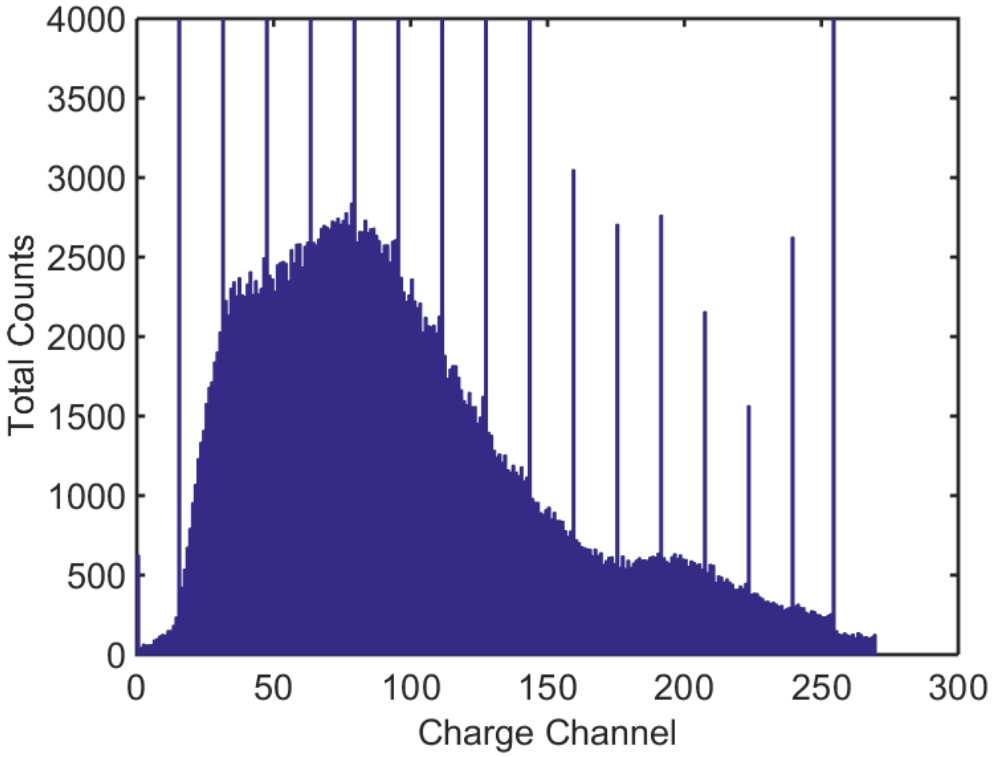

Figure 4.8: The PHD acquired when observing the Manson filament. The periodic spikes are an artifact created by the data's high count rate.

(at ~ -1 V), as these are the expected flight conditions. There is a large spike every 16 channels. This occurs when the count rate is large. The charge data take substantially longer to measure than the position data, so new data sometimes arrive before the charge has been fully integrated. When this occurs, the low-significance bits are lost, resulting in regular spikes in the PHD.

A notable feature of the filament PHD is that the high-energy bump is distinctly weaker than the low-energy bump, whereas the two bumps were of comparable strength in the flight data. The fact that the low-energy and high-energy bumps both appear to be present at all is evidence that electrons produce signal similar to the flight signal. The high-energy bump, corresponding to Al emission in our fluorescence model, may be weaker due to the increased gas density in the payload relative to flight conditions. During flight, the on-board pressure gauges bottomed out, indicating a pressure below 10^{-6} Torr. This corresponds to a mean free path of > 100 m, meaning electrons will

not collide with other gas molecules after being accelerated. Thus, all of their energy is available to produce internal fluorescence. In the laboratory, the payload pressure is generally around 5×10^{-5} Torr, with a mean free path of ~ 1 m. This is shorter than the length of the payload, so electrons in the laboratory are likely to experience collisions with other molecules before impacting the payload interior. Energy will be lost in these collisions, so the average accelerated electron will hit the payload interior with less energy in the laboratory, and high-energy fluorescence lines will be more difficult to excite.

We now compare this PHD to the same fluorescence model that we used for the flight data. As before, the line centers and widths will be fixed, and the norm values will be allowed to vary freely. The gratings and geometric area will be ignored in the instrument response. The energy resolution will be assumed to vary linearly from $\sim 100\%$ at low PH channels to $\sim 45\%$ near channel 200. Every 16th channel will be ignored. The best-fit parameters are listed in Table 4.4. Figure

Table 4.4: Best-fit Filament Parameters.

$\Delta\chi^2 = 1496/219$			
Emission Component	Energy (eV)	Line Width (eV)	norm
C-Kα	277	7.8	478.3
O-Kα	524.9	6.0	702.7
Al-Kα	1486.7	0.43	421.9
Cr-Lα	572.8	4.0	2238.2
Ni-Lα	851.5	2.7	1096.7

4.9 shows the filament PHD spectrum compared to the best-fit fluorescence model. For the best-fit model, $\Delta\chi^2 = 1497/219$, $\sim 61\sigma$ removed from the ideal value. From the chi-square value alone, this appears to be an extremely bad fit. We must remember, however, that the counts per bin in the filament data are much higher, leading to smaller uncertainties and a naturally higher chi-square value. As before, our uncertainties are likely much higher would be expected from simple Poisson noise. It is apparent by eye that the model matches the data quite well. Once again, we appear to have issues with the detector energy resolution. The aluminum feature is once again narrower than our energy resolution, despite our assumption that higher channels have better resolution.

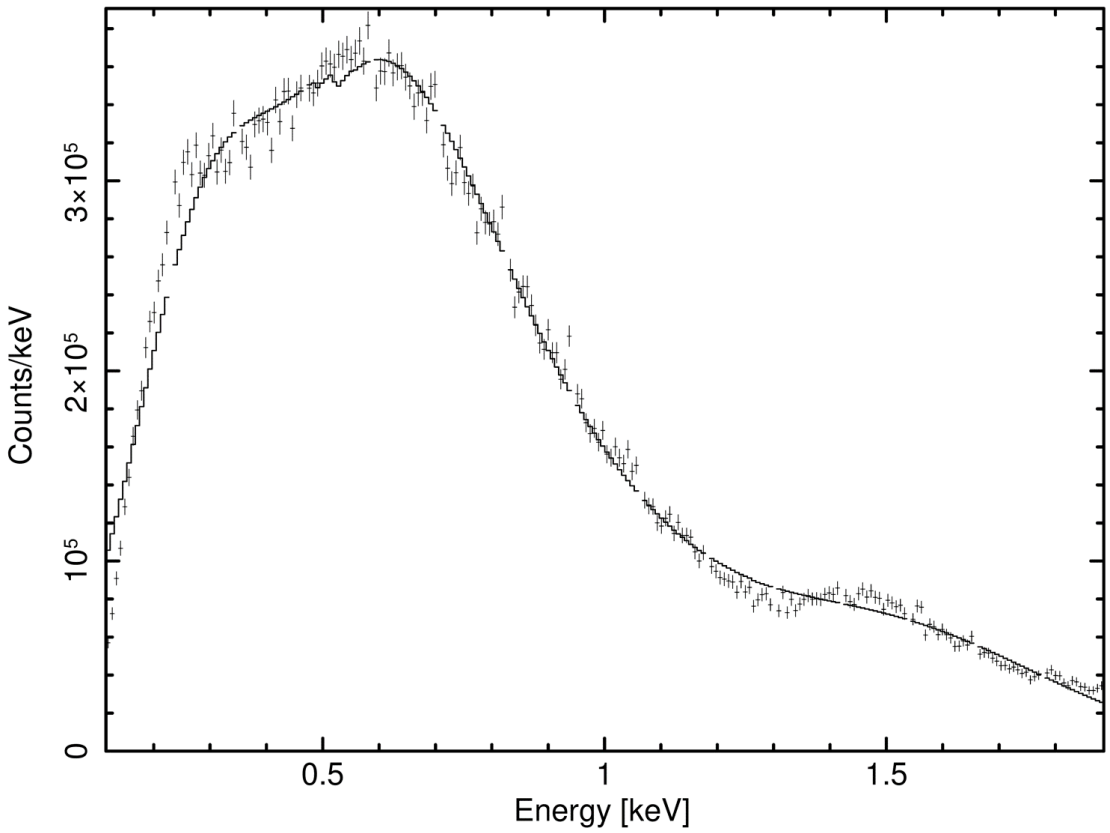

Figure 4.9: The PHD spectrum from the filament (crosses) fitted with 5 fluorescence lines (solid line). The instrumental FWHM energy resolution is assumed to vary linearly from ∼100% at low PH channels to ∼45% at high PH channels. The model tracks the data very well. The fit has a high chi-square value, however, due to the small errors associated with the data.

It may simply be the case that the detector resolution is variable between exposures. Figure 4.9 appears to have distinctly (though not vastly) improved resolution compared to the flight data. Regardless, the model appears to track the data quite well, despite using an apparently incorrect energy resolution.

The best-fit parameters for the filament data are noticeably different from those of the flight data. Obviously, the flux is much higher from the filament, so all norm values are substantially increased from their flight levels. Notably, C-Kα makes a substantial contribution to the filament signal, in contrast to the flight data where C emission was absent. Aluminum contributes a much smaller fraction of the filament signal, resulting in a much lower high-energy bump. Chromium

makes the largest contribution to the filament signal, whereas it had quite a weak contribution to the flight signal. What this all means is, of course, open to interpretation. On one hand, we have been able to model the electron PHD spectrum quite well with a fluorescence model. On the other, the best-fit parameters are distinctly different from those of the flight data. As already mentioned, the weak Al emission is likely a result of a relatively high gas density in the laboratory. Why carbon emission should exist strongly in the laboratory but be absent in flight is, perhaps, cause for some concern.

Although the filament PHD does not perfectly match that of the flight data, it is clear that electrons can produce substantial signal on the detectors in flight-like conditions. Electrons may generate most of the signal seen in the flight data's low-energy bump but only generate a small portion of the high-energy bump. This would imply that their is another distinct source of high-energy noise in the flight data that is absent from the laboratory data. Whether or not this is true, it seems that ionospheric electrons should be a very real source of signal contamination during flight. Thus, it is important to understand how electron signal is affected by spacecraft charging, the ion repeller grid, and the prototype 2-layer repeller grid.

Again, different voltages were applied to the payload skins to test the effects of spacecraft charging on electron signal. Results from a test run are shown in Table 4.5. As with the ion

Table 4.5: The Effects of Skin Voltage

Chassis Voltage	Count Rate
-25 V	∼23 Hz
Isolated (∼-1.3 V)	∼ 94 Hz
Ground	∼15 Hz
+25 V	∼1 Hz

gauge, there appear to be competing effects at work when charging the chassis. Applying a positive voltage suppresses the electron signal. This makes sense, as electrons will be attracted to the payload walls and will be removed from the system. When the payload is grounded, electrons can still be absorbed when hitting the interior walls, but they are not distinctly attracted to the walls,

so the signal is stronger. When the payload is electrically isolated, a small negative voltage builds up on the skins due to the electron current from the filament. In this case, the electrons have difficulty impacting the skins and have more opportunity to produce signal on the detectors, so the signal is higher. When the skin voltage becomes larger, however, the electrons are repelled from the detector bulkhead making it more difficult to interact with the detector, and the signal begins to drop again.

Preliminary testing showed the positive ion repeller grid to have an extremely ambiguous effect on the filament signal. Table 4.6 demonstrates this frustrating effect. The variability of the

Table 4.6: Filament Variability

Date	Positive Grid	Count Rate	Effect
10/6	Off	∼6	Increases Signal
	On	∼100	
10/7	Off	∼50	Decreases Signal
	On	∼15	
10/8	Off	∼2	No Effect
	On	∼3	
12/11	Off	∼60	Decreases Signal
	On	∼2	
12/14	Off	∼3500	Decreases Signal
	On	∼1	
12/15	Off	∼150	Increases Signal
	On	∼400	

filament makes it very difficult to interpret the true effect of the positive repeller grid. However, tests were also run in which the grid was turned on or off in the middle of an exposure. In every case in which this was done (12/11 and 12/14 tests in Table 4.6, as well as later testing), the positive grid had the effect of reducing the signal from the filament. This is not a completely intuitive result. We might expect the filament signal to respond in a fashion opposite to that of the ion gauge, since the particles produced are of opposite charge. Presumably, electrons are attracted to the positive grid and are lost in similar fashion to the ions when a negative voltage is applied to the skins. Thus, we have evidence that the positive repeller grid suppresses the electron signal as well as the ion signal. It is clear, however, that the suppression of the electron signal is much weaker

than that of the ion signal. Unfortunately, it is difficult to accurately quantify the suppression due to the natural variability of the filament.

The effect of a negatively charged repeller grid was tested, both alone and in conjunction with the positive repeller grid. These tests were run with the filament quite far from the detectors, leading to very low signal and low-quality results. Nevertheless, we discuss the results here, as they are still instructive. Table 4.7 shows the effect of the negative repeller grid. When the positive grid

Table 4.7: The Effect of the Negative Repeller Grid

Positive Grid OFF		Positive Grid ON (+100 V)	
Grid Voltage	Count Rate	Grid Voltage	Count Rate
Off	∼5 Hz	Off	∼1 Hz
-50 V	∼15 Hz	-50 V	∼1 Hz
-400 V	∼11 Hz	-400 V	∼1 Hz

is turned off, the negative repeller grid surprisingly serves to increase the electron signal. Powering the grid to -50 V may result in a weaker electric field at the position of the grid than would result from the detector alone. This might allow electrons to get closer to the detector before being suddenly exposed to the window voltage leading to higher signal. As the voltage is increased, the grid repels electrons more strongly, causing the signal to decline again.

Similar tests were run with both grids functional. We found, however, that the signal was too low to draw many substantial conclusions. The low signal was partially due to the placement of the filament far from the detectors in the payload interior. Also, the filament power supply achieved a maximum current that was substantially lower than normal. This is unfortunate as these tests were, in many ways, the most important to suppressing OGRESS' flight noise. The test is not a total loss, however. Based on the previous tests in the same configuration (shown on the left of Table 4.7), we know that some signal is being successfully emitted from the filament. Thus, the apparently null results show that the negative repeller grid is incapable of undoing the effect of the positive grid when observing electrons. The positive grid will lower the electron signal even when the negative grid has a higher voltage. This is quite distinct from its effect on ions. We now know

that adding a negative repeller grid of -50 V will not enhance the signal from ions or electrons. It is possible, even likely, that the electron signal is further suppressed by the negative repeller grid when the positive grid is also present. Unfortunately, the low signal levels of our tests do not allow us to confirm this.

4.4 Overall Test Results

Post-flight testing with two Fe-55 sources (see Fig. 3.25) confirmed that the detectors' window bar shadows are affected by the angle of incoming light and can therefore be suppressed in the presence of diffuse signal. This shows that our favored theory of internal fluorescence is a plausible explanation for the flight noise.

We have confirmed that ions interact with the detectors, repeller grids, and charged skins in the ways we expect and that our instrument in insensitive to ions in flight conditions. In some ways, the ion repeller grids were a great success, as they perform their intended task very well. This is important, as it shows that the flight noise was not simply due to malfunctioning hardware.

We are able to draw more tentative conclusions about OGRESS' response to electrons. The PHD of our laboratory electron signal can be adequately modeled with a fluorescence spectrum, but the best-fit parameters are distinctly different from those of the flight data. This indicates that electrons may not explain the flight noise in its entirety. Our electron source, the Manson filament, had an extremely variable output making the results of our tests very uncertain. The results of the testing can only be considered qualitative due to the large uncertainties in the source output. Nevertheless, the electron data do point in certain directions, and there are some important results worth noting:

1) The detectors can see signal in the presence of thermal electrons, even when the positive repeller grid (or in this case attractor grid) is turned on. Thus, ionospheric electrons are an expected source of signal contamination during flight.

2) Charging the payload skins has a noticeable effect on the electron (and ion) signal. At several negative volts or less, the ion signal is suppressed, and the electron signal is amplified. This

supports the theory that electrons, and not ions, are the source of flight noise.

3) The addition of a negative repeller grid to our system does not increase the ion signal as long as its voltage magnitude is substantially less than that of the positive repeller grid. As long as the positive grid is powered, the negative grid does not appear to increase the electron signal, even when the negative grid is held at a substantially higher voltage. Thus, the addition of a negative repeller grid can be considered safe for the instrument. Further testing is needed to determine whether the negative grid results in an actual *decrease* in electron signal.

Chapter 5

Discussion & Conclusions

5.1 Future Work

Although we have made substantial progress in understanding the flight noise, much work remains to be done. This work falls into three main categories: 1) instrument calibration, 2) flight simulation/testing, and 3) noise corrections.

5.1.1 Instrument Calibration

Although OGRESS has been tested extensively, there are some important calibrations which should be carried out to provide improved confidence in the instrument's abilities. The estimated count rate from Cygnus is quite low, so it is important to verify that OGRESS' throughput is not degraded from its theoretical value.

The off-plane grating arrays have not been fully calibrated since being used on the CyXESS payload. Thus, they have had over 10 years to become damaged, oxidized, corroded, or otherwise degraded from their theoretical efficiency. Even for CyXESS, the gratings were only calibrated at 277 eV, so it has never been known whether the true efficiency followed the theoretical curves at higher or lower energies. Laboratory testing of OGRESS has shown that the gratings still successfully disperse X-rays, but the quantitative efficiency and scatter properties are unknown. Substantial degradation of the gratings is a very real possibility which could easily ruin OGRESS' chances of successfully observing Cygnus, even if the noise issues are solved.

OGRESS has also never been tested with a diffuse X-ray source. The reason for this is

that it is very difficult to fabricate a source which fills the entire field of view of the focusers. A diffuse X-ray source was designed and fabricated for CODEX but never fully implemented due to time constraints. The source consisted of an aluminum plate which was coated with a layer of carbon. The plate is intended to be illuminated with high-energy X-rays from a Manson source and to subsequently fluoresce C-Kα. OGRESS was not tested with this source due to a change in available facilities. The plate source was intended to be used with OGRESS in the, so called, Long Tank at the University of Colorado. The Long Tank is a vacuum chamber large enough to comfortably fit a 22" diameter rocket payload. The payload would be installed in the Long Tank with the illuminated plate source stationed directly in front. OGRESS was assembled and tested at the University of Iowa which did not have a comparable vacuum chamber available. Vacuum testing for OGRESS was carried out by sealing the payload and pumping down its interior. The plate source designed for CODEX is too large to fit inside the payload. Before being flown again, OGRESS should be tested with a diffuse source, either by finding a suitable vacuum chamber to utilize CODEX's plate source or by designing a more compact source that can fit inside OGRESS. These tests would confirm that diffuse light is appropriately vignetted by the focuser structures without scattering onto the detectors from unwanted angles.

5.1.2 Flight Simulation/Testing

There are some flight conditions which have not been adequately tested in the laboratory. For instance, OGRESS turned on its detectors very shortly after experiencing intense launch vibrations. OGRESS went through vibration testing to confirm that functionality was maintained after experiencing launch-like vibrations, but the detectors have never been promptly turned on (within $\sim$1 minute) after vibration. It is possible that launch vibrations have a detrimental, but transient, effect on the detectors which only manifests for 10–20 minutes before disappearing. Vibrations may liberate dust or other contaminants within the detectors, produce a transient leak in the detectors or gas system, or confuse pressure sensors. Each of these effects could lead to modified detector behavior. This test has not been carried out because the payload pressure cannot be maintained

at a sufficiently low level to prevent arcing when the detectors turn on. All external pumps must be removed from the payload before beginning vibration. This problem could be solved with the addition of an interior getter pump, which would maintain low pressures long enough for the test to be carried out.

In flight, the payload is completely electrically isolated from ground. This has never been carried out in a laboratory setting. While testing spacecraft charging, OGRESS had a voltage applied to its chassis, but was never truly electrically isolated. There was always a connection to the power supply return line via a resistor. Thus, there has always been a pathway for electrons to bleed away from the detector interior, and we have never been able to adequately test whether the electron reservoir inside the payload can be maintained for 10 seconds or more. This test would require using batteries to power the payload.

Finally, the payload's response to electrons must be retested with a stronger and more stable electron source. This is required to fully understand the effects of using a 2-layer (positive and negative) repeller grid and whether or it can simultaneously suppress ion and electron signal.

5.1.3 Payload Modifications

There are many payload modifications which can be made and tested to suppress the flight noise. The most reliable method would probably be to make new GEM detectors which have grounded windows. This is not a trivial task, as the detector anode would need to be held at high voltage and yet connected to the low voltage preamplifiers. Much of the detector electronics would also have to be redesigned. Although this process would be expensive and time-consuming it is almost certain to remove the primary sources of noise – charged particles. In the absence of high voltage, ions and electrons would no longer generate signal on the detector.

Another modification which could suppress ion and electron noise would be the addition of two metal plates to the payload interior. If the plates were held at voltage (say ± 100 V), they would act as pumps to remove ions and electrons from the payload interior.

A simple modification which is likely to yield positive results would be more thorough baffling

of the detectors. OGRESS' detectors are completely unbaffled at present, because X-rays are not expected to scatter enough to warrant it. However, we have strong evidence that charged particles and/or interior fluorescence X-rays approach the detectors from wide angles. This contaminating signal could be substantially reduced by simple baffling techniques. This would, of course, also reduce the contaminating signal from scattered light, however weak that signal may be.

Finally, a 2-layer repeller grid utilizing both positive and negative voltages may be able to suppress signal from both ions and electrons. Preliminary testing has already shown that such a setup would have no detrimental effects. It remains to be seen whether a 2-layer grid actually decreases the electron signal.

5.1.4 Future Flight Plan

OGRESS' flight plan was designed to include both dark calibration and sky background calibration of the instrument. These tests were very useful, despite (or perhaps due to) the large amount of noise suffered by OGRESS during flight. If OGRESS is flown again, more substantial in-flight calibrations could shed considerably more light on the nature of OGRESS' flight noise and could reveal which countermeasures are truly effective. I would use the following flight plan for OGRESS' next launch:

1) Turn the detectors on before the shutter door opens (with no repeller grids). This would require the use of getter pumps to maintain adequately low pressure. This is the most important change to OGRESS' current flight plan. Because the payload interior will not have equilibrated with the surrounding ionosphere, this test will unambiguously verify whether the noise is internal or external to the detectors.

2) Open the shutter door and observe a dark patch of sky.

3) Turn on the positive repeller grid. Observe the change in signal.

4) Turn on the negative repeller grid, metal plates, or other additions one at a time. Observe the change in signal caused by each item. Ideally, any sources of noise will be suppressed by the end of this step, and the most useful components for noise suppression will be known.

5) Switch between dark sky and Cygnus, as before.

6) Close the shutter door.

7) Keep detectors turned on until reentry, or as long as possible. If the signal continues after the door closes, a longer observing time may allow us to see whether the signal is slowly changing.

This flight plan is intended to provide better calibrations and better understanding of each component of the instrument in flight conditions. This plan should also help distinguish between the different types of signal we are likely to observe. This is important, due to the difficulty of simulating flight conditions in a laboratory. Step 1, for instance, will give complete certainty about whether the flight noise is an external signal or internal to the detectors and electronics. Step 4 will unambiguously show the effects and levels of success of each noise-suppressing modification that has been implemented. Step 5 will provide our sky background signal, hopefully much reduced from the previous launch. Step 7 will increase our chances of seeing a change in signal, in the case that an internal electron population is maintained.

5.2 Discussion

5.2.1 The Noise

One of the great unresolved question associated with our flight results is: Why don't other missions appear to suffer from OGRESS' problems? If our signal is due to internal fluorescence, we might expect this to be a common and well-documented effect. Many suborbital missions utilize high-voltage detectors and are not swamped by noise. What makes this such an issue for OGRESS?

The main problem for OGRESS likely lies in the fact that the science signal is so weak. At the low count rate anticipated, even Poisson noise would ensure that OGRESS' spectrum would have relatively low S/N. Other missions in the UV and X-ray generally expect to have count rates of several hundred Hz or more. They also typically accomplish this with much smaller detectors than the GEMs used on OGRESS. The size of the detector acts as the collecting area for internally

produced X-rays, so a smaller detector would collect substantially less of this contaminating signal. Combined with the high count rates from their science targets, the typical UV or X-ray sounding rocket will be far less affected by internal fluorescence than OGRESS is. Because conditions are not as well understood or controlled, increased background levels are generally expected during spaceflight, so a mild increase in noise due to internal fluorescence may not motivate investigation for the typical suborbital mission.

Other missions, particularly those working in the UV, typically baffle their optical systems far more thoroughly than OGRESS. In the UV, scattered light is a serious problem, and baffling ensures that light approaches the detector(s) from the appropriate direction. This baffling would also naturally block signal from charged particles and internal fluorescence. Thus, internal fluorescence may be a problem that is accidentally solved on most missions.

Finally, internal fluorescence will only be present for instruments which have exposed high voltage to accelerate electrons. Standard gas proportional counters and CCD detectors will never suffer from internal fluorescence, as they operate at low voltage. This substantially reduces the number of payloads which are comparable to OGRESS in their detector voltage and bandpass of interest.

5.2.2 Reflying OGRESS

Because science and technology development moves forward rapidly, a discussion is warranted as to whether OGRESS is worth flying again. Instruments are often made obsolete by new technical developments or by other missions which can accomplish their science goals more effectively. Despite the substantial timespan between its original conception (as CyXESS) and present day, OGRESS still has an important role to play in the progress of X-ray science and technology. In the introduction of this document, OGRESS was compared to the current workhorses of X-ray astronomy – *Chandra*, *XMM-Newton*, and *Suzaku* – and found to provide important unique scientific capabilities. To warrant a future mission, OGRESS must also stand up to missions which are currently funded, but have not yet launched. In this section, we will compare OGRESS' capabilities

with several missions slated for future launches and show that OGRESS is still highly relevant.

OGRESS' main strengths compared to other instruments are its large FOV and its ability to probe below 0.3 keV. Other instruments are limited to observing above 0.3 keV, consequently missing many important diagnostic spectral lines in the 1/4 keV band. With FOVs substantially smaller than that of OGRESS, other instruments are also limited to observing smaller objects which will generally be more distant and more highly absorbed.

5.2.2.1 Athena

The Advanced Telescope for High Energy Astrophysics (Athena) is the next X-ray flagship mission selected by the European Space Agency (Nandra [2013]). Athena intends to generate a transformational leap in our understanding of two key questions: 1) how does ordinary (non-dark) matter assemble into the large-scale structures that we see today? and 2) how do black holes grow and shape the universe? Athena will answer these questions with spatially resolved X-ray spectroscopy. Fine spatial resolution will allow uncontaminated spectroscopy of small objects, such as black hole accretion disks, as well as spatially resolved spectroscopy of diffuse extended sources, such as the galactic halo and Intercluster Medium.

As the next great X-ray observatory, Athena will probe dimmer targets at higher redshifts with higher spectral resolution than ever before. Despite its many strengths, the instrument will have its limitations. In high-resolution mode, Athena's FOV is only 5' across. Thus, any diffuse targets observed by Athena must be very far away. Observing an object as large as the Cygnus Loop is out of the question for Athena. Also, Athena's energy range only extends down to 0.3 keV, missing the bulk of the 1/4 keV band and many important diagnostic spectral lines.

Athena's greatest weakness when compared to OGRESS is its nominal launch date of 2028. OGRESS, in contrast, can be calibrated, upgraded, and ready to fly again in < 2 years. Thus, OGRESS can contribute to science and technology development now, rather than in the distant future.

5.2.2.2 Astro-H

The Astro-H, or Hitomi, satellite (Takahashi [2013]) was an explorer-class mission similar in many ways to Athena, though scaled down substantially in its capabilities. Astro-H would have complemented OGRESS' capabilities with spatially resolved X-ray spectroscopy and excellent spectral resolution. Astro-H's sensitivity, however, only extended down to 0.3 keV, missing most of the 1/4 keV bandpass. Also, Astro-H's field of view was much smaller than that of OGRESS, so observing Cygnus in its entirety would still have taken considerable time. Unfortunately, Astro-H suffered a failure shortly after launch and became inoperable. This provides an example of the importance of low-budget technology demonstration missions, as many problems can be found and resolved before investing in a long-term high-budget mission.

5.2.2.3 OGRE

The Off-plane Grating Rocket Experiment (OGRE) is OGRESS' younger sibling, being funded on the same NASA grant and scheduled to launch in late 2018 (Tutt et al. [2015]). OGRE is pushing the boundaries of many X-ray technologies. OGRE utilizes polished silicon optics, radially grooved blazed off-plane gratings, and electron-multiplying CCD detectors. OGRE will observe Capella and demonstrate resolving powers of > 1000 from 0.2-1.0 keV. OGRE probes to significantly lower energies than Athena and Astro-H, but still does not reach the down to 0.1 keV, as OGRESS does. Also, OGRE is a slitless spectrograph and thus has the same resolution problems that *Chandra* and *XMM* do when observing point sources: the resolution degrades with the size of the target. Thus, OGRE is only suitable for observing point sources, rather than the extended sources sought by OGRESS.

5.2.2.4 X-ray Polarimetry Missions

Two explorer-class X-ray polarimetry missions were awarded Phase A funding in July of 2015. The missions, the Imaging X-ray Polarimetry Explorer (IXPE) and the Polarimeter for Relativistic Astrophysical X-ray Sources (PRAXyS), both intend to use X-ray polarimetry to explore black

holes, neutron stars, and SNRs (Weisskopf et al. [2014] and Kallman et al. [2016]). Because the instruments are polarimeters, rather than spectrometers, their capabilities do not overlap with those of OGRESS. Thus, OGRESS provides highly complementary capabilities to IXPE and PRAXyS, particularly for SNRs.

IXPE and PRAXyS utilize GEM detectors (in a different geometry than OGRESS) as time-projection chambers to determine the polarization of incident photons. Thus, there is overlap in the technology development of these missions and OGRESS. OGRESS remains the only mission to fly GEM detectors in space, thus its results are important for the success of these polarimetry missions. In particular, these missions may be victims of the same internal fluorescence noise which OGRESS experienced. Thus, OGRESS can play an important role by rapidly finding and demonstrating a solution to this problem. This can enable IXPE and PRAXyS to implement a similar solution to produce better signal to noise ratios of their measurements – and possibly to avoid a catastrophic failure of an explorer-class mission.

5.2.2.5 Microcalorimetry Rockets

Micro-X (a funded sounding rocket) and TEST Pilot (applying for funding at the time of writing) are sounding rockets which utilize microcalorimeters to enable spatially resolved X-ray spectroscopy (Figueroa-Feliciano [2014] and Zeiger et al. [2013b]). These are technology demonstration missions which aim to improve the state-of-the-art of microcalorimeters from Astro-H's capabilities to Athena's capabilities. Unlike Astro-H and Athena, these missions can produce high-quality science within the next several years.

OGRESS complements these instruments in the same way that it complements Athena and Astro-H. Micro-X and TESTPilot have small FOVs preventing them from observing targets as large as the Cygnus Loop. They cannot observe below 0.3 keV, once again missing the diagnostic lines in the 1/4 keV band. Also, their observations at low energies will have low resolving power. OGRESS accompanies these missions very well by supplying high resolution at low energies, while Micro-X and TEST Pilot supply high resolution at high energies.

5.2.2.6 OGRESS' Technological Importance

It is important for the entire field of X-ray astrophysics (and astrophysics, in general) that multiple avenues of technology development be pursued, because it is never known *a priori* which techniques will produce the best results for various scientific questions. OGRESS is currently the only low-budget mission capable of testing and developing GEM detectors. NASA has made it clear by funding IXPE and PRAXyS that these detectors are an important tool for X-ray polarimetry as well as X-ray spectroscopy. Thus, it is important to continue to fly OGRESS for its applicable technology development (for polarimetry missions) as well as it complementary spectroscopic capabilities (to microcalorimeter instruments and OGRE).

5.2.2.7 OGRESS' Scientific Importance

OGRESS remains the only mission capable of observing large diffuse X-ray sources in the near (or distant) future. Many important objects and phenomena are observable only with OGRESS' capabilities including: nearby SNRs and clouds, the galactic Soft X-ray Background (SXB), and Solar Wind Charge Exchange (SWCX). These phenomena are at their most unexplored in the 1/4 keV band which other instruments cannot reach. In the introduction, we focused on observing SNRs and their importance to the ISM and galactic evolution. The SXB and SWCX are also extremely important for X-ray astrophysics as they are local phenomena that contaminate virtually every X-ray observation ever taken. This alone is enough to warrant thorough investigation. They are also scientifically interesting in their own right.

The SXB consists of unabsorbed highly anisotropic emission in the 1/4 keV band. This emission must be produced locally, as X-rays at such low energies are rapidly absorbed by galactic gas and dust. The flux is believed to originate from a hot, ionized ISM close to the sun (40-130 pc) known as the Local Hot Bubble (LHB) (Snowden et al. [1998]). The strength of this background puts a limit on the dimness of targets that can be observed. High-spectral-resolution measurements make this background all the more important to understand, as it will not necessarily be known

which lines are coming from the science target, the SXB, or both. In addition to understanding an important source of noise, better measurements of the SXB are important for understanding the local conditions in the galaxy.

SWCX occurs in Earth's geocorona and the Sun's heliosphere when neutral atoms transfer electrons in collisions with heavy solar wind ions. The ions emit X-rays as the electrons cascade to lower states. This emission is highly correlated with solar activity, as it depends on the strength of the solar wind. This phenomenon was first noticed by Snowden et al. [1994] who found a time-varying background component in the ROSAT All-Sky Survey data. These periods of high flux were dubbed Long Term Enhancements (LTEs), as they typically lasted longer than a single pointing. At periods of high activity, the flux from SWCX can be as great as the galactic SXB. As with the SXB, high-resolution spectra have never been achieved for SWCX, leading to a lack of understanding of an important noise source for celestial X-ray measurements. It also implies a lack of understanding for conditions within the heliosphere and Earth's upper atmosphere. OGRESS' flight results are just one example of how a lack of understanding (or appreciation) of local conditions can lead to observational problems.

OGRESS is the only existing (or planned) instrument capable of observing the galactic SXB, SWCX, and large nearby SNRs in the 1/4 keV band. Thus, reflights of OGRESS can make substantial contributions to Earth science, heliophysics, and X-ray astrophysics.

5.2.2.8 OGRESS 2.0

I have already noted some useful upgrades and modifications that can be made to OGRESS. The modifications discussed in Section 5.1.3, are relatively minor with no need for a fully redesigned instrument. A full-scale redesign and rebuild could produce an instrument with vastly improved capabilities. OGRESS' greatest weakness in performance is its low throughput, resulting in low S/N and allowing sources of noise (like internal fluorescence) to dominate the science signal. A redesigned and upgraded OGRESS 2.0 can achieve throughput an order of magnitude higher than the original OGRESS.

The most obvious change is to design an instrument with a full complement of 6 focuser modules, rather than the 2 utilized by OGRESS. 6 modules was originally the end goal for the instrument prior to the modifications made to the CODEX payload. This will increase the instruments effective area by a factor of 3.

Improvements in grating technology can also improve OGRESS' capabilities. In recent years, Randall McEntaffer's group at the University of Iowa (and now Pennsylvania State University) has developed new techniques to fabricate radially grooved blazed off-plane grating arrays (DeRoo et al. [2016]). In addition to removing grating abberations (and thereby producing improved resolution), the blaze of the gratings is capable of concentrating the diffracted light into a single order of choice. Unlike OGRESS' gratings which diffract into both positive and negative spectral orders, blazed gratings can diffract all of the light into positive (or negative) orders. Blazed gratings can thus improved OGRESS' throughput by a factor of two in the 1/4 keV band where OGRESS only samples positive spectral orders.

OGRESS' detectors can also be upgraded. In the current instrument, nearly half of the signal is lost at the detector due to the mechanical transmission of the stainless steel window support mesh. The window manufacturer for OGRESS (LUXEL Corporation) has recently made advances in their window support structures that allow substantially increased transmission. By using newer window support structures, OGRESS' throughput can be increased by up to a factor of 1.5. In addition to increasing the geometric transmission, the absorption in the polyimide detector windows can be reduced by using thinner windows. Because OGRESS operates at lower pressure than its predecessors, the window can be made correspondingly thinner. This is a more minor effect, but it has the potential to increase the instrument's throughput by 15-20%.

These upgrades to OGRESS would improve the throughput of the instrument by an order of magnitude. This would extend OGRESS' observational targets from the Cygnus Loop and Vela SNRs to include much dimmer objects like the North Polar Spur, the Eridanus X-ray enhancement, the SXB, and SWCX. OGRESS 2.0 would be the undeniable powerhouse instrument for observing large diffuse X-ray sources.

5.3 Conclusion

OGRESS is a soft X-ray spectrograph designed to observe diffuse X-ray sources between 0.1 – 1 keV. Wire-grid passive "focusers" create a converging beam which is diffracted with off-plane grating arrays onto Gaseous Electron Multiplier detectors. OGRESS' wide field of view allows it to observe the Cygnus Loop supernova remnant in its entirety. By using dispersive optics, OGRESS can provide resolving power several times higher than state-of-the-art orbiting observatories, which must rely on the poor energy resolution of their detectors to spectrally analyze such a large target. OGRESS thus provides the opportunity to understand Cygnus on a global level by determining the global elemental abundances, ionization state, and dominant emission mechanism of the remnant.

OGRESS launched from White Sands Missile Range on May 2nd, 2015 and spent ∼280 seconds observing Cygnus. The remaining ∼ 70 seconds was spent observing dark sky for background calibration. During flight, OGRESS experienced a much higher count rate than expected and observed no difference between the dark sky and Cygnus. This behavior is attributed to the presence of ionospheric electrons which are exposed to the high-voltage detector windows and subsequently cause collisional excitation and X-ray fluorescence of the payload interior. Due to the intrinsically low level of signal from Cygnus, this noise dominates the flight signal causing the science target to be lost.

Post-flight testing confirmed that electrons produce signal on the detectors. There are indications that the addition of a negatively charged repeller grid could suppress the electron signal by shielding the electric field of both the positive ion repeller grid and negative high-voltage detector window. These findings are tentative due to the low strength and large variability of our electron source. Further testing with a stronger and more stable source is required to confirm these results. If the flight noise can be successfully suppressed, OGRESS can provide the first global spectrum of the Cygnus Loop with the highest resolving power ever achieved for soft X-rays.

Bibliography

R. G. Arendt, E. Dwek, and D. Leisawitz. Infrared emission from x-ray and optically emitting regions in the cygnus loop supernova remnant. The Astrophysical Journal, 400:562–578, 1992.

K. Arnaud, B. Dorman, and C. Gordon. Xspec. an x-ray spectral fitting package. user's guide for version 12.9.0. HEASARC, Astrophysics Science Division, NASA/GSFC, 805, 2015.

B. Aschenbach and D. Leahy. Rosat all-sky survey map of the cygnus loop: Overall structure and comparison with radio map. Astronomy and Astrophysics, 341:602–609, 1999.

J. Ballet, J. Caplan, R. Rothenflug, D. Dubreuil, and A. Soutoul. Fabry-perot observations of [fe x] and [fe xiv] in the cygnus loop. Astronomy and Astrophysics, 211:217–229, 1989.

S. Bauer and R. E. Bourdeau. Upper atmosphere temperatures derived from charged particle observations. Journal of the Atmospheric Sciences, 19:218–225, 1962.

P. Benvenuti, M. Dopita, and S. D'Odorico. Far-ultraviolet spectrophotometry of supernova remnants: Observations and astrophysical interpretation. The Astrophysical Journal, 238:601–613, 1980.

W. P. Blair, K. S. Long, O. Vancura, C. W. Bowers, A. F. Davidsen, W. V. D. Dixon, S. T. Durrance, P. D. Feldman, H. C. Ferguson, R. C. Henry, R. A. Kimble, G. A. Kriss, J. W. Kruk, H. W. Moos, and T. R. Gull. Discovery of a fast radiative shock wave in the cygnus loop using the hopkins ultraviolet telescope. The Astrophysical Journal, 379:L33–L36, 1991.

W. P. Blair, R. Sankrit, J. C. Raymond, and K. S. Long. Distance to the cygnus loop from hubble space telescope imaging of the primary shock front. The Astronomical Journal, 118:942–947, 1999.

W. P. Blair, R. Sankrit, and J. C. Raymond. Hubble space telescope imaging of the primary shock front in the cygnus loop supernova remnant. The Astronomical Journal, 129:2268–2280, 2005.

A. Bondar, A. Buzulutskov, F. Sauli, and L. Shekhtman. High- and low-pressure operation of the gas electron multiplier. Nuclear Instruments and Methods in Physics Research, 419:418–422, 1998.

A. Bondar, A. Buzulutskov, and L. Shekhtman. High pressure operation of the triple-gem detector in pure ne, ar and xe. Nuclear Instruments and Methods in Physics Research, 481:200–203, 2002.

R. Borken, R. Doxsey, and S. Rappaport. A soft x-ray survey of the galactic plane from cygnus to norma. The Astrophysical Journal, 178:L115–L120, 1972.

R. Braun and R. Strom. The structure and dynamics of evolved supernova remnants. shock-heated dust in the cygnus loop. Astronomy and Astrophysics, 164:208–217, 1986.

M. T. Cash. Cross-stitch based on the results of rappaport et al. (1973). Astrophysical Needlework, 1(1), 1974.

W. Cash. Echelle spectrographs at grazing incidence. Applied Optics, 21(4), 1982.

R. A. Chevalier. The interaction of supernovae with the interstellar medium. Ann. Rev. Astron. Astrophys, 15:175–196, 1977.

G. Cillié. The hydrogen emission in gaseous nebulae. Monthly Notices of the Royal Astronomical Society, 92:820, 1932.

M. Contini and G. Shaviv. Ultraviolet spectra of the cygnus loop - depletion of the heavy elements. Astrophysics and Space Sciences, 85:203–219, 1982.

E. Costa, P. Soffitta, R. Bellazzini, and A. Brez. An efficient photoelectric x-ray polarimeter for the study of black holes and neutron stars. Nature, 411:662–665, 2001.

R. Cumbee, D. Henley, P. Stancil, R. Shelton, J. Nolte, Y. Wu, and D. Schultz. Can charge exchange explain anomalous soft x-ray emission in the cygnus loop? The Astrophysical Journal, 787(L31), 2014.

C. W. Danforth, R. H. Cornett, N. Levenson, W. P. Blair, and T. P. Stecher. A comparison of ultraviolet, optical, and x-ray imagery of selected fields in the cygnus loop. The Astronomical Journal, 119:2319–2331, 2000.

C. DeRoo, R. McEntaffer, D. Miles, T. Peterson, H. Marlowe, J. Tutt, B. Donovan, B. Manz, V. Burwitz, G. Hartner, R. Allured, R. Smith, R. Gunther, A. Yanson, G. Vacanti, and M. Ackermann. Line spread functions of blazed off-plane gratings operated in the littrow mounting. eprint arXiv: 1603.04839, pages 1–25, 2016.

R. A. Fesen, W. P. Blair, and R. P. Kirshner. Spectophotometry of the cygnus loop. The Astrophysical Journal, 262:171–188, 1982.

R. A. Fesen, K. B. Kwitter, and R. A. Downes. H-alpha images of the cygnus loop: A new look at shock-wave dynamics in an old supernova remnant. The Astronomical Journal, 104(2), 1992.

E. Figueroa-Feliciano. The micro-x high-energy-resolution microcalorimeter x-ray imaging rocket. American Astronomical Society, HEAD meeting, 2014.

P. Gorenstein, B. Harris, H. Gursky, R. Giacconi, R. Novick, and P. V. Bout. X-ray structure of the cygnus loop. Science, 172:369–372, 1971.

R. Grader, R. Hill, and J. Stoering. Soft x-rays from the cygnus loop. The Astrophysical Journal, 161:L45–L50, 1970.

J. Graham, G. Wright, J. Hester, and A. Longmore. H_2 excitation by magnetic shock precursor in the cygnus loop supernova remnant. The Astronomical Journal, 101(1), 1991b.

J. R. Graham, G. S. Wright, and T. Geballe. The h_2 line profiles in the cygnus loop: Evidence for j-shocks with magnetic precursors. The Astrophysical Journal, 372:L21–L24, 1991a.

E. Gronenschild. X-ray observations of the cygnus loop by ans. Astronomy and Astrophysics, 85: 66–76, 1980.

M. Haungs. A brief table of x-ray line energies and widths. SRON Online Database, 1986.

A. Hedin and A. O. Nier. A determination of the neutral composition, number density, and temperature of the upper atmosphere from 120 to 200 kilometers with rocket-borne mass spectrometers. Journal of Geophysical Research, 71(17), 1966.

J. J. Hester and D. P. Cox. The cygnus loop: A detailed comparison of x-ray and optical emission. The Astrophysical Journal, 300:675–697, 1986.

H. Inoue, K. Koyama, M. Matsuoka, T. Ohashi, and Y. Tanaka. Emission line features in the soft x-ray spectra of the north polar spur and the cygnus loop. The Astrophysical Journal, 238: 886–891, 1980.

V. Istomin. Investigation of the ion composition of the earth's atmosphere on geophysical rockets 1957-1959. Planet. Space Sci., 9:179–193, 1962.

K. Jahoda. The gravity and extreme magnetism small explorer. Proc. of SPIE, 7732(773220W-1), 2010.

J. S. Kaastra, R. Mewe, and T. Raassen. New results on x-ray models and atomic data. Atomic Data for X-Ray Astronomy, 25th meeting of the IAU, Joint Discussion 17, 22 July 2003, Sydney, Australia 17, 2003.

S. M. Kahn, P. A. Charles, and S. Bowyer. X-ray line emission from the cygnus loop. The Astrophysical Journal, 242:L19–L22, 1980.

T. Kallman, K. Jahoda, C. Kouveliotou, and T. P. Team. Polarization from relativistic astrophysical x-ray sources: The praxys small explorer observatory. American Astronomical Society, HEAD meeting, 2016.

D. Kaplan, B. Gaensler, S. Kulkarni, and P. Slane. An x-ray search for compact central sources in supernova remnants. ii. six large-diameter snrs. The Astrophysical Journal Supplement Series, 163:344–371, 2006.

M. Kasha. The ionosphere and its interaction with satellites. 1969.

S. Katsuda, H. Tsunemi, M. Kimura, and K. Mori. *Chandra* observations of the northeastern rim of the cygnus loop. The Astrophysical Journal, 680:1198–1205, 2008.

S. Katsuda, H. Tsunemi, K. Mori, H. Uchida, H. Kosugi, M. Kimura, H. Nakajima, S. Takakura, R. Petre, J. W. Hewitt, and H. Yamaguchi. Possible charge-exchange x-ray emission in the cygnus loop detected with *Suzaku*. The Astrophysical Journal, 730(24), 2011.

S. Katsuda, H. Tsunemi, K. Mori, H. Uchida, R. Petre, S. Yamada, and T. Tamagawa. Discovery of a pulsar wind nebula candidate in the cygnus loop. The Astrophysical Journal, 754(L7), 2012.

R. P. Kirshner and K. Taylor. High-velocity gas in the cygnus loop. The Astrophysical Journal, 208:L83–L86, 1976.

M. Kundu and R. Becker. Observations of the cygnus loop at 6-cm wavelength. The Astronomical Journal, 77(6), 1972.

D. Leahy. X-ray spectrum variations in the south-west cygnus loop. Monthly Notices of the Royal Astronomical Society, 351:385–398, 2004.

D. Leahy and M. Hassan. Joint *Suzaku* and *XMM-Newton* spectral analysis of the southwest cygnus loop. The Astrophysical Journal, 764(55), 2013a.

D. Leahy and M. Hassan. Joint suzaku and xmm-newton spectral analysis of the southwest cygnus loop. The Astrophysical Journal, 764:55–64, 2013b.

D. Leahy, R. Roger, and D. Ballantyne. 1420 mhz continuum and polarization observations of the cygnus loop. The Astronomical Journal, 114, 1997.

D. A. Leahy and R. Roger. Radio spectral index variations in the cygnus loop. The Astrophysical Journal, 505:784–792, 1998.

N. Levenson, J. Graham, B. Aschenbach, W. Blair, W. Brinkmann, J. Busser, R. Egger, R. Fesen, J. Hester, S. Kahn, R. Klein, C. McKee, R. Petre, R. Pisarski, J. Raymond, and S. L. Snowden. The rosat hri x-ray survey of the cygnus loop. The Astrophysical Journal, 484:304–312, 1997.

N. Levenson, J. R. Graham, L. D. Keller, and M. J. Richter. Panoramic views of the cygnus loop. The Astrophysical Journal, 118:541–561, 1998.

N. Levenson, J. R. Graham, and S. Snowden. The cygnus loop: A soft-shelled supernova remnant. The Astrophysical Journal, 526:874–880, 1999.

N. Levenson, J. R. Graham, and J. L. Walters. Shell shock and cloud shock: Results from spatially resolved x-ray spectroscopy with *CHANDRA* in the cygnus loop. The Astrophysical Journal, 576:798–805, 2002.

J. McCoy, T. Schultz, J. Tutt, T. Rogers, D. Miles, and R. McEntaffer. A primer for telemetry interfacing in accordance with nasa standards using low cost fpgas. Journal of Astronomical Instrumentation, 5(1), 2016.

R. McCray and T. Snow. The violent interstellar medium. Ann. Rev. Astron. Astrophys., 17: 213–240, 1979.

R. McEntaffer and T. Brantseg. *Chandra* imaging and spectroscopy of the eastern xa region of the cygnus loop supernova remnant. The Astrophysical Journal, 730(99), 2011.

R. L. McEntaffer. Soft X-ray spectroscopy of the Cygnus Loop. PhD thesis, University of Colorado, 2007.

R. Minkowski. Cygnus loop and some related nebulosities. Reviews of Modern Physics, 30(3), 1958.

E. Miyata and H. Tsunemi. Reflection-shocked gas in the cygnus loop supernova remnant. The Astrophysical Journal, 552:624–638, 2001.

E. Miyata, S. Katsuda, H. Tsunemi, J. P. Hughes, M. Kokubun, and F. S. Porter. Detection of highly-ionized carbon and nitrogen emission lines from the cygnus loop supernova remnant with the suzaku observatory. Publ. Astron. Soc. Japan, 59:S163–S170, 2007.

P. Moffat. The cygnus loop at 1420 mhz. Monthly Notices of the Royal Astronomical Society, 153: 401–412, 1971.

K. Nandra. The hot and energetic universe: A white paper presenting the science theme motivating the athena+ mission. 2013.

M. Neviere, D. Maystre, and W. Hunter. On the use of classical and conical diffraction mountings for xuv gratings. Journal of the Optical Society of America, 68(8), 1978.

P. H. H. Oakley. A Suborbital Payload for Soft X-ray Spectroscopy of Extended Sources. PhD thesis, University of Colorado, 2011.

J. Oort. Some phenomena connected with interstellar matter. George Darwin Lecture for the Royal Astronomical Society delivered on May 10, 1946, 1946.

J. P. Ostriker and C. F. McKee. Astrophysical blastwaves. Reviews of Modern Physics, 60(1), 1988.

S. Rappaport, W. Cash, R. Doxsey, and G. Moore. Discovery of a central x-ray object in the cygnus loop. The Astrophysical Journal, 186:L115–L118, 1973.

S. Rappaport, R. Doxsey, and A. Solinger. X-ray structure of the cygnus loop. The Astrophysical Journal, 194:329–335, 1974.

S. Rappaport, R. Petre, M. Kayat, K. Evans, G. Smith, and A. Levine. X-ray image of the cygnus loop. The Astrophysical Journal, 227:285–290, 1979.

J. C. Raymond, R. J. Edgar, P. Ghavamian, and W. P. Blair. Carbon, helium, and proton kinetic temperatures in a cygnus loop shock wave. The Astrophysical Journal, 805(152), 2015.

S. R. Roberts and Q. D. Wang. X-ray emission from charge exchange in the cygnus loop snr. Monthly Notices of the Royal Astronomical Society, 449, 2015.

G. B. Rybicki and A. P. Lightman. Radiative Processes in Astrophysics. Wiley-Interscience, 1979.

F. Sauli. Principles of operation of multiwire proportional drift chambers. Lectures given in the Academic Training Programme of CERN, 77(09), 1977.

F. Sauli. Gem: A new concept for electron amplification in gas detectors. Nuclear Instruments and Methods in Physics Research, 386:531–534, 1997.

J. Sauvageot and A. Decourchelle. Kinematics of the 10^6 k gas derived from coronal iron lines in the cygnus loop supernova remnant. Astronomy and Astrophysics, 296:201–209, 1995.

F. Seward. The geographical distribution of 100-kev electrons above the earth's atmosphere. Proceedings of the workshop on electron contamination in X-ray astronomy experiments, 1973b.

F. Seward, R. Grader, A. Toor, G. Burginyon, and R. Hill. Electrons at low altitudes: A difficult background problem for soft x-ray astronomy. Proceedings of the workshop on electron contamination in X-ray astronomy experiments, 1973a.

P. Shull and H. Hippelein. A kinematic and proper-motion survey of the cygnus loop. The Astrophysical Journal, 383:714–728, 1991.

S. Snowden, G. Hasinger, K. Jahoda, F. Lockman, D. McCammon, and W. Sanders. Soft x-ray h i surveys of the low nh region in ursa major. The Astrophysical Journal, 430:601–609, 1994.

S. Snowden, R. Egger, D. Finkbeiner, M. Freyberg, and P. Plucinsky. Progress on establishing the spatial distribution of material responsible for the 1/4 kev soft x-ray diffuse background: Local and halo components. The Astrophysical Journal, 493:715–729, 1998.

P. Soffitta and T. X. S. Team. Xipe: the x-ray imaging polarimetry explorer. Experimental Astronomy, 36:523–567, 2013.

W. Straka, J. Dickel, W. Blair, and R. Fesen. A comparison of high-resolution radio and optical data for the northeast region of the cygnus loop. The Astrophysical Journal, 306:266–270, 1986.

T. Takahashi. The astro-h mission. Memorie della Societa Astronomica Italiana, 84:776–781, 2013.

T. Tamagawa, N. Tsunoda, A. Hayato, H. Hamagaki, M. Inuzuka, H. Miyasaka, I. Sakurai, F. Tokanai, and K. Makishima. Development of gas electron multiplier foils with a laser etching technique. Nuclear Instruments and Methods in Physics Research, 560:418–424, 2006.

T. Tamagawa, A. Hayato, K. Abe, S. Iwamoto, S. Nakamur, A. H. T. Iwahashi, K. Makishima, H. Hamagaki, and Y. L. Yamaguchi. Gain properties of gas electron multipliers (gems) for space applications. Proceedings of SPIE, 7011(70113V), 2008.

A. Tielens. The Physics and Chemistry of the Interstellar Medium. Cambridge University Press, 2005.

H. Tsunemi, S. Katsuda, N. Nemes, and E. D. Miller. The plasma structure of the cygnus loop from the northeastern rim to the southwestern rim. The Astrophysical Journal, 671:1717–1725, 2007.

H. Tsunemi, M. Kimura, H. Uchida, K. Mori, and S. Katsuda. Another abundance inhomogeneity in the south east limb of the cygnus loop. Publ. Astron. Soc. Japan, 61:S147–S153, 2009.

J. H. Tutt, R. L. McEntaffer, C. DeRoo, T. Schultz, T. Rogers, N. Murray, A. Holland, D. Weatherill, K. Holland, D. Colebrook, and D. Farn. Technological developments of the ogre focal plane array. Proc. of SPIE, 9601:960105–1 – 960105–11, 2015.

H. Uchida, H. Tsunemi, S. Katsuda, M. Kimura, H. Kosugi, and H. Takahashi. Abundance inhomogeneity in the northern rim of the cygnus loop. Publ. Astron. Soc. Japan, 61:503–510, 2009a.

H. Uchida, H. Tsunemi, S. Katsuda, M. Kimura, H. Kosugi, and H. Takahashi. Line-of-sight shell structure of the cygnus loop. The Astrophysical Journal, 705:1152–1159, 2009b.

H. Uchida, H. Tsunemi, S. Katsuda, K. Mori, H. Nakajima, and M. Kimura. A detailed suzaku study of an evolved snr, the cygnus loop. AIP Conference Proceedings, 1427(94), 2012.

P. Vedder, C. Canizares, T. Markert, and A. Pradhan. High-resolution x-ray spectroscopic evidence of nonequilibrium conditions in the cygnus loop. The Astrophysical Journal, 307:269–274, 1986.

P. Vincent, M. Neviere, and D. Maystre. X-ray gratings: the gms mount. Applied Optics, 18(11), 1979.

J. Vink. X-ray high resolution and imaging spectroscopy of supernova remnants. Proceedings of the The X-ray Universe 2005 (ESA SP-604). 26-30 September 2005, El Escorial, Madrid, Spain, 2006.

J. Vink. Supernova remnants: the x-ray perspective. The Astronomy and Astrophysics Review, 20 (49), 2012.

M. Weisskopf, R. Ballazzini, C. Enrico, M. Giorgio, H. Marshall, S. O'Dell, G. Pavlov, B. Ramsey, and R. Romani. Transforming our understanding of the x-ray univers: The imaging x-ray polarimeter explorer (ixpe). American Astronomical Society, HEAD meeting, 2014.

E. C. Whipple. Potentials of surfaces in space. Reports on Progress in Physics, 44:1197–1250, 1981.

B. Woodgate, H. Stockman, J. Angel, and R. Kirshner. Detection of the [fe xiv] coronal line at 5303 angstroms in the cygnus loop. The Astrophysical Journal, 188:L79–L82, 1974.

B. Zeiger, W. Cash, and D. Swetz. The test pilot sounding rocket payload. American Astronomical Society, HEAD meeting, 2013b.

B. R. Zeiger. Soft X-ray spectroscopy of the Vela supernova remnant. PhD thesis, University of Colorado, 2013.

X. Zhou, F. Bocchino, M. Miceli, S. Orlando, and Y. Chen. The origin of the x-ray-emitting plasma in the eastern edge of the cygnus loop. Monthly Notices of the Royal Astronomical Society, 406: 223–229, 2010.